Erosion, deposition and material migration in the JET divertor with carbon and ITER-like walls

James Michael Beal

Doctor of Philosophy

University of York
Physics

March 2016

Abstract

This study investigates erosion, deposition and material migration in the divertor of the fusion tokamak JET. Nuclear fusion provides a potential method for sustainable energy generation without large carbon emissions or long-term radioactive waste. Toroidal chambers with magnetic field coils known as tokamaks are used to contain the plasma of hydrogen fuel. The fuel ions can erode the plasma-facing materials, leading to degradation of plasma performance, limitation of vessel lifetimes and fuel retention. Plasma-material interaction is particularly significant in the divertor region of the tokamak. The carbon walls of JET-C have been replaced with the beryllium/tungsten walls of JET-ILW in anticipation of their use in the larger ITER tokamak. Determination and analysis of the different erosion/deposition characteristics provides vital information for the efficient, economic and safe operation of ITER.

A combination of diagnostics and modelling techniques have been applied to produce a detailed study of the important processes and results. Rotating collectors provide time-resolved deposition measurements through varying the surfaces deposited on; quartz microbalances (QMBs) use piezoelectric crystals to measure changes in deposited mass. A simple, geometrical model is used to describe the rotating collector depositions over long timescales, incorporating experimental data from sources such as spectroscopy. More detailed, higher time resolution modelling of erosion, deposition and transport in the JET-ILW divertor is performed with a Monte Carlo code written for this study.

The rotating collectors demonstrate a replacement of carbon by beryllium as the dominant impurity deposit in JET-ILW relative to JET-C and an associated reduction in deuterium retention. The total deposition rate on the JET-ILW collectors is reduced by an order of magnitude. In general, time-dependent modelled and experimental collector deposition profiles show good qualitative agreement. A lack of carbon deposition in the remote JET-C outer divertor for corner strike points is determined from the collector modelling and QMB measurements; similar behaviour is not observed for beryllium in JET-ILW. Additionally, there is a reversal of deposition asymmetry between the inner and outer divertor corners in JET-ILW. These different distributions of deposits are attributed to the different chemical properties of carbon and beryllium and their associated responses to elevated temperatures.

Local beryllium surface coverages have a considerable impact on erosion and deposition behaviour in JET-ILW due to reduced impurity concentrations. Monte Carlo modelling is used to assess the impact of varying strike points, beryllium fluxes, beryllium coverages and plasma temperatures/densities. Further insight is gained through comparison of modelling and experimental results. Peaking of the beryllium influx is investigated using divertor spectroscopy and modelling, revealing the importance of the limiter phase and initial divertor phase for beryllium erosion, deposition and transport.

Contents

List of Figures

List of Tables

Acknowledgements

First and foremost I would like to thank my supervisors, Prof. Kieran Gibson and Dr. Anna Widdowson, for their support and advice over the last three and a half years. I am grateful to them for dedicating their time and experience to provide guidance throughout my research, without which the results would be far sparser and the wrong turns far more frequent.

I would like to thank EPSRC and CCFE for funding my PhD. The York Plasma Institute and CCFE have both hosted me and provided material resources and valuable intellectual input through the wealth of knowledge of the resident research communities. In particular, the other members of the Erosion and Deposition group at CCFE, namely Kalle Heinola, Aleks Baron-Wiechec, Paul Coad and Charlie Ayers, have provided considerable guidance on many technical issues. Guy Matthews and Bruce Lipschultz have also been generous in relating their knowledge of a variety of topics.

The Fusion Doctoral Training Network/Fusion Centre for Doctoral Training have given me an academic foundation in fusion science and provided the framework for continued learning throughout my studies. Having access to such a large and diverse fusion research community has been of huge benefit.

I am grateful to the student communities at York and CCFE for providing advice on their particular areas of expertise and contributing to the enjoyment of my PhD in a wider sense. Their feedback and (constructive) criticism has been invaluable. Finally, I would like to thank my family, my friends and my partner Betsy for their unconditional support and encouragement throughout my studies.

Declaration

The work presented in this thesis was conducted under the supervision of Prof. Kieran Gibson and Dr. Anna Widdowson at CCFE while working on JET. I declare this work to be my own except where indicated below or by appropriate citation. This document has not been submitted for any other award at the University of York or at any other institution.

The ion beam analysis of the JET-C rotating collectors was conducted at the University of Sussex before the commencement of my PhD, lead by Paul Coad.

The ion beam analysis of the JET-ILW collectors was performed with the help of equipment and colleagues at IST University of Lisbon, led by Eduardo Alves.

Some of the results contained in Chapter 5 were previously published together with co-authors in the following article:

- J. Beal, A. Widdowson, K. Heinola, A. Baron-Wiechec, K. J. Gibson, J. P. Coad, E. Alves, B. Lipschultz, A. Kirschner, G. F. Matthews, S. Brezinsek and JET-EFDA contributors, "Analysis of rotating collectors from the private region of JET with carbon wall and metallic ITER-like wall," Journal of Nuclear Materials, vol. 463, pp. 818, 2015.

Some of the results contained in Chapter 6 were previously published together with co-authors in the following article:

- J. Beal, A. Widdowson, K. Heinola, A. Baron-Wiechec, K. J. Gibson, J. P. Coad, E. Alves, B. Lipschultz, A. Kirschner, H.G. Esser, G. F. Matthews, S. Brezinsek and JET-EFDA contributors, "Deposition in the inner and outer corners of the JET divertor with carbon wall and metallic ITER-like wall," Physica Scripta, vol. 2016, no. T167, pp. 014052, 2016.

Calculations of campaign-averaged deposition on the rotating collectors and advice on the operating features of the diagnostic were provided for the article below:

- A. Kirschner, D. Matveev, D. Borodin, M. Airila, S. Brezinsek, M. Groth, S. Wiesen, A. Widdowson, J. Beal, H.G. Esser, J. Likonen, N. Bekris, R. Ding and JET-EFDA Contributors, "Modelling of the material transport and layer formation in the divertor of JET: Comparison of ITER-like wall with full carbon wall conditions", Journal of Nuclear Materials, vol. 463, pp. 116-112, 2015.

Discussions of this work provided stimulus for some of the results explored in Chapter 5 and Chapter 6.

Chapter 1

Introduction

1.1 Energy supply and demand

A reliable supply of energy is essential for a wide range of human needs and endeavours, including heating, lighting, transport and food production. The methods by which energy is generated have varied significantly at different times and in different places, but a unifying characteristic is the ongoing increase in demand and a necessary growth in supply. This trend, particularly pronounced over the last 1-2 centuries, may be attributed to two main sources. Firstly, rapid growth in world populations due to medical advancements has naturally increased the absolute amount of energy that is used. Secondly, technological and economic progress have stimulated a desire for improved living standards, increasing the per capita energy demand due to the extra production and automation of services that is required.

Technological progress, as well as indirectly increasing demand, has also allowed this demand to be met through an expanded, more varied and more efficient energy sector. In order to be able to plan for future energy supply, it is necessary to ask to what extent the increases in demand are likely to continue. The Department of Economic and Social Affairs of the United Nations estimates that world populations will increase from 7.3 billion people in 2015 to 9-10 billion by 2050, with considerable uncertainty in the rate of increase thereafter [1]. Despite gains in energy efficiency, the International Energy Agency expects global energy demand to grow by 37% between 2014 and 2040, mostly due to growth in developing countries [2]. From one perspective, increasing energy usage is promising since it is generally seen to correspond to improved standards of living ([3], Figure 1.1). However, it is prudent to consider if the global energy sector is capable of the growth required to match the expected increases in demand.

The reliance of the energy sector on non-renewable fossil fuels is a significant liability, since it depends on the discovery and extraction of finite reserves of coal, oil and gas. Of these, it has been estimated that oil and gas reserves will have been exhausted by 2042, with coal reserves lasting until 2112 [5], leaving the energy sector exposed to a lack of resources in the second half of the 21st century. The burning of fossil fuels to satisfy the majority of the world's energy demands also gives rise to environmental concerns. The resultant increases in atmospheric carbon dioxide cause higher global

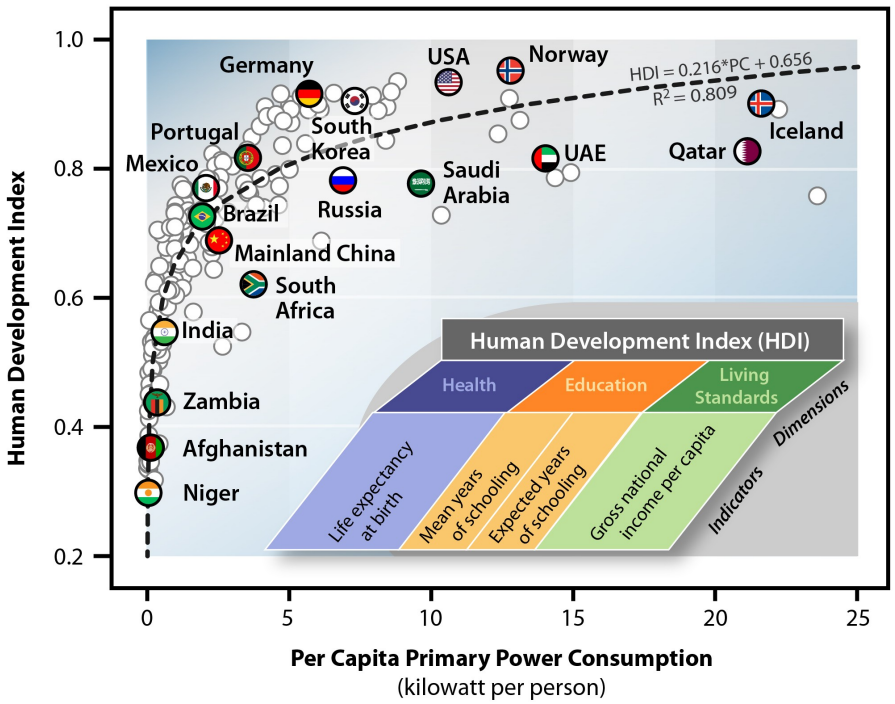

Figure 1.1: Plot showing the human development index for different countries as a function of their per capita power consumption [4]. The human development index is calculated based on both economic and social considerations, as depicted in the inset. Higher human development indices, corresponding to higher living standards, correlate with higher power consumptions.

surface temperatures through radiative forcing, giving rise to higher sea levels, loss of habitats and increases in extreme weather [6]. Thus, due to both finite resources and environmental considerations, it is increasingly necessary to diversify the global energy mix away from fossil fuels.

Though nuclear fission offers lower emissions than the burning of fossil fuels, fears over safety and the storage of long-term radioactive waste have limited largescale uptake. Recent decades have seen significant scientific and political efforts to expand the use of renewable energy from solar, wind and hydroelectric sources, among others. These generation methods have the advantage that the sources are non-depleting, allowing long-term energy security and low running costs. However, the reliance on meteorological conditions makes renewable energy vulnerable to intermittency, meaning it is not generally suitable for 'baseload' energy supply. Thus, having an energy mix dominated by renewables is difficult to achieve without large overcapacity, greatly improved energy storage capabilities and an expansion of electricity grids. It is desirable to develop an energy generation method which is amenable to human control, while also being safe, non-polluting and non-depleting.

1.2 Nuclear fusion

Nuclear fusion is the combination of light atomic nuclei to form a heavier nucleus and a net release of energy. Given that the reacting nuclei consist of protons (and

usually neutrons), both are positively charged and therefore repel each other due to the Coulomb force. If the nuclei can be brought into close proximity, at short ranges the attractive strong nuclear force overcomes the repulsive Coulomb force and a new nucleus is formed. In order to give the nuclei enough energy to overcome the repulsion, the reactants must be heated to very high temperatures and therefore usually exist in the plasma state.

A plasma is an ionised gas comprising a quasineutral ensemble of ions and electrons that exhibit collective effects. To be defined as a plasma, it must be of sufficient density for each charged particle to interact with many others and for bulk interactions to dominate over boundary effects. Additionally, it must be sufficiently hot for electrostatic effects to dominate over collisions with neutrals. The motion of the charged particles is prescribed by electromagnetic fields, but this motion also gives rise to feedback currents that result in changes to the fields themselves. This feedback and self-consistency demonstrates the collective nature of plasmas, as well as hinting at the complex range of drifts, waves and instabilities that this state of matter can exhibit.

For elements lighter than iron, the binding energy per nucleon, and equivalently the mass defect between the nucleus and the sum of its constituent nucleons, increases with atomic number. Thus, when light nuclei fuse to form elements of lower atomic number than iron, the reaction is exothermic and energy is released in the form of the kinetic energy of the reaction products. The Coulomb repulsion increases with atomic number due to the higher charges involved, making hydrogen a suitable choice of reactant. At achievable temperatures, the fusion reaction with the highest cross-section combines deuterium and tritium nuclei to form helium, a neutron and a net release of energy:

$${}^{2}_{1}\mathrm{D} + {}^{3}_{1}\mathrm{T} \longrightarrow {}^{4}_{2}\mathrm{He} + {}^{1}_{0}\mathrm{n} + 17.6\ \mathrm{MeV}.$$

Fusion has several advantages that have led to it becoming seen as one of the most promising contenders to supply future energy demands. Deuterium may be extracted from sea water and tritium bred from lithium through a fission reaction initiated by a fast fusion neutron. Thus, although the fuel cycle requires close control, the fuel reserves are in principle plentiful. This case is furthered by the high energy efficiency of fusion fuel relative to fossil fuels and even fissile fuels. Moreover, this high energy efficiency also means that a gigawatt-scale fusion device would only contain a few grams of fuel at any one time, lowering the risk of a large-scale nuclear accident.

In contrast to fission, there is no long-lived radioactive waste created by fusion; in contrast to the burning of fossil fuels, fusion does not release atmospheric pollutants such as carbon dioxide. Finally, fusion has the advantage of human control over the fuel and the energy production mechanisms, meaning that it could take the role of conventional power stations in providing baseload electricity supply. While fusion has been shown to have potential for energy generation, there are numerous technical issues that have prevented the achievement of net fusion energy to date. One of the most fundamental challenges is the confinement of the fusion plasma.

At the requisite temperatures, the plasma vaporizes any solid material surface it comes into contact with. Neglecting the gravitational confinement that holds the fusion reactants together in stars, terrestrially there are two main confinement approaches. Inertial confinement fusion typically uses lasers to ablate the outer layers of a fuel pellet, initiating an equal and opposite force that causes the fuel inside the

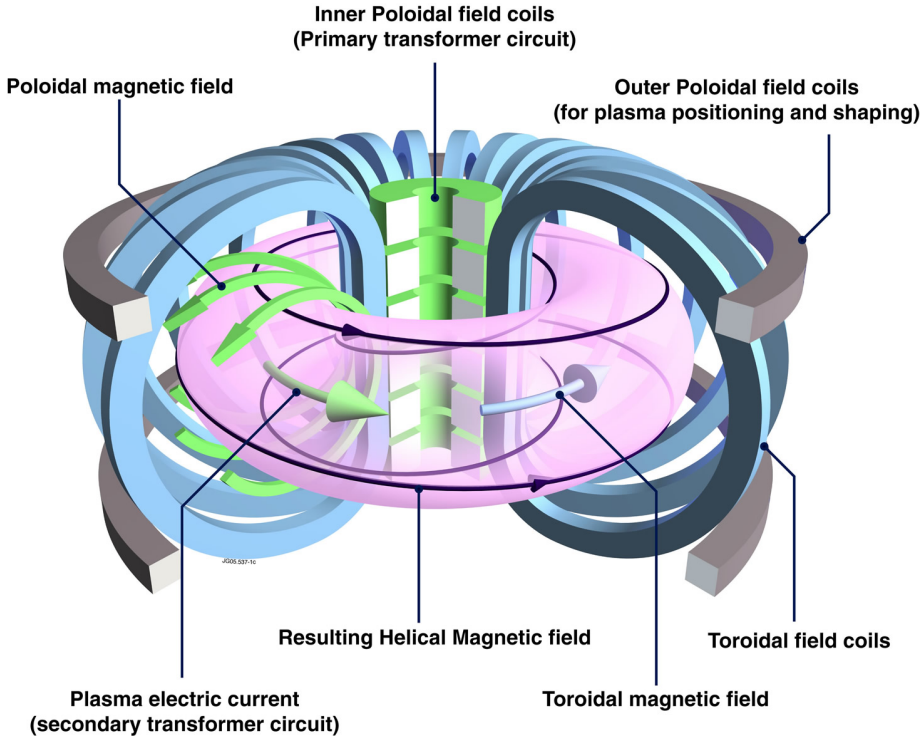

Figure 1.2: Schematic of a tokamak: poloidal and toroidal field coils create helical magnetic field lines that the charged particles of the plasma follow [7].

pellet to compress and reach very high temperatures and densities. Thus, this is an inherently pulsed approach to confinement and to energy generation. Magnetic confinement fusion exploits the charged nature of the plasma's constituent species to hold the reactants in a magnetic field, obviating the need for material contact. At present, a toroidal magnetic confinement configuration known as a tokamak represents the most developed fusion technology for the pursuit of energy generation.

1.3 Tokamaks

An introduction to the design and operation of tokamaks is presented here; for a comprehensive explanation of the concepts described in this section see the discussion in [8]. A tokamak holds the charged particles of the plasma fuel inside a toroidal vacuum chamber using a combination of magnetic fields (Figure 1.2). Confinement of the plasma is achieved by using both toroidal and poloidal fields to maintain an equilibrium between the plasma pressure gradient and the magnetic forces. A driven current in the inner poloidal field coils sets up a toroidal electric field in the plasma through transformer action. This in turn generates a toroidal current in the plasma, which produces a poloidal magnetic field. In practice, it is possible to operate in scenarios where a significant fraction of the toroidal current is self-generated by the plasma. The toroidal magnetic field is produced by currents driven in the external toroidal field coils. Additionally, outer poloidal field coils are used to help shape and position the plasma. The combination of poloidal and toroidal fields causes the charged particles of the plasma to flow around the torus along helical paths on closed flux surfaces. This helical topology is necessary to avoid particle losses due to plasma

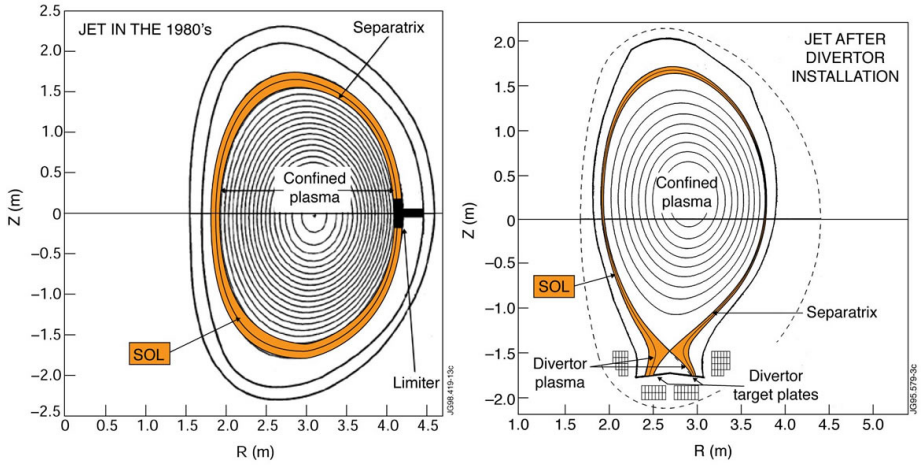

Figure 1.3: The interaction of the plasma with tokamak walls is localized to either limiters (left) or divertors (right) [9].

drifts.

A vacuum is created inside the torus using external pumps, with the low density deuterium-tritium fuel injected by gas puffing or in pellet form. The heating of the fuel, to temperatures of order 10 keV (∼100 million °C), is accomplished using a combination of three main methods. Firstly, Ohmic heating occurs when the current induced in the plasma by the magnetic fields causes heating due to the plasma's finite resistance. Since the resistivity of a plasma decreases with increasing temperature, there is a limit beyond which this is ineffective for further heating. Secondly, neutral-beam injection introduces high-energy, neutral, hydrogen isotopes to the tokamak. These heat the plasma through collisional energy transfer and also supplement fuelling. Finally, radio-frequency heating uses electromagnetic waves with frequencies matched to resonances of the plasma motion to transfer energy to the charged particles.

The heating mechanisms are focused towards generating very high temperatures (and relatively high densities) in the core plasma region located at the centre of the poloidal cross-section of the torus. It is this region where the fusion reaction has the greatest cross-section and consequently the longer the fuel ions can be kept in the core, the greater the fusion yield that can be achieved. However, the confinement provided by the magnetic fields is not perfect, with a net flow of particles from the core to the walls typically giving confinement times of order 1 s in the largest tokamaks operating today. Classical transport describes the radial motion of particles out of the plasma due to Coulomb collisions, which give diffusion with a step length of the Larmor radius. However, the toroidal geometry of the tokamak causes particles to undergo 'banana orbits', resulting in a larger diffusion step length of order the width of these orbits. Although this goes some way to accounting for the worse than expected confinement in tokamaks, most of the transport is 'anomalous', being due to as yet imperfectly understood turbulent processes. In addition to these mechanisms, there exist myriad plasma instabilities that can cause rapid ejections of particles and heat from the plasma.

At radii outside the core region, the temperature and density of the plasma decreases. In 'L-mode' low confinement regimes, this decrease is gradual; in 'H-mode' high confinement regimes, an edge 'pedestal' region forms with steep gradients in density

and temperature. The limiting boundary to the confinement region is the last closed flux surface. Inside this boundary, the field lines are closed and transport is mainly diffusive; outside the boundary, in the scrape-off layer (SOL), transport is mainly convective and particles travel along the open field lines. Close to the tokamak walls a Debye sheath forms, in which an electrostatic potential accelerates ions into the material surfaces. The high particle and heat fluxes in the SOL are known as the plasma exhaust and can cause severe material damage to surfaces on which they are incident. These areas of plasma-material interaction are localized at limiters or divertors (Figure 1.3).

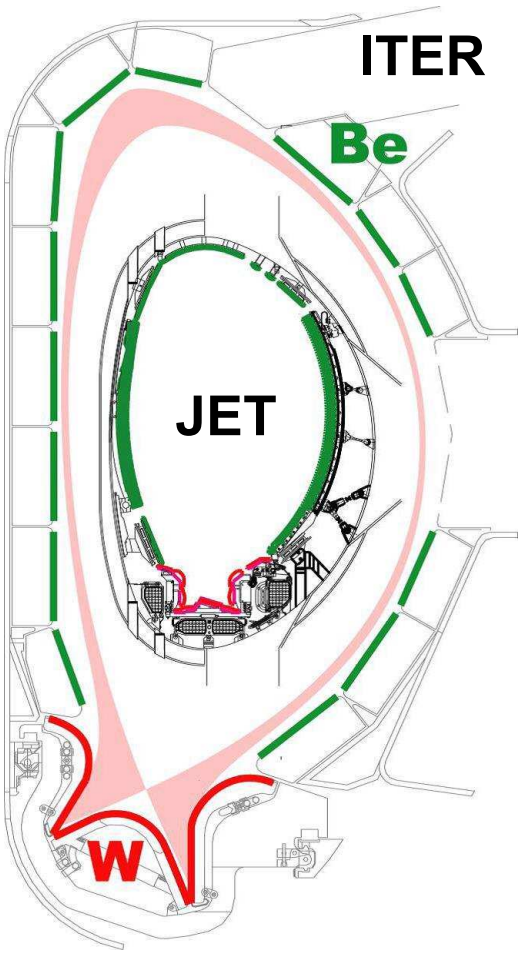

Figure 1.4: Comparison of the poloidal cross-sections of JET and ITER. The ITER-like wall of JET mimics the plasma-facing material combination to be used in ITER: beryllium main chamber (green) and tungsten divertor (red) [10]. ITER is approximately twice as large as JET in all dimensions.

A limiter is a solid projection of the vessel wall into the SOL, which reaches to the last closed flux surface. Since the limiter represents the material surface located furthest into the plasma, the heat and particles fluxes in the SOL are preferentially incident on the limiter rather than the rest of the wall, effectively limiting damage to the majority of the wall surface. In this configuration the limiter is in some sense sacrificial; its lifetime in a high-power, long-pulse tokamak is likely to be prohibitively short. In addition, material eroded from the limiter can enter the core plasma, degrading plasma performance (see Section 1.4). For these reasons, modern tokamaks usually localize the plasma-surface interaction at a divertor, far removed from the core plasma.

In a divertor configuration, the magnetic topology is altered using the outer poloidal field coils, such that the SOL transports the heat and particles of the plasma exhaust to the bottom (and/or top) of the torus. The locations on the divertor target plates where the plasma exhaust is incident are known as the strike points. These are narrow in poloidal extent due to the dominance of parallel over perpendicular transport in the SOL and thus the particle and heat fluxes on the material surfaces are considerable. In this configuration, the last closed flux surface is referred to as the separatrix, and the inboard and outboard sides of the SOL intersect at a region of zero poloidal magnetic field known as the X-point. The localization of the plasma-material interaction at the strike points restricts transport of eroded impurities to the core plasma.

This study will focus on the world's largest and most powerful tokamak - the Joint European Torus (JET). JET has a minor radius of 1.25 m and a major radius of 2.96 m. Plasma currents of 2 - 3 MA and discharge times of approximately 20 - 30 s are typical. The surface temperatures of the divertor tiles are generally of order 100 - 200°C, though at the strike points the temperatures can rise to around 1,000°C [11].

One of JET's key missions is to inform the physics basis in preparation for the completion of ITER, a tokamak currently under construction that is expected to produce a net energy gain from fusion for the first time. In particular, the ITER-like wall of JET currently offers the only opportunity to study the new plasma-facing material combination of beryllium and tungsten in a tokamak environment (on a reduced scale - see Figure 1.4) [12]. This is crucial for efficient operation of ITER, since the erosion and deposition of plasma-facing materials has a strong impact on vessel lifetime, plasma performance and the safe and economical use of fuel.

1.4 Erosion and deposition

There are a variety of mechanisms that can cause plasma-facing surfaces to be eroded (see e.g. Figure 1.5), some of which are briefly introduced here and their importance established. The simplest erosion mechanism is physical sputtering, which occurs

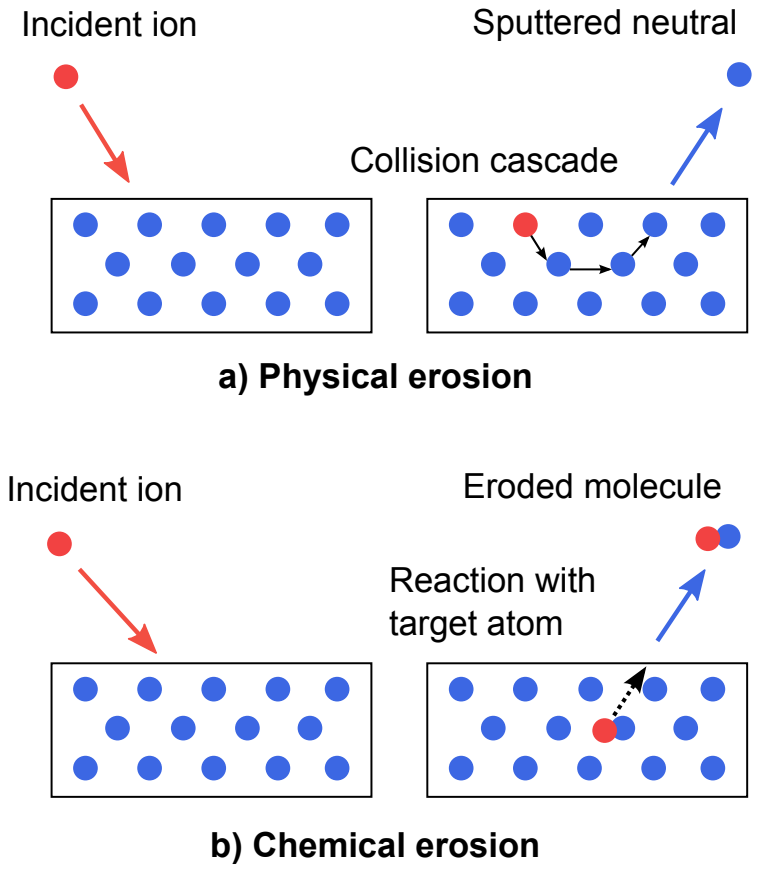

Figure 1.5: Schematic diagrams of physical (a) and chemical (b) erosion mechanisms from plasma-facing surfaces.

when ions from the plasma are incident on material surfaces, collisionally transferring energy to the material lattice. This has some probability of ejecting surface atoms into the plasma, depending on such quantities as the mass of the target atoms and the mass, energy and angle of approach of the incident ion. Chemical erosion, and chemically-assisted physical sputtering, can occur when incident and target species undergo chemical reactions, releasing the reaction products into the plasma. Wall materials may also be eroded by thermal mechanisms, leaving the material surface as a liquid through melting, or as a gas through sublimation. Eroded species can return to a material surface and redeposit on the surface, reflect from the surface, or sputter more impurities into the plasma, depending on the species involved and the local conditions. Similarly, eroded species may return to surfaces locally, be transported into the core plasma, or migrate to remote regions of the tokamak.

The most obvious challenge that erosion in tokamaks poses is the damage to wall materials that it entails. First walls are complex in their design and must be manufactured and installed with very high precision, meaning regular replacement of first walls would be prohibitively expensive and time-consuming. The amounts of erosion and deposition seen in present day tokamaks are generally on the order of microns to hundreds of microns per year. However, these devices are generally only operating plasmas for a fraction of a percent of the time. Fusion power plants would require far greater availabilities and would also be more powerful, suggesting that they would be vulnerable to macroscopic tile erosion on the order of centimetres. For fusion energy to succeed it must be both physically and economically feasible, necessitating the study and control of erosion in the tokamak environment.

As well as causing damage to the wall materials themselves, erosion can also degrade plasma performance. Impurities that migrate into the plasma radiate energy via line radiation and bremsstrahlung. These are both strong functions of the atomic number (Z) of the impurity. Low-Z impurities are fully stripped of electrons in the core plasma and thus radiative losses from these are lower, being only due to bremsstrahlung [13]. Radiative power losses may represent a significant fraction of the input power, thus reducing the energy confinement time and limiting the core temperature and fusion cross-section that can be achieved. Therefore, it is important to limit the erosion of impurities and their migration into the core plasma, particularly for higher-Z species (see Figure 1.6).

A second impact of impurity migration into the plasma is fuel dilution. There is an empirical upper bound on the electron density that can be achieved in tokamaks, described by the Greenwald limit [15]. Quasineutrality implies that this also sets an upper bound on the density of ions in the plasma, meaning that the ingress of impurities entails replacement of deuterium and tritium fuel ions in the plasma. This effectively lowers the fuel density, leading to lower cross-sections for fusion reactions and hence reduced energy gains. Since an impurity ion replaces a number of fuel ions equal to the number of protons it itself contains, this effect increases linearly with the atomic number of the impurity.

Impurities can also cause problems when they return to plasma-facing surfaces. Since they are generally in higher charge states than the fuel ions, they reach higher energies when being accelerated in Debye sheaths towards material surfaces. The self-sputtering yields for impurities can be significantly higher than those for impact by fuel ions, in some cases leading to runaway self-sputtering (with yields exceeding unity). The deposition of impurities on plasma-facing surfaces can also cause

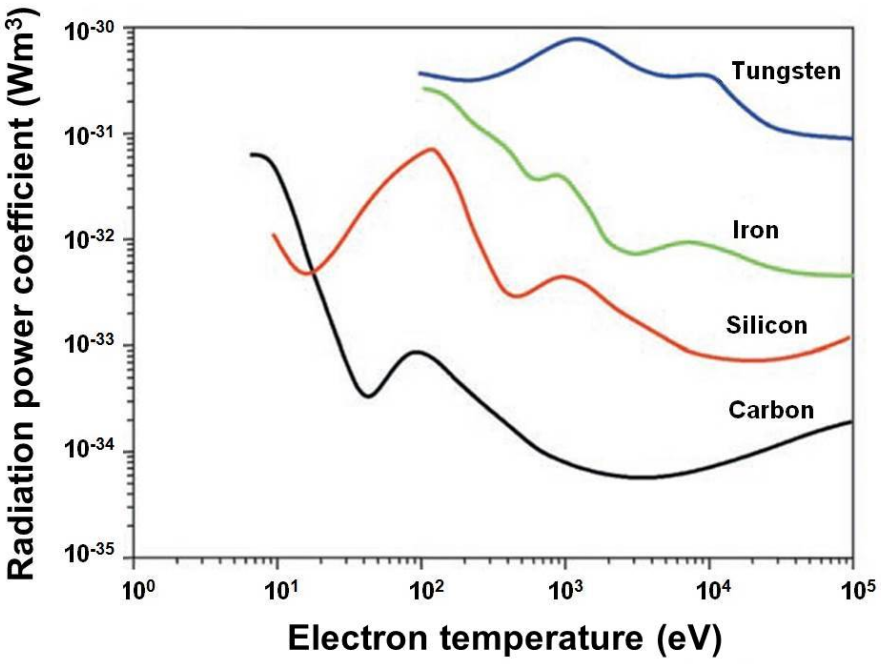

Figure 1.6: Impurities cause radiative power losses from the plasma due to line radiation and Bremsstrahlung, which are larger for higher-Z species [13]. The radiation power coefficient describes the power loss divided by the product of the number densities of electrons and impurities in the plasma (data from [14]).

operational uncertainty due to the different thermal and mechanical properties of redeposited wall species and clean tile surfaces [16]. Chemical bonding of impurities with fuel ions or mixing of different wall material species can result in plasma-facing surfaces that are unable to withstand the impinging heat and particle fluxes. For example, alloying of beryllium and tungsten can result in material with poor thermomechanical properties, which is of concern for beryllium/tungsten devices such as ITER [17].

The bonding of fuel ions with impurities also leads to deposits with high fuel retention. In particular, the chemical affinity between carbon and hydrogen isotopes can lead to the formation of hydrocarbons. Codeposition of carbon with fuel ions is especially prevalent in remote regions of the tokamak where high deuterium and tritium ratios have been found [18]. These areas are not directly exposed to the plasma and are generally much cooler than surfaces which are, allowing greater fuel retention. The retention of tritium in deposits is problematic from the perspectives of both safety and fuel conservation. Firstly, the amount of tritium in tokamaks is subject to strict legal limits due to the risks associated with its radioactivity. Secondly, having large concentrations of tritium in remote, unrecoverable regions makes achieving the required tritium self-sufficiency practically impossible. The expected tritium breeding ratios are not sufficient to allow for significant in-vessel tritium deposits that are lost to the fuel cycle.

Thus, the control of erosion, deposition and material migration in tokamaks is crucial for first wall lifetime, plasma performance, and the mitigation of fuel retention. The observed erosion/deposition characteristics are strong functions of the composition of the plasma-facing surfaces used. Therefore, the choice of wall materials must be

optimized in consideration of the issues outlined in this section. Carbon has until recently been the most popular plasma-facing material due to its excellent thermal properties and limited deleterious effects on the plasma through radiation and fuel dilution. This results in an advantageous lack of sensitivity to the sudden, and sometimes unexpected, plasma behaviour that is unavoidable in attempts to further the understanding of tokamak plasmas. However, in recent years it has become clear that the chemical erosion and high fuel retention effected by the chemical affinity of carbon and hydrogen isotopes make it incompatible with long-term tokamak operation.

As described in Section 1.3, the current preferred material combination uses beryllium plasma-facing materials in the main chamber and tungsten in the divertor. A crucial advantage of these materials is that they are relatively unreactive with hydrogen, limiting codeposition and fuel retention. The low atomic number of beryllium allows moderate impurity contamination of the core plasma without it becoming prohibitive, but its thermal properties are too poor for it to be used in the divertor. The high melting point of tungsten makes it suitable for withstanding the high heat fluxes at the strike points; its high atomic number limits physical sputtering.

1.5 Outline

The study reported here investigates the erosion, deposition and material migration in JET under ITER-like wall operation, comparing and contrasting to the corresponding behaviour under carbon wall operation. Analysis of the different erosion and deposition characteristics exhibited by these plasma-facing materials provides vital information for the efficient, economic and safe operation of ITER.

Proceeding from this introduction, Chapter 2 will describe and critique previous work on erosion, deposition and material migration in tokamaks in detail. This will enable the relevance and importance of the current study to be identified in the context of previous research. Chapters 3 and 4 will explain the experimental and computational methods that have been used to obtain the results that follow. The first of these results are presented in Chapter 5, in which the time-dependent depositions on passive diagnostics, located under the central divertor tile in JET-C and JET-ILW, are examined and compared to the results of a geometrical modelling approach. Chapter 6 extends this analysis to diagnostics in the inner and outer divertor corners, additionally characterizing the differences in the distributions of deposits in terms of the differing chemical properties of carbon and beryllium. Chapter 7 presents results gained from Monte Carlo modelling of erosion, deposition and migration of beryllium in the JET-ILW divertor. In Chapter 8, this Monte Carlo model is used to investigate a range of experimental results, furthering insight into the relative significance of the different processes involved. Finally, Chapter 9 summarises the previous chapters, enabling a set of comprehensive conclusions to be drawn.

Chapter 2

Erosion and deposition of plasma-facing components: origins and consequences

2.1 Introduction

As fusion research has progressed, the focus has begun to shift from the conceptual feasibility of energy gain to more technical issues associated with sustainable, efficient and economical fusion devices. The control of plasma-material interaction via the study of erosion and deposition of plasma-facing components (PFCs) is crucial for this pursuit. As such, a wide range of experimental and computational methods have been employed in researching this area. This section will describe and critique previous work on erosion, deposition and material migration in tokamaks. One aim of this is to present a cross-section of existing methods and results in order to provide scientific context. Secondly, the analysis of this previous work will enable gaps in the present research and understanding to be identified, using which the role of the current study will be outlined.

Erosion and deposition of wall materials have been studied in JET for the majority of its operational lifetime. For the most part, the discussion here is limited to the more recent campaigns with the most relevant divertor geometries. The MkII-HD divertor was installed in 2005, the general shape of which has been preserved in JET to the present day. This enables direct comparisons of results between campaigns. Selected erosion/deposition results from other tokamaks are also discussed where appropriate.

Section 2.2 will describe the literature underpinning the knowledge of sputtering yields and their importance in the tokamak environment. In Section 2.3, the determination of tile erosion and deposition using surface analysis methods will be discussed. A brief history of first wall materials used in tokamaks and their respective benefits and drawbacks will be covered in Section 2.4. Section 2.5 analyses the contribution of long-term diagnostics, while Section 2.6 focuses on diagnostics with time resolutions of milliseconds or below. In Section 2.7, previous uses of modelling

techniques for the analysis of erosion and deposition will be presented. Finally, Section 2.8 will draw together the various techniques used in research into erosion and deposition and define the approach and purpose of the current study.

2.2 Sputtering yields

The sputtering yields associated with plasma-facing materials in tokamaks directly relate the incident fluxes on material surfaces to the fluxes of eroded material entering the plasma. These are vital for determining the lifetimes of first wall components and assessing the degradation of plasma performance. The yields are not only functions of the incident and target species, but also the incident energy, incident angle, and sometimes the incident flux and target temperature. There are extensive studies in the literature covering a wide range of these variables.

2.2.1 Experimental

Measuring sputtering yields accurately in tokamaks can be challenging due to incomplete knowledge of both surface and plasma conditions. Although this makes extrapolation to other devices or conditions difficult, these in-situ studies do at least provide the most relevant sputtering yield data for the tokamak environment. Most such studies utilize spectroscopy to diagnose the prevalence of different species in the plasma close to material surfaces.

By examining the emission lines of molecular as well as atomic species, it has been possible to individually measure the contributions of physical and chemical sputtering of PFCs. This has been used to demonstrate a reduction of the carbon chemical sputtering yield in JET-C for large incident deuterium fluxes [19], and identified chemically-assisted physical sputtering of beryllium by deuterium in JET-ILW [20]. Spectroscopy has also been used in JET-ILW to determine that the sputtering yield of the tungsten divertor is only significant for incident beryllium impurities and during ELMs [21]. This reinforces the importance of the limitation of impurities and mitigation of ELMs in JET and ITER.

Since it can be difficult to prescribe or measure all of the possible variables in tokamak conditions, often yields have been measured using laboratory plasma-surface interaction devices such as PISCES-B [22] and Magnum-PSI [23]. These linear plasma generators seek to replicate the plasma conditions of tokamaks, allowing the study of sputtering yields in a more controlled and systematic way. This has been particularly useful for investigating the sputtering of beryllium (see e.g. [24]), since as a material it is far less well characterised than carbon due to its relative scarcity and the more stringent safety precautions that it imposes.

2.2.2 Computational

Calculations of sputtering yields have been made using computational models such as TRIM.SP [25] and ACAT [26], which employ the binary collision approxima-

tion. Under this assumption, ions propagate in matter by undergoing a series of independent binary collisions with target nuclei, while travelling in straight lines in between collisions [27]. In particular, Eckstein and Yamamura have contributed extensively to the population of sputtering yield databases, mainly using TRIM.SP and ACAT respectively. The large range of species to which these modelling efforts have been applied provides a valuable basis for ongoing studies of erosion and sputtering yields.

While the available data provides an indication of the sputtering yields in certain situations, for predictive purposes it is more useful to have analytic formulae that describe the yield as a function of quantities such as the incident energy. The most successful of these has been that provided by Eckstein and Preuss [28], based on an earlier treatment by Bohdansky [29]. The yield is described in terms of the atomic numbers, atomic masses, incident energy, incident angle and fitting parameters obtained via a Bayesian statistical analysis. A thorough listing of fitting parameters, as well as comparisons of fitted yields to those obtained from experiments and modelling, is provided in [30].

The above treatment provides the necessary formulae and data for calculation of physical sputtering due to a wide range of plasma ion and target material combinations. However, chemical sputtering occurs in tokamaks at energies below the threshold for physical sputtering [31], necessitating an alternative description. For the particular combination of hydrogen isotope ions incident on carbon, Roth and Garcia-Rosales [32] provided an analytical description encompassing physical sputtering, thermal breakdown of amorphous carbon-deuterium layers and chemically-assisted physical sputtering of weakly bound hydrocarbon molecules. This treatment has the advantage of additionally describing the variation of the yield with target temperature and incident flux, which have been seen to have a major influence on the degree of chemical erosion of carbon [33], [34].

The sputtering yield is the most important single measure of the scale of erosion due to plasma-material interaction. Accordingly, considerable effort has been devoted to determining the yields associated with many different ion-target combinations across a large range of conditions and using a variety of techniques. In many cases, the uncertainty associated with knowing local plasma conditions and hence prescribing the input to sputtering calculations can exceed the uncertainties inherent in the calculations themselves. The derived analytical sputtering formulae described above will be used in the current study for calculation of the sputtering sources from plasma-facing surfaces (see Section 4.1.3, Section 4.2.4 and Appendix A).

2.3 Tile analysis

The definitive measure of erosion and deposition in tokamaks is obtained by analysis of the tile surfaces themselves. The extreme conditions and engineering complexity of tokamaks make it difficult to apply advanced material analysis techniques in situ. For this reason, tiles are usually retrieved from the vessel during breaks in operations, typically after thousands of discharges. The post-mortem characterization of tiles offers the most complete understanding of changes to the material surfaces, but suffers from the temporal infrequency with which it can be applied.

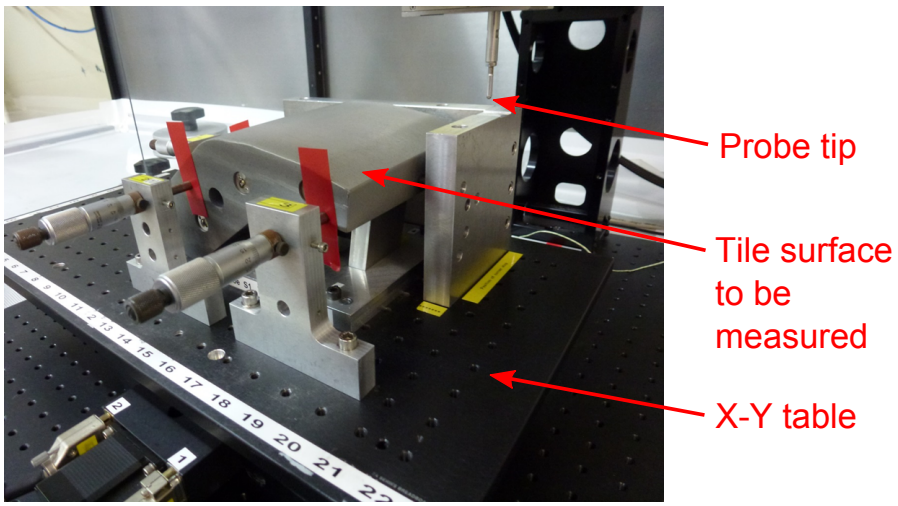

Figure 2.1: Tile profiling setup: the tile to be profiled is secured on an X-Y table, which moves under the probe tip to a series of pre-determined x-y locations. The probe tip descends in the z-direction, measuring the height of the tile surface.

2.3.1 Tile profiling

The simplest method for determining the erosion from or deposition on tiles is to physically probe their plasma-facing surfaces (Figure 2.1). By performing measurements covering a 2-D grid of a tile surface before and after it has been exposed to the plasma, a map of erosion/deposition is obtained by subracting one set of data from the other [35]. Possible translational and rotational misalignments between the before and after measurements result in an uncertainty of ∼5 μm in the z-direction.

The tile profiling results require calibration with optical microscopy measurements of cores cut from the tile in order to be made fully quantitative. This is due to the need to negate the effects of before/after misalignments of the tile. When additionally cross-calibrated with dust collection, this provides a powerful technique for global impurity accounting [35]. This enables relation of the total deposits found in the divertor to the total erosion observed in the main chamber, allowing impurity migration to the divertor to be inferred. The benefits of the combination of tile profiling and optical microscopy are also demonstrated in [36]. By calibrating the thickness of deposits on the edges of an inner wall limiter tile using microscopy, erosion of up to ∼60 μm was identified at the centre of the tile. This provides important experimental data regarding the lifetime of beryllium limiters.

The flexibility of tile profiling is a key benefit of the technique, since it enables the wide range of different tile shapes installed in JET to be analysed. However, while the ∼5 μm resolution was adequate for most JET-C measurements, it becomes close to marginal for the small surface changes seen in much of the JET-ILW divertor (though it does at least provide an upper limit on the scale of erosion or deposition) [37]. In order to probe smaller surface changes, and to determine the concentrations of different species, it is necessary to use more precise surface analysis techniques such as ion beam analysis.

2.3.2 Ion beam analysis

Ion beam analysis (IBA) encompasses a collection of techniques that use high energy ion beams to probe the surfaces of materials. The interaction of the incident ions with the target material results in a fraction of the incident ions/reaction products emanating from the sample, thereby becoming available for measurement by particle detectors. The energies at which they are collected are characteristic of the species and/or their depth within the sample, allowing species-specific, quantitative measurements to be made. In fusion applications, two of the most useful IBA techniques are nuclear reaction analysis (NRA) and Rutherford backscattering spectrometry (RBS). NRA relies on incident ions undergoing nuclear reactions with target atoms and is used to detect light target species; RBS exploits Coulombic collisions between incident ions and target nuclei and is more useful for the detection of heavier species.

IBA techniques have long provided important information on the changes to tile surfaces due to exposure in tokamaks. They are widely used across a range of devices, and have been used to show the similarities in deposition distribution/magnitude and deuterium retention between ASDEX, JET and DIII-D [38]. This provides an important examination of the accuracy and cross-machine applicability of erosion and deposition results. The species-dependence capabilities of NRA are demonstrated by results examining variations in the beryllium-carbon ratios comprising divertor deposits [39, 40]. Such results show the importance of chemical sputtering via the preferential removal of carbon from deposits, relative to beryllium [41].

The high sensitivity of NRA is necessary for characterising the often sub-micron deposits in the JET-ILW divertor [37, 42]. Whereas current tokamaks such as JET typically run discharges for a total of several minutes a day, future fusion reactors will have to have much greater operational availabilities, amplifying the scale of erosion or deposition. Thus, the ability to measure these small surface changes in today's devices is crucial for anticipating the larger changes that are expected in future tokamaks.

While NRA and RBS can be used to quantify thin deposits on tiles accurately, they are not immediately suitable for determining small amounts of erosion from bulk tiles. The limited range of the incident ions in target materials means that unexposed and eroded tiles would both yield spectra characteristic of the bulk tile material. In order to study erosion, marker tiles are installed in areas of a tokamak that are judged likely to undergo net erosion.

In JET-ILW, bulk beryllium marker tiles were coated with a 2-3 μm layer of nickel, with a further 7-10 μm layer of beryllium at the tile surface [43]. The degree of erosion of the upper beryllium layer can be detected via RBS, with the nickel layer acting as a substrate. Similarly, thin molybdenum interlayers inserted into tungsten-coated CFC and bulk tungsten tiles allow measurements of tungsten erosion using RBS [43]. During JET-C, carbon tiles were coated with thin layers of tungsten in order to measure tungsten erosion in preparation for the installation of the ILW [44]. Such coatings represent an important exercise in risk management, offering experimental experience and small-scale testing before costly and time-consuming machine upgrades are undertaken.

2.3.2.1 Microbeam IBA

In JET-C, the thicknesses of divertor deposits often exceeded 100 μm [40]. However, the penetration depth of ions into the target materials, at typical measurement energies of 2-3 MeV, is usually less than ∼10 μm. In such situations, IBA only measures the concentrations of different species in the near-surface regions of a deposit, with the total quantities extrapolated over the total thickness of the deposit as determined from cross-sectional microscopy. Depending on the operational history of each campaign and the degree of material mixing, this can leave results vulnerable to errors occurring due to variations in the prevalence of different species with depth.

One way to overcome this and probe the full depths of deposits is to cut cross-sections of tiles. Instead of taking IBA measurements with the ion beam incident perpendicular to the surface, they can be taken with the incident beam perpendicular to a cross-section of the tile, allowing characterisation of the full thicknesses of deposits. Typically measurements are taken with an ion beam spot size of ∼1 mm, which is clearly far too large to profile a 100 μm deposit. Ion microbeam techniques use magnetic lensing to produce spot sizes and hence depth resolutions of a few microns [45].

The reduced spot size of ion microbeams has allowed detailed measurements of the spatial distribution of deuterium trapped in Tore Supra carbon tiles, as well as relation of this distribution to the porosity of the carbon obtained by scanning electron microscopy [46]. Non-uniform deuterium retention has also been found in JET-C [47] and JET-ILW [48] divertor tiles, with preferential accumulation in pits and cracks. Such studies offer insights into the processes underpinning fuel retention, which is a key concern for future devices.

2.3.3 Fuel retention

Minimising in-vessel tritium inventories is critical for reasons of both safety and fuel efficiency. The scale and mechanisms of fuel retention must be understood in order for ITER to be fully exploited in terms of the number of pulses and the range of studies than can be accomplished (see Figure 2.2).

Tore Supra is the only large tokamak currently using superconducting magnetic coils, actively cooled plasma-facing surfaces and non-inductive current drive, allowing it to be used to investigate issues associated with long-pulse/steady-state operation [49]. The Deuterium Inventory in Tore Supra (DITS) project sought to investigate discrepancies between deuterium inventories measured by gas balance and post-mortem analysis and to better characterize the deuterium retention mechanisms involved [50].

Calculations of fuel retention in tokamak walls found from the difference between the deuterium pumped in and out of the vessel can be a factor of 5-10 greater than those found by post-mortem ion beam analysis techniques, leading to considerable uncertainty in fuel inventories [53]. The DITS project involved complementary use of techniques such as Secondary Ion Mass Spectrometry (SIMS), Thermal Desorption Spectroscopy (TDS) and NRA to determine the post-mortem global deuterium retention, spatial variations in deuterium inventory and concentrations of impurities

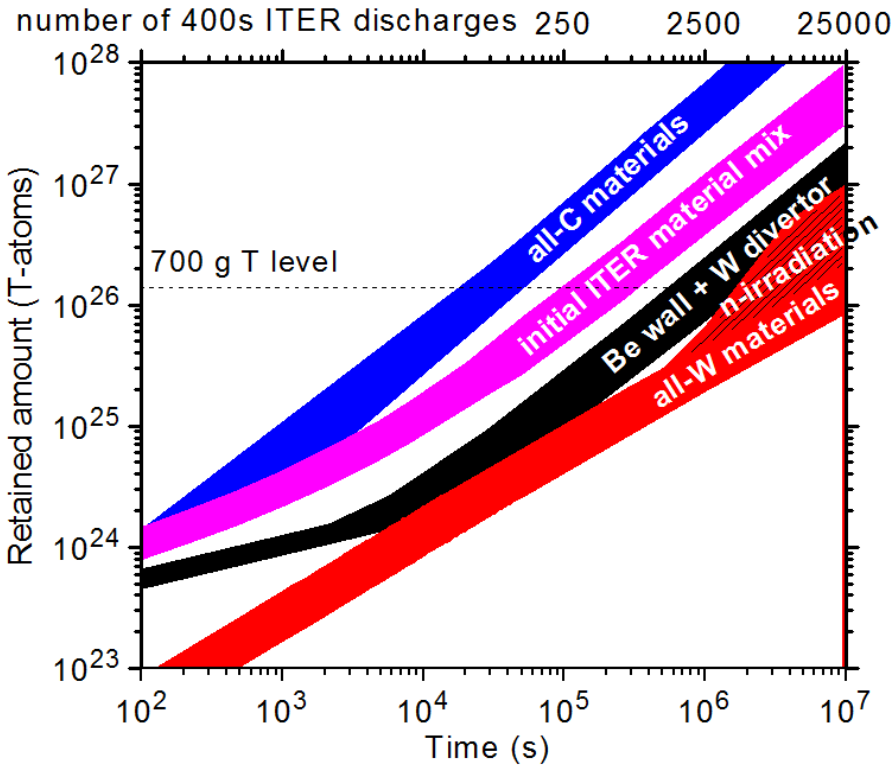

Figure 2.2: Projected tritium retention in ITER as a function of time for different choices of first wall materials. Licensing requires staying below a tritium inventory limit due to safety considerations, which was expected to be 700 g at the time this analysis was performed [51]. (The limit has changed over time and currently 1 kg of retained tritium is the prescribed limit [52].)

[54]. This detailed study found post-mortem deuterium retention equivalent to 50% of that calculated by gas balance. In particular, the gaps between castellations were found to be significant for deuterium retention, contributing approximately a third of the total inventory [54, 55]. 90% of the retention was attributed to codeposition of deuterium with carbon [54] and Raman microscopy suggested that deposited layers consisted mainly of amorphous hydrocarbon layers [56]. These analyses reinforce previous evidence of the strong dependence of fuel retention on the use of carbon plasma-facing materials.

Erosion and deposition in the JT-60U tokamak have been studied using a detailed range of surface analysis techniques, including tile profiling [57], SIMS [58] and Scanning Electron Microscopy (SEM) of deposit cross-sections [59]. These have shown the inner divertor to be dominated by carbon redeposition and the outer divertor to be mainly an erosion region, providing useful qualitative agreement with results from other tokamaks such as JET [18]. Surface analysis of the JT-60U tiles indicates that fuel retention has been mitigated by precise tile alignment, divertor geometry that limits transport to shadowed areas and high wall surface temperatures, which lessen the negative impacts of the carbon PFCs [60].

JET-ILW offers a unique opportunity to assess fuel retention in a beryllium/tungsten tokamak environment. Post-mortem IBA of tiles has indicated a reduction in the rate of deuterium retention by a factor of 18 relative to JET-C [61]. The largest areal densities of deuterium were measured in locations where the deposition of impurities

(dominated by beryllium) were also highest, such as on tile 1 at the top of the inner divertor. Conversely, deuterium concentrations at erosion-dominated regions such as at the midplane of the inner wall limiter were found to be very low. This highlights the fact that redeposited impurities in tokamaks continue to provide trapping sights for fuel retention.

Surface analysis of plasma-facing materials encompasses a wide range of methods, including mechanical probing of tile surfaces and ion beam analysis techniques. Tile profiling provides a cheap and flexible method for determining volumetric surface change on the scale of microns and above, but does not enable the highly quantitative, species-specific measurements that may be obtained by ion beam analysis. The ability to determine the relative amounts of different deposited species with high sensivity is crucial for understanding the performance of different plasma-facing materials and for the quantification of fuel retention.

The weakness that all the surface analysis techniques described in this section share is that they can usually only be applied ex situ. Hence, only a single temporal set of data is obtained for an entire operating campaign, limiting what can be inferred about the effects of varying plasma conditions. This will be returned to in section 2.5.2 through discussion of techniques capable of providing temporally-resolved data. Post-mortem analysis nevertheless provide the most accurate measure of the long-term erosion, deposition and migration behaviour in tokamaks, which ultimately sets a limit on the lifetime of vessels. Since the material composition of PFCs has such a significant impact on plasma-material interaction, the next section will provide an analysis of different first wall materials.

2.4 Choice of first wall materials

As the discussion in the preceding sections has made clear, the nature and degree of tokamak erosion, deposition and material migration processes are strong functions of the composition of the plasma-facing surfaces. This section provides a brief history of the first wall materials used in tokamaks and critiques their relative merits and vulnerabilities. Since the current study involves comparing and contrasting erosion/deposition between JET-C and JET-ILW, this discussion provides a backdrop to some of the analysis and results to be presented in the following chapters.

2.4.1 Carbon PFCs

Throughout most of the history of tokamak research, carbon has been the preferred choice of plasma-facing material. The most obvious hazard that first wall materials must endure is the high heat loads that they are subject to. The preferred carbon fibre composite (CFC) from which the tiles are made remains in the solid state up to high temperatures; above these temperatures the material sublimates rather than melting, preventing splashing of melt droplets. Additionally, the CFC has good thermal shock resistance to transient events such as disruptions or vertical displacement events [62].

As described in Section 1.4, the fact that carbon is low-Z means that, if it is eroded and transported into the core plasma, it radiates less then heavier elements would and results in less fuel dilution. This lack of sensitivity enables maintenance of good plasma performance despite erosion occurring. As a counterweight to this advantage, as a low-Z material carbon is more easily physically sputtered than heavier elements.

However, the chief difficulty with the use of carbon as a first wall material is its high reactivity with hydrogen isotopes. Carbon is chemically eroded by deuterium both through reaction with thermalised ions and via a chemically-assisted physical sputtering process [33]. This chemical affinity has also been observed to lead to high deuterium and tritium retention, particularly in remote divertor areas [18]. Such fuel retention is unacceptable in future devices due to the safety concerns associated with large tritium inventories and the implications of the effective loss of a large fraction of the tritium from the fuel cycle.

It has been suggested that maintaining the first wall at $\simeq$ 800 K could nevertheless allow ITER to operate with carbon PFCs [60]. However, such temperatures are incompatible with the planned active cooling with pressurized water and the required power handling capabilities [63]. Ultimately, the issue of fuel retention has, in recent years, led to a broader adoption of metal PFCs. In particular, ITER will utilise beryllium in the main chamber and tungsten in the divertor, a material combination that is mimicked in JET's ITER-like wall [12].

2.4.2 Beryllium and tungsten PFCs

The main advantage of beryllium and tungsten is their limited reactivity with hydrogen isotopes, which has been seen to result in decreased fuel retention in JET-ILW [61]. Like carbon, beryllium is low-Z, meaning that power losses and fuel dilution due to beryllium in the core plasma are relatively low. In addition, beryllium is efficient at gettering of oxygen, reducing the impurity content of the plasma [64].

Beryllium has relatively high sputtering yields at moderate incident energies and its thermal properties are considerably poorer than those of carbon. It melts above 1,560 K, leaving the PFCs susceptible to melt damage and the splashing of droplets. For these reasons, beryllium is not suitable for use in the divertor and ITER will use tungsten PFCs in this region. The high-Z nature of tungsten and its high melting point render it robust to the high heat and particle loads in this area. Even low levels of tungsten contamination in the core plasma result in unacceptable radiative losses. This is offset by the spatial separation of the tungsten divertor PFCs from the core plasma and the propensity of eroded tungsten to promptly redeposit close to its point of origin [65].

Several concerns remain regarding the long-term thermomechanical properties of tungsten PFCs. Melt layers have been found to develop on tungsten surfaces, reducing power-handling capabilities via recrystallization and bubble formation [66]. Additionally, the formation of helium-rich porous surface layers known as 'tungsten fuzz' has been observed [67]. The temperature window in which tungsten can operate as an effective PFC is limited at the lower end by embrittlement and at the upper end by creep, with the effects of neutron irradiation further limiting this temperature

range [68]. Finally, a possible difficulty associated with using multiple materials as PFCs is the formation of mixtures with eutectic melting points. Alloying of tungsten with beryllium has been found to significantly lower its melting point and thus its power-handling capabilities. Continued investigation of the thermal and mechanical properties of all-metal PFCs is vital for the achievement of sustainable fusion power generation.

The strong thermal properties of carbon walls and their limited deleterious effects on plasma performance have made them popular choices for tokamak first walls. However, the high chemical erosion and fuel retention associated with carbon PFCs is unacceptable for future fusion reactors. The lower fuel retention of beryllium and tungsten has prompted an adoption of these materials in recent years. The low radiative losses associated with beryllium and its gettering of oxygen make it appropriate for the tokamak main chamber; the high melting point and sputtering threshold of tungsten make it a suitable divertor material.

2.5 Long-term erosion/deposition diagnostics

2.5.1 Campaign-averaged diagnostics

This section will describe the use of louvre clips, deposition monitors and mirrors as erosion/deposition diagnostics. These provide reliable long-term deposition data relating to the specific locations in which they are placed. This can be used to infer aspects of the relevant deposit formation or migration processes. All these diagnostics can act as passive substrates for deposition, with post-mortem IBA yielding the cumulative deposition due to whole operating campaigns. The limitation of these diagnostics is that it is not possible to correlate material deposition with varying operating conditions as only campaign-averaged measurement is possible. Nevertheless, such results are useful in the current study for comparison with the aggregate deposition on time-resolved diagnostics such as rotating collectors and quartz microbalances (QMBs).

2.5.1.1 Louvre clips

The water-cooled louvres (see Figure 2.3) are located in the remote corners of the JET divertor and protect the magnetic field coils from radiation from the plasma [42]. These shadowed areas can contribute considerably to the total fuel retention due to their relatively low temperatures. In particular, after the deuterium-tritium fuelled DTE1 campaign, the majority of the retained tritium was determined to be on the inner louvres or bound in flakes that had spalled from them [41]. In order to make the study of the deposition in these locations easier, clips were attached to the inner and outer louvres. These louvre clips can be detached during shutdowns, allowing them to be analysed easily using IBA techniques. These continue to provide quantitative data on the migration of impurities to remote areas and the degree of fuel retention in these deposits, allowing important comparisons to be made between JET-C and JET-ILW [42].

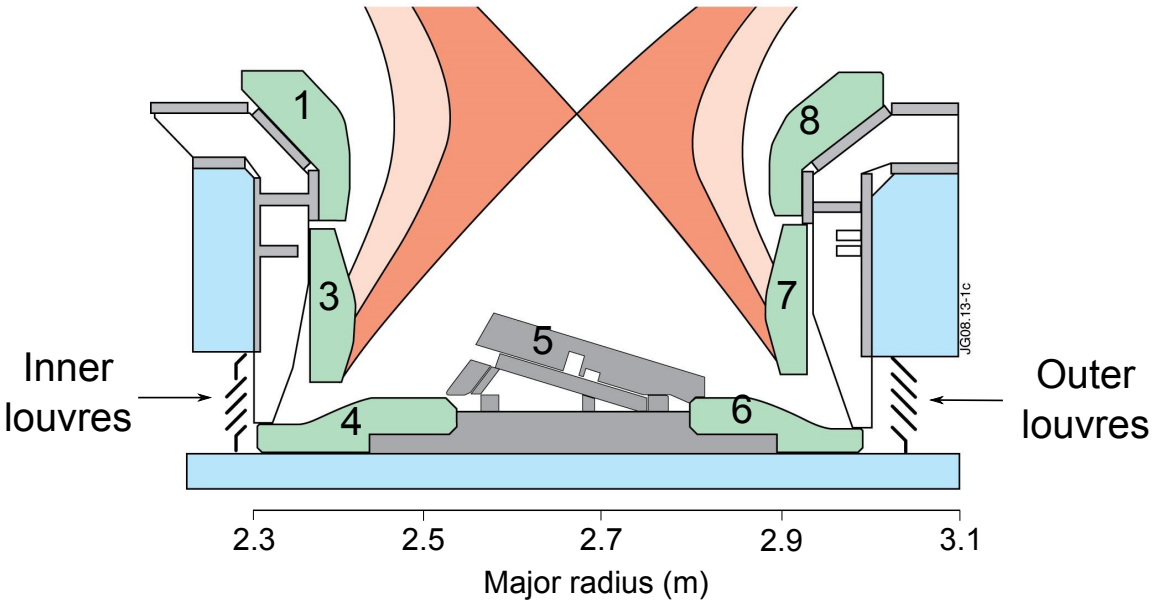

Figure 2.3: Diagram showing the JET-C MkII-HD divertor, with tile numbers labelled. The louvres clips are attached to the water-cooled louvres in the remote inner and outer divertor corners as indicated

.

2.5.1.2 Deposition monitors

The migration of a given species to a surface does not necessarily entail its permanent deposition on that surface. The incident particle may adsorb/stick to the surface, react with a surface molecule, or be reflected from the surface. The probability of these processes occurring can be investigated using deposition monitors (or 'cavity samples'). These consist of two parallel silicon plates, with a thin aperture in the upper plate closest to the plasma. By comparing the deposition on the lower and inner and outer upper plates, the sticking probability of the incident species can be determined [69].

Deposition monitors have been used in ASDEX Upgrade to infer the formation of hydrocarbon layers due to sticking of hydrocarbon radicals with high surface loss probabilities [70]. Similar studies in JET have produced comparable results and linked the deposition to the campaign-averaged strike point distributions [71, 72]. The importance of strike point locations for erosion/deposition is a major aspect of the current study. Time-dependent diagnostics such as rotating collectors and QMBs further allow the effects of variations in strike point distributions during campaigns to be investigated.

2.5.1.3 Mirrors

Mirrors are important for a wide range of imaging and visible spectroscopy diagnostics in tokamaks, which in turn are crucial for understanding plasma behaviour and protecting the vessel walls. Both erosion from and deposition on mirrors can degrade reflectivity and distort the reflected images. In order to understand the limits to the lifetime of the metallic mirrors that will be used in ITER, a 'First Mirror

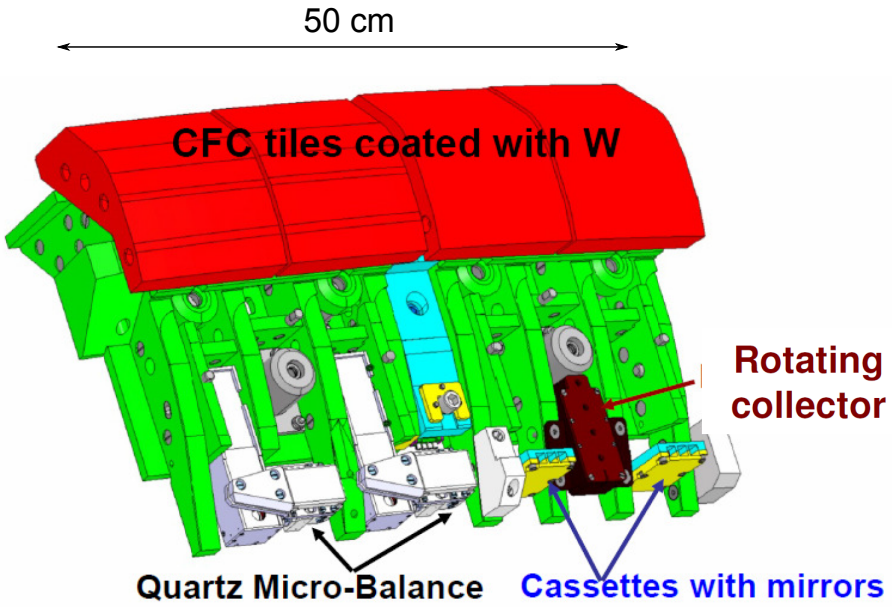

Figure 2.4: Diagram showing the positioning of two mirror casettes, a rotating collector and two quartz microbalances in the JET inner divertor.

Test' was initiated in JET [73]. The surface alterations and changes in reflectivity were determined for both JET-C [74] and JET-ILW [75] operation. In both cases, mirrors located in the main chamber suffered limited degradation in reflectivity. In the divertor, although deposits on the mirrors were thinner for JET-ILW than for JET-C, the reflectivity of the mirrors was still reduced by 50 - 85%, suggesting that this issue remains a major technological challenge for future tokamaks.

As well as providing information regarding reflectivity, it is noted that the mirrors can be treated more simply as substrates for deposition, in a similar way to the louvre clips. Via ion beam analysis, they provide species-dependent deposition information from a range of recessed vessel locations. This information is useful for quantitative comparisons with other deposition measurements, particularly as many of the mirrors are located in similar positions to rotating collectors and quartz microbalances (Figure 2.4).

2.5.2 Time-resolved diagnostics

2.5.2.1 Rotating collectors

The extensive post-mortem analysis of a wide range of tiles and stationary diagnostics provides the ultimate test of material erosion and deposition over the course of a campaign (Section 2.3). Unfortunately, since each campaign typically comprises approximately a year of operation and thousands of discharges, such results necessarily average over a large range of plasma conditions. In order to separate the effects of different periods of operation, rotating collectors vary the surface that is available for deposition.

Rotating collectors were developed to study erosion and deposition in JET, as first described in [76]. A rotating collector consists of a silicon disc that is shadowed by a metal casing with a thin slit in it. By gradually rotating the disc, different

regions around the circumference of the disc are exposed for deposition. Through post-mortem IBA of the deposits and mapping of the locations on the disc to discharge number, the deposition as an approximate function of discharge number may be obtained. The finite size of the collector, slit width and IBA beam width do not allow a time resolution of single pulses. However, the resolution of around 50 pulses, or approximately two days of operation, nevertheless represents a marked improvement on the resolution of whole campaigns associated with post-mortem tile analysis. To improve the reliability of the diagnostic, the collectors utilize no electronic components, with rotation driven by the pulsed magnetic field.

Rotating collectors were first installed in JET in 2005 in the inner, central and outer divertor and on the outer wall [77]. The poloidal locations of the collectors coincide with those of the mirror casettes and quartz microbalances (see Figure 2.4). The deposition on the collector under the central divertor tile was correlated with strike points with a line of sight to the collector, demonstrating the importance of the line of sight transport of neutrals to remote regions [77]. The deposition on the outer wall collectors is harder to interpret since this is generally a net erosion region. However, the periodic beryllium evaporations that were performed for surface conditioning purposes were captured in stripes of beryllium seen on the collector discs [40]. This was used to infer that the beryllium evaporator heads (that were used to achieve the surface conditioning) reduced in efficiency with time due to the formation of oxide films on their surfaces.

Rotating collectors are of considerable value as a medium time resolution deposition diagnostic in JET. The resolution is sufficient to analyse the deposition in terms of the long-term variation of plasma parameters and configurations present in different experiments. However, if the operating conditions vary over too short a timescale, the effects of the variations on the deposition are difficult or impossible to resolve. The time-dependent, species-specific measurements from several JET-C/JET-ILW locations that are provided by the collectors are used widely in the current study. The detailed working mechanisms of rotating collectors will be described in Section 3.1.1 and results from them are presented and analysed in Chapter 5 and Chapter 6.

2.5.2.2 Quartz microbalances

Quartz microbalances (QMBs) exploit the dependence of the frequency of vibration of an oscillating quartz crystal on its mass to determine erosion and deposition. The effective mass of the crystal may be increased by material from the plasma depositing on it, with re-erosion from the crystal causing a decrease in mass. Thus, by monitoring the frequency of the crystal, a time-dependent measure of erosion and deposition is obtained.

The measurement crystals are typically exposed for ∼1-5 seconds during a targeted period of a pulse, through the opening of a cover (Figure 2.5). The frequency of vibration of the crystal is dependent on temperature as well as mass, which is corrected for by comparison to the frequency change of a second, unexposed crystal. In order to further limit the thermal effects, the final frequencies are taken several minutes after the pulse, when the system is more thermally equilibrated. Thus, although the sampling resolution of the QMBs is of order 1 s, only one data point is obtained for

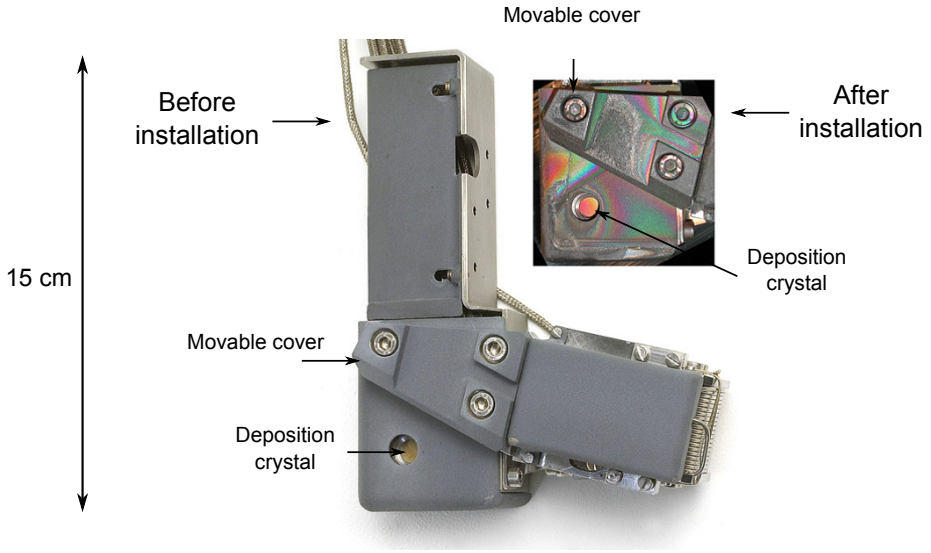

Figure 2.5: Image showing a QMB system before (left) and after (right) installation in JET-C. Deposition occurring during the time the QMB spends in the vessel is visible in the after image. The cover is pivoted away from the crystal for several seconds during a discharge in order to measure the erosion/deposition during this time window [78].

each discharge. The resulting measurement of erosion/deposition is the total mass change that has occurred during the time that the cover was open for. The ability to temporally target the QMBs means that the plasma parameters during this time window are well-known. The plasma conditions are more exactly specified than those corresponding to the ∼50-discharge average taken by the rotating collectors.

While quartz microbalances have long been used in laboratory conditions to measure thin film growth, their first application to fusion was in the Canadian TdeV tokamak [79]. QMBs with electronics resilient to high temperatures [80] were developed based on the similar demands imposed by their use in oil wells, and tested in TEXTOR [81]. Subsequently, QMBs were installed to measure erosion and deposition in the divertors of ASDEX [82] and JET [83]. In JET, the QMBs occupy analogous positions to the rotating collectors and mirror cassettes (Figure 2.4). Although precautions have been taken to attempt to improve the reliability of the QMBs, the harsh tokamak environment has still prematurely reduced their lifetimes on several occasions. Despite this, they have been used widely and provided valuable erosion and deposition data over the past decade.

The deposition on the QMB under the central divertor tile in JET-C has been shown to qualitatively agree with that on a rotating collector in a similar location [77]. The periods of operation with strike points with a line of sight to the collector/QMB showed high collector/QMB deposition. Conversely, when strike points did not have a line of sight to the collector, the net deposition on the collector was very low and the QMB exhibited re-erosion. This reinforces the importance of the line of sight transport of eroded neutral impurities. The ability to measure net erosion as well as net deposition is an advantage of the QMBs over the collectors. However, since the quartz crystals are strongly thermally isolated, their surface temperatures can become much higher than those of the rotating collectors. These high temperatures can limit deposition and promote thermal re-erosion of deposits. This demonstrates a key weakness of the QMBs. The high temperatures they reach mean that quantitat-

ive deposition results from the QMBs can be unrepresentative of their surroundings. The net deposition rate on the central divertor QMB was found to be only a quarter of that on the corresponding collector [77].

The improved time resolution of the QMBs relative to the rotating collectors and other diagnostics has enabled investigation of the importance of shot history effects. This was demonstrated in the JET-C inner divertor, where the degree of re-erosion from tiles was found to depend on the position of the strike points, and the inferred material re-distribution, during preceding pulses [84]. Deposits on the horizontal base tile appeared to be 'refreshed' by sputtering from strike points on the vertical tiles. When the strike point was subsequently moved to the horizontal tile, this caused large re-erosion and hence large deposition on the local QMB. The local surface composition is an even more important factor for the reduced impurity concentrations seen in JET-ILW, analysis of which is presented in Section 7.5.3.

Overall, in the inner divertor there was a correlation between strike points with a line of sight to the QMB and deposition on the QMB [84], yielding similar conclusions on line of sight transport to those that were reached in [77]. However, the situation in the outer divertor was less clear, with some of the deposition being attributed to transport from the inner divertor and differing erosion mechanisms [84]. Differences in erosion and deposition between the inner and outer divertor are analysed in Chapter 6.

Another study enabled by the improved time resolution of the QMBs is the investigation of the dependence of erosion and deposition on ELM size [85]. It was found that the deposition on the QMB, and by implication the erosion from the tile, increased non-linearly with ELM size. This was found to be consistent with the degradation of amorphous carbon-deuterium layers on tiles due to a thermally-activated Arrhenius process. The ability to target time windows of a few seconds in this study allowed the plasma conditions to be precisely specified. With a poorer time resolution, descriptions of average ELM size would become close to meaningless due to an excessive spread in energies.

QMBs do not offer species-specific deposition data and care must be taken when drawing quantitative conclusions from their output. However, their high time resolution allows a specific determination of the plasma parameters corresponding to each data point. This makes it easier to infer the significance of different variables in producing the erosion and deposition measured by the QMBs. This improved resolution is also used in the current study to inform the interpretation and modelling of the deposition on the rotating collectors and to investigate the causes of deposition asymmetry between the inner and outer divertors (see Chapter 6).

2.6 High time resolution diagnostics

2.6.1 Spectroscopy

Optical emission spectroscopy can be used to measure the intensity of spectral light emitted due to electronic transitions in atoms/ions that have been sputtered by plasma-material interaction [86]. Impurity species may be differentiated by the

wavelengths of emission and their prevalence in different vessel locations can be found by taking measurements along multiple lines of sight. As with many optical methods, this technique is easily capable of temporal resolutions of 1 ms or below.

Spectroscopy has been used to study the decomposition of deposited hydrocarbon layers at strike points [87], which contributes strongly to subsequent divertor deposition. This analysis was enabled by the high time resolution of the spectroscopy system and the ability to examine the content of the local plasma rather than just the tile surfaces. The combination of different spectroscopy signals can be used to calculate more complex quantities such as sputtering yields and the degree of detachment [88], which have profound implications for the degree of plasma-material interaction that occurs. This may be achieved by examining spectroscopic lines associated with both the incident deuterium flux and the resulting sputtered impurity flux. Understanding and utilizing detachment is vital for the lifetime of divertor tiles in ITER and beyond. Within the current study, analysis of sputtering yields calculated from spectroscopic signals is presented in Chapter 7.

Another application of spectroscopy is the estimation of whole-vessel impurity sources over campaigns [89]. This is a useful method for estimating global erosion, but has large uncertainties since it typically relies on scaling up the measurements from a small number of lines of sight to the surface area of the tokamak. This scaling assumes uniform erosion in toroidal and poloidal directions, whereas in reality variations are likely to exist. Nevertheless, spectroscopy is useful for providing a clear demonstration of general changes in the impurity content of plasmas during and between campaigns. It has been used to show a reduction in the carbon content of the plasma by a factor of $\sim$20 between JET-C and JET-ILW operation (Figure 2.6). In addition, [90] and [91] demonstrated a decrease in carbon content and increase in beryllium content in the JET divertor during early ITER-like wall operation. Spectroscopy generally offers the most reliable measurements of the impurity content of plasmas, which has direct implications for the amount of erosion occurring at material surfaces and the amount of deposition that is likely to subsequently occur.

A key difficulty associated with calculating magnitudes of eroded material from spectroscopy signals is the accuracy with which the inverse photon efficiencies are known. These quantities are derived from atomic physics models [92] and effectively give the scaling between the collected light and the number of particles of each species present. However, the inverse photon efficiencies are functions of temperature and density, and hence dependent on changeable plasma conditions [93]. Local temperature and density measurements are often poorly known, adding uncertainty to the interpretation of spectroscopy data. Caution must also be exercised so as not to overestimate the erosion from surfaces due to the difference between gross and net erosion. Not only can reflected light and transport of particles misrepresent local erosion, but a significant fraction of the ionised impurities can return to tile surfaces, reducing the net erosion.

In the current study, the high time resolution data provided by spectroscopy will be used to improve the accuracy of the modelling of the long-term rotating collector depositions (4.1.3). It also acts as a key motivator and source of comparable data for the Monte Carlo modelling results presented in Chapter 7 and Chapter 8.

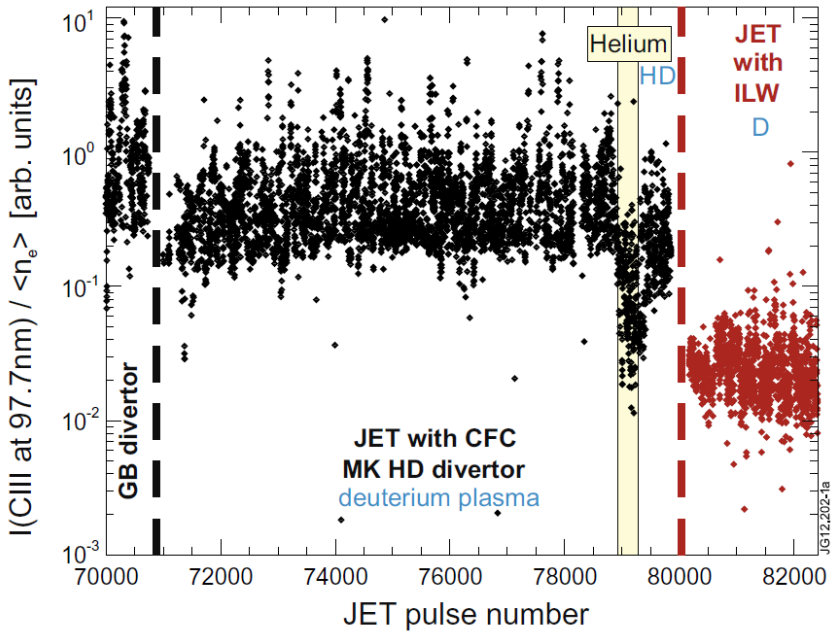

Figure 2.6: Spectroscopy was used to verify the large reduction in carbon impurities in JET plasmas after the installation of the ITER-like wall [90].

2.6.2 Interpretive diagnostics

In addition to the erosion/deposition diagnostics described in the previous sections, there are numerous diagnostics that provide data which aid the interpretation of erosion and deposition. These diagnostics provide information regarding the conditions tiles and other diagnostics are subject to, enabling comparisons between different experimental results and between experimental and modelling efforts. Specific experimental data used in the current study will be explained in the following chapters. Here, the previous uses of some of the most relevant diagnostics for erosion/deposition studies are briefly discussed.

2.6.2.1 IR thermography and thermocouples

One of the most important tile properties for erosion and deposition is the surface temperature, which can affect the chemical sputtering yield [31] and the structure of deposited layers [94]. Infrared (IR) thermography determines the temperature of a surface through the measurement of the infrared radiation emitted by that surface. Using this, it is also possible to derive the heat flux incident on the surface [95], which is useful both as a vessel safety feature and in the interpretation of the degree of erosion. In JET, a wide-angle IR camera views a complete poloidal cross-section and a significant fraction of the toroidal extent of the vessel (Figure 2.7), with time resolutions of 100 μs achievable [96]. This allows the investigation of the effects of transient events such as ELMs, which have thereby been found to deposit energy on the outer limiters as well as on divertor surfaces [97]. IR thermography has also proved useful in verifying the predicted power-handling capabilities of the beryllium limiters in JET-ILW [98], which is of critical concern for ITER. The same analysis

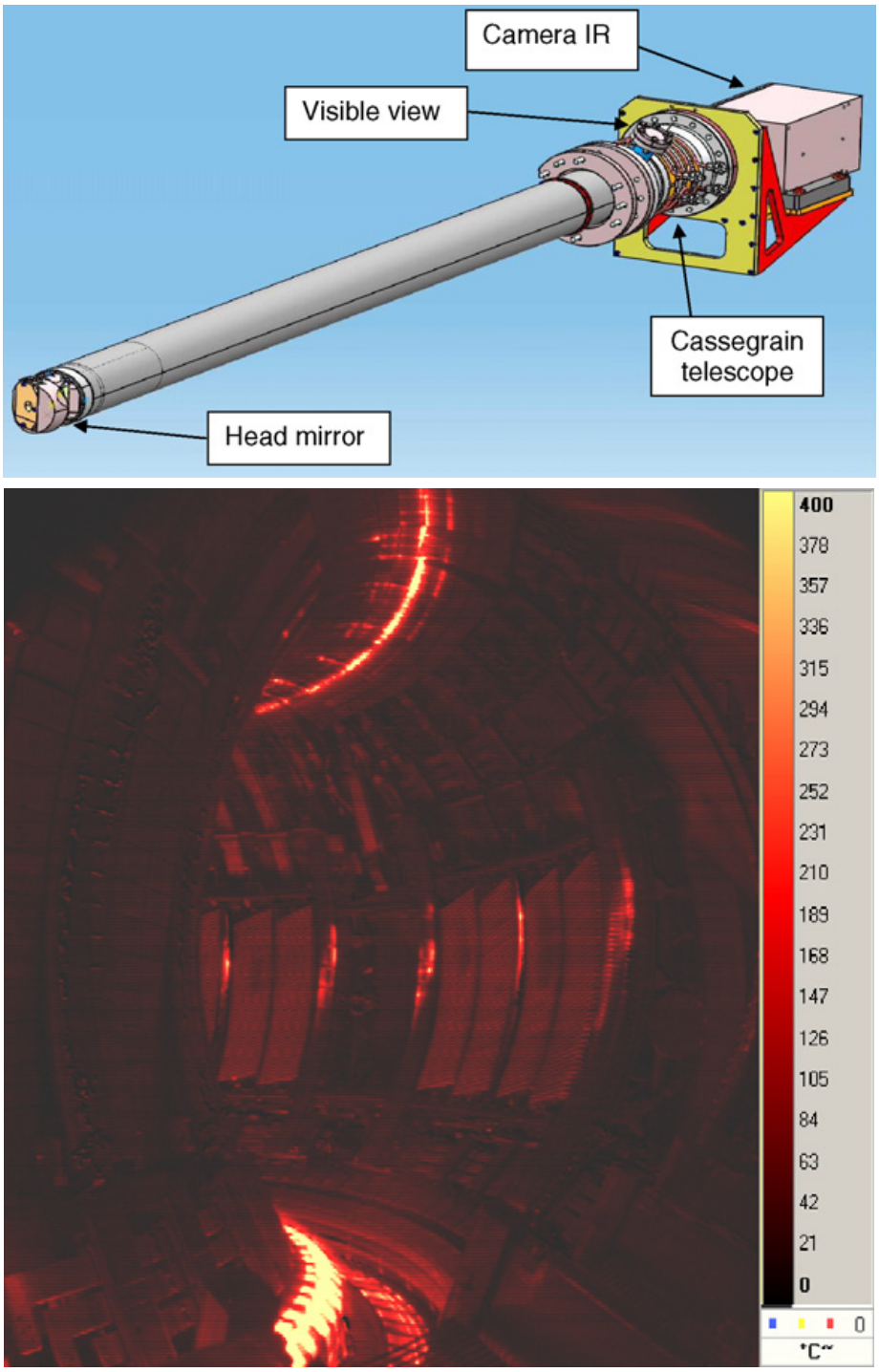

Figure 2.7: Optomechanical design of the wide-angle visible and IR diagnostic installed on JET (top) with example results (bottom) [96].

stressed the importance of toroidal asymmetries in heat loads, which were found to lead to localised melting events. The ability of IR thermography to provide 2-D temperature maps was crucial for this study.

Temperature data may also be obtained from thermocouples embedded in first wall tiles. Unlike IR measurements, these are not suitable for studying short timescale effects. The positions of the thermocouples away from the surface of the tiles mean that their temperature variations rely on conduction from the tile surfaces. This means that they typically measure lower temperatures than at the surface, and that there is

a time delay/damping related to this conduction. However, IR thermography suffers from temperature uncertainties resulting from the unknown emissivities of varying surface deposits on tiles [99]. Thus, thermocouples typically provide a more stable, long-term measure of temperature, but are not suitable for studying transient events. The thermocouples provide temperature measurements at their discrete spatial locations, whereas IR thermography provides more comprehensive, continuous data. Conversely, there are vessel locations with thermocouples that IR cameras cannot view, particularly in remote divertor areas. The temperatures in such areas affect the amount of fuel retention in remote deposits [100] and hence measurement of these local temperatures can be of great significance.

2.6.2.2 Langmuir probes

Langmuir probes are important in the determination of the local plasma conditions which material surfaces are subject to. In its simplest form, a Langmuir probe consists of a wire inserted into the plasma at varying applied voltages. By measuring the current to the wire, 'I-V' (current-voltage) curves are obtained, from which quantities such as the plasma electron temperature and density and the ion flux to the probe can be derived [8].

Knowing the ion flux to a surface is fundamental for the prediction of the degree of erosion we expect, since at a basic level the sputtering source can be found by multiplying the incident flux by the sputtering yield. For chemical sputtering of carbon, the sputtering yield itself is also observed to have a flux dependence [34]. The local plasma temperature can be used to estimate the incident energy of ions impinging on the surface [101], which can strongly affect the sputtering yield. As noted in Section 2.6.1, temperature and density measurements are needed for calculation of inverse photon efficiencies, allowing calibration of the quantities of different plasma species found from spectroscopy. Finally, measurements of divertor temperatures, densities and ion fluxes have been used in the characterisation and understanding of divertor detachment [102], the utilization of which aids the mitigation of the material damage caused by plasma-surface interaction.

2.7 Modelling

While experimental techniques ultimately offer the most reliable indication of the effects of plasma-material interaction, there are significant gaps in what can currently be obtained from them. As described in the preceding sections, post-mortem techniques provide long-term surface evolution data, but suffer from poor time resolution. In situ diagnostics can provide better time resolutions, but yet cannot access the very small timescales and length scales that are often described via modelling. The areas investigated using modelling techniques include the complex interplay between changing plasma conditions, incident fluxes/transport, erosion and deposition processes and surface composition. When related or benchmarked to experimental results, modelling techniques can provide added insight into the mechanisms that are important in plasma-material interaction, as well as serving as a powerful tool allowing predictions to be made for future experiments and future tokamaks. This section

describes some of the codes used for plasma-material interaction modelling, and analyses their suitability for different applications.

2.7.1 Edge fluid modelling

The characteristics of the edge plasma can have a significant impact on the degree of erosion from plasma-facing surfaces. For example, to first order the rate of cross-field transport determines the width of the SOL and hence the power density at the strike point, which affects the sputtering yield from the tile surfaces. Typically, edge fluid codes are finite-difference models that map the outer plasma and SOL using a curvilinear grid with dimensions defined parallel and perpendicular to the magnetic flux surfaces [103].

One such example of these edge fluid codes is EDGE2D [104]. In the parallel direction, the transport is treated classically through conservation of particles, energy and momentum, while in the perpendicular direction anomalous transport coefficients are used to describe the transport resulting from turbulence. Fluid codes like EDGE2D typically rely on Monte Carlo codes such as EIRENE [105] or NIMBUS [106] to describe the contribution of neutrals. The simulations are useful for both the interpolation between and extrapolation beyond experimental measurements of edge temperature and density profiles [107]. One application of this is the calculation of inverse photon efficiencies for the interpretation of spectroscopy signals (see Section 2.6.1). EDGE2D has also been used to model the transport of ^{13}C tracer puffed into the outer divertor of JET [108]. By fitting to post-mortem tile analysis data, the migration pathways of carbon impurities were inferred, providing valuable information that would be extremely difficult to obtain using experimental techniques alone.

The use of a fluid description of the edge plasma can offer significant savings in computational time relative to following individual particles. However, edge fluid codes have a number of disadvantages relative to their Monte Carlo counterparts. In particular, Monte Carlo codes are generally easier to write, numerically stable, and better at treating the period before eroded impurities become ionised [103]. The next section will examine such codes in more detail.

2.7.2 Monte Carlo modelling

Monte Carlo methods use random sampling to obtain quantitative solutions to problems with many coupled degrees of freedom, for which analytical solutions are impractical or impossible. These methods are well suited to tracking single particles in their erosion from plasma facing components, transport through the plasma and deposition on or reflection from surfaces. Often, the specific calculation of erosion/deposition at the surface is performed using dedicated ion-material interaction models such as SRIM/TRIM [109]. Monte Carlo methods typically use reference plasma background solutions coupled to self-consistent sputtering of material from surfaces at each time step. A related weakness is that these codes require quantities such as densities and temperatures to be known from experiments or other modelling efforts in advance so that they can be entered as inputs.

An early tokamak Monte Carlo modelling approach was the REDEP/WBC code package, which has been used to study erosion and material transport in DIII-D [110]. This couples the erosion/deposition code REDEP with the impurity transport code WBC. The approach has proved successful in reproducing the experimental erosion, deposition and transport behaviour of the carbon divertor, as well as of a variety of metal films exposed to the plasma via an inserted probe [111]. This code package has also been applied to such crucial issues as chemical erosion of carbon, detachment and tritium retention in ITER [111].

The ERO code [112], [113] has been used extensively to examine erosion, deposition and material migration in a wide range of tokamaks. Impinging ions erode neutrals from plasma-facing surfaces, which have some ionisation probability at each time step depending on the local electron temperature and density. They are then acted on by the magnetic and electric fields and may return to a material surface, where probabilities of reflection/redepostion/further erosion are calculated.

Comparisons of experimental deposits in TEXTOR and JET with modelled results has assisted the inference of an increased chemical erosion yield for deposited carbon-deuterium layers [114]. This is of vital importance in informing the choice of future plasma-facing materials (see Section 2.4). ERO has also been used to interpret spectroscopy measurements relating to erosion from the beryllium limiters in JET, allowing prediction of erosion rates in ITER [115]. Such benchmarking of codes to experimental results both aids understanding of current experiments and crucially allows predictive modelling for future devices. However, these predictions must be treated with caution. They are in general subject to the uncertainties inherent in extrapolating the effects of a wide range of non-linear processes.

The WallDyn code [116] has recently proved successful in coupling local erosion and deposition behaviour to global impurity fluxes. The approach offers a solution to the problems of computational expense associated with extending the modelling of complex plasma-wall interaction over large surface areas and simultaneously preserving feedback to and from the plasma background. The transport of material from each wall element to every other wall element is described via a redistribution matrix calculated using DIVIMP [117]. The description of erosion/deposition/reflection at surfaces is treated using parameterizations of TRIM [109] or molecular dynamics results. This yields rate equations for erosion and deposition for each wall element, which are coupled via the impurity influx as calculated using the redistribution matrix.

Results from WallDyn have demonstrated good qualitative agreement with the beryllium deposition pattern found experimentally in JET-ILW, particularly as regards the large deposits at the top of the inner divertor [118]. The code has also reproduced the transport of beryllium from the main chamber to the divertor during the limiter phases of pulses, as inferred from spectroscopic analysis [118, 119]. The characterization of this long range transport of beryllium is important for understanding and predicting the global impurity balance and distribution of deposits in ITER.

Modelling can be used to probe elements of plasma-material interaction that are currently inaccessible to experimental techniques. Where possible, free parameters in the codes should be set based on experimental measurements. When models are benchmarked to experimental results, it can become possible to infer the values of various parameters that would otherwise be difficult to measure. If care is

taken to ensure that the modelled description of the system remains physical, it is then of considerable value to perform predictive modelling for future experiments or devices.

Most of the modelling techniques described in this section are computationally intensive and typically describe the evolution of plasma-material interaction on the order of seconds. However, the data provided by the rotating collectors encompasses whole campaigns of operation with varying plasma conditions. Thus, the modelling of the collector deposition described in Section 4.1 seeks to simplify description of the plasma, while using a range of experimental data to try to preserve an accurate representation of the physical system. Monte Carlo modelling, as described in Section 4.2, is also performed in order to investigate the effects of changing plasma and surface conditions on erosion/deposition/migration in the JET-ILW divertor in more detail.

2.8 Conclusions and strategy

The most important quantity underpinning erosion and deposition is the sputtering yield, which determines the lifetime of plasma-facing materials and the influx of impurities into the plasma. A range of techniques for diagnosing erosion, deposition and material migration have been discussed. The most fundamental measure of surface change in tokamaks is post-mortem tile analysis, though it generally cannot provide time-resolved data. Extensive research over the last three decades has led to the conclusion that carbon PFCs exhibit unacceptably high levels of fuel retention, leading to a move towards metal PFCs and in particular beryllium and tungsten. Diagnostics used to study erosion and deposition range from long-term static samples to medium time resolution rotating collectors and QMBs to sub-millisecond time resolution spectroscopy. For analyses that are currently inaccessible to experiment, or for extrapolating to future experiments, modelling techniques are employed.

Erosion and deposition is an area of study that by its nature relates to long-term changes in material surfaces. This is demonstrated by the considerable research efforts focused on post-mortem analysis of tiles, offering campaign-aggregated erosion and deposition data. Despite this, the mechanisms underpinning erosion and deposition can vary by orders of magnitude over very small length and time scales. This mismatch in resolution is addressed in the current study by mainly concentrating on diagnostics that provide medium time resolution data, namely the rotating collectors and QMBs, while taking inputs from both ends of the time resolution spectrum.

The rotating collectors offer the advantages of post-mortem IBA of tiles, in that quantitative, species-specific information is obtained, while adding a time dependence that allows the effects of varying plasma conditions to be investigated. QMBs enable the examination of erosion and deposition over timescales of order 1 s, enabling the impacts of the conditions during particular periods within discharges to be analysed. On the low time resolution side, the aggregate deposition on the collectors will be compared and contrasted with the depositions on static diagnostics. Conversely, on the high time resolution side, data from spectroscopy and other techniques will be used to take into account the changing surface and plasma conditions over short timescales. This will be used as input to a geometric modelling approach,

which will simulate the deposition on the rotating collectors in order for comparisons to be made with the experimental results. Analysis of QMB data will inform this modelling and aid in the understanding of the differences between the mechanisms involved in erosion/deposition in JET-C and JET-ILW. Monte Carlo modelling and spectroscopy will also be used to investigate erosion, deposition and material migration in the JET-ILW divertor in more detail and over shorter timescales. Comparison to experimental results will enable understanding of the important mechanisms involved and their significance for long-term deposition to be furthered. The following two chapters will describe the technical details of the diagnostics, analyses and modelling that are used in these studies.

Chapter 3

Experimental techniques

This chapter provides a detailed technical description of the major experimental tools and techniques that are used to produce the results presented in later chapters. Section 3.1 will describe the operation of the two most important erosion/deposition diagnostics used in this study, namely the rotating collectors and quartz microbalances (QMBs). Section 3.2 will explain the measurement principles and uses of ion beam analysis techniques for post-mortem quantification of deposits. A summary of these topics and the conclusions from this chapter are provided in Section 3.3.

3.1 Diagnostics

3.1.1 Rotating collectors

Post-mortem analysis of tiles provides erosion/deposition data on the timescale of whole campaigns, meaning that any observed changes to surfaces are due to the accumulated effects of thousands of discharges. It is difficult or impossible to be confident of ascribing particular instances of erosion or deposition to specific plasma parameters or configurations. However, post-mortem characterisation of surfaces has the distinct advantage that a full suite of material analysis techniques may be applied in laboratory conditions, enabling highly useful, species-specific, quantitative measurements to be made. It is desirable to both achieve time-resolved measurements and retain the benefits of post-mortem material analysis. This may be accomplished by varying the surfaces that are exposed to the plasma over the course of a campaign.

Enabling such a variation in plasma-facing surfaces is non-trivial. Lack of access to the tokamak during operating campaigns prevents human intervention and the harsh tokamak environment renders any in-vessel electronics vulnerable to failure. Since measurement of the long-term evolution of erosion and deposition is required, it is necessary to implement a diagnostic that is robust and reliable throughout campaigns. Therefore, instead of being electronically driven, it is preferable for the variation in plasma-facing surfaces to occur autonomously as a by-product of normal operations. Additionally, it is of fundamental importance that, when it

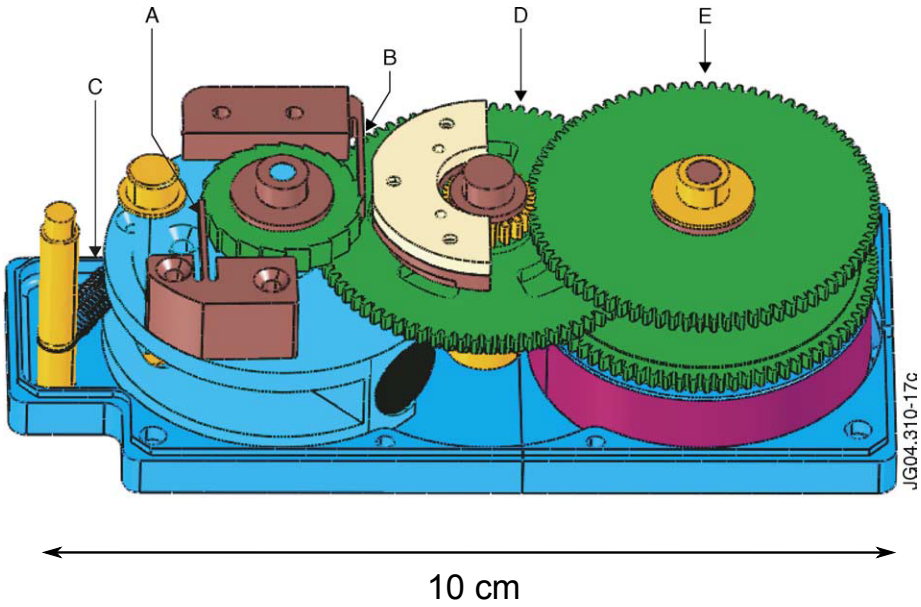

Figure 3.1: Diagram showing the driving mechanism of the rotating collector diagnostic. For clarity, the cover and the collector plate, which fits onto the large gear train (E), have been removed. Rotation due to the magnetic field is controlled by drive (A), stop pawls (B) and a return spring (C). D is an intermediate gear train [76].

comes to post-mortem analysis, different surfaces can be related to different periods of operation. The strong magnetic fields that are produced during each discharge can provide both the necessary driving force for variation of plasma-facing surfaces and a metric for relation of these surfaces to the number of discharges that have elapsed.

Rotating collectors are time-resolved erosion/deposition diagnostics consisting of silicon discs that rotate behind apertures and act as substrates for deposition. These were developed at JET, as first described in [77], in response to the diagnostic requirements described above. A schematic diagram of the driving mechanism of the rotating collectors is shown in Figure 3.1. Each time the magnetic field coils are ramped up for a discharge, the first gear wheel (A in Figure 3.1) is driven to rotate one step by means of a ferromagnetic pendulum, which aligns with the magnetic field lines and is restored via a return spring (C). The ratchet, consisting of the gear wheel (A) and pawls (B), prescribes regulated rotation of one step for each pulsed discharge, providing a linear relationship between the total rotation and the number of discharges that have elapsed. Through calibration of the mechanism it was found that toroidal magnetic fields of 0.5 T and above are sufficient to cause rotation [77]. Since far larger magnetic fields of 2-3 T are typical in JET, all 'successful' JET discharges can be expected to cause a single step of rotation.

The silicon disc on which deposition occurs, located on the large gear train (E), is thus driven to rotate incrementally by 0.106° per discharge via the intermediate gear train (D). Since this rotation occurs behind a cover with a 2 mm aperture, the plasma-facing surface that is exposed to deposition through this aperture varies over the course of campaigns (Figure 3.2). The choices of gearing ratio and aperture width collectively determine the total number of discharges that can be studied and the resolution of the diagnostic. Since the quantification of deposits is performed

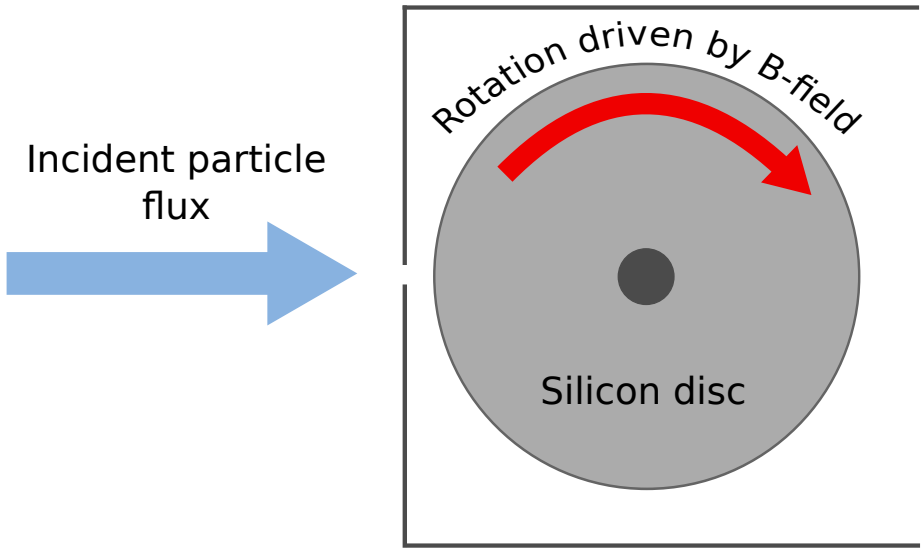

Figure 3.2: The silicon disc of a rotating collector is located behind a thin aperture and driven to rotate by the pulsed magnetic field. This varies the part of the surface of the disc that is exposed to deposition from the plasma.

using ion beam analysis, a lower bound on resolution, and hence on useful aperture widths, is established by the width of the ion beam that is to be used. Additionally, the number of discharges that contribute to deposition at any one location on the disc must be sufficient that the deposition is measurable in a reasonable time period via ion beam analysis. Conversely, if the aperture width is too large, the time-dependent data is too coarse and of less practical use. The aperture width of 2 mm is chosen as a good compromise between these upper and lower bounds, giving a resolution of approximately 50 discharges. This is sufficient to investigate the effects of varying plasma conditions on erosion and deposition as long as conditions do not change too rapidly. The 0.106° per discharge resolution gives a lifetime of approximately 3,000 discharges. This represents a large fraction of the length of operations between shutdowns, at which times the discs can be retrieved and replaced.

Rotating collectors are most usefully located in net deposition areas of the tokamak where there is no direct plasma contact. Hence, in JET there are three collectors located in remote locations in the inner, central and outer divertor, though there are also two positioned on the outer main chamber wall (Figure 3.3). Depending on the geometry of the collectors and their locations, deposition occurs around the outer circumference of a disc and/or on its upper face (Figure 3.4). After ion beam analysis (see Section 3.2) of the disc deposits, the deposition as a function of angle is obtained. These angles are mapped to pulse number using the fact that each 'successful' discharge causes the same degree of rotation. The magnetic field history must be used to neglect from the indexing any discharges that did not meet the minimum field strength necessary to achieve rotation. Using this mapping, the deposition as a function of discharge number is obtained, which allows the effects of varying plasma conditions on the magnitudes and constituent species of deposits to be investigated.

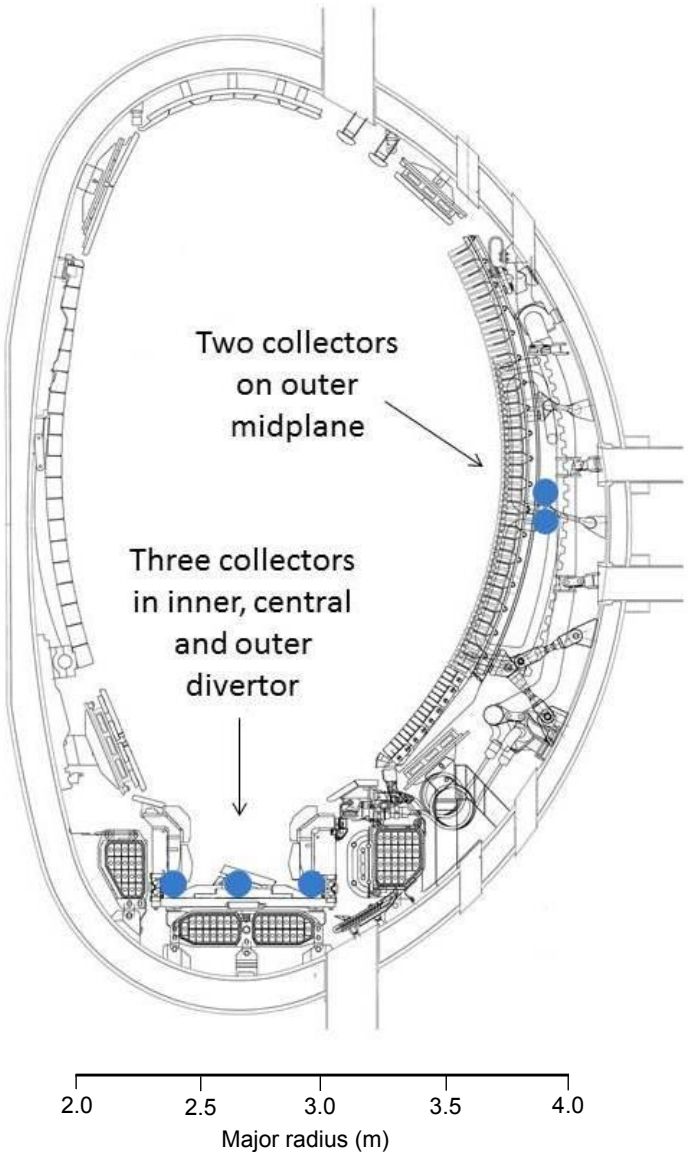

Figure 3.3: Poloidal cross-section of JET-C with the locations of the five rotating collectors marked by blue circles.

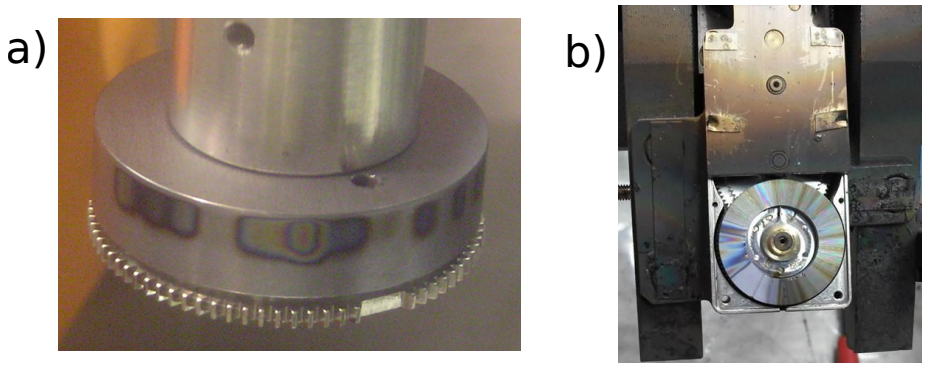

Figure 3.4: Where on the discs deposition occurs depends on the location and mounting geometry of the collectors: a) removed collector disc from the central divertor with deposition around the outer circumference; b) mounted rotating collector from the outer divertor with part of the cover removed, showing deposition on the upper face of the disc.

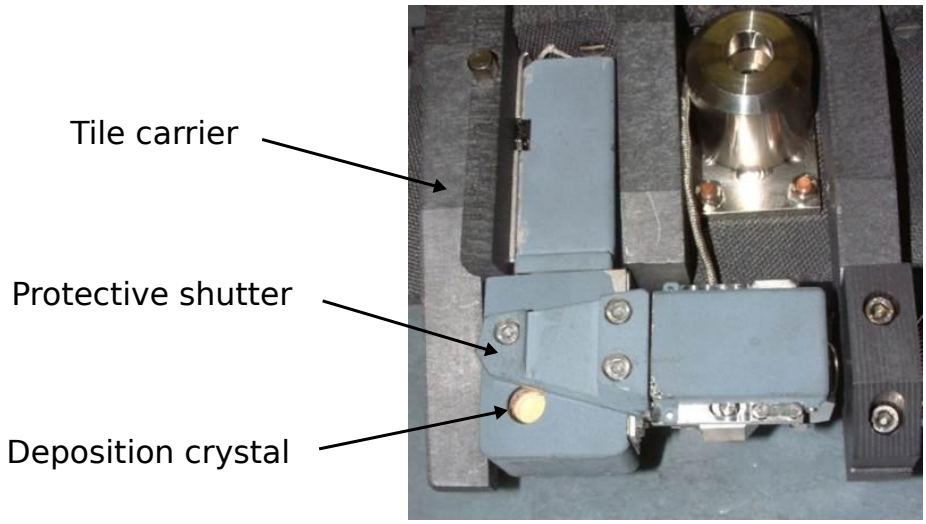

Figure 3.5: View of a QMB mounted on a carrier, ready to be installed in the JET vessel. The shutter may be opened to reveal the deposition crystal and take measurements or closed to protect the system.

3.1.2 Quartz microbalances

While the rotating collectors offer improvements in time resolution relative to post-mortem tile analysis, there are many situations when measurement of the erosion or deposition due to a single discharge, or part of a discharge, is desired. This is particularly the case when plasma conditions vary significantly between consecutive discharges. Since the extent of net erosion or deposition during a period of a few seconds is likely to be very low, a diagnostic that is capable of resolving very small surface changes is required. Quartz microbalances (QMBs) exploit the frequency dependence of a vibrating quartz crystal on its mass to determine erosion or deposition from the crystal surface. Unlike the rotating collectors, the QMBs do not provide species-specific deposition data (though post-mortem analysis of the QMB components can provide campaign-averaged, species-specific data [78],[120]). However, this is compensated for by the improved time resolution and high sensitivity to changes in the mass of deposits. QMBs were first installed and operated successfully in JET in 2002. A full discussion of the design and engineering of this diagnostic is provided in [121] and the references therein. A summary of the most important features is presented here.

By applying an alternating electric field across a quartz crystal, the crystal may be induced to vibrate via the piezoelectric effect. A significant amplitude of mechanical vibration is achieved by approximately matching the frequency of the electric field to a resonant mode of vibration of the quartz. In this case, the resonant frequency is constant in the absence of changes to mass or temperature. Deposition of material on the quartz crystal increases its effective mass, increasing the inertia of the system and decreasing the resonant frequency of vibration. Conversely, if this material is re-eroded from the crystal surface, the reduction in mass causes an increase in the resonant frequency. Therefore, by monitoring the frequency of vibration, a measure of erosion or deposition is obtained.

The narrow resonance, and hence stability of oscillation, of quartz crystals enables very precise measurements of mass changes to be made. Laboratory calibration

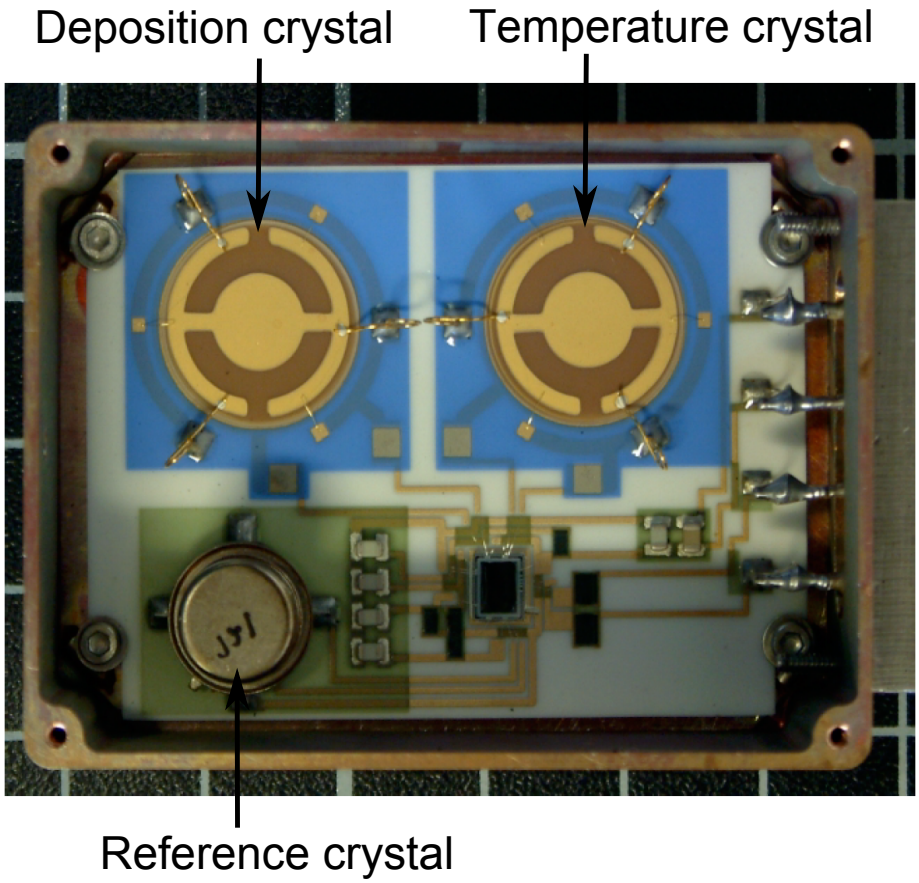

Figure 3.6: View of an open QMB unit showing the different measurement crystals and associated electronics [121]. By comparing the frequency changes of the crystals, the frequency change due solely to erosion or deposition is obtained.

has been used to calculate a mass sensitivity of $\Gamma_{mass} = 7.5 \times 10^{-9}$ g/Hz [121]. The high accuracy of the frequency readings given by the resonator circuit allows frequency changes of $\sim$1 Hz to be measured. For the 0.5 cm^2 area of the deposition crystal, the resulting nanogram-scale resolution corresponds to sub-monolayer measurements of carbon or beryllium deposits. This satisfies the requirement of high sensitivity imposed by the short, discrete time periods over which erosion/deposition measurements are taken.

In order to preserve the system, a protective shutter covers the deposition crystal for the majority of the in-vessel time (Figure 3.5). By passing a current through a coil attached to the shutter in the presence of the vessel's magnetic field, a Lorentz force is generated that acts to open the shutter. The shutter is generally set to open for a few seconds during a pulse, for a particular period during which there is interest in taking measurements. The dependence of the resonant frequency on temperature as well as mass is managed by incorporating a second, 'temperature', crystal that is never exposed to the plasma (Figure 3.6). By subtracting the frequency change of the temperature crystal from that of the deposition crystal, the change due to mass deposition or erosion alone is determined. The frequency readings are taken several minutes after a discharge in order to try to ensure thermal equilibrium of the system. For the purposes of easier transmission of frequency signals, a constant 'reference crystal' frequency is subtracted from the deposition and temperature crystal frequencies.

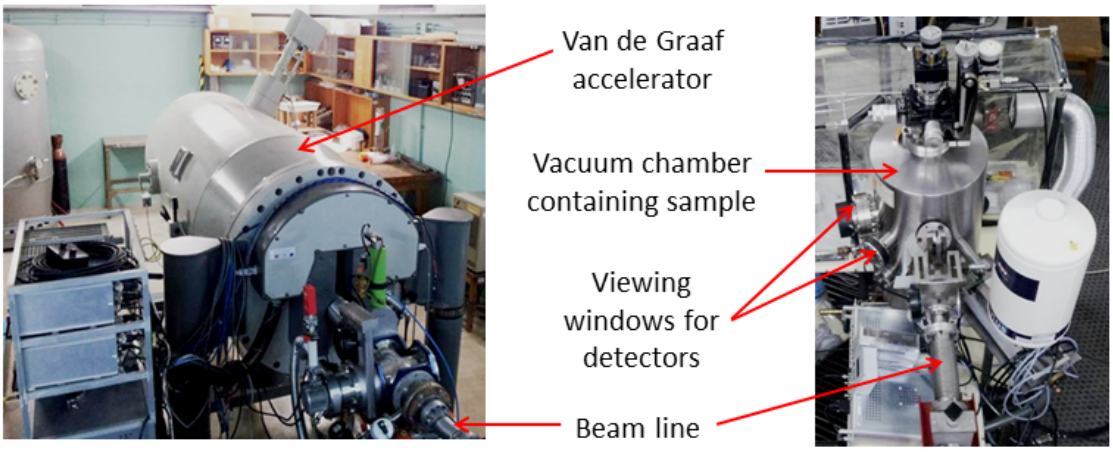

Figure 3.7: Labelled photographs showing some of the ion beam analysis apparatus used at Instituto Superior Técnico [122]. Ions from the ion source/accelerator pass down beam lines and are incident on the target material surface in the vacuum chamber.

Although efforts have been made to thermally and electrically shield the QMBs from the harsh tokamak environment, any in-vessel electronics are vulnerable to failure. This has limited the amount of data that can be gained from the QMBs for some campaigns. However, the ability to target the erosion/deposition measurements to a specific period of a pulse, and the knowledge of a multitude of plasma parameters during that period, means that even relatively small amounts of data can prove very informative. The QMBs in JET are located in remote, plasma-shadowed areas in the inner, central and outer divertor. These locations coincide closely with those of the divertor rotating collectors (Figure 3.3), enabling the data from the two diagnostics to be compared. In particular, in the current study, the high time resolution data provided by the QMBs is used to help interpret the mechanisms underpinning the longer timescale deposition on the rotating collectors.

3.2 Ion beam analysis

Ion beam analysis (IBA) encompasses a suite of techniques that involve using high energy ion beams to probe the composition and/or structure of material surfaces. The interaction of the incident ions with the target nuclei and electrons can produce reaction products that are released from the material surface and become available for measurement. This reveals information regarding the species and concentrations present within the sample, providing non-destructive, quantitative and sensitive measurements. IBA techniques are thus used extensively to characterize material surfaces that have been exposed to fusion plasmas.

Typically the main apparatus needed for ion beam analysis comprises an ion source, an accelerator and transport system, a vacuum chamber holding the sample that the ion beam will be incident on, and detectors that characterize the reaction products. The ion beam analysis performed as part of the current study was completed in collaboration with Instituto Superior Técnico in Lisbon (Figure 3.7). A Van de Graaff

generator is used to achieve a large potential difference and a gas discharge gives a source of ions, which are accelerated by the electric field and impact the sample in the vacuum chamber. After reaction of the ions with species in the surface of the sample, solid-state detectors are used to detect the resulting reaction products.

The large range of IBA techniques are differentiated by the species of incident ions, the types of reactions that incident and target species undergo and the species that can be measured using the interactions. In the current study, nuclear reaction analysis (NRA) and, to a lesser extent, Rutherford backscattering spectrometry (RBS) have proved most useful. These techniques are described in the following sections.

3.2.1 Nuclear reaction analysis

Ions and target nuclei that come into sufficiently close proximity may undergo nuclear reactions via the strong nuclear force. For this to occur, the reactants must overcome the repulsive electrostatic force. Since this force scales with the product of the atomic numbers of the reactants, NRA is most applicable to light incident and target species. The cross-sections for nuclear reactions can vary significantly with incident beam energy, reacting species and the angle at which reaction products are being detected [123]. Thus, it is generally necessary to target particular nuclear reactions and incident beam energies in order to measure particular species with reasonable accuracy. In addition, since nuclear reaction cross-sections are generally relatively low compared to those of electrostatic interactions, high beam currents and large detection solid angles are required [124]. Typically, a particular nuclear reaction:

$$A + b \longrightarrow c + D$$

is denoted by the contraction A(b,c)D, where the incident ion b reacts with the target species A, yielding a light reaction product c and a heavy reaction product D. The light reaction product c has a relatively high energy and can be ejected from the material surface. The energy of c is characteristic of the particular nuclear reaction it orginated from and thus of the target species A present in the sample. Three of the species of most interest for JET deposits are carbon, beryllium and deuterium. These all have significant cross-sections, at similar energies, for nuclear reactions with incident ^{3}He ions:

Carbon: $^{12}_{6}\mathrm{C}(^{3}_{2}\mathrm{He},^{1}_{1}\mathrm{p})^{14}_{7}\mathrm{N}$;

Beryllium: $^{9}_{4}\mathrm{Be}(^{3}_{2}\mathrm{He},^{1}_{1}\mathrm{p})^{11}_{5}\mathrm{B}$;

Deuterium: $^{2}_{1}\mathrm{D}(^{3}_{2}\mathrm{He},^{1}_{1}\mathrm{p})^{4}_{2}\mathrm{He}$.

The light reaction product ejected from the target for each of these reactions is a proton, which has a different characteristic energy for each of the three reactions. It follows that by exposing a sample to impinging ^{3}He ions, the carbon, beryllium and deuterium in the sample may be identified from the resulting proton energy spectrum. An example of this for the detection of deuterium is shown in Figure 3.8. By integrating the peaks and subtracting the low-level background, a measure of the concentrations of the different species is obtained. In theory it is possible to derive quantitative measurements of concentrations purely from this through considerations

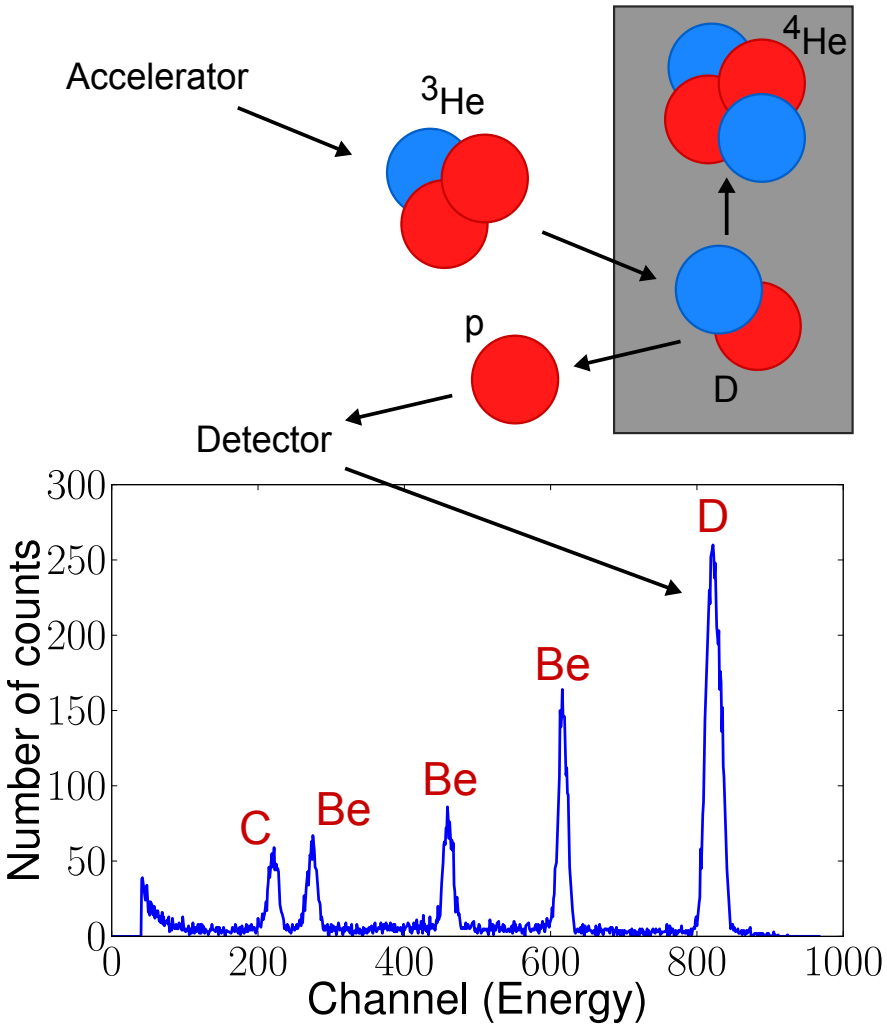

Figure 3.8: The upper diagram shows the nuclear reaction ${}^{2}_{1}\mathrm{D}({}^{3}_{2}\mathrm{He},{}^{1}_{1}\mathrm{p}){}^{4}_{2}\mathrm{He}$, i.e. a ${}^{3}\mathrm{He}$ ion incident on deuterium in the target, producing a ${}^{4}\mathrm{He}$ (which stays in the target) and a proton (which is ejected and detected using a solid state detector). In this case, the proton energy is characteristic of the reaction with deuterium. The lower plot shows the number of protons measured at different energies, with the peaks labelled by the target species they are indicative of.

of cross-sections, attenuations and solid angles. However, in practice it is simpler and more accurate to calibrate the concentrations by scaling against a reference sample with a well-known concentration of the species in question.

NRA is widely used as a post-mortem technique to determine the concentrations of different species in samples from JET and many other tokamaks. In the current study, it is applied to the rotating collectors (see Section 3.1.1) in order to determine the depositions on the discs. Incident ${}^{3}\mathrm{He}$ ions with energies of 2.3 - 2.5 MeV were used to quantify the carbon, beryllium and deuterium deposits around the disc circumferences and hence over the course of campaigns.

3.2.2 Rutherford backscattering spectrometry

At achieveable incident ion energies, nuclear reactions become vanishingly improbable for heavy elements due to increased Coulombic repulsion. RBS relies on detecting ions that are reflected from the target after undergoing Coulombic collisions with target nuclei. Since heavier target species have greater inertia than lighter species, they are more likely to result in reflection of light incident ions. Thus, RBS is suitable for providing measurements of the concentrations of heavy species, but is less useful for detecting lighter species. NRA and RBS provide complimentary diagnostic capabilities.

The ability to determine the species of a target nucleus relies on calculating the ratio of the energy of the ion projectile after the collision (E_1) to that before the collision (E_0). This ratio is known as the kinematic factor, K:

$$K = \frac{E_1}{E_0} = \left\{ \frac{\sqrt{1-[(M_1/M_2)sin\theta]^2}+(M_1/M_2)cos\theta}{1+(M_1/M_2)} \right\}^2,$$

where M_1 is the mass of the incident ion, M_2 is the mass of the target nucleus and θ is the angle between the angle of incidence and angle of reflection [125]. For a known E_0 and M_1, a measured E_1, and a fixed θ, M_2 is the only unknown and thus may be calculated from the above equation.

The incident ion also undergoes numerous collisions with electrons in the target both in the forward and reflected directions. This reduces the measured energies E_1, and does so by a greater extent for target nuclei deeper into the sample. Therefore, a lower measured energy E_1 could either be the result of a lower target nucleus mass M_2, or a target nucleus located deeper into the sample surface. The convolution of mass and depth can make it impossible to describe the species and their depths within a sample using RBS at a single incident energy E_0 [126].

In practice, in JET there are limited high-Z impurity species present in the vessel. RBS can therefore be used to identify deposits of high-Z species as tungsten with a high degree of certainty in JET-ILW. Since the strongest reflection is found for $M_2 >> M_1$, for which K tends towards 1, protons are used here as the incident ion species. The quantification by integration of peaks in the detected energy spectrum, subtraction of background counts and comparison to reference samples follows a similar methodology to that used for NRA (Section 3.2.1). In the current study, the post-mortem measurement of tungsten deposits on the rotating collectors via RBS compliments the associated measurements of beryllium, carbon and deuterium via NRA.

3.3 Conclusions

This chapter has provided an overview of the main diagnostics and analysis methods used in the current study. Rotating collectors provide long-term, time-dependent, species-specific deposition data by varying the surfaces that are exposed to the plasma. QMBs determine the erosion or deposition during time windows of a few seconds by exploiting the dependence of the vibrational frequency of a quartz crystal on its mass. Ion beam analysis techniques, in particular NRA and RBS, are used to provide quantitative, species-specific measurements of deposits through probing

with high energy ion beams. These methods are used to characterise the erosion and deposition in the JET divertor and constitute the source of the experimental results presented in Chapter 5 and Chapter 6. The next chapter will describe the modelling techniques used to complement these experimental methods.

Chapter 4

Modelling techniques

This chapter describes the technical details of the modelling approaches used in the current study. A simple, geometrical model describing the time-varying deposition on the rotating collectors is decribed in Section 4.1. Section 4.2 details a Monte Carlo model that is used to study the impacts of varying surface and plasma conditions on erosion, deposition and transport in the JET-ILW divertor. These models are summarised and conclusions are drawn in Section 4.3.

4.1 Rotating collector model

4.1.1 Modelling approach

There are many highly sophisticated codes that are used to model erosion, deposition and material migration in tokamaks. The detailed range of physics that such codes describe usually necessitate using a fundamental time step of a microsecond or below. The rotating collectors are a slightly unusual diagnostic in that their resolution is approximately 50 discharges, corresponding to an accumulated 500 - 1000 s of divertor plasma and potentially to a wide range of different conditions. One approach to reconciling the mismatch in timescales is to compare the modelled deposition over 1 s of particular plasma conditions to the deposition rate on a collector averaged over its whole lifetime [127]. Conversely, the modelling approach used here is to try to describe the variations in deposition on the collectors over their whole periods of operation [128]. A code written as part of the current study to apply this approach is detailed in this section.

A rotating collector operates for a large fraction of a campaign, representing approximately a year of operation. This necessarily imposes simplifications on the model used to describe the deposition. In particular, the description of transport in the plasma is simplified, with eroded neutrals assumed to travel line of sight from the locations that they were sputtered from. In an attempt to compensate for the simplifications that are made, various experimental data are incorporated. While it is hoped that the model achieves tolerable quantitative agreement with experimental depositions, the primary interest is the evolution of the deposition profile as the

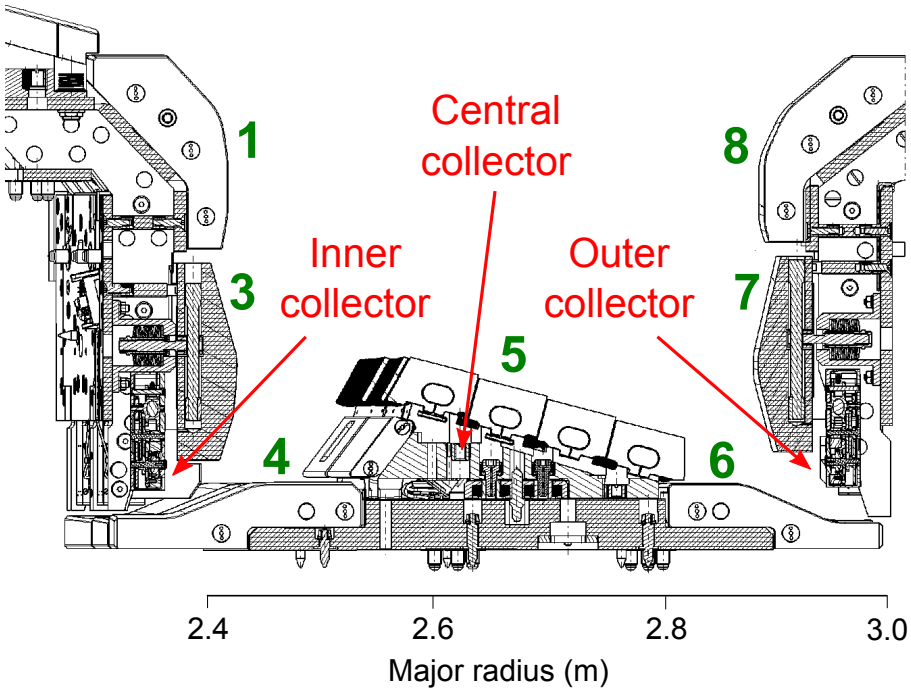

Figure 4.1: Diagram showing a poloidal cross-section the JET-ILW divertor, with tile numbers labelled in green and the locations of the rotating collectors indicated.

plasma conditions vary during campaigns. Due to the assumptions made and the focus on the changes in deposition, the modelled deposition profile on a collector requires scaling by a constant attenuation factor. The approach taken is to find the constant factor that best fits the modelled deposition magnitude to that of the experimental deposition magnitude, followed by an examination of how reasonable such a value is and what can be inferred from it.

The model seeks to reproduce the time-dependent deposition patterns found on rotating collectors located in the remote areas of the JET divertor for carbon wall and ITER-like wall operation. The correlation between strike points that have a line of sight to the rotating collector located under the central divertor tile and deposition on that collector has previously been established in [77]. In the model, sputter cones of neutral impurities are generated from time-varying strike point locations and propagated geometrically, allowing the deposition at the collector locations to be predicted.

4.1.2 Geometry

Due to the established importance of line of sight transport of neutral impurities to remote collector locations [77], the geometry and respective locations of the collectors and strike points are very important in determining collector deposition. The collectors in the divertor are located in plasma-shadowed regions in the inner and outer corners and under tile 5 (Figure 4.1). The JET-ILW divertor geometry depicted in Figure 4.1 is almost identical to that of the JET-C MkII-HD divertor, making comparison of depositions between the two cases easier. The following discussion will focus on the geometry of the central rotating collector located under tile 5, but the

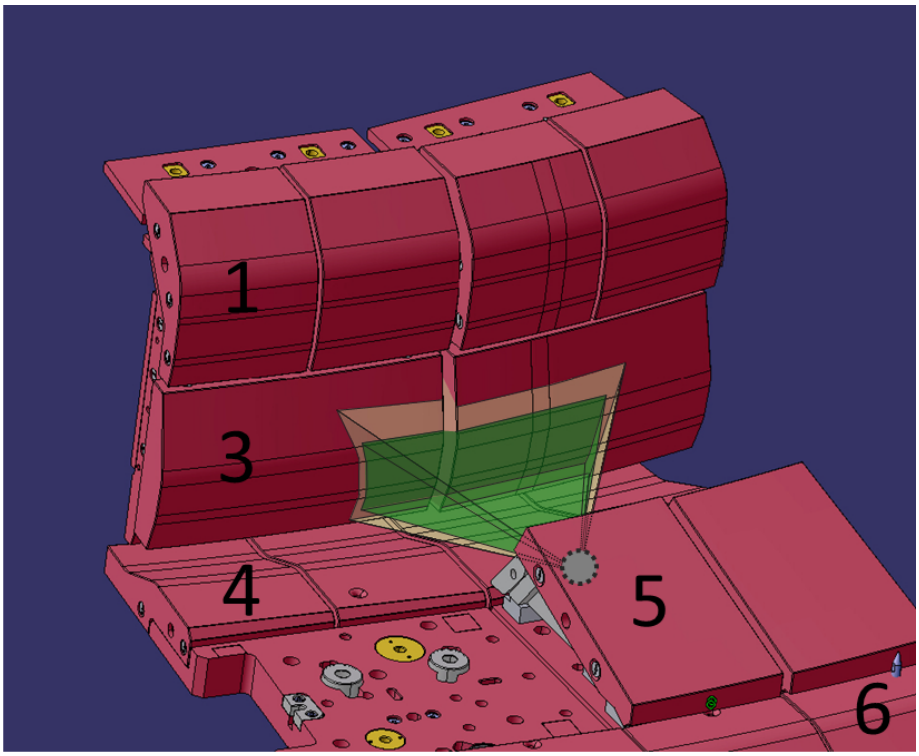

Figure 4.2: 3-D diagram showing the JET-C inner divertor (which is almost identical to that of JET-ILW), with tile numbers labelled in black. The central rotating collector is located under tile 5, as represented by the dotted grey circle. The inner, green projection indicates the areas of the inner divertor that have a line of sight to the whole collector, while the areas encompassed by the beige, outer projection only have lines of sight to a fraction of the collector surface.

general method is the same for the other collectors in their respective locations.

Figure 4.2 shows the areas of the inner divertor tiles that are viewed by the centrally located rotating collector. Strike points falling within this area can contribute to deposition on the collector disc. Thus, when the strike point falls within the poloidal range prescribed by the dotted lines in Figure 4.3, the model generates impurities from the strike point. The neutral impurities sputtered from material surfaces are generally found to follow an approximate cosine distribution, or some power of a cosine distribution, with respect to emission angle [30]. At low incident energies and off-normal incident angles, the distribution of emission angles is often found to be tilted away from the normal. This is due to the importance of few-collision and direct-recoil sputtering events in the first layer(s) of the target material, as opposed to the full collision cascades that can occur at higher incident energies [30].

Based on the above, an approximate cosine distribution is used here for the emission angles, with the peak of the distribution shifted away from the normal by 30 degrees in order to take some account of the directionality of the incident ions. While there is some uncertainty in this distribution, the exact shape of it is likely to have a greater effect on the magnitude of the resultant time-dependent deposition profile rather than the shape of this profile. Since this modelling does not aim at quantitative predictions, this is of secondary concern. Test runs examining the effect of the shape of the sputter distribution on the shape of the deposition profile showed only minor

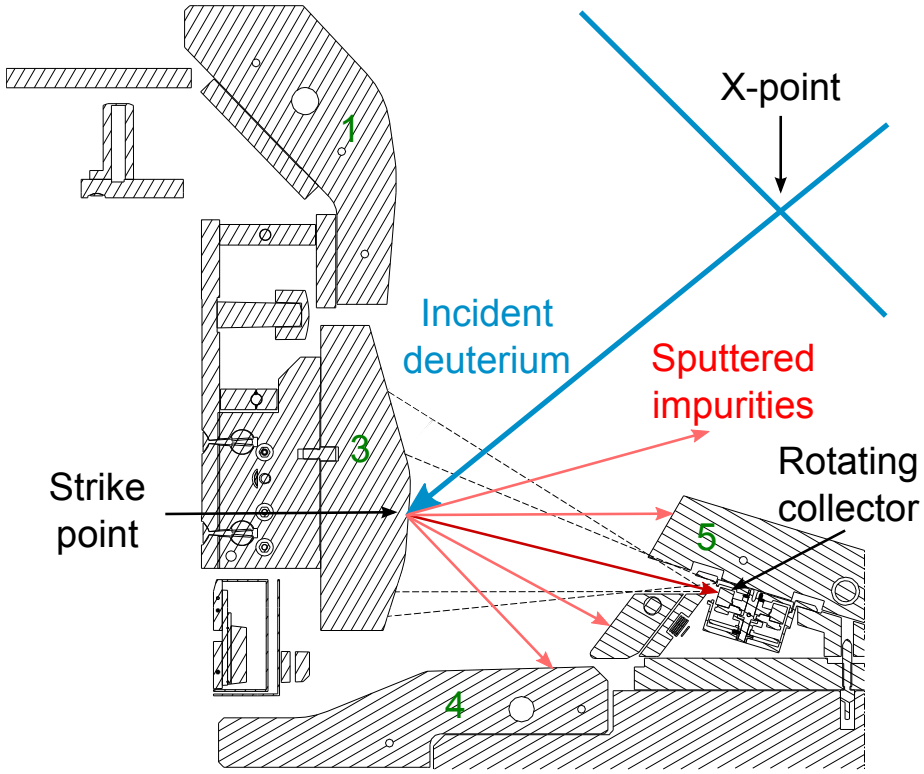

Figure 4.3: Diagram showing a poloidal cross-section of the JET-C inner divertor with tile numbers labelled in green. The separatrix is shown in blue, with the inner strike point located on tile 3. The incident deuterium flux at the strike point sputters impurities (red), some of which reach the central divertor rotating collector located under tile 5. The dotted lines emanating from the collector show the full and partial views it has of the inner divertor tiles.

differences.

The locations of strike points are found from the outputs of EFIT equilibrium magnetic reconstruction [129], with a ∼30 ms time resolution. This gives the fundamental time interval of the model on which calculations are performed. Since the peaks of the incident ion flux profiles from Langmuir probe measurements were found to differ slightly from the locations of the strike points as indicated by EFIT, an offset in the strike point locations based on the probe data is incorporated.

The neutral impurities are not deviated by the electromagnetic fields and thus travel in straight lines. For every strike point location along tile 3 that is viewed by the collector, equations for the upper and lower bounds on the acceptance angle to the collector are known. For each time point, the sputter cone is integrated between these upper and lower bounds in order to determine the proportion of the sputtered impurites with trajectories allowing transport to and deposition on the rotating collector.

4.1.3 Impurity sources

Carbon eroded from the main chamber during JET-C operation may migrate to and deposit on divertor tiles, before being re-eroded by incident deuterium ions

and redeposited in remote areas [130]. Similarly, in JET-ILW, beryllium from the main chamber may be eroded and deposit on the tungsten divertor tiles, becoming available for re-erosion. Alternatively, since the reflection coefficient of beryllium on bare tungsten can be ∼50-90% depending on the incident energy [127], the beryllium may be reflected from the divertor tiles (as neutral atoms). Tungsten sputtering is relatively low and has been found to only occur appreciably due to incident beryllium ions or during ELMs [21]. The sputtering or reflection of carbon and beryllium from divertor tiles to the remotely located collectors is desribed in the model.

For the case of beryllium, it is assumed that the incident flux contains 0.2% beryllium, which is reflected with 80% efficiency [127]. Physical beryllium sputtering and physical and chemical carbon sputtering/erosion are calculated with analytical yield equations using fits to experimental and modelling results [32],[28]. The formulae describe the yields in terms of the incident and target species, incident energy, incident angle and, for the case of carbon chemical sputtering/erosion, incident flux and target temperature. These equations are detailed in Appendix A.

4.1.4 Model inputs

As alluded to in the previous section, the calculated yields vary depending on the angle of incidence of the incoming ion with respect to the target surface. Based on results from modelling of ion trajectories [131], the angle of incidence was assumed to be 60°, which increases the yield relative to normal incidence impacts due to the higher proportion of energy that is deposited in the near-surface region. Incident deuterium energies E_i were estimated using

$$E_i = 3ZT_e + 2T_i \simeq 5T_e,$$

with electron temperature T_e, ion temperature $T_i = T_e$, and atomic number Z, where the first term is due to acceleration in the electrostatic sheath and the second term is thermal energy [101]. Assuming characteristic values of $T_e = 10eV$ at the inner strike point and $T_e = 25eV$ at the outer gives $E_i = 50eV, 125eV$ at the inner and outer strike points respectively. Since for the JET-ILW case the sputtering is predominantly physical, the assumption of constant ion energy is more vulnerable as variations can cause greater changes in expected yields. While there are likely to be significant variations in incident energies for individual pulses, the smoothing of discrepancies that the ∼50-discharge collector resolution imposes makes the constant assumptions reasonable approximations.

The temperature of the tile surface is calculated using a combination of thermocouple and IR thermography measurements and used as an input to the carbon yield calculations. IR thermography data is not always available for the large numbers of discharges that are relevant for the rotating collectors. Thermocouple data is reliably available, but underestimates surface temperatures due to conduction and radiation losses. By comparing thermocouple data to IR thermography data for the relevant tiles, when it is available, a linear scaling is obtained that allows estimation of the surface temperatures from the thermocouple data alone.

Surface ion fluxes are obtained from Langmuir probes and are used as an input to the yield calculations for the carbon case. In addition, for both carbon and beryllium, the sputtering yields are multiplied by these ion fluxes in order to calculate the

sputtering sources (i.e. the fluxes of eroded impurities due to the incident fluxes and the relevant yields). A full width at half maximum of the ion flux profile around the strike point is taken as the strike point width. The magnitude of the peak ion flux is taken from the closest Langmuir probe to the strike point. All eroded impurities are assumed to originate from the strike point in the model and the number of eroded impurities to be ejected is calculated assuming the constant, peak ion flux over the range of the full width half maximum. This will sometimes be an underestimate of the ion flux, due to the true peak of the ion flux profile being between Langmuir probes, or an overestimate, due to the assumption of the measured peak flux applying across the full width half maximum. However, such errors are random in nature and the 50-discharge sampling period of the rotating collectors is sufficient to average over these discrepancies. The consideration of only the full width half maximum region rather than the full ion flux profile is likely to mean that the total amount of eroded impurities is underestimated. However, it is noted that both the ion flux and the incident ion energy decrease further away from the strike point, which reduces the effect of this contribution.

If ion flux data is not available, the fluxes are estimated from the energies deposited on tiles using a power balance. An estimate of the power reaching the divertor at the strike points is calculated through consideration the total input power to the plasma and the power radiated from the plasma. Using the assumption of constant incident ion energies, the ion fluxes at the strike points may then be calculated. In reality, the power to the divertor is affected by the sheath power transmission coefficient in the SOL. The effect of this is incorporated by correlating ion fluxes measured using the Langmuir probes and those calculated using the power balance method for discharges when probe data was available. This comparison allowed the power balance method to be used as a proxy for ion flux when probe data was not available, which was more common for the corner collector locations. Though such approximations represent a compromise, when thousands of discharges are studied, it becomes necessary to provide reasonable estimates for quantities when some data is unavailable.

For the JET-ILW case, the sputtering and reflection contributions to beryllium deposition on the collectors are not entirely mutually compatible. A divertor tile completely covered with beryllium will maximize the sputtering contribution, but will minimize reflection since beryllium is far more efficiently reflected from tungsten than from beryllium, to which it sticks. Conversely, a coverage fraction close to zero will maximise reflection from the tungsten tile, but there will be little or no deposited beryllium to be sputtered.

For the earlier, central rotating collector modelling, the mean of the deposition due to the sputtering and reflection processes was taken, reflecting their opposite dependencies and the fact that they cannot be simultaneously maximised [128]. For later work [132], the treatment of this topic was improved. Spectroscopy was used to incorporate the fact that there are varying levels of beryllium in the incident flux and on the tile surfaces available for sputtering or reflection at different times.

The dependencies of the sputtering, self-sputtering and reflection processes on the fraction of surface beryllium as calculated using TRIM modelling [109] of the relevant conditions are shown in Figure 4.4. It may be seen that the opposite dependencies of the sputtering and reflection processes partially negates the dependence of the total beryllium ejection from the surface on the proportion of surface beryllium, though there is still a gradual increase with greater beryllium fractions. Increasing

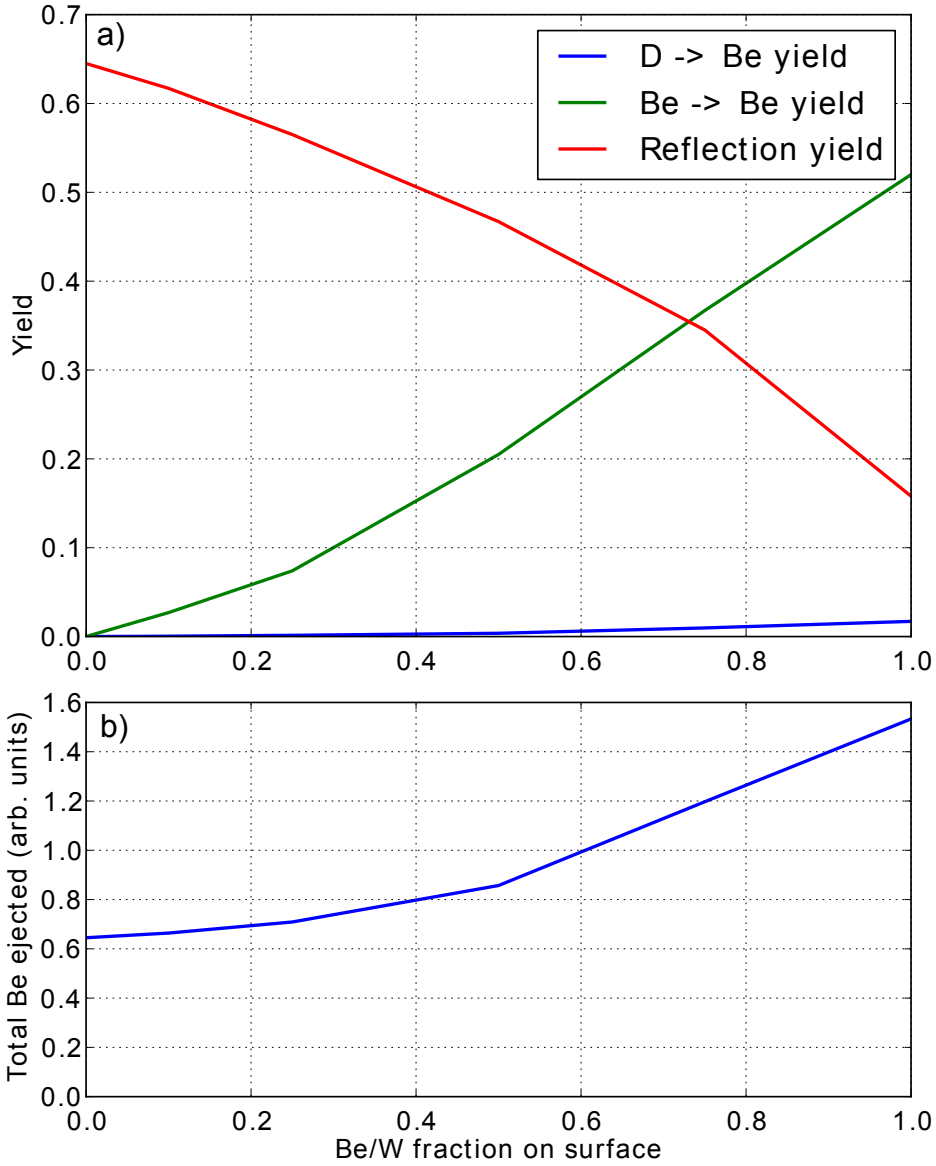

Figure 4.4: Plot a) shows the dependence of Be sputtering, self-sputtering and reflection on the fraction of Be relative to W in the surface layer, as calculated using TRIM. The sputtering yield is low relative to the self-sputtering, but for a 0.2% Be fraction in the incident flux, incident D is a factor of 50 more prevalent than incident Be. This factor of 50 has been applied, and the contributions summed, to calculate the dependency of the total ejected beryllium source on the fraction of Be at the surface as shown in plot b).

concentrations of beryllium in the incident flux and on the tile surface give rise to increases in the total beryllium ejected from the surface.

A measure of this beryllium availability was incorporated by scaling the beryllium source by the beryllium brightness as measured from divertor spectroscopy. This provides a reduced beryllium source when there is little beryllium in the incident flux or on the tile surface, relative to cases when the beryllium brightness and availability is high and the source is considered to be 'maximised'. While this method may be unsuitable for more detailed quantitative analyses, for the consideration of the qualitative variation of the collector deposition profiles this incorporation of the beryllium availability represents a good approximation. The spectroscopic diagnostics viewing the JET-ILW divertor include a series of 16 independent chords with different lines of sight. This allows a chord to be selected by the model for each time point, such that the tile location viewed by this line of sight coincides with the strike point at that time.

4.1.5 Relation to experimental depositions

The deposition on the rotating collectors is modelled on the ∼30 ms time resolution of EFIT, and output with the resolution of 1 data point per discharge. However, as described in Section 3.1.1, the resolution of the collectors is approximately 50 discharges. In essence, the mechanical setup of a rotating collector is designed to take a moving sum of deposition. Each rotation of the disc results in the deposition from one discharge being removed from the moving sum and the deposition from a new discharge being added. In order to replicate this temporal aggregation imposed by the finite aperture width, a 50-discharge moving sum is applied to the modelled deposition results.

As described in Section 4.1.1, the focus of the modelling is on the long-term variations in deposition over whole campaigns, occurring due to changes in plasma conditions. For more quantitative modelling of the deposition over short timescales, the reader is directed to [127], which treats the plasma-material interaction and plasma transport in more detail using ERO. In order to aid qualitative comparison of the variations in the experimental and modelled deposition results, the method preferred here is to scale the modelled depositions by constant attenuation factors found by fitting to experimental deposition magnitudes. It is worth stressing that since these attenuation factors are constants, they do not affect the time-variation of the modelled depositions. Therefore, they are independent of any qualitative agreement or otherwise with the experimental deposition profiles.

Due to the necessary simplifications and the focus on variations in deposition, it is not suprising that the modelled deposition magnitudes do not exactly coincide with those found experimentally. Although no strong quantitative claims are made regarding the modelled deposition magnitudes, typically the attenuation factors are in the range ∼0.1-1, suggesting that the quantities of deposition found using this simple description incorporating experimental data are at least within an order of magnitude of the true experimental depositions. Physically, the attentuation factors represent losses due to ionisations of the neutral impurities as they pass through the plasma and failure of impurities to permanently deposit on the collector disc surfaces. Discussion of the attenuation factors will be incorporated into analysis

of the modelled results, which are presented with the corresponding experimental collector depositions in Chapter 5 and Chapter 6.

The geometrical modelling approach detailed in this section is designed to describe long-term changes in erosion and deposition over the course of whole campaigns. These long timescales are the result of focusing on producing deposition profiles that are relatable to those found from the rotating collectors. Conversely, the modelling described in the following section aims to investigate erosion, deposition and material migration processes in the JET-ILW divertor on the timescale of seconds and below.

4.2 Monte Carlo model

4.2.1 Modelling approach

The Monte Carlo code detailed in this section was written as part of the current study to investigate the erosion, deposition and transport of beryllium in more detail and over shorter timescales than was the case for the rotating collector modelling (Section 4.1). This approach was motivated by an analysis of sputtering yields calculated using spectroscopy, which suggested that the surface conditions and beryllium erosion from divertor tiles can vary significantly over short periods of time.

In basic terms, this Monte Carlo model sputters and reflects beryllium neutrals from tiles, follows them through the plasma, calculates ionisation probabilities at each time step and describes further redeposition, self-sputtering and reflection events. The probabilistic nature of ionisation and sputtering processes makes a Monte Carlo modelling approach suitable to the physical system being described. By following millions of beryllium neutrals or ions through the plasma, overarching characteristics of the erosion, deposition and transport are identified.

An important aspect of the code is that it should be flexible, allowing easy modification of properties such as the plasma parameters, the strike point locations, the surface conditions and the percentage of beryllium in the incident flux. This enables the effects of changing these inputs to be investigated so that the erosion/deposition behaviour may be related to different JET-ILW experimental conditions and results, yielding insights for future ITER operation.

4.2.2 Area modelled

The model aims to both incorporate experimental data as inputs and to compare modelled and experimental results. For these reasons, it is a necessary requirement that the modelled area concides with a region of good diagnostic coverage. The chosen area in the outer divertor of JET-ILW is indicated in Figure 4.5. The good coverage of Langmuir probes allows the temperature and density of the plasma and the incident flux to the tile surfaces to be described in the model based on these experimental measurements. The spectroscopy chords allow not only the magnitude,

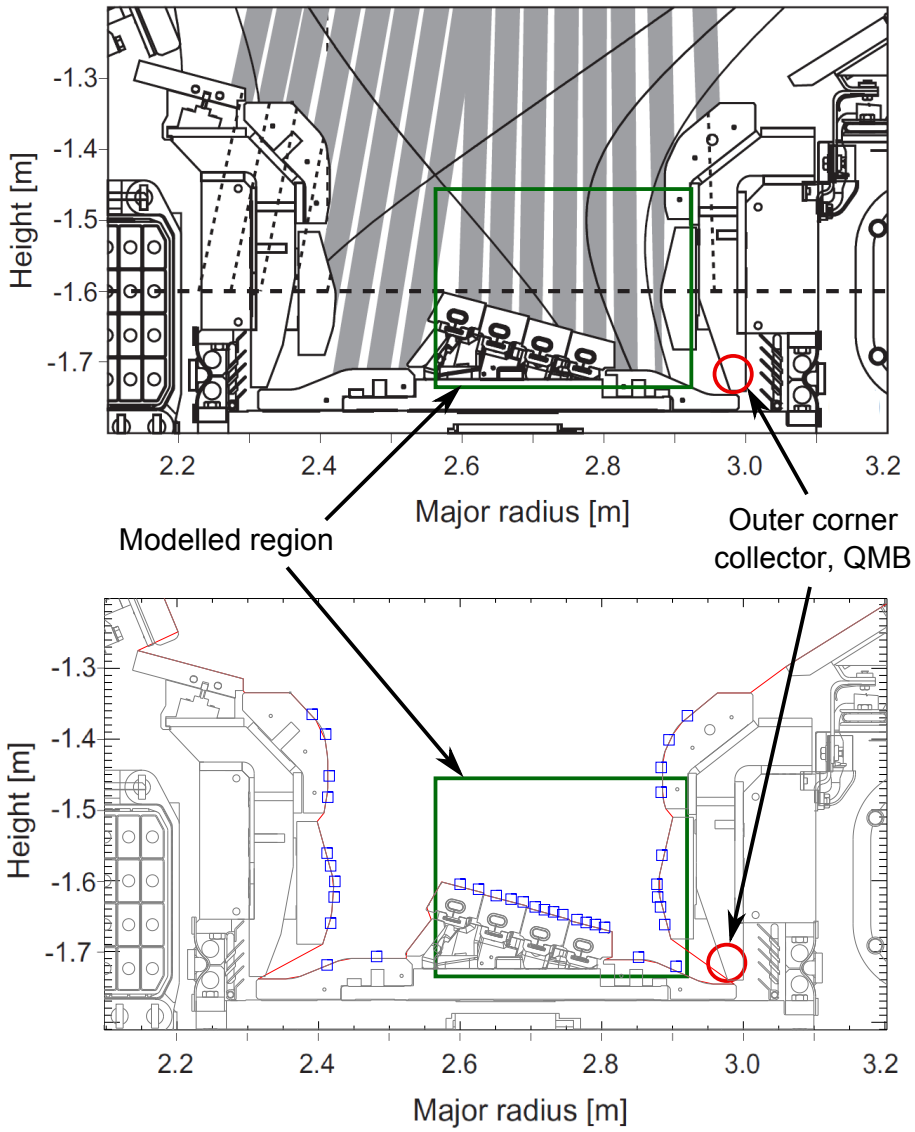

Figure 4.5: Diagrams showing the area described in the model, located within the green boxes, and the position of the outer divertor rotating collector and QMB, circled in red. The upper diagram shows the views of different spectroscopic chords in grey and the lower diagram shows the locations of Langmuir probes, marked by blue squares.

but the shape of the beryllium brightness profile to be compared between experiment and model.

The modelled area comprises a 2-D region 330 mm wide and 270 mm high, incorporating tile 5 and the part of tile 6 accessible to direct plasma contact. The shadowed region in the outer corner, including the location of the rotating collector and QMB, is also incorporated into a related code. Beryllium neutrals/ions leaving the modelled area are assumed to be lost to the rest of the plasma or remote regions and do not feature in later time step calculations. While the code is essentially 2-D in nature, a basic treatment of toroidal effects is included in the consideration of deposition on the outer corner diagnostics.

Calculations are performed on a 1 mm by 1 mm grid covering the modelled area. Particles falling between grid points, for example after propagation through the

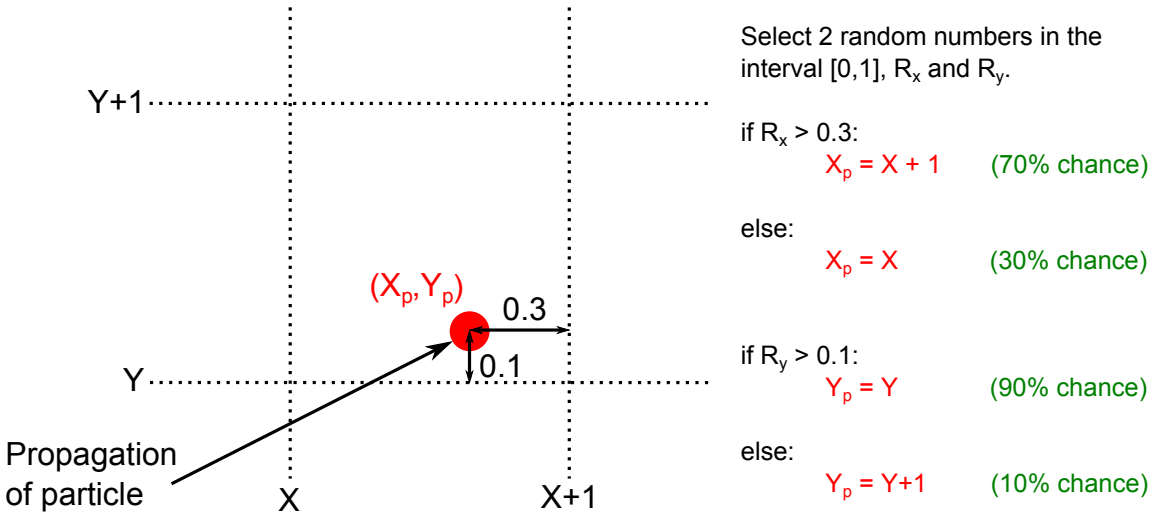

Figure 4.6: Diagram and associated logical operations for resolving a particle (shown in red) onto the 2-D grid (shown by dotted black lines).

plasma during the previous time step, are assigned to one of the closest four grid points through a random weighting approach (Figure 4.6). The distance in mm between the particle and the closest grid point in the x-dimension is compared to a random number between 0 and 1. The particle is assigned to the x-coordinate of that closest grid point if the random number is greater than the separation, and assigned to the x-coordinate of the more distant grid point on the opposite side otherwise. This calculation is repeated in the y-dimension. The particle is thus projected onto a grid point in a way that preserves some randomness and simultaneously is probabilistically inclined to attribute any given particle to its closest grid point.

4.2.3 Plasma background

The properties of the plasma background can have a significant impact on the erosion, deposition and transport behaviour that is observed. Monte Carlo codes often set the plasma background using the output of edge fluid modelling codes. While it is possible to use this input to define the plasma background in the current model, this can compromise the stated requirements of flexibility and easy modification. A further aim of the modelling efforts is to use experimental measurements as input. Therefore, in general the plasma background for the Monte Carlo model is defined using Langmuir probe measurements and an approach that enables the background to be varied quickly and simply.

The Langmuir probes provide spatial profiles of the electron temperature, electron density and ion flux along the tile surface, which are interpolated onto the grid points along this surface. EFIT provides the locations of the strike point and the X-point, from which the angle that the separatrix follows is found. The values of temperature and density found at the surfaces are applied to all points along the separatrix, in effect tracing the profile upwards along the angle that the separatrix follows. An example profile for the electron temperature is shown in Figure 4.7. For the area relatively close to the tile surface that is modelled, this approach provides a reasonable approximation to the profiles seen from fluid codes. However, tracing the profile

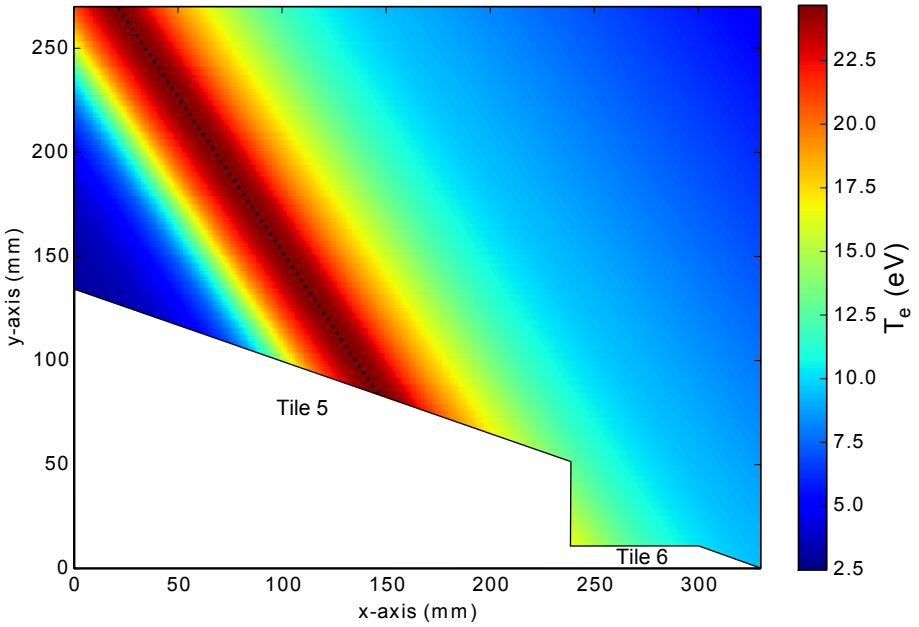

Figure 4.7: Example plot of the 2-D plasma electron temperature distribution used as an input to the model, based on Langmuir probe measurements. The black dotted line indicates the separatrix, as found from EFIT.

along the separatrix is not fully accurate when there is significant detachment and steeper parallel gradients in parameters exist. It is possible to incorporate this by manually scaling the parameters with distance from the divertor surface. Alternatively, the plasma background may be taken from a detached profile generated by an edge fluid code.

The distributions gained from analysis of the Langmuir probe measurements are, in fact, extended over a total x-range comprising double the width of the modelled region. This, coupled with the assumptions regarding the tracing of the profiles along the angle of the separatrix, allows the location of the separatrix, and hence the strike point, to be moved by shifting the plasma background laterally with respect to the tile geometry defined in the model. While it is possible to use experimental data as input from particular discharges or specific periods of discharges, the approach described above also preserves considerable flexibility for ad hoc modifications. The shifting of strike points by translation of the plasma background relative to the tile geometry may be performed both between and during modelling runs, allowing the effects of strike point sweeping to be investigated. Furthermore, the effects of broad changes in the plasma conditions may be determined by the scaling of a reference scenario. For example, if the dependence on plasma temperature is being investigated, the 2-D temperature distribution of Figure 4.7 may be multiplied by a constant factor and the code re-run using this altered input. Thus, the approach is designed to both preserve experimental input and make it a simple exercise to investigate a wide range of input conditions.

4.2.4 Pre-calculations

Many quantities within the model are determined by the temperature, density and ion flux plasma background. As many quantities as possible are pre-calculated on the 2-D grid using this background in order to achieve good code performance. The use of such look-up tables is often orders of magnitude faster than performing interpolations or detailed calculations within the main code itself.

The sputtering yields for deuterium on beryllium and beryllium self-sputtering are calculated with the use of analytical yield formulae (see [28] and Appendix A.1). As input to these formulae, the angles of incidence are assumed to be 60° [131]. The incident energies E_i are calculated using

$$E_i = 3ZT_e + 2T_i, \tag{4.1}$$

with electron temperature T_e, ion temperature $T_i = T_e$, and atomic number Z, where the first term is due to acceleration in the electrostatic sheath and the second term is thermal energy [101]. Thus, the theoretical sputtering yields only vary with T_e, allowing them to be defined at every grid point along the tile surface using the T_e distribution that is used as input. Such arrays of quantities are automatically translated if the plasma background is shifted to describe different strike point locations or strike point sweeping.

The velocities of ions v_i are calculated using

$$v_i = \sqrt{2E_t/m_{Be}}, \tag{4.2}$$

where m_{Be} is the mass of a beryllium ion and E_t is the thermal energy of the ions. Ion trajectories follow flux surfaces, which are assumed to follow the angle of the separatrix for x-values smaller than or equal to the separatrix location. For larger x-values, the flux surfaces become steeper (i.e. more closely aligned to the vertical y-axis and directed towards the horizontal tile surfaces), as seen from magnetic reconstructions using EFIT. If the strike point location is shifted as input to a particular discharge, these flux surfaces and ion trajectories also get shifted automatically.

Ionisation coefficients $< \sigma v >^{-1}$, with ionisation cross-sections σ and electron velocities v, are used to calculate the probabilities that beryllium neutrals are ionised as they pass through the plasma. These coefficients are functions of the plasma electron temperature and density, and are provided by ADAS [92]. Apart from these ionisations, the beryllium neutrals are assumed to travel in straight lines through the plasma, with changes in direction/velocity due other collisional events being neglected. The ionisation time t_{ion} for a neutral travelling through a plasma of electron density n_e is given by

$$t_{ion} = \frac{1}{n_e < \sigma v >}. \tag{4.3}$$

For normal JET outer divertor conditions, the ionisation times reach a lower limit of ∼μs at the separatrix. Though the time step on which calculations are performed

can be changed by user input, this suggests the use of a 1 μs time step as the default choice. The probability of ionisation P_{ion} during a time step Δt is then given by

$$P_{ion} = 1 - \exp\left(-\Delta t / t_{ion}\right), \tag{4.4}$$

which only varies with T_e and n_e. Since the 2-D temperature and density distributions are determined as input to the model, a 2-D grid of ionisation probabilities may also be generated in advance. The probability of ionisation of any given beryllium neutral is then just a function of its location on the 2-D grid, and may be found via a look-up table. This is performed for each beryllium neutral in the plasma at each time step. Following the procedure used in ERO [112], in order to account for the statistical nature of the process, each value of P_{ion} is compared to a random number between 0 and 1. Ionisation occurs for the subset of neutrals for which the ionisation probabilities are greater than these random numbers. This treatment of the ionisation probabilities, incorporating pre-calculation and look-up tables, is particularly efficient relative to performing the billions of calculations that would otherwise be required within the main code.

4.2.5 Varying inputs

As described in Section 4.2.3, the plasma background is defined in such a way as to make it easy to modify the temperature, density and flux profiles, including the location of the strike point. These may be defined either from Langmuir probe measurements of specific experimental discharges, or by scaling reference cases in order to investigate the effects of broad changes to the inputs. There also exist other user inputs which further increase the range of conditions that can be investigated using the model.

The user sets the percentage of beryllium in the incident deuterium flux to the divertor surfaces. The impurity concentration in JET-ILW plasmas is relatively low, with experiments and modelling indicating percentages of order 0.1-0.2% [127] (and references therein). Another important parameter is the initial beryllium surface coverage on the tungsten divertor tiles. Again, this initial coverage is expected to be relatively low in the ITER-like wall divertor, with WallDyn suggesting that coverages are typically sub-monolayer and dependent on preceding divertor and limiter operations [118]. The incident flux fraction and initial coverage have a strong impact on the magnitudes and balance of erosion and deposition at the divertor tiles. Results from parameter scans over these quantities will be presented in Section 7.5 in order to identify the key parameter spaces and their physical effects.

Finally, the user must set some practical quantities related to each run. As noted in Section 4.2.4, the time step is by default set to 1 μs, and should be kept larger than the smallest ionisation time for the beryllium neutrals. The total time the code runs for is generally set to 2 s; depending on the other inputs, the erosion/deposition behaviour can stabilise and make longer runs of little practical use. The particle reduction factor, generally set to 5×10^{12}, describes the number of 'real' particles that each particle described in the model represents. This reflects the fact that it is computationally impractical to model the very large number of inidividual particles in a macroscopic system. Setting the value of the reduction factor too low makes

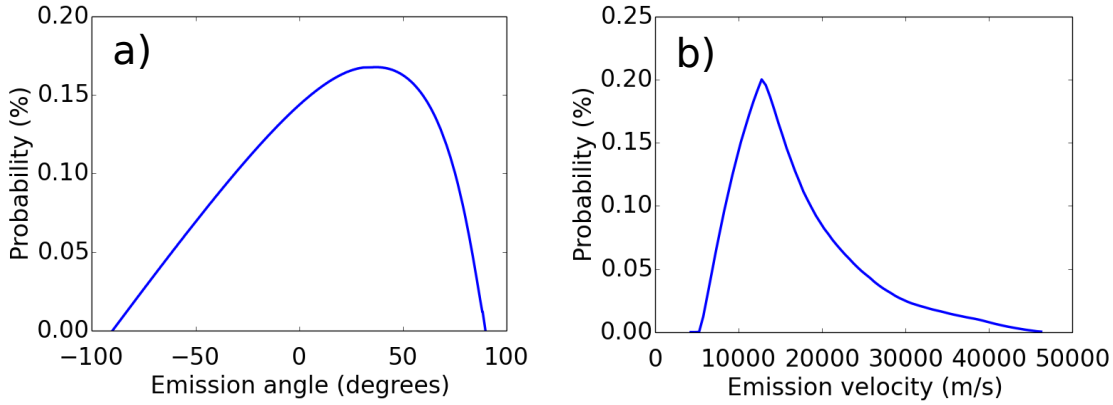

Figure 4.8: Plots showing the probability distributions for sputtered beryllium neutrals: a) emission angle with respect to surface normal; b) emission velocity

the code run more slowly due to the larger number of calculations required. Conversely, setting the reduction factor too high makes the code run faster at the risk of introducing inaccuracies or artefacts to the results.

4.2.6 Sputter distributions

At each grid point along the tile surface, the pre-calculated erosion yields are scaled by the local beryllium surface coverage and multiplied by the incident flux in order to determine the beryllium source profile. This is performed for both sputtering of beryllium by deuterium and beryllium self-sputtering. Reflection is assumed to be 75% efficient for a bare tungsten tile [127]. Higher beryllium coverages enable more sputtering and self-sputtering, but limit reflection of incident beryllium due to the lower spatial fraction of bare tungsten tile.

Plots showing the probability distributions for sputtered beryllium neutrals are shown in Figure 4.8. Since the ions impinging on the surface are incident at -60° to the normal, some preservation of directionality is assumed based on literature results and the angle of ejected beryllium is tilted away from the surface normal [30]. The emission velocities were found from the outputs of a series of SRIM/TRIM runs [109]. These were performed at different incident energies, with the plot in Figure 4.8b representing the reference case. Since the emission velocity scales approximately with the square root of the incident energy, scaling of this reference profile provides the appropriate probability distribution for different incident energies within the model. It may be calculated that the eroded neutrals can reach the corner region from the strike point region in of order 10 μs. Therefore, direct transport to this remote region, or many redeposition/sputtering/reflection steps, is possible within the typical 2 s run time. For each beryllium neutral sputtered, the angle and velocity of emission are randomly selected over these custom distributions. An equivalent procedure is followed for self-sputtered and reflected beryllium neutrals.

Table 4.1: Steps performed in each loop of the Monte Carlo code.

1) Sputter beryllium
a) Calculate sputter, self-sputter and reflection sources from each tile surface grid point using pre-calculated yields, background and returning fluxes to the surface and beryllium surface coverage. b) Move sputtered, self-sputtered and reflected beryllium from surface beryllium store to neutral store. c) Randomly assign emission angles and velocities using custom distributions. d) For each beryllium neutral, calculate and store constant x and y components of emission velocity, v_{nx} and v_{ny}.
2) Move beryllium neutrals
a) Propagate neutrals in x by a distance $v_{nx}\Delta t$ and in y by a distance $v_{ny}\Delta t$. b) Resolve new positions of neutrals onto grid points using random weighting approach. c) If propogation causes neutrals to leave the system or impact a tile surface, record the positions of escape/contact and update the boundary/surface stores. d) Update neutral store.
3) Ionise beryllium
a) Look up the probability of ionisation for each beryllium neutral based on its location on the spatial grid. b) Compare each probability to a random number in the range 0 to 1 to determine whether each neutral is ionised. c) For the subset of neutrals that are ionised, move from neutral store to ion store.
4) Move beryllium ions
a) Add the fraction of beryllium in the incident deuterium flux to the surface beryllium on tiles. b) Look up the velocity and trajectory (flux gradient) of each beryllium ion in the plasma based on the pre-calculated spatial grids for these quantities. c) Propagate the ions and resolve onto grid points using the random weighting approach. d) If propagation causes ions to leave the system or impact a tile surface, record the positions of escape/contact and update the boundary/surface stores. e) Update ion store.

4.2.7 Program flow

Each time step, the model loops over the four following operations: 1) sputter beryllium; 2) move beryllium neutrals; 3) ionise beryllium; 4) move beryllium ions. The code keeps track of the number of particles in the system and those leaving it in arrays storing the beryllium ions, berylllium neutrals, surface beryllium and beryllium leaving the boundaries of the modelled area. The four main steps that are looped over are expanded on in more detail in Table 4.1.

The code loops over the above steps n = total time/Δt times, which under default settings is equivalent to 2 million time steps. Several quantities are recorded periodically and output at the ends of runs. These quantities are both spatially resolved along tile surfaces or boundaries to the modelled area and temporally resolved so that changes in the system with time can be examined. The most important of these outputs are the beryllium on surface tiles, the yields from tile surfaces, the beryllium brightnesses due to ionisations and the beryllium ions and neutrals escaping from the system to remote regions.

The pre-calculation of many parameters in the code (see Section 4.2.4) enables quantities to be determined within each time step just by reference to spatially-resolved look-up tables. Since runs typically comprise millions of time steps, this provides a significant speed up relative to performing detailed calculations within each loop. Importantly, the code is also written to be efficient in user time. Changes in input conditions are quick and easy to implement, providing good approximations to a wide range of experimental conditions and in general taking input from them. Examining the modelled results this produces, and comparing to experimental results, provides a powerful method for investigating erosion, deposition and transport of beryllium in the JET-ILW divertor.

4.3 Conclusions

This chapter has described the technical details of the two main codes used in the current study. The first of these models the time-varying deposition on rotating collector probes located in remote regions of the JET divertor. Since these deposition profiles represent a year or more of plasma operations, the modelling is necessarily simplified, using assumptions of geometrical, line of sight transport. This is offset by the inclusion of various experimental data to improve the accuracy with which the physical system is described. Results from the rotating collector code are presented and interpreted in Chapter 5 and Chapter 6.

The second code is a Monte Carlo description of the JET-ILW outer divertor. This follows beryllium ions/neutrals through the sputtering, self-sputtering, reflection, ionisation and redeposition processes that may occur, subject to the surface and plasma conditions. It provides a higher time resolution, more detailed investigation of the impurity erosion, deposition and migration. This enables an examination of the effects of varying input conditions, a comparison to various experimental results and an investigation of the increased importance of the initial divertor phase. These results are presented and discussed in Chapter 7 and Chapter 8.

Chapter 5

Rotating collector deposition

5.1 Introduction

This chapter presents deposition results from rotating collectors located in the central JET divertor (Figure 5.1). The time-dependent deposition results will be compared to modelled deposition profiles and comparisons will be drawn between the JET-C and JET-ILW results. The locations of the JET-C and JET-ILW collectors are similar, with views of the vertical tiles of the inner divertor. However, while the JET-C collector views only tile 3, in JET-ILW the collector also has a partial view of the bottom of tile 1. These differences are incorporated into the modelling descriptions of the two geometries. The analysis focuses on collectors from the 2005-7 JET-C campaign and the 2011-12 JET-ILW campaign.

Section 5.2 will present the experimental deposition results from these collectors. In Section 5.3, these experimental deposition profiles will be compared and contrasted with the modelled deposition profiles. Section 5.4 will consider the changes in the average deposition rates on the collectors between campaigns in light of the differences in wall materials and strike point distributions. The deposition results from the rotating collectors will be compared to other, related deposition measurements in Section 5.5 and the chapter will be summarised and concluded in Section 5.6.

5.2 Experimental results

The species-specific, experimental deposition results presented in this section were obtained by post-mortem nuclear reaction analysis (Section 3.2.1) of the silicon collector discs. The resulting data, describing deposition as a function of angle, are mapped to give deposition as a function of discharge number through a consideration of the magnetic field histories of the campaigns.

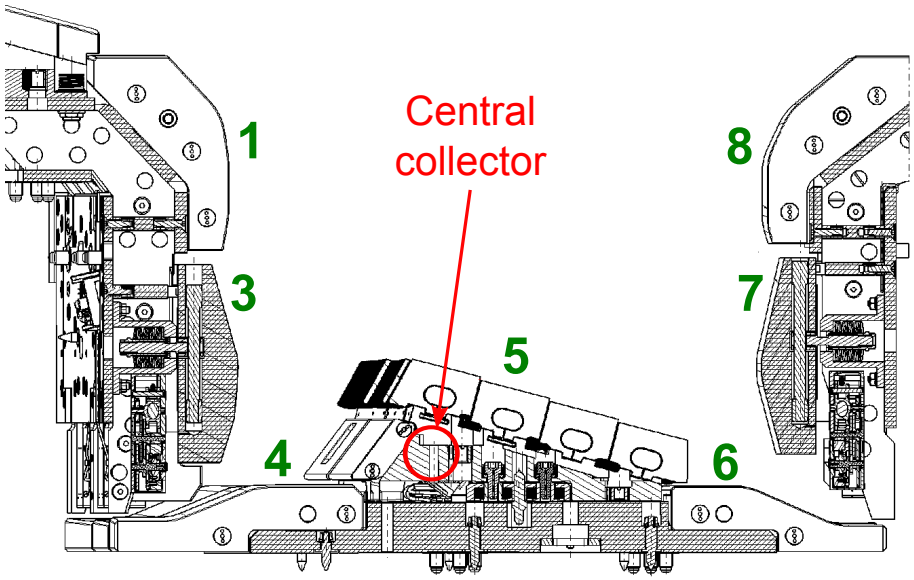

Figure 5.1: Poloidal cross-section of the JET-ILW divertor showing tile numbers in green and the location of the central rotating collector in red.

5.2.1 JET-C

The time-dependent deposition results for the 2005-07 carbon wall rotating collector, which were first published in [77], are shown in Figure 5.2. The deposition profile on the collector shows strong peaks and troughs at different times during the campaign. As noted in [77], the periods showing high deposition correlate with periods when the inner strike point was located on tile 3 for the majority of the divertor time; the periods showing low deposition correspond to periods when the strike point was generally located on tile 4. This shows the importance of the line of sight transport of eroded impurities from divertor tiles to remote regions.

The exception to this correspondence is the steep peak at the end of the plot. This peak is due to the collector reaching the end of its rotation before the end of the campaign, causing all subsequent deposition to aggregate at that one point. Thus, since this is where the relationship between deposition and discharge number breaks down, the x-range of the plot has been curtailed at this point and the deposition has been allowed to go off the scale in the y-dimension. This 'end-peak' is a common feature of these time-dependent collector deposition plots due to the finite lifetime of the collectors. However, the rotating collectors have recently been redeveloped in order to approximately double the number of discharges that they can operate for (though results from these collectors are not yet available).

As may be expected from the composition of the plasma-facing surfaces, carbon is the dominant impurity on the JET-C collector. Periodic evaporations of beryllium in the vessel resulted in some beryllium deposition being identified on the collector. However, the concentrations of beryllium were very low and have not been plotted here due to the poor statistics. As further noted in [77], carbon is preferentially chemically eroded from tile 3 and is transported to the collector. This leaves a relatively high Be/C ratio on tile 3, with a lower ratio being found on the collector. This reduced transport of beryllium to the remote collector location anticipates the behaviour seen under ITER-like wall operation (deposition magnitudes will be considered

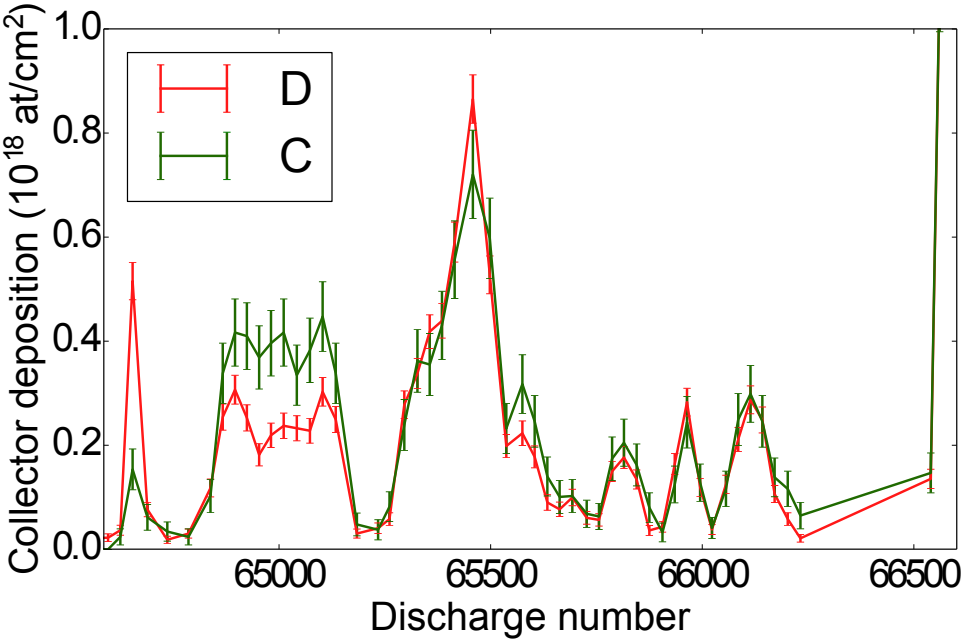

Figure 5.2: Plot of deposition as a function of discharge number for the 2005-7 collector from the JET-C central divertor. The evolution of the deuterium deposition is shown in red and the carbon deposition in green. The nuclear reaction analysis measurement process is Poissonian, giving $n^{1/2}$ uncertainties in the concentration of each species at each measurement point.

and compared in Section 5.4).

The time-variations of the deuterium and carbon deposition profiles are very similar. This strongly suggests the importance of chemical erosion/sputtering of carbon by deuterium, resulting in subsequent codeposition on the collector disc. Early in the campaign, though the deuterium and carbon profiles are still qualitatively similar, there are deviations in their relative magnitudes. Such variations in deuterium retention are usually associated with changes in substrate temperature or incident ion energy, with lower retention corresponding to higher temperatures and higher incident energies [100], though it is not clear why this should be the case for the particular discharges identified here.

5.2.2 JET-ILW

The deposition results for the corresponding collector from the 2011-12 ITER-like wall campaign are shown in Figure 5.3 and were previously pulished in [128]. The installation of the ITER-like wall resulted in an almost complete replacement of carbon impurities in the plasma with beryllium [90]. This is clear from the collector results, which show that beryllium became the dominant deposit on the JET-ILW collector. The beryllium deposition profile here is more constant than the carbon deposition profile in the JET-C case, showing fewer strong peaks and troughs. In terms of the campaign history, this is likely to be due to the prevalence of strike points on tile 3 during the 2011-12 campaign, resulting in less temporal variation in deposition. The 2011-12 collector exhibits a comparatively small end-peak due to

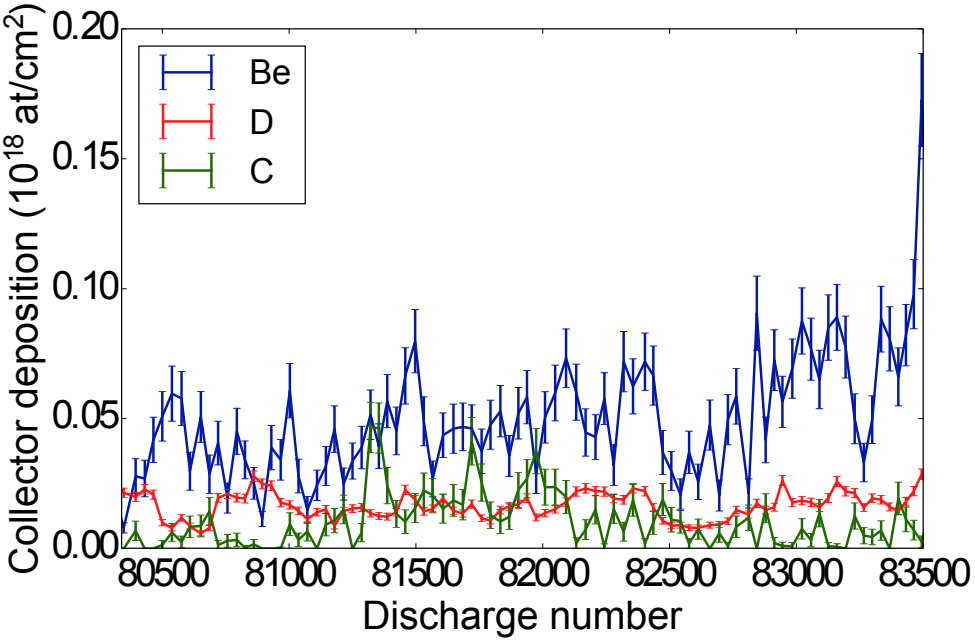

Figure 5.3: Plot of deposition as a function of discharge number for the 2011-12 collector from the JET-ILW central divertor. The evolution of the beryllium deposition is shown in blue, the deuterium deposition in red and the carbon deposition in green.

this campaign being relatively short, resulting in time-dependent deposition being measured for almost all discharges.

Carbon is still used in the JET-ILW divertor, for example in tungsten-coated CFC tiles, and is identified on the collector at a reduced concentration approximately an order of magnitude lower than that of beryllium. The relatively poor statistics make it difficult to judge definitively, but the time-variation of the carbon deposition profile does not appear to follow that of the deuterium deposition profile, indicating a reduction in the importance of codeposition of carbon and deuterium. Although there is not as strong a chemical affinity between deuterium and beryllium, chemical sputtering of beryllium by deuterium has been identified [20]. This could contribute to some of the deuterium deposition found on the collector. In general, the deuterium to beryllium ratio decreases over the course of the campaign. This may be the result of higher power discharges later in the campaign causing increased collector surface temperatures via increased heat fluxes to the collector and thermal conduction through tile 5. Empirical scaling equations for deuterium retention in beryllium deposits [133] indicate that this decrease is compatible with a moderate temperature increase of $\sim$100 K.

Since the divertor of JET-ILW comprises tungsten plasma-facing surfaces, a significant tungsten presence might be expected in the collector deposits. However, relatively low deposits of $\sim 5 \times 10^{14}$ at/cm^2 were measured on the collector using Rutherford backscattering spectrometry (Section 3.2.2), approximately two orders of magnitude below the beryllium concentrations. The high atomic mass of tungsten results in low physical sputtering yields and it is not sputtered chemically. The erosion of tungsten in the JET divertor has been shown to only occur significantly due to incident beryllium ions and during ELMs [21]. Even when tungsten is eroded, its high atomic number gives a large cross-section for ionisation, often resulting in

prompt redeposition. Thus, the tungsten concentration found on the remotely located rotating collector is comparatively low and beryllium originally from the main chamber comprises the dominant deposit. This lack of tungsten erosion/deposition in JET-ILW supports its use as a robust divertor plasma-facing material.

5.3 Comparison of model and experiment

5.3.1 JET-C

As noted in Section 5.2.1, the impurity deposition on the JET-C rotating collector was dominated by carbon. Figure 5.4 again shows the carbon deposition profile as a function of discharge number, which is here compared to the deposition profile obtained from the geometrical modelling approach (Section 4.1). Since the modelled results have been scaled by a constant attenuation factor, the overlap in magnitude is the result of applying a free parameter. However, the purpose of this modelling is to compare the long-term evolutions of the profiles with time.

The good qualitative agreement of the experimental and modelled deposition profiles further indicates the importance of the line of sight transport of neutral impurities as described by the model. Although the long timescales considered in the modelling mean that assumptions and approximations have had to be imposed, the inclusion of a range of experimental data improves the accuracy of the modelling description and hence the accuracy of the results. In addition, the temporal smoothing, which is inherent in the operation of the collectors and hence is imposed in the model, limits large, short-timescale deviations in the deposition profiles. The long-term variations over hundreds or thousands of discharges are thereby seen to exhibit considerable agreement.

In general, the attenuation factors used for scaling each modelled deposition profile are calculated by dividing the average of the experimental depositions by the average of the modelled depositions. Multiplying each modelled profile by each attenuation factor then results in experimental and modelled profiles with the same average depositions, making it easier to make qualitative comparisons. In this central divertor JET-C case, the decision was made to calculate the attenuation factor only from the discharges prior to discharge 66,000, due to the apparent differences in the deposition magnitudes before and after this point. After discharge ∼66,000, there are still strong time variations in collector deposition, which are reproduced in the modelled results. However, the magnitude of the deposition seen experimentally is lower than might be expected based on the model. The model's over-estimate of deposition after this point could suggest a physical reduction in the attenuation factor later in the campaign.

The sputtered neutrals have large mean free paths in the private flux region, implying that most losses of sputtered particles are likely due to ionisation and redepostion close to their point of origin. The greater fraction of high power/ELMy discharges later in the campaign led to higher plasma temperatures and radiated powers in the divertor. This may have increased the proportion of eroded neutrals that were ionised as they passed through the plasma. Additionally, an increased heat flux to, and hence an increased surface temperature of, the collector may have decreased the

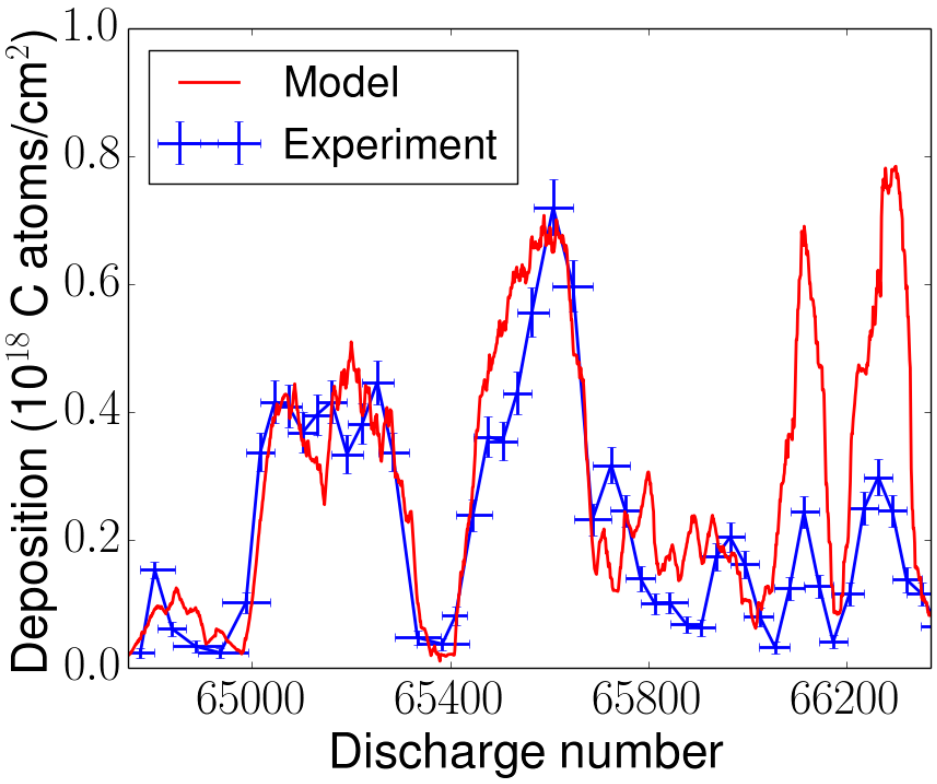

Figure 5.4: Plot showing the time-dependent carbon deposition profile on the rotating collector located in the central divertor of JET-C, comparing the experimental (blue) and modelled (red) results. The modelled results have been scaled by a constant attenuation factor of 0.12 in order to fit to the magnitude of the experimental results and make qualitative comparisons easier.

net deposition due to increased thermally-driven chemical re-erosion from the disc surface [32]. Increased surface temperature has previously been found to limit the net deposition on a co-located QMB to a quarter of that on the collector [77]. Increases in substrate temperature of approximately 100 K can be sufficient to increase this thermal re-erosion by a factor of 4 [32]. The collector is less thermally isolated than the QMB, suggesting that any temperature rise is likely to be moderate. The experimental deposition is a factor of 2.5-3 lower than the modelled deposition at the end of the campaign (Figure 5.4), suggesting moderate substrate temperature increases could be sufficient to contribute to the observed discrepancies in the deposition magnitudes.

ELMs may also drive the formation of particle clusters, which could dominate the material migration during ELMs due to their longer mean free paths and change the deposition characteristics [85]. Finally, an examination of the ion flux and D-alpha signals in the inner divertor indicates increased detachment in the inner divertor later in the campaign. The associated reduction in the ion flux to the surface is naturally accounted for in the model through the incorporation of the Langmuir probe data. However, this detachment may also reduce the physical and chemical sputtering yields [88], leading to a decreased carbon impurity source relative to that described in the model.

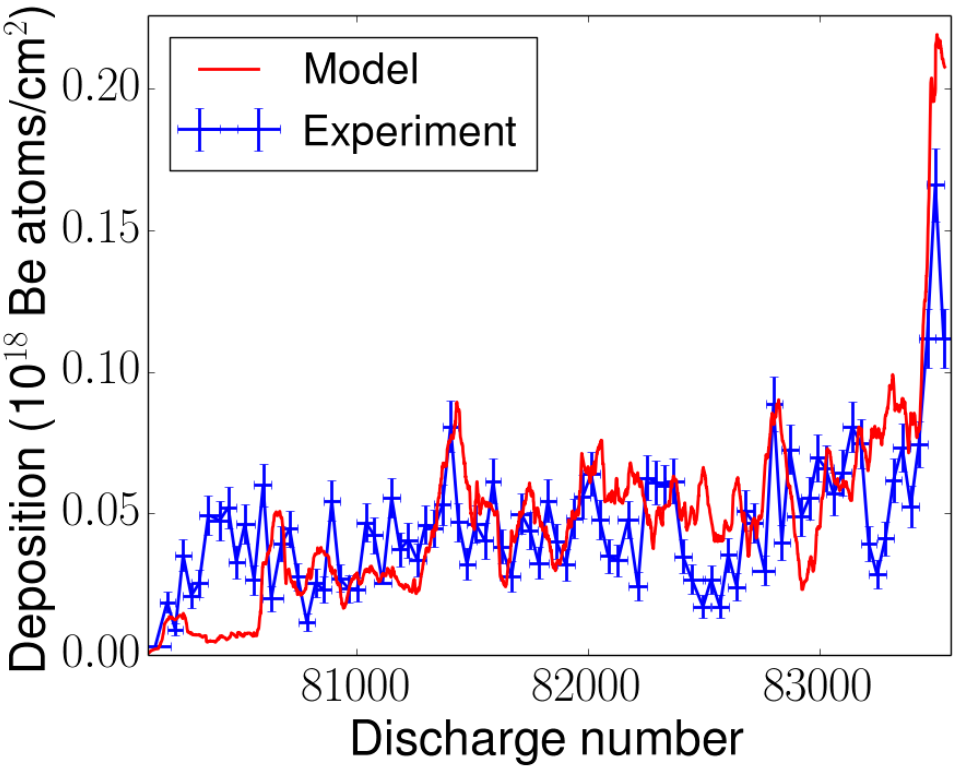

Figure 5.5: Plot showing the time-dependent beryllium deposition profile on the rotating collector located in the central divertor of JET-ILW, comparing experimental (blue) and modelled (red) results. The modelled results have been scaled by a constant attenuation factor of 0.64 (calculated by dividing the average experimental deposition by the average modelled deposition across the entire discharge range).

5.3.2 JET-ILW

The exchange of PFCs involved in the transition from JET-C to JET-ILW resulted in beryllium comprising the dominant deposit on the collector. Figure 5.5 compares the time-dependent experimental and modelled beryllium deposition profiles on the centrally-located rotating collector. The experimental and modelled results demonstrate reasonable qualitative agreement, though there are many small peaks and troughs that are missed or imperfectly captured by the modelling. In any case, the comparative lack of distinctive features relative to the carbon case makes comparison between the experimental and modelled profiles more difficult.

Though there is time-variation in the deposition profiles, inner strike points were more consistently located with a line of sight to the collector than in the carbon case, resulting in more consistent deposition periods. Not only was there a greater proportion of strike point time on tile 3, but the JET-ILW collector had a wider poloidal view than the JET-C collector, additionally incorporating the lower part of tile 1 (located above tile 3). However, different strike points still cause different modelled depositions due to variations in the acceptance angles to the collectors. Additionally, the beryllium impurity sources calculated in the model depend linearly on the ion fluxes to the tiles, making variations in ion fluxes during the campaign important for the calculated depositions.

As described in Section 4.1.3, the contributions of both sputtering and reflection of beryllium to deposition on the collector are interdependent. Since they have opposing dependencies on the surface coverage of beryllium on the tungsten tiles, overall the dependence of collector deposition on surface coverage is weakened. However, it is noted that the experimental deposition on the collector exceeds that expected from the modelling during the initial ∼400 discharges. Beryllium deposits have been shown to accumulate on divertor tiles during initial limiter discharges that occurred at the beginning of the 2011-12 ITER-like wall campaign [119], [118]. Such transient differences in impurity concentrations and surface coverages early in the JET-ILW campaign may have increased the beryllium sputtering sources available for deposition on the rotating collector, causing a discrepancy relative to the modelled results. The importance of the surface coverage of beryllium in the ITER-like wall divertor will be investigated in detail in Chapter 7, analysing under which conditions sputtering or reflection are more prevalent.

5.4 Aggregate deposition

While the previous two sections have focused on the variations in deposition on the rotating collectors, the total magnitudes of deposition, or alternatively the average deposition rates, also yield important information. This section will consider the deposition rates on the rotating collectors and examine the key reasons for the differences between them. The data will be presented as deposition rates averaged over the campaigns (i.e. around the disc circumferences). There is a slight subtlety in that a simple sum of the depositions represented by the data points in the figures from Section 5.2 is not appropriate. This is due to the fact that the width of the ion beam used for quantifying the deposits is 1 mm (E. Alves, personal communication, March 2014), while the width of the aperture in the collector housing is 2 mm. Thus, when performing measurements each mm, a division of the total deposition by a factor of 2 is necessary in order to eliminate this overlap and prevent it from distorting the average deposition rates.

A rotating collector from the central divertor was also operational during the 2007-9 JET-C campaign. The time-dependent deposition profile for this collector has not been modelled for two main reasons. Firstly, the lack of collector data from other divertor locations during this campaign prevents comparison and hence makes this data less useful. Secondly, the plasma conditions generally varied over a much shorter timescale than those during the 2005-7 campaign, making it more difficult to identify trends in the deposition profiles and compare between experimental and modelled results. However, these objections do not affect a consideration of the average deposition rate on this collector. Here, the 2007-9 data is examined along with the 2005-7 and 2011-12 data. This will aid the drawing of conclusions regarding the reasons for the different magnitudes of collector deposition during different campaigns.

The qualitative agreement of results in Section 5.3 suggests that line of sight transport from strike points is very important in determining deposition in remote locations. Thus, when analysing the average deposition rates on the collectors, it is important to consider the overall distributions of strike points during the discharges that each collector was operational for. This information is plotted in Figure 5.6. For the 2005-7 campaign, strike point time on tiles 3 and 4 was relatively evenly dis-

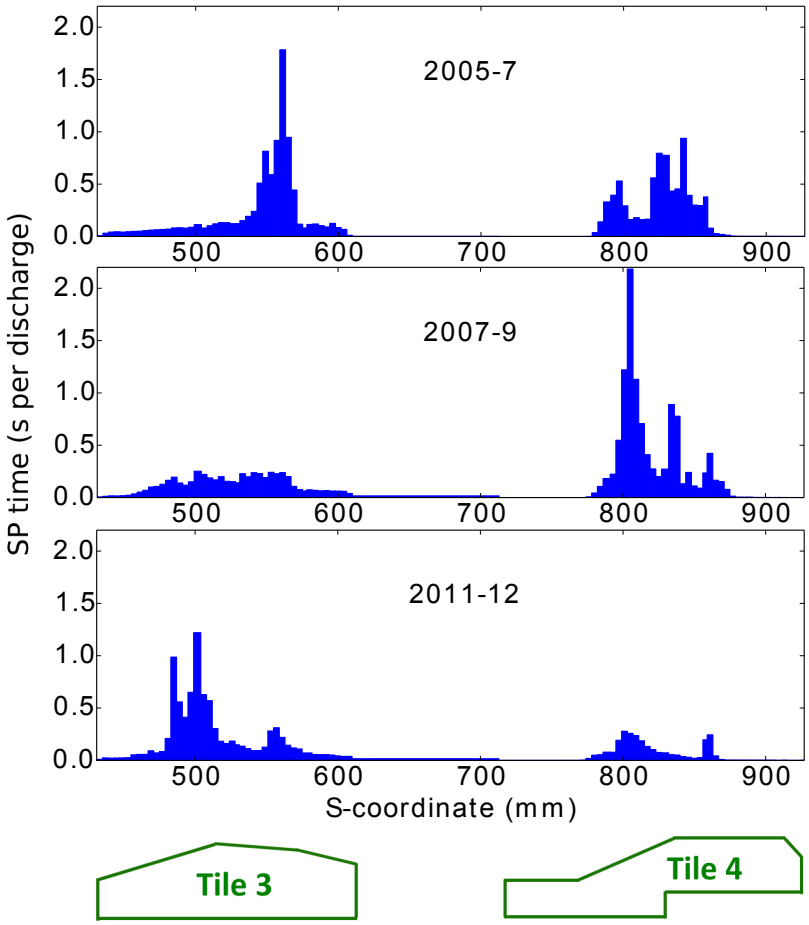

Figure 5.6: Inner strike point distributions, averaged over the collector lifetimes and shown as strike point time per discharge. The S-coordinate system follows the divertor surface poloidally, with the tile outlines shown below the plots aligned with their S-coordinate locations as represented on the x-axes. The collectors view the majority of tile 3 strike points, but do not view tile 4. A minority of discharges also had strike points on tile 1 (not shown), which has a partial line of sight to the 2011-12 collector.

tributed between the two tiles. However, in 2007-9 the majority of strike point time was on tile 4 and in 2011-12 most strike points were on tile 3. This information is used to inform Figure 5.7. The deposition rates are presented both per discharge (a) and per second of time for which the strike point had a line of sight to the collector (b). This enables the effects of the strike point distributions as shown in Figure 5.6 to be extracted and normalised to.

The most significant difference between the campaigns is the large reduction in beryllium deposition for JET-ILW operation relative to carbon deposition for JET-C operation. The impurity source from the main chamber and the transport of these impurities to the divertor is lower in the JET-ILW case [134]. Additionally, for beryllium impurities there is no chemical erosion from tiles and only a reduced level of chemically-assisted physical sputtering relative to the case for carbon [20]. Even though there was a lot of strike point time on tile 3 for the JET-ILW campaign, these effects resulted in a reduction in deposition per discharge by a factor of 4-9 compared to the two JET-C collectors (plot (a)). If the differences in the solid angles

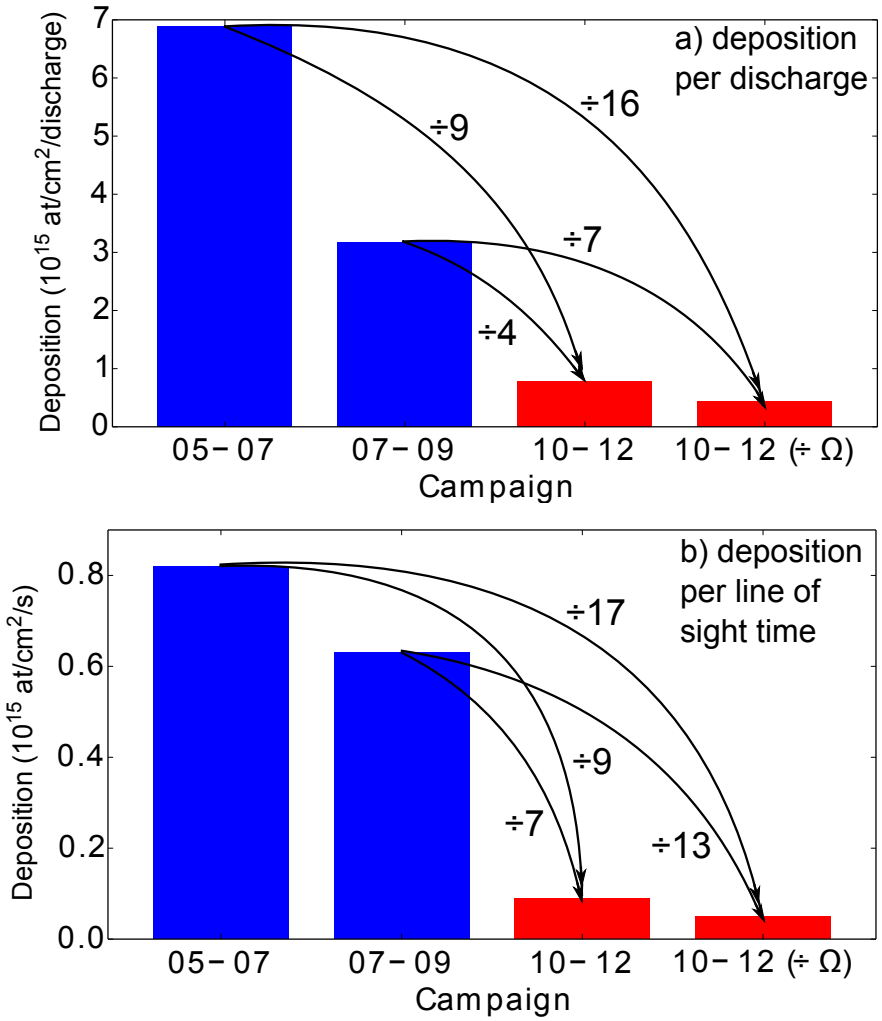

Figure 5.7: Plots showing the average deposition rates on the collectors: a) Average deposition per discharge; b) Average deposition per second for which the strike point had a line of sight to the collectors. The final bar in both plots shows the equivalent JET-ILW deposition rates after normalising to the solid angle Ω subtended by the carbon collectors. The factors by which the JET-ILW deposition rates are reduced by relative to the JET-C deposition rates are indicated.

subtended by the JET-C and JET-ILW collectors are adjusted for, this becomes a factor of 7-16.

When the differences in the strike point distributions are normalised to using the line of sight times to the collectors (plot (b)), the ranges of these reductions become smaller. The average deposition rate for JET-ILW is then reduced by a factor of 7-9 relative to JET-C, which equates to a factor of 13-17 when the difference in solid angle is adjusted for. The ranges narrow when line of sight times are considered due to the improved agreement between the deposition rates on the two JET-C collectors under this analysis. The prevalence of tile 4 strike points rather than tile 3 strike points during the 2007-9 campaign resulted in a lower deposition rate relative to the 2005-07 campaign. However, once the differences in strike points are normalised to, the reduction amounts to less than 25% of the 2005-07 deposition rate. The remaining difference may be explained by the high proportion of tile 4 strike points

causing re-erosion from the 2007-9 collector. QMB measurements have indicated that moving the strike point from tile 3 to 4 changes the area under tile 5 from deposition-dominated to erosion-dominated due to a reduction in the C/D flux ratio to the region under these conditions [135].

It is worth stressing the importance of the order of magnitude reduction in deposition rate on the JET-ILW collector relative to the JET-C collector. As described above, this is the result of both a lower impurity source from the main chamber and a reduction in chemical sputtering (and absence of chemical erosion). Thus, the rotating collector results, together with studies by other authors (Section 5.5), demonstrate the success of the ITER-like wall in terms of the observed reduction in erosion and deposition. The erosion source from material surfaces is limited, validating the use of beryllium and tungsten PFCs. Furthermore, the impurity deposition and fuel retention in remote areas is greatly reduced, which has beneficial implications in terms of both safety and fuel efficiency. These results provide valuable experience and encouraging results for the successful operation of ITER in the coming years.

5.5 Comparison to other results

5.5.1 QMBs

It is informative to compare the results from the rotating collectors to deposition results from other sources, in order to gain an understanding of their generality. There is a QMB located under tile 5, in an analogous location to the rotating collector considered here. This QMB does not have a shutter due to lack of space, meaning that it was continuously exposed to the plasma during the 2005-07 campaign (results were limited for other campaigns due to electronic failure). The time-evolution of the erosion and deposition, as calculated from the QMB frequency, was compared to the rotating collector deposition profile in [77].

The time-dependences of the collector and QMB deposition profiles show excellent agreement. Periods for which the collector showed high deposition corresponded to net deposition on the QMB; periods for which the collector showed low deposition corresponded to net erosion from the QMB. The operating mechanism of the collectors restricts the measurement of net erosion periods since material deposited during previous discharges becomes hidden as it rotates beyond the area exposed by the aperture. A factor of 4 higher deposition was measured on the collector relative to that on the QMB during the net deposition periods. The most likely reason for this difference in magnitude is the greater thermal isolation of the QMB crystal relative to the collector disc, which increases surface temperatures and restricts the net deposition on the QMB [77].

5.5.2 Passive diagnostics

When considering the deposition magnitudes rather than time dependences, it is more instructive to compare to passive, campaign-averaged deposition diagnostics

such as cavity samples [71],[72] or test mirrors [136]. These were positioned in similar locations to the JET-C rotating collector, but the data available comes from different campaigns (1999-2001 and 2007-9 respectively). The different strike point distributions and plasma parameters during the campaigns, relative to each other and to the 2005-7 campaign, make direct comparison more difficult. However, the average deposition rates measured on both the cavity samples and mirrors agree with the deposition rate on the collector within a factor of two. In addition, the deuterium to carbon ratio on the cavity samples was approximately equal to 1 (D/C ratio on the mirrors not quoted in [136]), indicating chemical sputtering/erosion and codeposition in good agreement with the rotating collector results (Section 5.2.1).

5.5.3 JET-C vs. JET-ILW

The replacement of the carbon wall of JET with the ITER-like wall [12] represents a major machine alteration that is on the critical path for successful implementation of ITER. As such, considerable effort has been dedicated to analysing changes in erosion and deposition between JET-C and JET-ILW. The global erosion and deposition balance for the 2011-12 JET-ILW campaign has been analysed and compared to JET-C conditions in [37] and [137]. These studies show an order of magnitude reduction in deposition in the JET-ILW divertor relative to that in the JET-C divertor, which is in good agreement with the reduction seen in the specific location of the central divertor rotating collectors.

It is also instructive to compare the reduction in deposition rate on the JET-ILW collectors to that observed on diagnostics from similar locations. The mirror tests were continued in 2011-12, showing a reduction in deposition relative to JET-C by at least an order of magnitude, depending on the depth by which the mirrors were recessed [75]. In addition, the deuterium to beryllium ratio of $\sim$0.25 is similar to that seen for the JET-ILW collector deposits (Section 5.2.2). The QMB located under tile 5 was not operational during the 2011-12 campaign. However, post-mortem analyses of the aggregate depositions on the QMB crystal and QMB housing cover have been performed and presented in [120]. The reduction in deposition by a factor of 14 relative to JET-C agrees well with that seen for the rotating collectors (Figure 5.7).

5.5.4 Modelling

As described in Section 4.1, the focus of the rotating collector modelling is on the variations in deposition as plasma conditions vary during campaigns. The constant attenuation factors that are applied to the deposition profiles are free parameters that are simply found by fitting to the experimental deposition magnitudes. For the JET-C case, if the attenuation factor of 0.12 is solely due to ionisation and redeposition of the eroded impurities as they travel through the plasma, this agrees well with the 84% redeposition of eroded impurities calculated using ERO [138]. Similarly for the JET-ILW case, the attenuation factor of 0.64 relates well to redeposition rates of 27-41% (dependent on strike point location) found using ERO [127]. No quantitative claims are made regarding the attenuation factors, but it is noted that these fitting factors show approximate agreement with those that would be expected

from modelling of the plasma transport. This provides encouragement that the rest of the physical description implemented in the rotating collector model is adequately representative of the system, which is attributed to the wide use of campaign-relevant experimental data in the modelling.

5.6 Conclusions

Results showing the time-dependent, species-specific deposition profiles for rotating collectors located in the central JET-C/JET-ILW divertors have been presented. These experimental deposition profiles have been compared to those produced via a geometrical modelling approach that utilises experimental data, showing good qualitative agreement. The line of sight transport of impurities from divertor tiles to remote regions and the locations of strike points have been shown to be significant for deposition on the collectors. The JET-ILW collectors demonstrate a replacement of carbon by beryllium as the dominant impurity in the deposits, along with a reduction in the retention of deuterium. Deposition on the JET-ILW collector is reduced by an order of magnitude relative to that on the JET-C collector, which is in good agreement with results obtained from other diagnostics. The reduced deposition and retention in JET-ILW validates the use of beryllium and tungsten PFCs and offers encouragement for future ITER operation, satisfying a major objective of JET's ITER-like wall.

The principles involved in measurement and mapping of collector deposits, comparison between JET-C and JET-ILW and modelling of the deposition profiles are all broadly applicable to other divertor locations. The following chapter will extend the analysis described in this chapter by applying it to the collectors located in the inner and outer JET-C and JET-ILW divertor corners.

Chapter 6

Deposition asymmetry

6.1 Introduction

While Chapter 5 examined the experimental and modelled deposition results for rotating collectors located in the central divertor, this chapter focuses initially on similar results for those collectors located in the inner and outer divertor corners. The inner corner collector views inner strike points on tile 4; the outer corner collector views outer strike points on tile 6 and also has a narrow line of sight to those on tile 5. These locations and geometries, which are similar for both the JET-C and JET-ILW campaigns considered, are shown in Figure 6.1. The JET-C rotating collector data is from the 2005-7 campaign and the JET-ILW data is from the 2011-12 campaign.

Section 6.2 will present the experimental, time-dependent deposition results from the carbon wall collectors, before comparing them to modelling results. Similarly, Section 6.3 will show the experimental and modelled results for the ITER-like wall collectors. In Section 6.4, the average deposition rates on the four collectors will be examined. Following this, Section 6.5 will use outer divertor QMB data to help interpret the depositions, with a discussion of the mechanisms involved presented in Section 6.6. Section 6.7 compares the deposition results to those found from other sources and conclusions from the chapter are drawn in Section 6.8.

6.2 JET-C results

6.2.1 Experimental results

The species-specific, time-dependent deposition profiles on the inner and outer divertor JET-C rotating collectors are shown in Figure 6.2 and Figure 6.3. These experimental results were obtained using nuclear reaction analysis (Section 3.2.1) of the collector discs, followed by mapping of the deposits to discharge number using the magnetic field history.

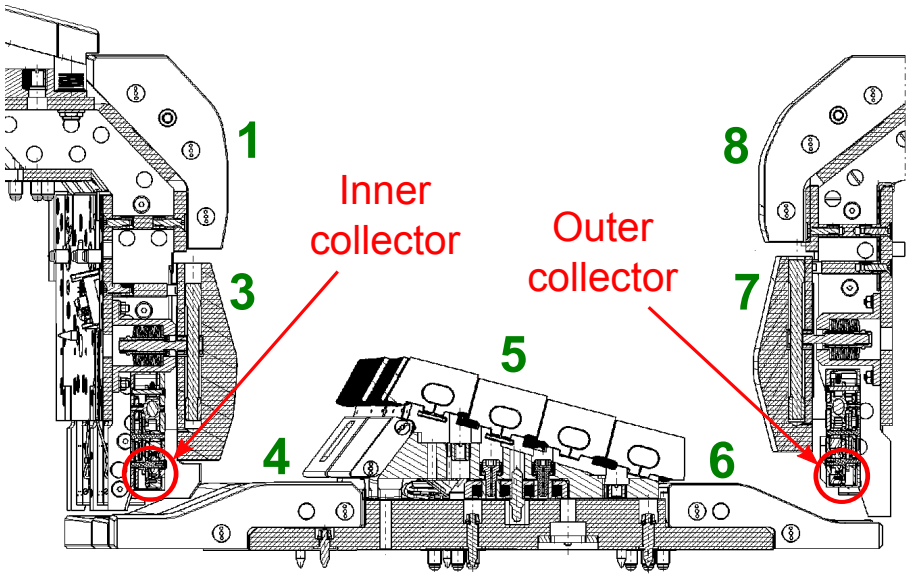

Figure 6.1: Poloidal cross-section of the JET divertor, showing tile numbers in green and the locations of the inner and outer corner rotating collectors in red.

For the inner divertor case, the peaks in the deposition profile correspond to periods of the campaign when there was significant strike point time on tile 4, which has a direct line of sight to the inner collector location. Though the outer divertor collector has a view of both tile 5 and tile 6, the proximity of tile 6 to the outer collector suggests that an analogous deposition dependence on tile 6 strike points might be expected. However, this was not apparent from the deposition and strike point data. This will be examined in more detail in Section 6.2.2 and possible explanations will be discussed later in the chapter.

As seen for the centrally-located JET-C rotating collector (Chapter 5), and as expected from the wall composition, here again carbon is the dominant impurity species in the disc deposits. The highly similar time dependences of the carbon and deuterium deposition profiles for both collectors is indicative of chemical sputtering/erosion and codeposition of the two species. However, while the deuterium to carbon ratio on the inner corner collector is above 1, that on the outer corner collector is only ∼0.5. This may be explained by the higher power fluxes and hence higher surface temperatures in the outer divertor, which have been shown to limit fuel retention due to increased thermal release of deuterium atoms. [139], [100].

6.2.2 Comparison of model and experiment

The experimental and modelled deposition profiles on the collectors from the inner and outer corners of the JET-C divertor are shown in Figure 6.4 and Figure 6.5 (first published in [132]). The focus here is on the variations in deposition throughout the campaigns. Thus, the modelled results have been scaled by constant attenuation factors found by dividing the campaign-averaged experimental deposition by the campaign-averaged modelled deposition, allowing easier qualitative comparisons (Section 4.1.5). Both collectors show strong variations in deposition with discharge

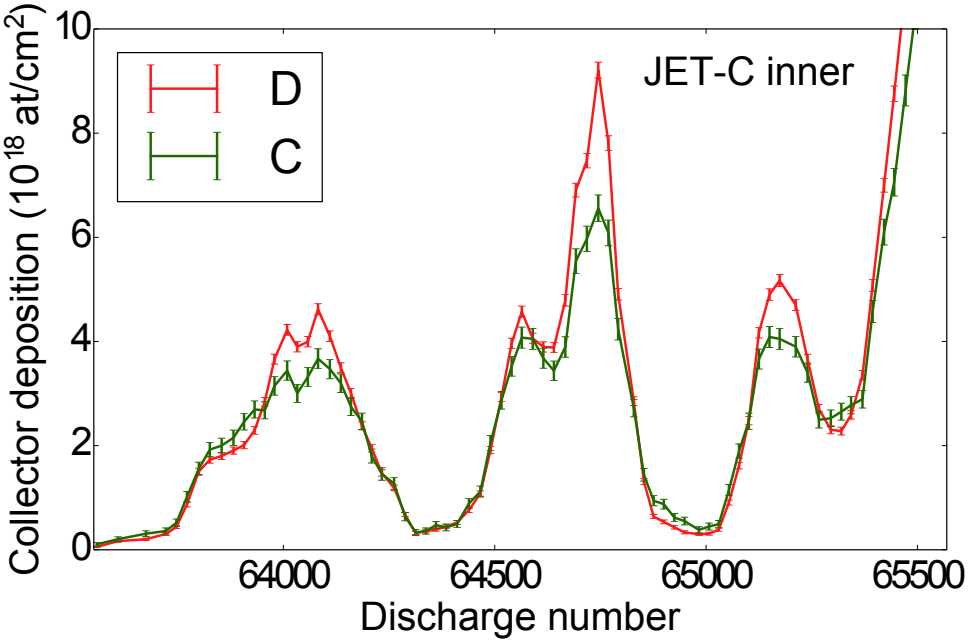

Figure 6.2: Plot of the deposition as a function of discharge number on the 2005-7 rotating collector from the JET-C inner divertor. The evolution of the deuterium deposition is shown in red and the carbon deposition in green.

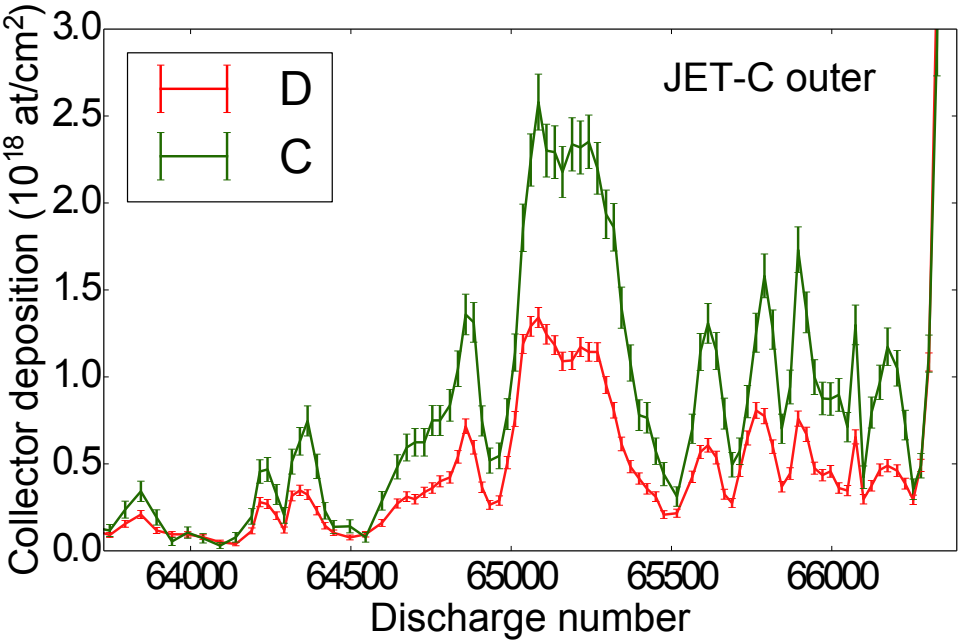

Figure 6.3: Plot of the deposition as a function of discharge number on the 2005-7 rotating collector from the JET-C outer divertor. The evolution of the deuterium deposition is shown in red and the carbon deposition in green.

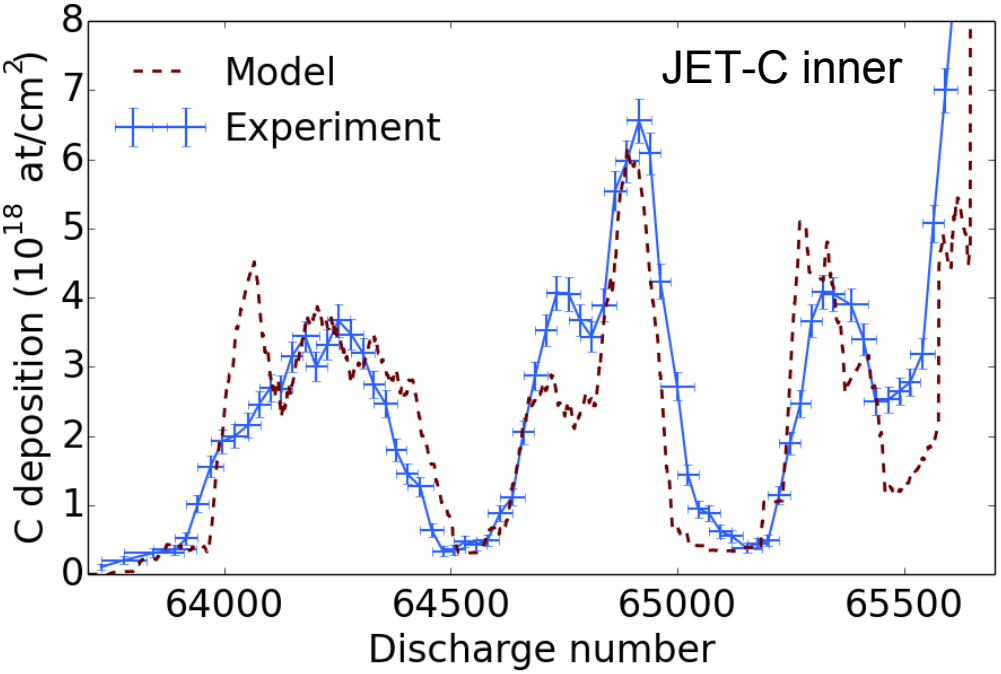

Figure 6.4: Plot showing the time-dependent carbon deposition profile on the rotating collector located in the inner divertor of JET-C. The experimental (blue) and modelled (red) results are compared. The modelled results have been scaled by a constant attenuation factor of 0.76.

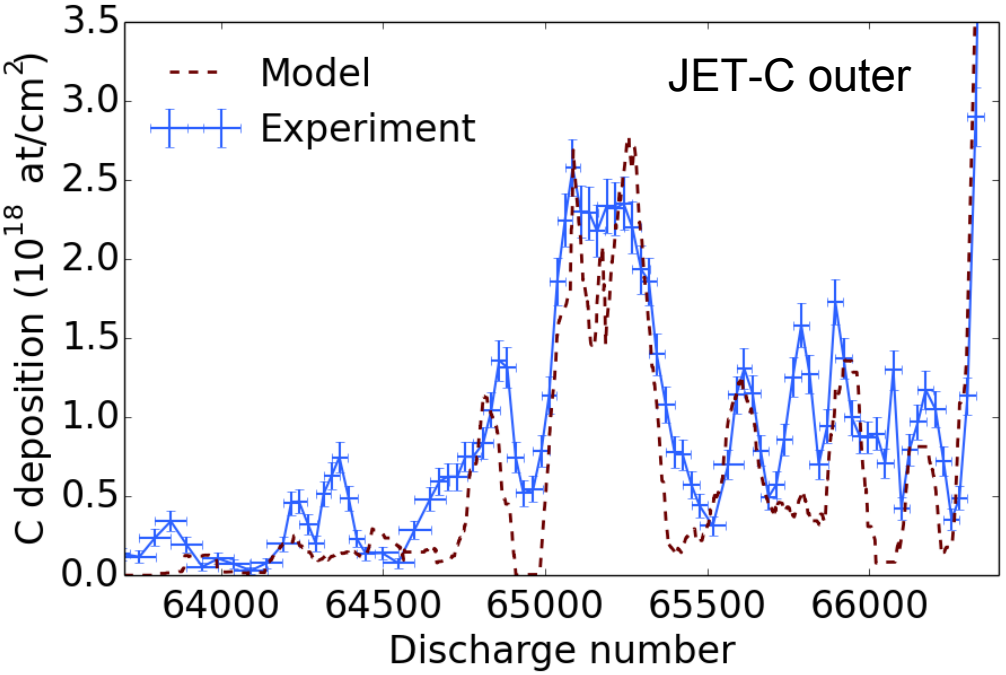

Figure 6.5: Plot comparing the time-dependent experimental (blue) and modelled (red) carbon deposition profiles on the rotating collector located in the outer divertor of JET-C. The modelled results have been scaled by a constant attenuation factor of 0.26.

number. This aids the relation of deposition results to varying plasma configurations and parameters.

The inner collector results show good qualitative agreement between experiment and model, demonstrating the importance of line of sight transport of neutral impurities from divertor tiles to remote locations. The 2005-07 campaign had relatively long, relatively uniform periods with inner strike points predominantly on tile 4 or tile 3 (causing peaks and troughs in the collector deposition respectively). These long-timescale features are well-suited to being captured by the collectors and the modelling, resulting in considerable qualitative agreement.

Initial attempts to model the JET-C outer divertor deposition yielded very poor agreement with experiment in both time-dependence and magnitude. The reasonable agreement seen in Figure 6.5 is the result of assuming that only tile 5 strike points contributed to deposition on the collector, which ostensibly seems flawed due to the proximity of the collector to tile 6. It also suggests that the simplified geometrical modelling treatment is not fully appropriate for the JET-C outer divertor case. The approach used here was prompted by an analysis of outer divertor QMB data (Section 6.5) and the physical basis of this treatment will be discussed in Section 6.6.

6.3 JET-ILW results

6.3.1 Experimental results

The species-specific, time-dependent deposition profiles on the inner and outer divertor JET-ILW rotating collectors are shown in Figure 6.6 and Figure 6.7. As seen for the centrally-located collectors (Chapter 5), in JET-ILW beryllium replaces carbon as the dominant deposit on the corner collectors. The tungsten depositions found from Rutherford backscattering spectrometry (Section 3.2.2) are again low, with aggregate deposits over the campaign of $\sim 10^{16}$ at/cm^2. This is due to the fact that the tungsten divertor tiles are only significantly sputtered during ELMs and by incident beryllium [21].

The similar time-dependences of the three different species on the inner divertor collector suggests that codeposition of deuterium with impurities may be preserved at a reduced level in this JET-ILW location. While codeposition of deuterium with carbon is well established, codeposition with beryllium is also possible; beryllium deuteride has previously been identified in tokamak plasmas through spectroscopy [140] and in laboratory plasma-surface interaction devices [141], [100]. The deposition profiles do not appear to follow a similar time-dependence for the outer collector, suggesting that codeposition is less important here. The deuterium to beryllium ratio is lower on the outer collector than the inner, which may be explained by the suppression of retention by the high surface temperatures in the outer divertor [142].

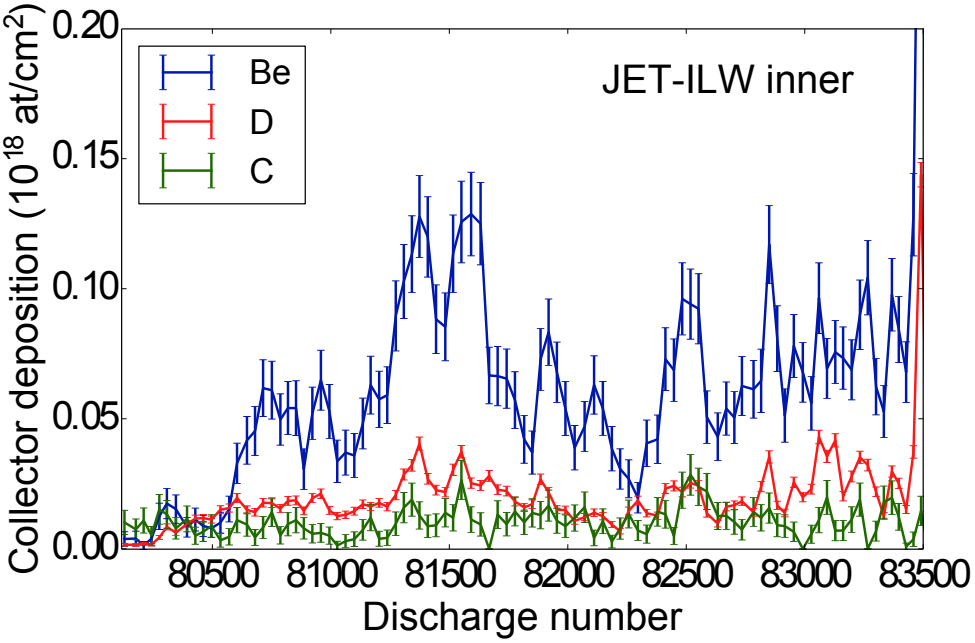

Figure 6.6: Plot of the deposition as a function of discharge number on the 2011-12 rotating collector from the JET-ILW inner divertor. The evolution of the beryllium deposition is shown in blue, the deuterium in red and the carbon in green.

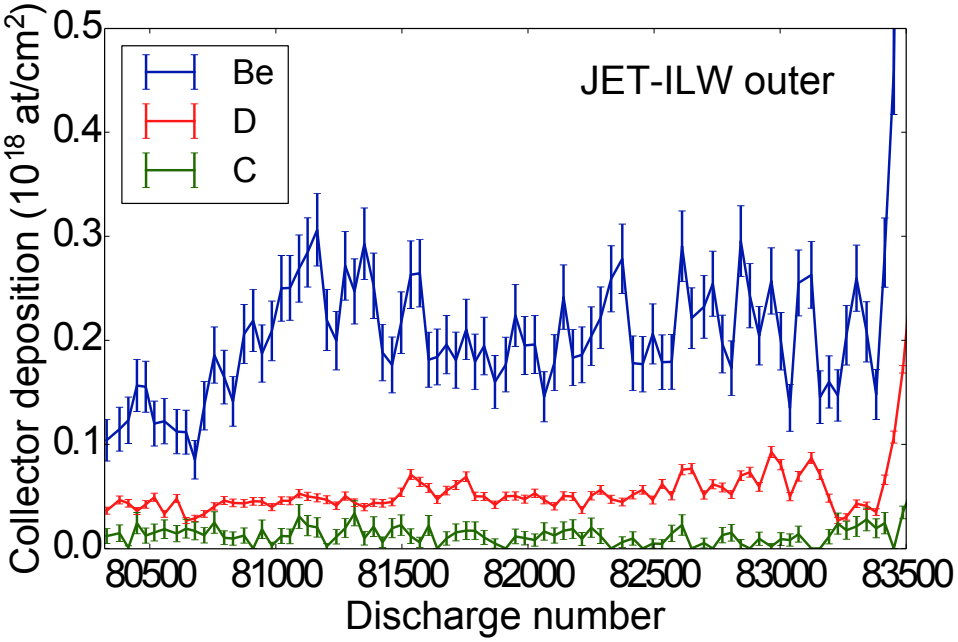

Figure 6.7: Plot of the deposition as a function of discharge number on the 2011-12 rotating collector from the JET-ILW outer divertor. The evolution of the beryllium deposition is shown in blue, the deuterium in red and the carbon in green.

6.3.2 Comparison of model and experiment

The experimental and modelled beryllium deposition profiles on the inner and outer JET-ILW rotating collectors are shown in Figure 6.8 and Figure 6.9. The experimental and modelled results in general show good qualitative agreement, though a close examination of individual features, particularly towards the end of the campaign, reveals significant disparities between the time dependences of the profiles. The relative lack of distinctive peaks and troughs, particularly in the outer divertor case, can make a critical assessment of agreement or otherwise difficult.

Despite these issues, the experimental and modelled deposition profiles do exhibit similar time dependences. This is believed to be mainly due to the inclusion of experimental data in the modelling, such as the strike point locations, ion fluxes and beryllium sources from spectroscopy. Though the description of the plasma is very limited, the incorporation of this data yields some of the end results of changes in plasma conditions in terms of what is important for the surface interactions. In fact, the model is in some sense better described as a convolution of experimental data from campaigns, which, over long timescales, provides a good approximation of the experimental depositions in the collector locations.

For the outer divertor case, deposition due to both tile 5 and tile 6 strike points has been allowed to occur. This contrasts with the JET-C case, when a good agreement was only achieved by not allowing tile 6 strike points to contribute to deposition on the collector. The agreements achieved using these different treatments in the two cases suggests a physical difference in the erosion/deposition balance between JET-C and JET-ILW. Analysis and discussion of this will be returned to in Section 6.5 and Section 6.6.

6.4 Aggregate deposition

As well as examining the time-dependent deposition profiles on the rotating collectors, it is also informative to analyse the average deposition rates. This can help general conclusions to be drawn regarding the importance of the different collector locations and plasma-facing materials. The average depostion rates on the four collectors discussed in this chapter are shown in Figure 6.10. Although for individual discharges the deposition rates on the inner/outer collectors will differ from the results shown here, the plot shows the deposition rates averaged over the whole campaigns and therefore over a wide range of plasma conditions.

The most obvious result apparent from the figure is that the total deposition rate on the JET-ILW collectors has been reduced by an order of magnitude relative to the total deposition rate on the JET-C collectors. This reduction between JET-C and JET-ILW deposition agrees well with that observed for the central divertor collectors (Figure 5.7). The lower main chamber impurity source and transport to the divertor in JET-ILW [134] contributed to this reduced deposition. There is also limited chemical sputtering of beryllium impurities and no chemical erosion, contrary to the case with carbon [20]. Finally, differences in strike point distributions can limit transport to the divertor corners. The proportion of tile 4 strike points in the JET-ILW campaign was a factor of 2.1 less than that in the JET-C campaign, reducing

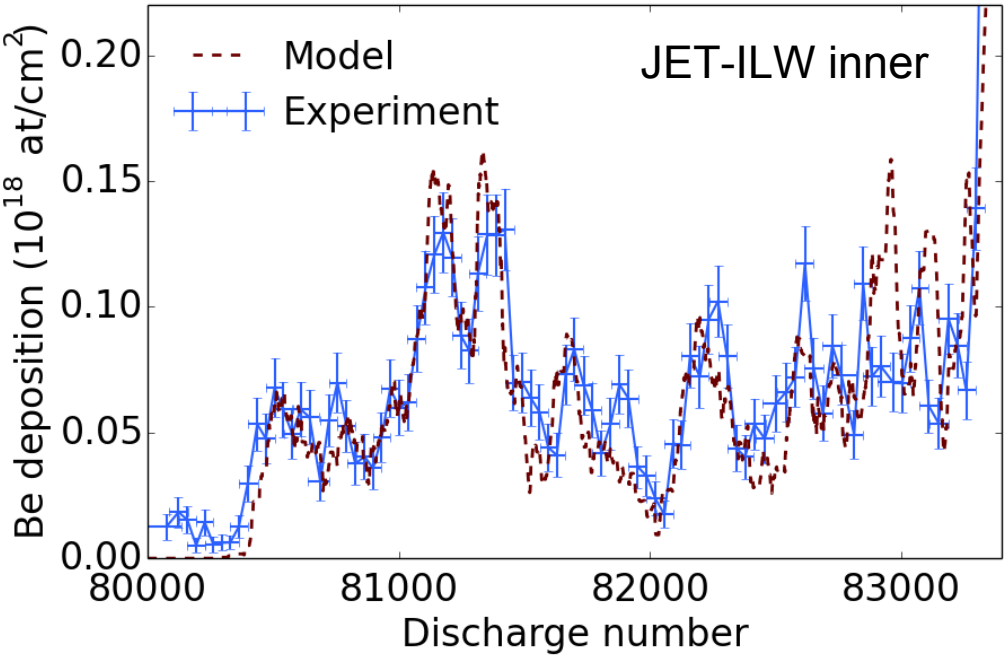

Figure 6.8: Plot comparing the time-dependent experimental (blue) and modelled (red) beryllium deposition profiles on the rotating collector located in the inner divertor of JET-ILW. The modelled results have been scaled by a constant attenuation factor of 0.88.

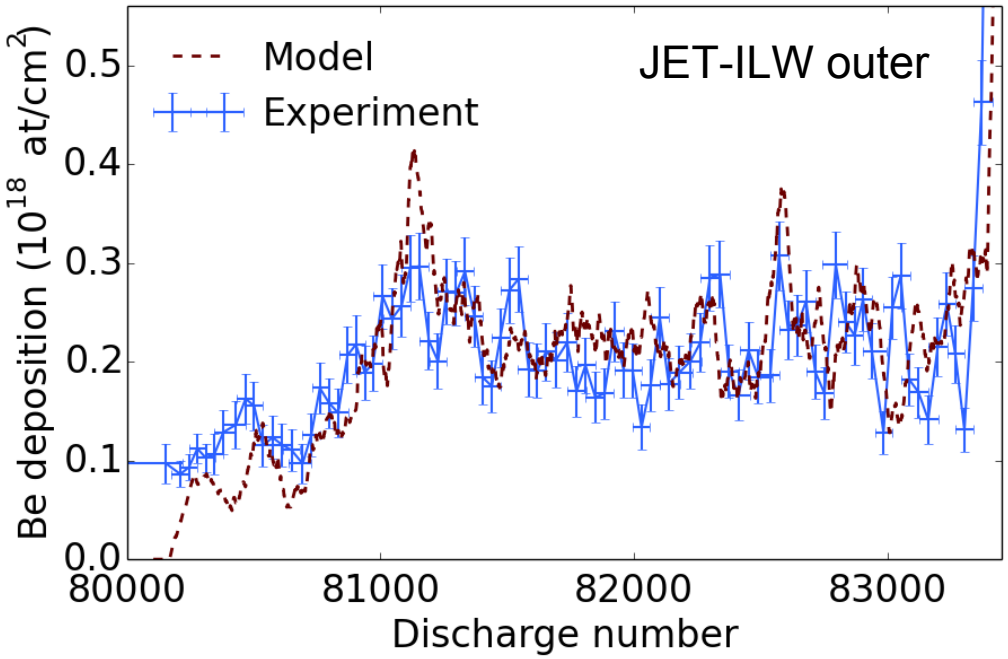

Figure 6.9: Plot comparing the time-dependent experimental (blue) and modelled (red) beryllium deposition profiles on the rotating collector located in the outer divertor of JET-ILW. The modelled results have been scaled by a constant attenuation factor of 0.17.

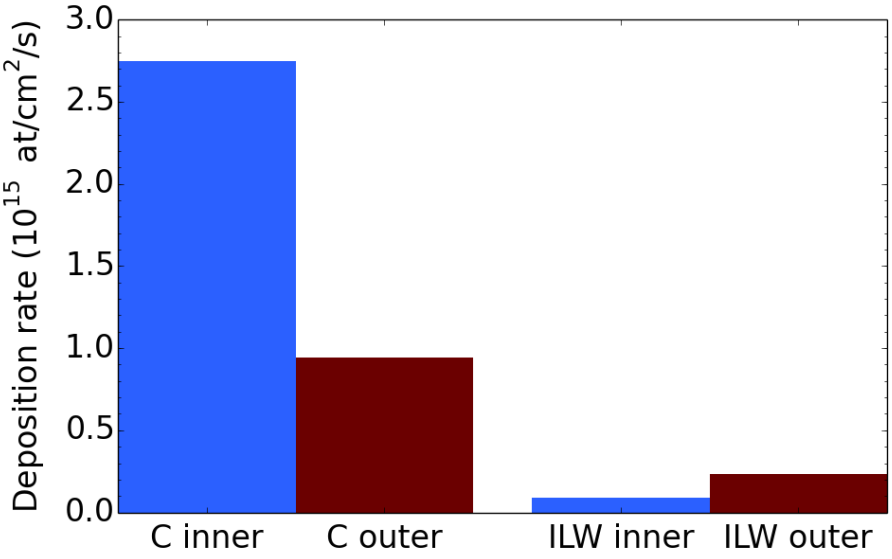

Figure 6.10: Deposition rates on the inner and outer JET-C collectors and inner and outer JET-ILW collectors, averaged over their whole periods of operation. The deposition rates refer to those of the dominant impurity in each case, i.e. carbon in the JET-C case and beryllium in the JET-ILW case.

deposition on the inner corner collector.

The second important result from Figure 6.10 concerns the distributions of deposits between the inner and outer divertor collectors. Greater deposition has generally been observed in the JET-C inner divertor than the outer due to outboard to inboard SOL flows [41] and the dependence of impurity sticking and desorption of carbon on substrate temperature [69]. The JET-C results shown in the figure agree with this trend; the inner divertor JET-C collector had a higher deposition rate than the outer divertor JET-C collector.

However, for the JET-ILW collectors this trend is reversed and more deposition is observed on the outer divertor collector than the inner. This cannot be explained by changes in the strike point distribution; there was a reduction in strike point time on both tile 4 and tile 6 in the JET-ILW campaign. The greater deposition on the outer collector than the inner represents another difference between the JET-C carbon and JET-ILW beryllium cases. Firstly, the modelling of the collector deposition profiles suggested that there were differences in whether outer corner deposition occurred or not for tile 6 strike points (Section 6.2.2). Secondly, this analysis of average deposition rates has revealed a reversal in deposition asymmetry between the inner and outer divertor corners. In order to investigate these differences in erosion/deposition/transport behaviour between JET-C and JET-ILW, analysis of outer divertor QMB measurements was performed.

6.5 QMB results

The QMBs have a higher time resolution than the rotating collectors, making it easier to identify changes in erosion or deposition and relate them to changes in

plasma conditions. The outer divertor QMBs are in analogous locations to the outer divertor rotating collectors. The QMB data is from the 2005-7 JET-C campaign and the 2013-14 JET-ILW campaign (since the QMBs were not operational during 2011-12). Although there were differences in operating conditions between the 2011-12 and 2013-14 campaigns, the general analysis of the effects of wall materials and strike point locations that is conducted here is unlikely to be affected significantly by this.

The shutters covering the QMB deposition crystals are opened for a few seconds during particular discharges. The deposition during that period is calculated by comparing the deposition crystal frequency before and after the discharge with the temperature crystal frequency before and after the discharge (Section 3.1.2). Here, the database for the measurements recorded by each QMB is split into two depending on whether strike points were located on tile 5 or tile 6 while the shutter was open (data points with non-stationary conditions are neglected). Thus, for each QMB, two graphs may be plotted showing the cumulative frequency change while the shutter was open and the strike point was on tile 5, and the cumulative frequency change while the shutter was open and the strike point was on tile 6. By splitting the database in this way, the two configurations may be considered separately, allowing trends in the erosion and deposition to be identified.

Plots of the cumulative frequency changes of the outer divertor JET-C QMB for tile 5 and tile 6 strike points are shown in Figure 6.11. After comparison between deposition, temperature and reference crystal frequencies, increasing frequencies shown in these plots represent net deposition on the QMB and decreasing frequencies represent net erosion from the QMB. The figure shows that when the strike point was located on tile 5, the QMB generally recorded net deposition; when the strike point was on tile 6, there was net erosion from the QMB. This agrees with the way that the modelling of the JET-C outer collector deposition profile had to be set up in order to achieve a good fit with the experimental results. Deposition was restricted for tile 6 strike points and only allowed for those on tile 5 (Section 6.2.2).

It is noted that the modelling of the deposition on the JET-C outer divertor collector assumed that no deposition occurred for tile 6 strike points, but Figure 6.11 suggests that re-erosion for tile 6 strike points should also be applied. In practice, the collector surface temperature is likely to be significantly lower than that of the QMB (and more representative of wall temperatures). In [77], the greater thermal isolation and hence higher surface temperature of a QMB crystal was inferred to have lowered the net deposition by a factor 4 relative to a co-located rotating collector.

Without direct surface temperature measurements, it was therefore decided inappropriate to extrapolate erosion rates found from the QMB to the collector. The JET-C outer collector temperature is nevertheless likely to be higher than that of the inner collector, as suggested by the lower deuterium to carbon ratio of $\sim$0.5, compared to $\sim$1 in the inner divertor. The blunt assumption of no net erosion or deposition for tile 6 strike points is preferred to more complex and uncertain conjectures. This modelling approach, though it does not yield as close a match with experiment as for the other collectors, nevertheless shows reasonable agreement (Figure 6.5). For example, the period of discharges from $\sim$65,000 - 65,350 had consistent strike points on tile 5, resulting in a strong peak in collector deposition.

Though there is a line of sight from tile 5 strike points to the collector/QMB, a

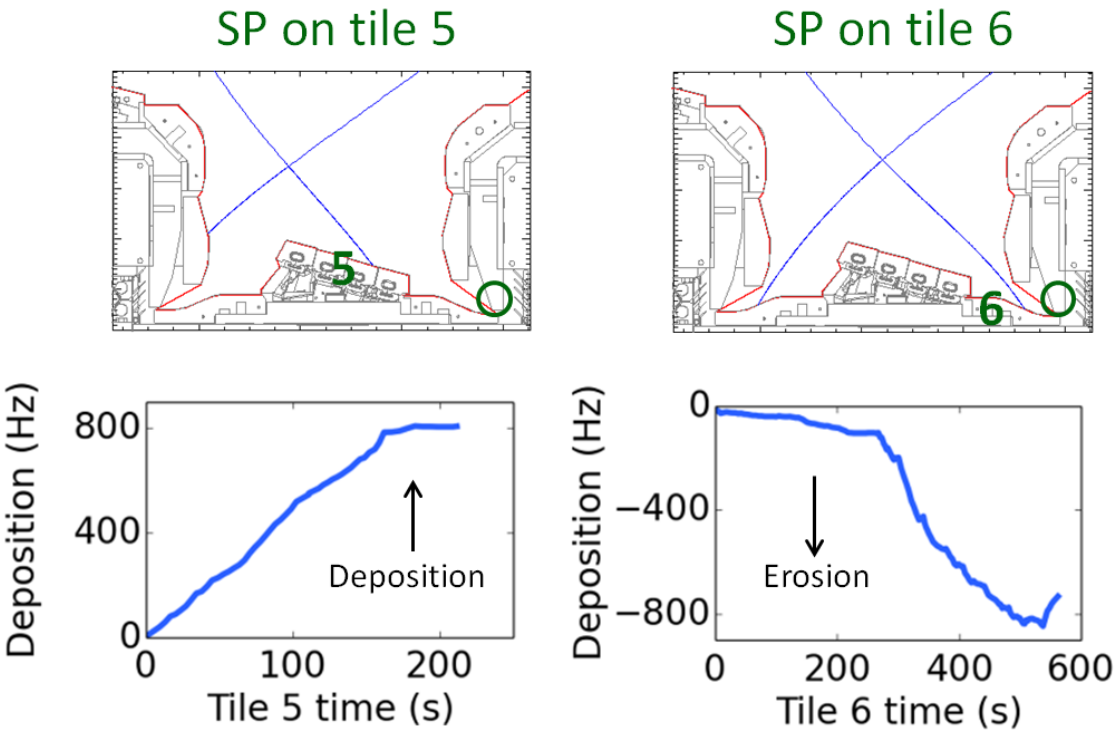

Figure 6.11: The upper diagrams show the position of the separatrix for a tile 5 strike point (left) and a tile 6 strike point (right), with the QMB location circled in green. The lower plots show the QMB frequency evolution for JET-C operation for these two configurations. The database has been split in order to consider the tile 5 and tile 6 strike points separately.

significant contribution to deposition from the tail of the strike point, closer to the outer corner, is also likely for these configurations. The attenuation factor of 0.26 neglects tile 6 strike points, since all deposition due to tile 6 strike points is neglected in this case, and is thus not directly comparable to the other values. In terms of matching magnitudes, including all strike points would require reducing this factor to 0.03, suggesting significant losses of eroded neutral impurities for tile 6 strike points through ionisation/redeposition or re-erosion.

Figure 6.12 shows the equivalent QMB frequency evolutions for tile 5 and tile 6 strike points during the JET-ILW campaign. Contrasting with the JET-C case, here net deposition is observed for both tile 5 and tile 6 strike points. Again, this agrees with the way the modelling of the collector deposition was set up. For the ITER-like wall case, both tile 5 and tile 6 strike points contributed to deposition on the rotating collector (Section 6.3.2).

This QMB analysis aims to provide general trends of outer corner deposition for tile 5 and tile 6 strike points for impurities in the JET-C and JET-ILW divertors. This information was used to compare to and inform the modelling of the rotating collector deposition profiles. Depending on how much QMB data is available and to what degree plasma conditions varied, it can also be possible to relate changes in the gradients of the QMB frequency evolutions to changes in plasma parameters. This is apparent, for example, in the steepening of the re-erosion at t $\simeq$ 230 s in the plot of the JET-C QMB frequency for tile 6 strike points (Figure 6.11, bottom right). This

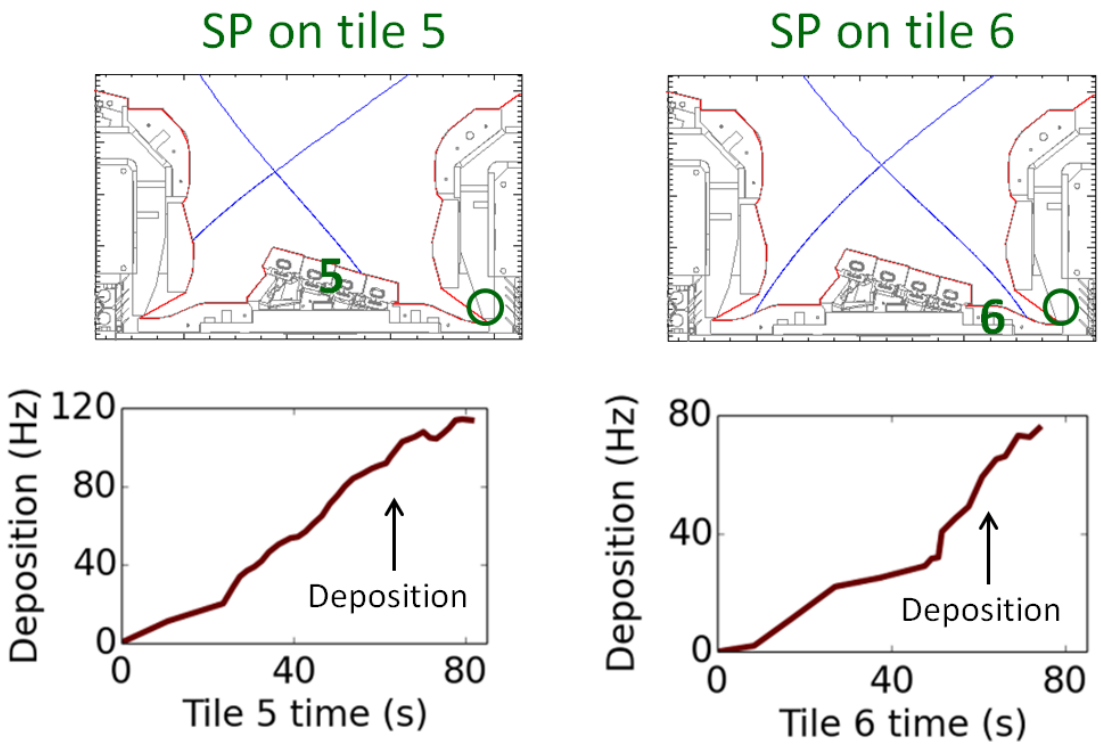

Figure 6.12: The upper diagrams show the position of the separatrix for a tile 5 strike point (left) and a tile 6 strike point (right), with the QMB location circled in green. The lower plots show the QMB frequency evolution for JET-ILW operation for these two configurations.

coincides with the point in the campaign when neutral beam injection began to be used, resulting in higher powers to the outer divertor corner.

The rotating collector results/modelling and the QMB results appear to show good agreement in their dependencies on strike point locations and wall materials. However, this does not itself provide the physical reasons for the differences in erosion and deposition for tile 6 strike points in JET-C and JET-ILW, or for the different magnitudes of deposition between the inner and outer divertors. The next section will discuss possible explanations for these differences in erosion and deposition behaviour observed for the JET-C carbon and JET-ILW beryllium cases.

6.6 Discussion of erosion and deposition mechanism

The erosion and deposition at a particular tokamak surface is determined by a combination of the global flows to that area and the local surface conditions/interactions. Investigation of any possible differences in global flows between JET-C and JET-ILW operation is left to more complex modelling efforts. It is hoped that the experimental deposition results presented may be useful for comparison to or benchmarking of future work in this area. Here, an explanation for the observed erosion and deposition behaviour is offered based on the local plasma and surface conditions.

	Tile 5 strike point	Tile 6 strike point
JET-C	✓	✗
JET-ILW	✓	✓

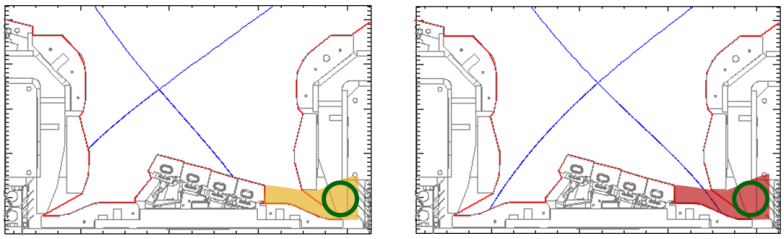

Figure 6.13: The table summarises the results of the previous sections, showing for which situations deposition is observed in the outer divertor corner (represented by ticks). The diagrams below represent the higher outer corner temperatures seen for tile 6 strike points relative to tile 5 strike points. The green circles indicate the locations of the outer divertor rotating collector and QMB.

The table in Figure 6.13 represents the general dependences observed for outer corner deposition on strike point locations and operating campaigns/wall materials. When the strike point is on tile 6 in JET-C, the modelling suggests that generally deposition does not occur on the rotating collector and the QMB shows net erosion. For these tile 6 strike points the outer corner surfaces relatively hot (as observed from local thermocouples), due to the greater power fluxes to this area. These tile 6 strike points and high resulting temperatures are represented in the bottom right diagram in the figure.

These high surface temperatures limit deposition on the diagnostics and promote chemical re-erosion of carbon deposits that do form [70]. There is a substrate temperature maximum for chemical erosion beyond which the erosion yield begins to fall again due to deuterium release overcoming hydrocarbon formation. This temperature maxiumum varies depending on the incident flux is, but has been found by experiment and modelling to exceed 600 K for most conditions [32]. Though the plasma-exposed tile surfaces can reach and exceed these temperatures, the plasma-shadowed surfaces in the divertor corner region are lower (as can be seen from thermocouple data or a consideration of the incident heat fluxes). The closer the strike point is to the outer corner, the greater the heat flux is to the corner and the higher the surfaces temperatures become in this region. Since the temperatures are below the substrate temperature maximum, higher temperatures increase the chemical re-erosion from the surfaces. Moderate temperature increases of 100 K are sufficient to increase this re-erosion by a factor of 4 or more [32].

While the rotating collector is assumed to show on average no net erosion or deposition, the higher QMB surface temperature results in net re-erosion from its surface. It is likely that the steepening of the QMB re-erosion for the higher power discharges using neutral beam injection is due to increases in this thermally-driven chemical re-erosion process. When the strike point is on tile 5 in JET-C, the rotating collector

results/modelling and the QMB results both indicate net deposition. This is enabled by the greater distance between the separatrix and the outer corner causing lower corner surface temperatures and thus a reduction in chemical re-erosion. These lower temperatures are represented in the bottom left diagram of Figure 6.13.

The question remains why this same strike point dependence is not observed for the JET-ILW campaign. Beryllium is not subject to the same thermally-driven chemical re-erosion processes that carbon is subject to [20], leaving it unaffected by the higher surface temperatures caused by the tile 6 strike points. This means that net deposition is observed for both tile 5 and tile 6 strike points (Figure 6.12). The contribution of both of these configurations results in the relatively high deposition rate observed on the outer divertor JET-ILW collector (Figure 6.10). In fact, the deposition rate is higher on the outer collector than the inner, giving the reversal in deposition asymmetry observed in the JET-ILW divertor.

Thus, the different distributions of deposits between the JET-C and JET-ILW divertors is here attributed to the different chemical properties of carbon and beryllium and their associated responses to elevated temperatures. This explanation provides a possible explanation for both the collector results/modelling and the QMB results. The next section will discuss deposition results from the JET-ILW divertor that come from other sources. This acts as a further check on the validity and generality of the reversal in deposition asymmetry that has been observed here.

6.7 Comparisons with other deposition results

The rotating collectors are not the only diagnostic that show a higher deposition rate in the outer divertor than the inner divertor for JET-ILW. This section will briefly discuss some other diagnostics located in the divertor corners and their deposition results.

In the remote JET divertor corners, a set of baffle plates known as louvres protect the magnetic field coils from the plasma. Clips are installed on these louvres, which can be removed easily during shutdowns so that they may be analysed ex situ using ion beam analysis techniques. Deposition results for the louvre clips that were installed in the vessel during the 2011-12 ITER-like wall campaign are reported in [42]. The outer louvre clip was found to have beryllium deposits of 4.4×10^{18} at/cm^2, a factor of 1.6 higher than the 2.8×10^{18} at/cm^2 concentration found on the inner louvre clip.

Results from the First Mirror Test in JET-ILW may also be used to assess the deposition asymmetry. Each mirror cassette held a series of mirrors recessed by between 0 - 4.5 cm within channels. The outer divertor mirrors recorded beryllium deposition of 1.35 - 4.96×10^{18} at/cm^2; mirrors from the inner divertor were found to have beryllium deposition of 0.17 - 4.50×10^{18} at/cm^2 [75]. The upper ranges of these concentrations come from the mirrors that were not recessed within channels at all. Though there appears to be differences in the degree of asymmetry depending on the depth at which the mirrors were located, the mirrors again demonstrate higher deposition in the outer divertor corner than the inner.

A summary of post-mortem analyses of tiles removed from the JET-ILW divertor

was presented in [143]. The inner base tile 4 and outer base tile 6 are the tiles located closest to the respective divertor corners. The spatially averaged deposition on tile 6 was $\sim 3 \times 10^{18}$ at/cm^2, while that on tile 4 was a factor of 3 less at $\sim 1 \times 10^{18}$ at/cm^2. In addition, the same study notes a reduction in material transport to the remote divertor corners by a factor of 4 in the outer divertor and a factor of 20 in the inner divertor. This agrees very well with the decreases in deposition seen on the inner and outer collectors (Figure 6.10).

Finally, it would be instructive to determine if the deposition asymmetry was also shown by rotating collectors from later ITER-like wall campaigns. The collectors from the 2013-14 campaign have been retrieved from the vessel, but not yet fully analysed. Although it is thus impossible to make any definite statements regarding the depositions at this stage, it is noted that a visual inspection of the discs again indicates heavier deposition on the outer divertor collector than the inner.

In addition to the rotating collectors, various other studies have shown higher beryllium deposition in the outer divertor corner than the inner. The confirmation of this through independent analyses adds confidence to the reversal of deposition asymmetry demonstrated by the collectors.

6.8 Conclusions

This chapter has extended the analysis of rotating collectors described in the previous chapter to those located in the inner and outer divertor corners. The time-dependent deposition profiles on these corner collectors from the JET-C and JET-ILW divertors have been presented. Modelling of the deposition profiles of the dominant deposits has, in general, shown good qualitative agreement with the experimental results. In the JET-C outer divertor, deposition due to tile 6 strike points had to be neglected in order to achieve a reasonable fit to the experimental results. The average deposition rates on the 4 rotating collectors show an overall order of magnitude reduction in deposition rate for JET-ILW relative to JET-C. While long experience with JET-C has shown more deposition in the inner divertor corner than the outer, in JET-ILW more deposition was observed on the outer collector than the inner. The distributions of impurity deposits are important to know so as to understand where the majority of tritium/deuterium is likely to be retained in ITER. Though the fuel retention of beryllium deposits is reduced relative to carbon, a strong correlation is still observed in JET between the locations of high impurity deposition and high deuterium retention [61].

Analysis of outer divertor QMBs indicated that for tile 5 strike points there was net deposition in the outer corner, but that tile 6 strike points caused net erosion; both tile 5 and tile 6 strike points caused net deposition in JET-ILW. Thus, a lack of net deposition in the JET-C outer corner is apparent for tile 6 strike points, as inferred from modelling of the collector deposition and observed from QMB results. This has been explained via the high surface temperatures in the outer corner for tile 6 strike points limiting carbon deposition and promoting thermally-driven chemical re-erosion. The different chemical properties of beryllium mean that it is not susceptible to this re-erosion process, resulting in net deposition in the outer divertor for both tile 5 and tile 6 strike points. This has caused a reversal in the deposition asymmetry

between the inner and outer divertors relative to the JET-C case. Finally, this differing distribution of deposits was further confirmed by comparison to those seen on other divertor corner diagnostics. The following chapter will analyse erosion, deposition and material transport in the JET-ILW outer divertor in more detail and over shorter timescales.

Chapter 7

Monte Carlo modelling of beryllium migration in the JET-ILW divertor

7.1 Introduction

This chapter presents and discusses results gained from Monte Carlo modelling of erosion and deposition in the JET-ILW outer divertor. A full description of the model is provided in Section 4.2 and its key features are briefly revisited here. The model encompasses the erosion, ionisation and redeposition or reflection of beryllium impurities. This is performed in four main steps: 1) sputtering of impurities from divertor tiles; 2) propagation of neutrals; 3) ionisation of impurities; and 4) propagation of ions. The aim of this work is to provide a more detailed, higher time resolution analysis of the beryllium migration in order to complement the longer timescale work focusing on the rotating collectors. This enables an analysis of the effects of changes in plasma and surface conditions on erosion, deposition and migration of beryllium to be performed.

Section 7.2 will provide motivation for these modelling efforts and Section 7.3 extends this through comparison of theoretical sputtering yields with those inferred from spectroscopy. Section 7.4 will explain the general features of the results seen and how they evolve with time. In Section 7.5, the effects of changes in different input parameters on the time-varying distributions of impurities will be analysed. Conclusions from this chapter will be drawn in Section 7.6.

7.2 Motivation

The replacement of the carbon wall of JET-C with the beryllium and tungsten wall of JET-ILW caused a large reduction in the impurity content of the plasma [134]. While in JET-C amorphous hydrocarbon layers formed on divertor surfaces, in JET-ILW long-term growth of beryllium layers on divertor tiles was not observed in most

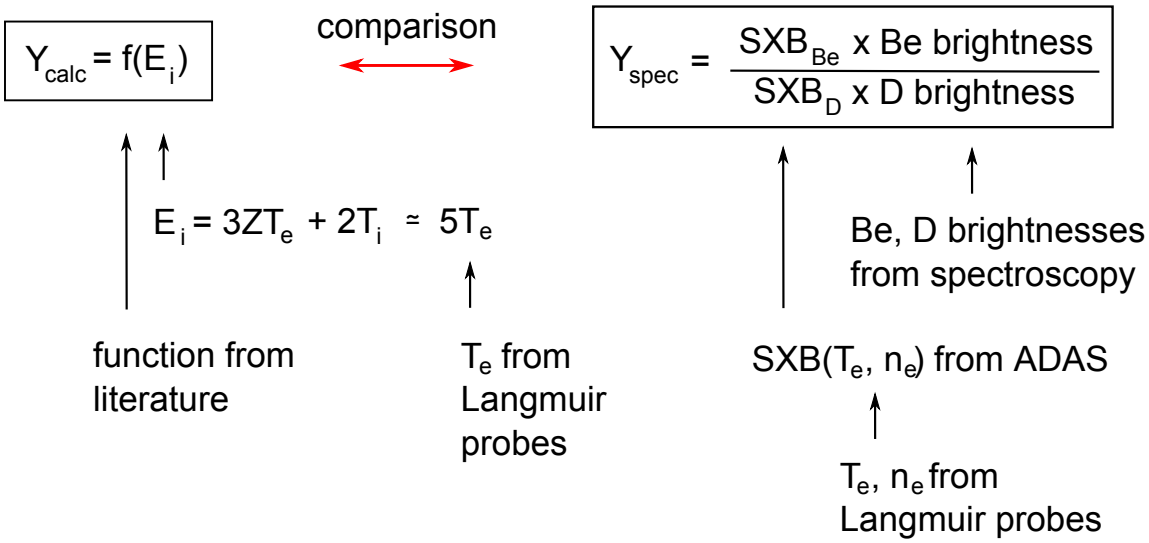

Figure 7.1: Diagram explaining how different sources of data are combined to find and compare calculated and spectroscopic yields for sputtering of beryllium.

locations [37]. The degree of beryllium coverage on different areas of the tungsten tiles may be expected to vary dynamically over the course of campaigns due to changes in the experimental conditions. The amount of beryllium on a given surface clearly has a large effect on the amount of beryllium erosion that can occur from that surface. Indeed, this has already been seen implicitly from the modelling of the JET-ILW collector depositions. Observation of beryllium via divertor spectroscopy was used to modify the impurity sources from the tiles, taking account of the time-varying availability of beryllium.

The importance of the availibility of beryllium impurities on the JET-ILW divertor tiles has been suggested in [119]. In particular, the prevalence of limiter discharges early in the first JET-ILW campaign were inferred to lead to relatively high beryllium transport to the divertor tiles. This resulted in the observation of initially high beryllium brightnesses in the divertor, which subsequently decayed. Further investigation of this using WallDyn again demonstrated the importance of these limiter discharges [144]. It also indicated that the limiter phases of later discharges 'refreshed' beryllium coverages on the divertor tiles, which were removed by sputtering during the following divertor phases. These results show the dynamic nature of the beryllium coverage on divertor tiles. The importance of this surface coverage for sputtering from the tiles will be discussed in the following section.

7.3 Comparison of yields

First attempts at investigating the beryllium surface coverage within the current study involved comparison of sputtering yields calculated using analytical yield equations [28] and those inferred from divertor spectroscopy. The calculated sputtering yields give the yields expected if the divertor surfaces were bulk beryllium, while the spectroscopic yields implicitly include the effects of incomplete surface coverage of

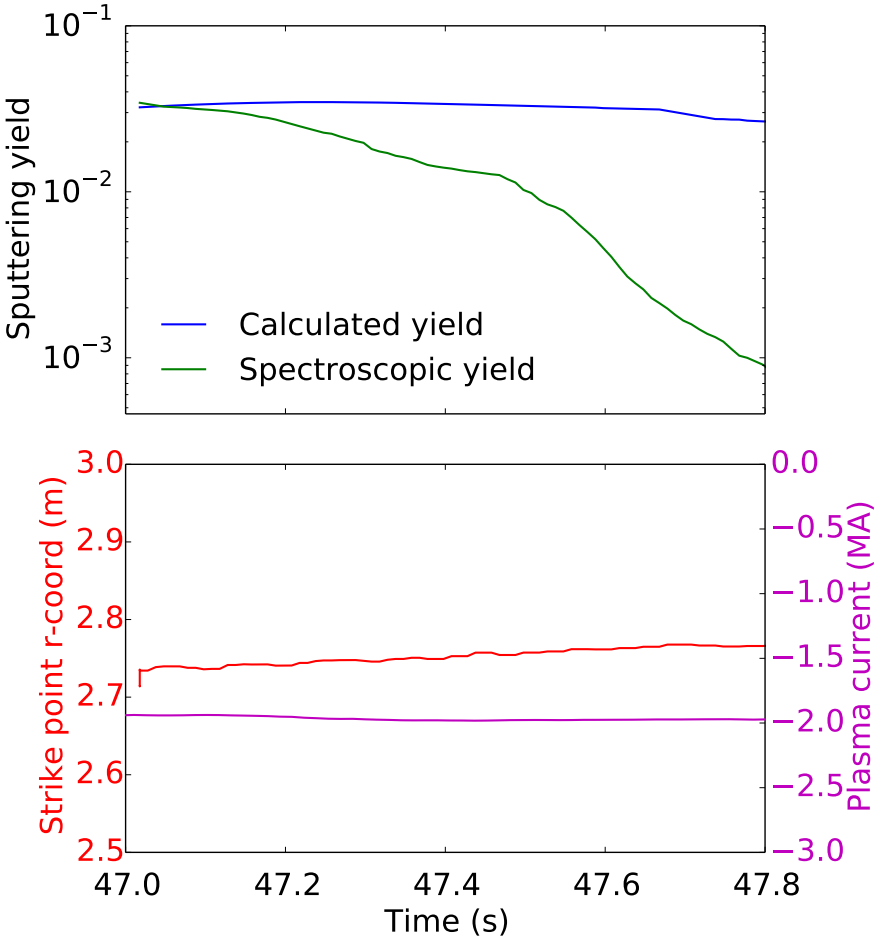

Figure 7.2: The top plot shows an example comparison of calculated and spectroscopic beryllium sputtering yields in the JET-ILW outer divertor for discharge 81768. The spectroscopic yield quickly falls below the level of the calculated yield after the start of the divertor phase (at ∼47 s), which may suggest a decrease in the surface coverage of beryllium on the tiles. The bottom plot shows the location of the relatively stationary outer strike point on tile 5 and the stable plasma current.

beryllium through the experimental observations. Hence, a comparison of the two provides an indication of the importance of this surface coverage.

The steps involved in finding the calculated and spectroscopic yields are shown diagrammatically in Figure 7.1. Calculated yields are based on plasma temperatures as found from langmuir probes. These are used to find incident energies of the deuterium ions and hence calculate the sputtering yields. The determination of the spectroscopic yield utilises deuterium and beryllium divertor spectroscopy measurements. The measurements are of beryllium and deutrerium brightnesses, in units of photons/cm^2/s/sr. The relation of these brightnesses to the real concentrations of different species ejected into the plasma from the tile surfaces is determined using inverse photon efficiencies (SXBs), which are functions of plasma temperature and density. Hence, the temperature and density data from Langmuir probes and SXB data from ADAS [92] are used to determine the spectroscopic yields, which can then be compared with the calculated yields.

Table 7.1: Reference input conditions for the Monte Carlo code.

Parameter	Value
Initial Be surface coverage	0.1 monolayers
Be/D incident flux fraction	0.2%
Strike point x-coordinate	145 mm
Peak T_e	25 eV
Peak n_e	1×10^{19} m^{-3}
Peak ion flux	1×10^{22} m^{-2}s^{-1}

An example of the application of this analysis is shown in Figure 7.2. Early in the divertor phase, the spectroscopic and calculated yields are of similar magnitudes, which may suggest relatively high beryllium coverage. Thereafter, the spectroscopic yield decreases while the calculated yield remains relatively constant. This may suggest 'burn-off' of beryllium from the divertor surfaces during the initial divertor phase, leaving little beryllium available for sputtering later in the discharge.

This initial work motivated a more in-depth investigation of beryllium erosion, deposition and transport in the JET-ILW divertor. The sputtering, ionisation and redeposition/reflection of individual beryllium impurities is studied using a Monte Carlo approach, allowing the dominant processes and outcomes to be elucidated. This work focuses on the JET-ILW outer divertor in order to maximise diagnostic coverage for both inputs to the modelling and comparison of modelled results to experimental results. The following section will present some characteristic modelling results and explain the key features.

7.4 Typical features of results

The model utilised here enables investigation of a range of different plasma conditions. As an introduction to the main features of the results, a reference case is provided and explained here. The reference case has characteristic input conditions as detailed in Table 7.1 (for a more detailed description of the inputs to the code, see Section 4.2).

At each time step, at each spatial point along the tile surfaces, the sputtering, self-sputtering, deposition, re-deposition and reflection are calculated within the modelled area as defined in Figure 7.3. This, coupled with the passage of ions and neutrals through the plasma and the ionisations of some subset of these neutrals, results in significant changes to the surface coverage over many time steps. Some characteristic features of these surface changes are shown in Figure 7.4.

Initially, the surface coverage is constant across the tile surfaces. The erosion of surface beryllium is strongest around the strike point where there is the highest ion

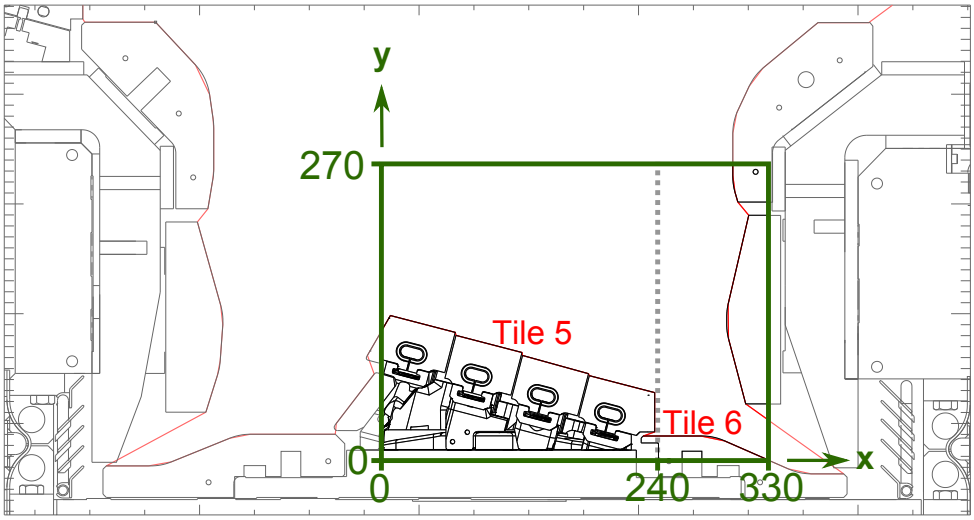

Figure 7.3: Diagram showing the JET-ILW divertor, with the area modelled in the outer divertor enclosed in the green rectangle. Numbers in green along the x- and y-axes give the coordinates in mm as defined in the model. Tiles 5 and 6 are identified in red, and vertical grey dashed line indicates the boundary between these tiles. This diagram acts as a reference for the results that will later be presented. Subsequent plots follow the coordinate system defined here, with the boundary between tiles 5 and 6 again indicated by a grey dashed line.

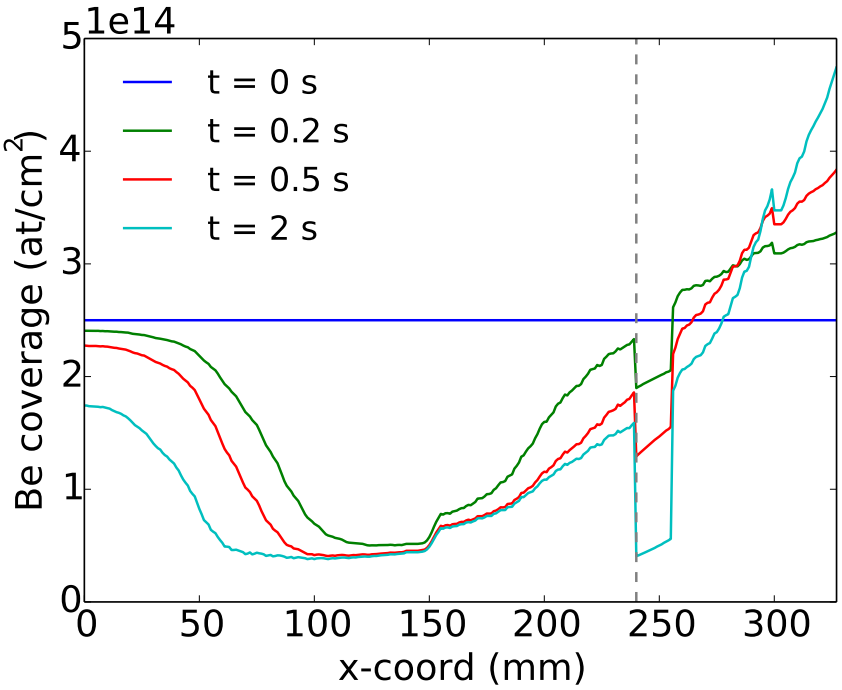

Figure 7.4: Plot to demonstrate typical features of the surface coverage evolution seen from modelling of the reference case, with each line representing a different time during the run. The x-coordinate follows the horizonatal coordinates of the surfaces of tile 5 and the upper part of tile 6. The vertical grey dashed line indicates the boundary between tiles 5 and 6.

flux and plasma temperature/ion energy. The eroded beryllium may get ionised and subsequently follow field lines to return to tile surfaces at larger x-values, leading to an increase in surface coverage on tile 6. As the beryllium source from tile 5 depletes, this redistribution to tile 6 is reduced, which can cause the tile 6 coverage to stabilise or decrease in certain cases. The occurrence of this erosion/deposition behaviour on tile 6 is dependent on the plasma and initial surface conditions. For example, a large fraction of beryllium in the incident flux may prevent tile 6 from becoming a net erosion region.

The continued addition of beryllium to the system from the contribution of the incident flux counteracts the loss of beryllium to regions outside of the modelled area, e.g. the outer corner. This can cause moderate migration of beryllium to the outer corner region, which is also seen in results from WallDyn [118]. The deposition rates in the outer corner will be examined further in Section 8.2.

Higher surface coverages on the tiles enable greater sputtering yields, which clearly act to reduce surface coverage. The degree of coverage that can be 'sustained' by the incoming beryllium and the outgoing sputtered beryllium flux varies spatially across the tile surfaces, due to the spatial variation of the various modelled parameters. Hence, an approximate equilibrium profile is often reached in the model where the surface coverage stabilises. This is generally evident after less than 2 s of modelled time (2 million time steps), setting the standard time that the model is run for.

The suppression of coverage at $x \simeq 250$ mm is due to this upper region of tile 6 being shielded from the plasma by the lower corner of tile 5 (see Figure 7.3). The width of this region depends on the proximity of the strike point to the tile boundary. The field lines are shallower closer to the strike point, which can shield a larger region of tile 6 from the plasma for strike points close to the boundary. The discontinuity in the profiles at $x = 300$ mm is the result of a physical discontinuity in the tile surface at this point. The tile changes from a horizontal topology to a downward tilted surface closer to the outer divertor corner.

The general features of the results described here are present to varying extents for different input conditions. The following section provides a detailed analysis of the modelled results that occur when a range of plasma and surface conditions are varied.

7.5 Parameter scans

In this section, modelling results produced through systematic variation of the input conditions will be presented. Generally one parameter is varied at a time, with the other parameters remaining equal to those applied in the reference case as described in the preceding section. The results shown take two main forms. The first shows the change in the beryllium surface coverage on the tiles during a single timestep. The 100^{th} time step is chosen as a balance between the initial surface coverage still being mostly preserved and the redeposition and redistribution processes being underway. The second form of results shows the evolution of the surface coverage with time for the different input conditions. In all cases, interpretation and explanation of the results seen are provided in terms of these input conditions and the physical processes involved.

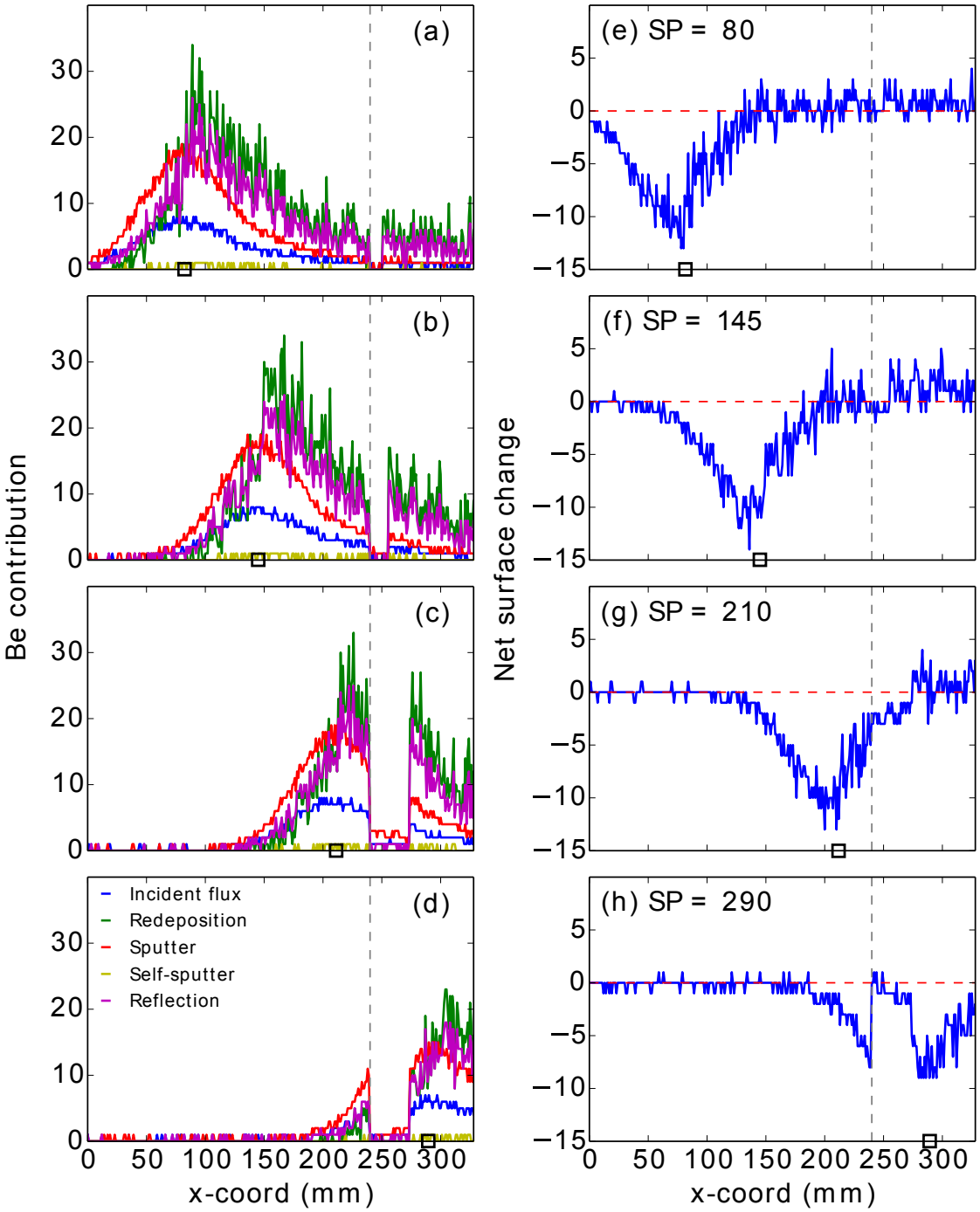

Figure 7.5: Plots showing the beryllium surface coverage changes over a single time step for different **strike points**. Plots a)-d) show the contributions of different processes to the surface changes. Plots e)-h) show the corresponding net surface changes due to the sum of the different contributions. Adjacent plots (e.g. a) and e)), show the same strike point case, with strike point locations labelled in units of mm with respect to the x-axes and marked with black squares on these axes. The units are in terms of numbers of modelled beryllium neutrals or ions. Vertical grey dashed lines indicate the boundary between tile 5 and tile 6; horizontal red dashed lines mark the level of zero surface change.

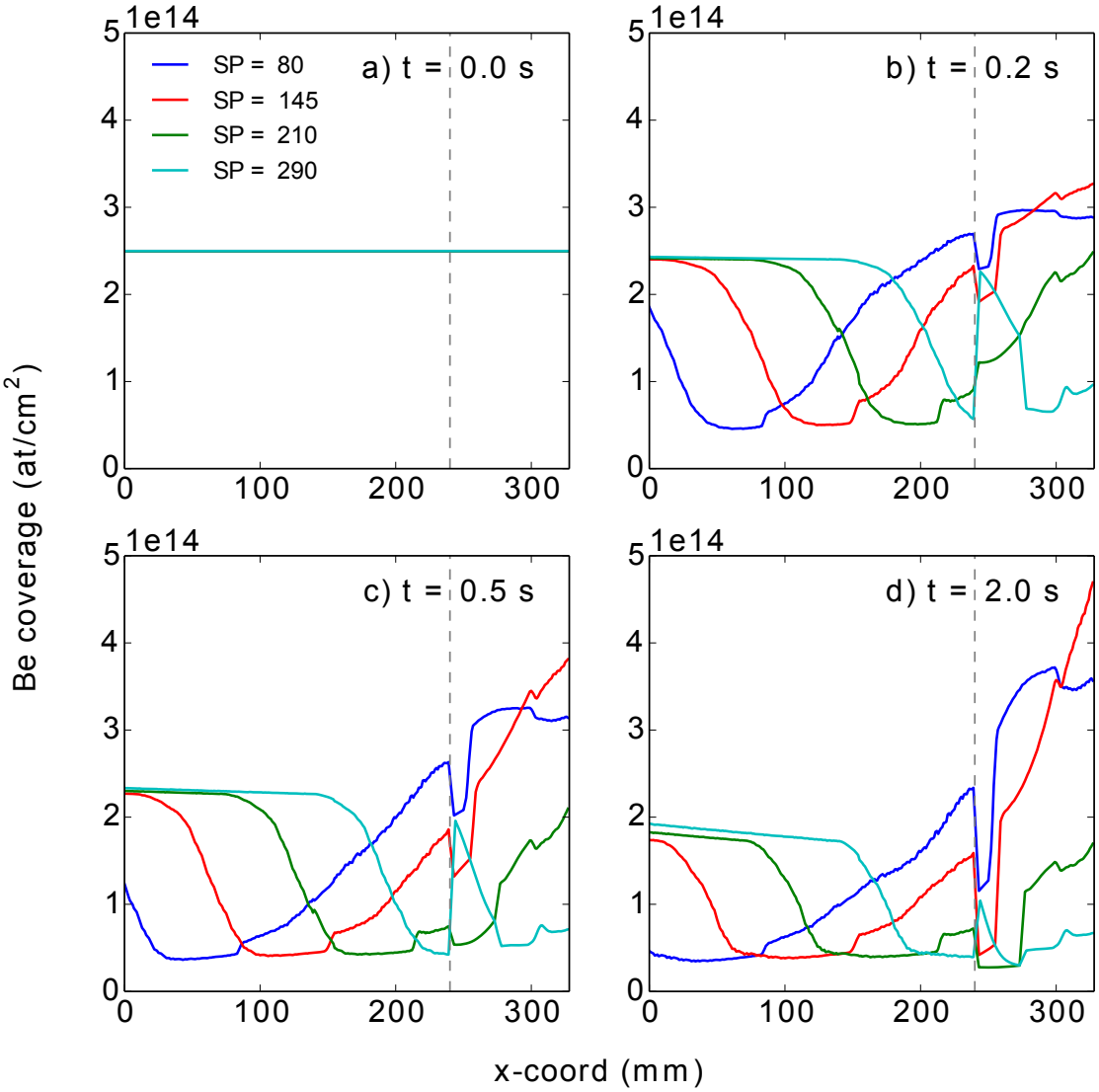

Figure 7.6: Plots showing the time-evolution of surface coverage for different **strike points**. Different lines within each plot indicate different strike point locations; different plots a)-d) show snapshots of the coverages at different times during runs. Vertical grey dashed lines indicate the boundary between tiles 5 and 6.

7.5.1 Strike points

Figure 7.5 shows the surface change over a single time step for four different strike point locations. The y-axis units are in terms of the number of modelled beryllium neutrals/ions, which are related to the 'real' numbers of beryllium neutrals/ions by the particle reduction factor (necessary for computational efficiency). The plots on the left show the contributions of different processes to surface change. Specifically, the 'incident flux' lines show the beryllium incident on the surface due to the fraction of beryllium in the incident deuterium flux. The 'redeposition' lines show the beryllium returning to the surface after previous sputtering/self-sputtering/reflection steps. These two processes clearly describe additions to the beryllium surface coverage. The 'sputtering' lines show the erosion of surface beryllium by incident deu-

terium and the 'self-sputtering' lines show the erosion of surface beryllium due to impacts of beryllium (whether from the fraction of the incident deuterium flux or from beryllium returning to the surface). The 'reflection' lines show the beryllium that gets reflected from the tile surface. These three processes clearly deplete the beryllium surface coverage and thus are in competition with the 'incident flux' and 'redeposition' contributions. The summation of all of these processes, as a function of the spatial x-coordinate, comprises the net surface change profile as shown in the plots on the right of Figure 7.5.

The sputtering (and incident beryllium flux) profiles peak at the strike points. The returning beryllium profiles peak at slightly larger x-values than those of the strike points due to the outward movement of the beryllium neutrals/ions between being sputtered and returning to the surface. Since the beryllium coverage is relatively low, a considerable fraction of the returning beryllium is reflected from the tungsten tiles, continuing towards the outer corner. For this surface coverage and the relatively low fraction of beryllium in the incident flux, the self-sputtering contribution is very low.

The variation of the profiles with strike point is as expected, with the locations of maximum erosion shifting in x with the strike point locations. Tile 6 can be seen to show a slight positive surface change, i.e. net beryllium deposition, when the strike point is on tile 5. For this consideration of a single time step, the plots show significant statistical effects in the lack of smoothness of the profiles. However, when the cumulative effects of hundreds of thousands or millions of time steps is considered, these statistical fluctuations are suppressed (Figure 7.6).

Each plot in Figure 7.6 shows the spatial surface coverage for the four different strike point runs at a different time. As expected from Figure 7.5, the locations of maximum erosion vary in x with the locations of the strike points, where the maximum ion fluxes and incident energies occur. A 'notch' in each surface coverage profile is observed at a slightly larger x-value than that of the strike point, e.g. at $x \simeq 90$ mm for the case with the strike point at $x \simeq 80$ mm. This reflects the separation in x between the peaks of the beryllium sputtered from the surface and the beryllium returning to the surface. For the strike points at $x = 80$ and 145 mm, growth of the coverage on tile 6 is observed, as expected from the consideration of a single timestep.

In general, the shifting of strike points acts to shift the location of the maximum erosion of surface beryllium from the tiles. The effects of varying the strike point on the magnitude of erosion are relatively minor. However, the tile 5 strike points enable redistribution of eroded beryllium to tile 6, which results in slight net deposition in this region. This is inhibited when strike points are at large x-values, when significant sputtering of tile 6 deposits occurs.

7.5.2 Flux fraction

Figure 7.7 shows the different contributions to surface coverage changes, and the net effects of these contributions, for a variety of beryllium percentages in the incident flux. When there is no beryllium in the incident flux (a), clearly there is no contribution to the beryllium surface coverage from this incident flux. The self-sputtering,

though low, is not zero since returning beryllium also self-sputters beryllium from the tile surfaces. However, this self-sputtering remains low even for a beryllium flux fraction of 0.5% (d) due to the low surface coverage of beryllium on the tiles. Conversely, the higher flux fraction plots clearly show increases in the contribution of the beryllium in the incident flux to surface coverage, as specified in the input conditions. The higher flux fractions also lead to larger amounts of beryllium returning to the surface and being reflected from the surface. This is simply a result of there being more beryllium in the system under these conditions.

The plots on the right of Figure 7.7 show the spatially resolved net surface changes due to these contributions. A decrease in the degree of erosion from the strike point region is observed for higher beryllium flux fractions. Physically, this is mainly due to the higher beryllium contributions from the incident flux adding more to surface coverage, which is only partially offset by higher self-sputtering and reflection. The increased availability of beryllium under these conditions also allows more redeposition of beryllium, causing a slight increase in large-x surface coverage for higher flux fractions. In fact, the total surface change, averaged spatially over the tiles, is slightly positive for the case of 0.5% beryllium in the incident flux (h). More beryllium is coming into the system than leaving, implying a net deposition of beryllium on the tiles for these conditions. It is noted that the JET-ILW divertor has shown very limited long-term deposits, with only the top of tile 1 showing significant net beryllium deposition [37]. This implies that a beryllium flux fraction as high as 0.5% is not physical. Indeed, this conclusion is also reached in [127] (and references thererin), with flux fractions of 0.1 - 0.2% appearing to be more appropriate.

Figure 7.8 shows snapshots of the beryllium surface coverage at different times, with the different flux fraction cases represented within each plot. As suggested by Figure 7.7, the cases with lower beryllium flux fractions lead to more strongly decreasing beryllium coverages on the tiles. For the case with no beryllium in the incident flux, the only source of beryllium is that on the tile initially, which is depleted as time progresses. Thus, after 2 s of run time (d), the coverage is fully depleted to $\sim$0 for most tile locations. However, with 0.2% incident flux, growth of surface coverage is seen on tile 6. For 0.5% surface coverage, there is large net deposition of beryllium on tile 6 and to some extent on the lower part of tile 5. The high incident beryllium flux is not matched by the sputtering and self-sputtering and hence the coverage increases.

Low or zero beryllium flux fractions allow rapid depletion of the beryllium initially on tile surfaces due to the lack of a significant incoming beryllium source. Higher flux fractions provide a greater incoming beryllium source, with the model results exhibiting decreased erosion from the strike point region and net deposition outside the strike point on tile 6.

7.5.3 Initial coverage

Figure 7.9 shows the contributions and changes to surface coverage over a single time step for varying initial surface coverage. The amount of beryllium initially on the tiles has a large effect due mainly to the dependence of sputtering, self-sputtering and reflection on the spatial coverage of beryllium. Sputtering and self-sputtering increase with increasing availability of beryllium on the tile; reflection of beryllium

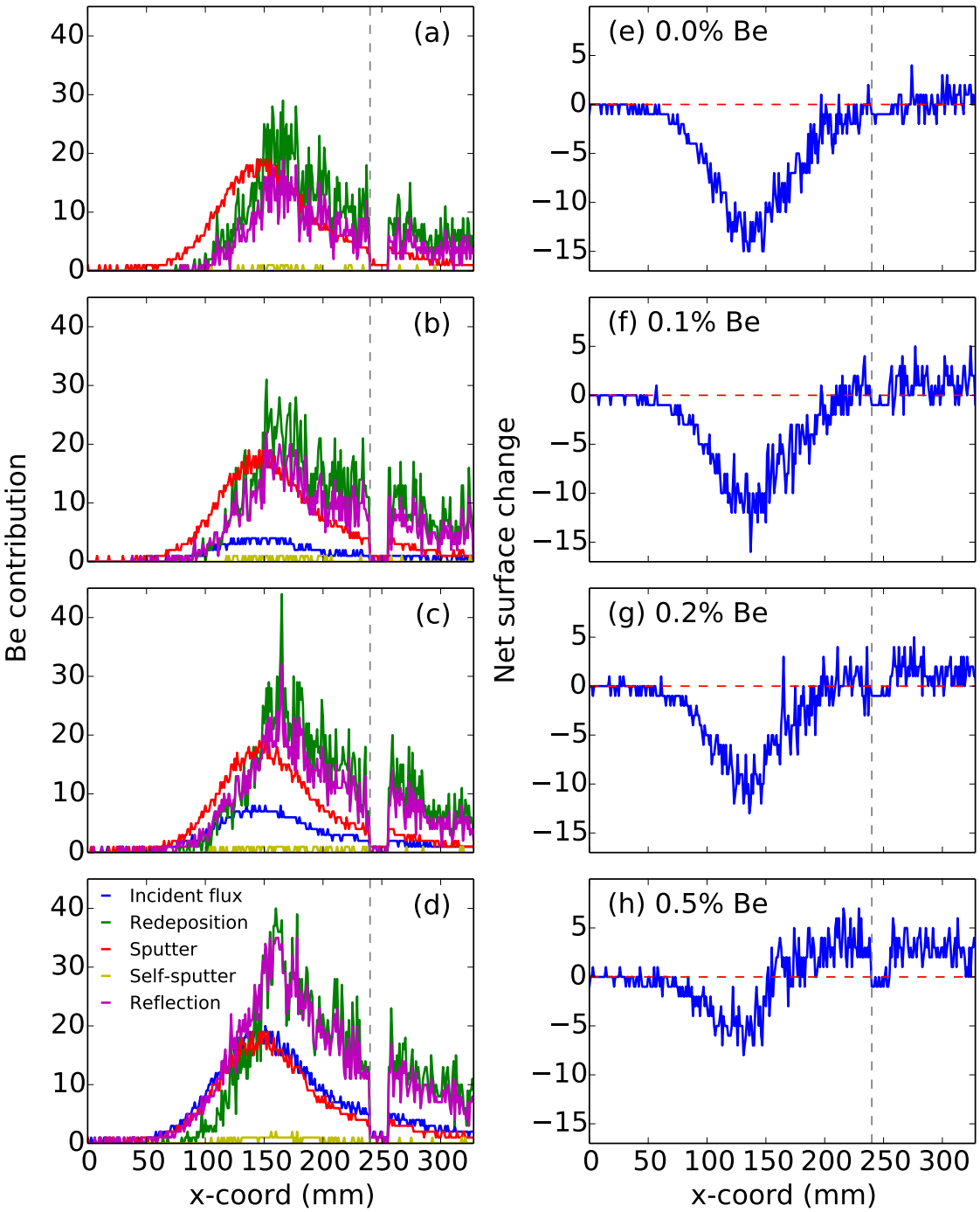

Figure 7.7: Plots showing the beryllium surface coverage changes over a single time step for different beryllium **flux fractions**. Plots a)-d) show the contributions of different processes to the surface changes and plots e)-h) show the corresponding net surface changes. Adjacent plots show the same flux fraction case.

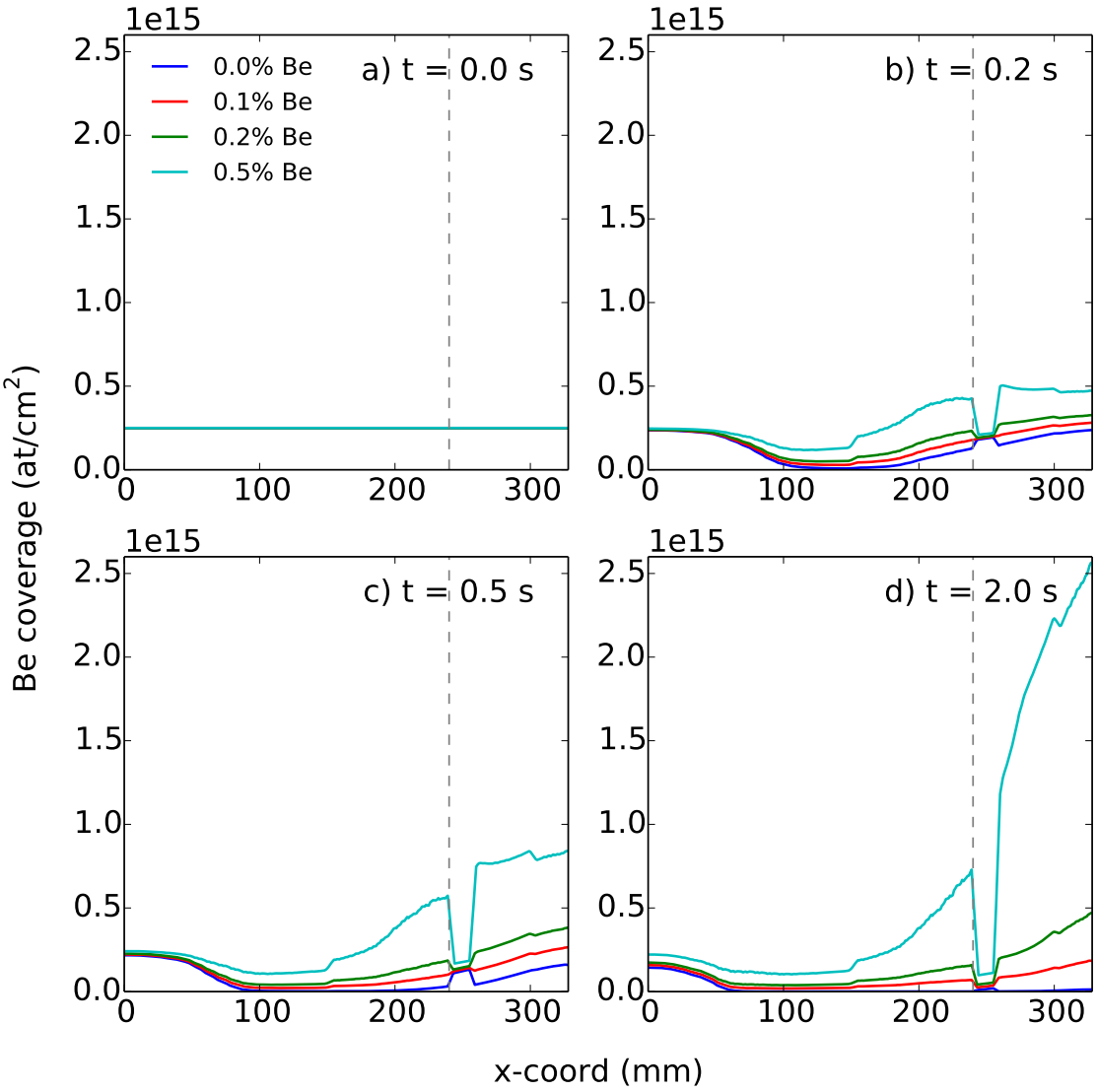

Figure 7.8: Plots showing the time-evolution of surface coverage for different **flux fractions**. Different lines within each plot indicate different flux fractions; different plots a)-d) show snapshots of the coverages at different times during runs.

is greater for lower surface coverages since it only efficiently occurs from tungsten surfaces.

For the case of zero initial beryllium coverage (a), there is almost no sputtering or self-sputtering (by the 100$^{\text{th}}$ timestep a low level of coverage may have formed, allowing some very limited erosion). The lack of a beryllium source from the tiles means that there is also relatively little beryllium to return to the surface and thereby little beryllium to be reflected. The beryllium coverage, which begins at zero, shows slight growth for this case (e). The source of beryllium from the incident flux has not yet resulted in a surface coverage that can support significant sputtering or self-sputtering of beryllium, resulting in net growth of surface coverage.

As expected, higher initial coverages enable increasing levels of sputtering and self-sputtering of beryllium due to the higher availability of beryllium on the tiles. The

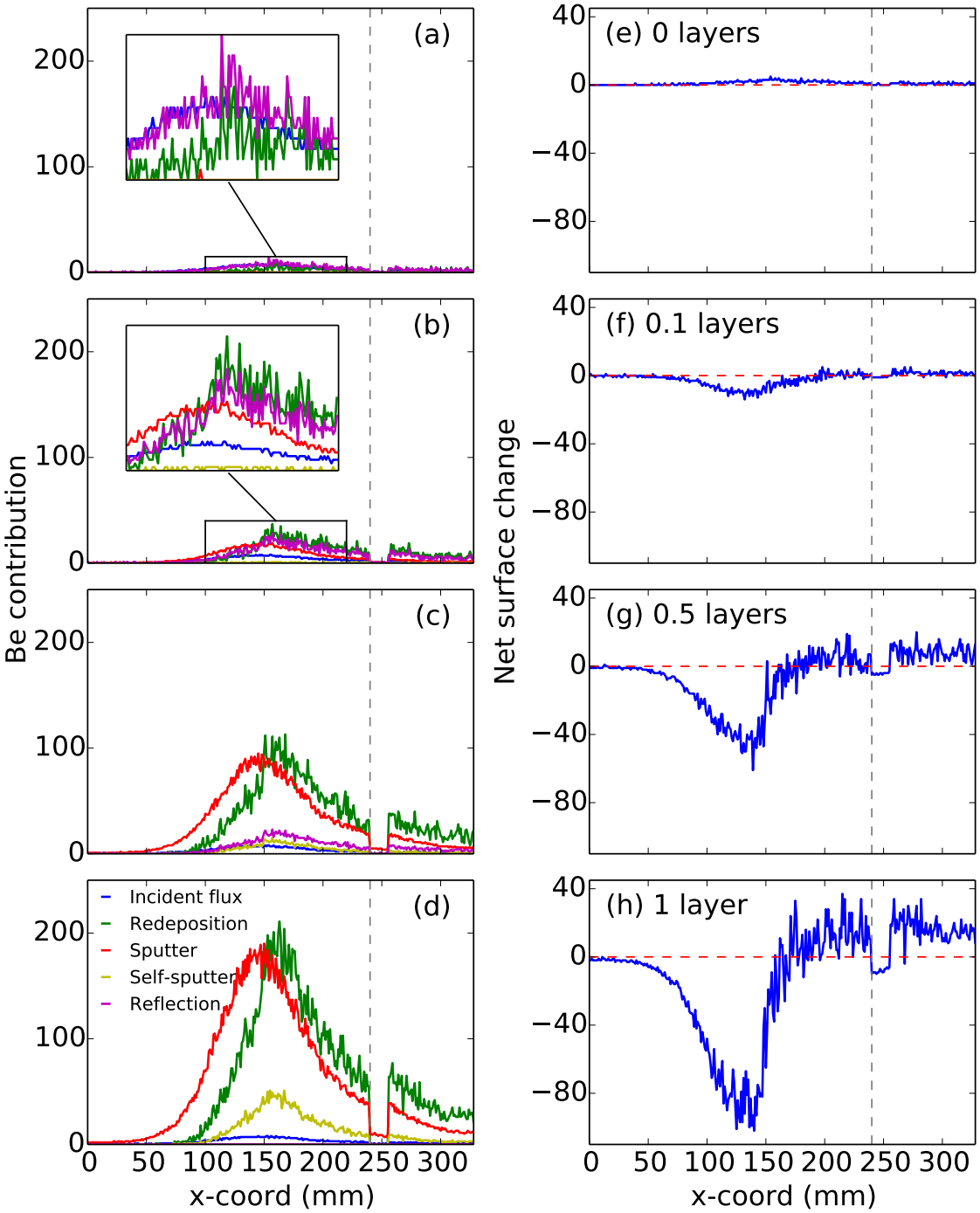

Figure 7.9: Plots showing the beryllium surface coverage changes over a single time step for different **initial coverages** (in units of monolayers). Plots a)-d) show the contributions of different processes to the surface changes and plots e)-h) show the corresponding net surface changes. Adjacent plots show the same initial coverage case.

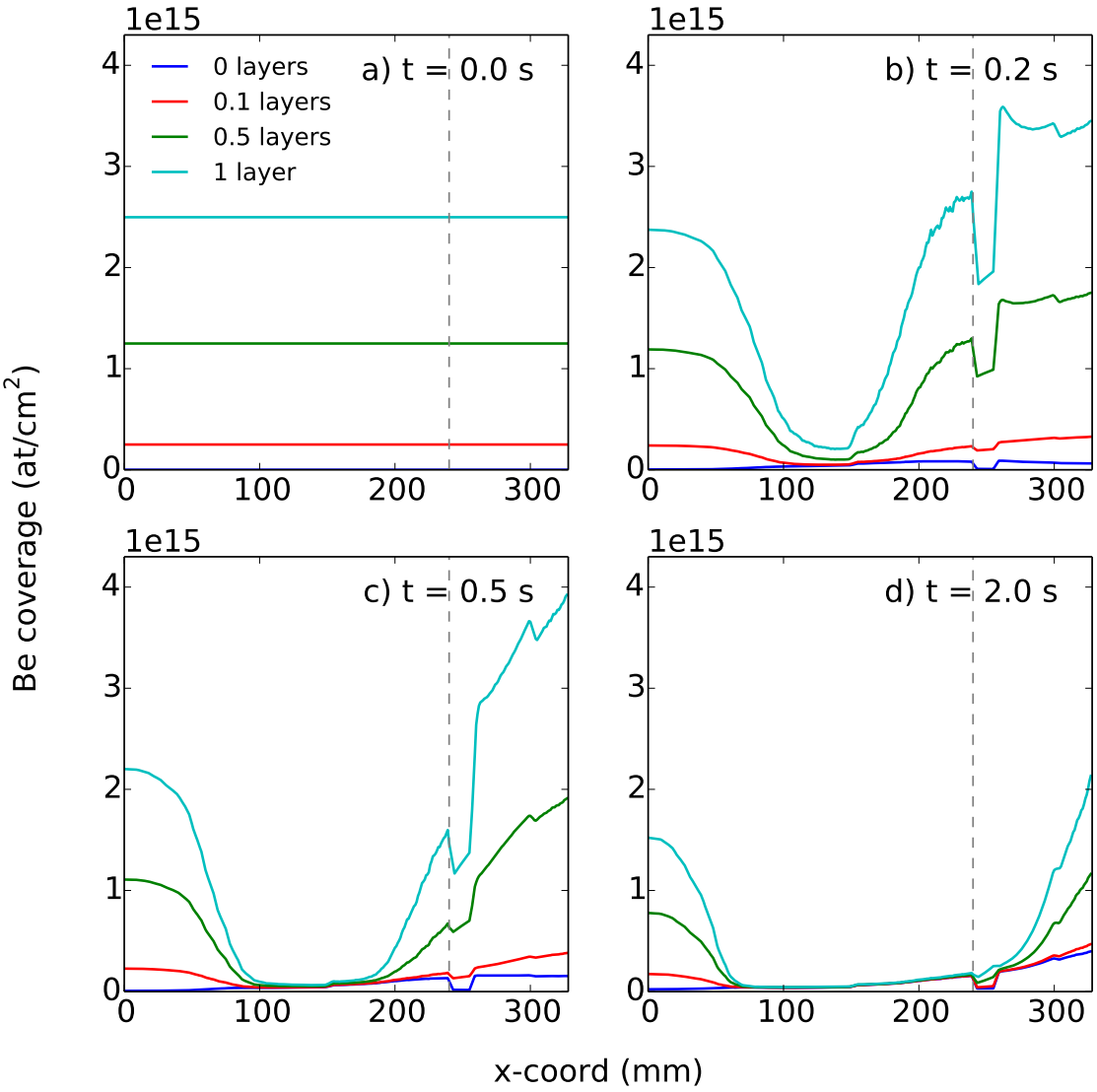

Figure 7.10: Plots showing the time-evolution of surface coverage for different **initial coverages**. Different lines within each plot indicate different initial coverages; different plots a)-d) show snapshots of the coverages at different times during runs.

reflection of beryllium has the opposite dependence, with higher coverages suppressing reflection. Thus, sputtering (and self-sputtering) are seen to be more and more dominant over reflection for the higher coverages. For 1 monolayer initial surface coverage, reflection is suppressed completely (d) due to efficient sticking of beryllium on beryllium substrates.

The higher coverages are observed to result in greater net erosion rates from the area around the strike point. These greater initial coverages enable a greater 'burn-off' of the beryllium through increased sputtering. Additionally, the redeposition at large x-values is observed to increase. This is again due to the efficient sticking of beryllium on beryllium, which promotes redeposition of returning beryllium over reflection. The larger initial source of beryllium also means that there is more beryllium available to be redeposited.

Figure 7.10 shows the evolution of the surface coverages with time. As defined in the inputs, at t = 0 s, the initial coverages are at different levels (a). After 0.2 s of run time, the higher coverage cases show strong erosion from the strike point region and redeposition at large x-values. However, the zero initial coverage case shows increasing beryllium coverage. As time progresses, the spatial coverage grows to a point where the sputtering and self-sputtering of beryllium can balance the incoming beryllium flux and an approximate equilibrium is reached.

For the higher coverage cases, between ∼1-2 s, tile 6 changes from a net deposition region to a net erosion region. Physically, this is because the strong erosion from the strike point has depleted the tile 5 beryllium source, resulting in reduced redeposition further towards the corner. The increased sputtering that the higher tile 6 coverage enables is greater than the incoming contributions of beryllium and the coverage begins to decrease. After ∼2 s, these cases also begin to reach an approximate equilibrium in beryllium coverage as the incoming and outgoing fluxes balance. Though there is a spatial variation in coverage across tiles 5 and 6, the equilibrium profile tends towards beryllium coverages of between 0 and 0.1 monolayers. This range agrees well with the equilibrium beryllium concentrations found using WallDyn [118].

Higher beryllium coverages on the tiles promote greater sputtering and self-sputtering, but suppress reflection of beryllium. For larger initial beryllium deposits, higher initial erosion rates are seen close to the strike point, which contributes to significant large-x redeposition. When the reservoir of tile 5 beryllium is depleted, tile 6 changes from a net deposition to a net erosion region.

7.5.4 Temperature and density

The plasma temperature affects the degree of sputtering (and self-sputtering), and both the plasma temperature and density affect the cross-sections for ionisation of neutrals. In contrast to the preceding sections, here it is less reasonable to vary one parameter and leave all others fixed. Higher plasma temperatures are generally associated with lower plasma densities. Therefore, a series of input conditions are examined here ranging from low temperature and high density plasma to high temperature and low density plasma.

Figure 7.11 shows the surface changes over a single time step due to different input temperatures and densities. For case (a), the sputtering is suppressed due to the low temperatures giving low incident energies and hence low sputtering yields. The high plasma density ensures that what beryllium does get eroded is likely to be redeposited. This combination of effects results in relatively low erosion from the strike point and net deposition closer to the outer corner.

For higher temperatures and lower densities, the sputtering gets progressively more significant and the redeposition at large x-values decreases. For case (d), the sputtering in particular is seen to dominate over the other contributions due to the high temperature increasing incident energies and the low density limiting redeposition. This prevents significant redeposition on tile 6 and the overall change in surface coverage (h) is everywhere negative or approximately zero, indicating strong net erosion.

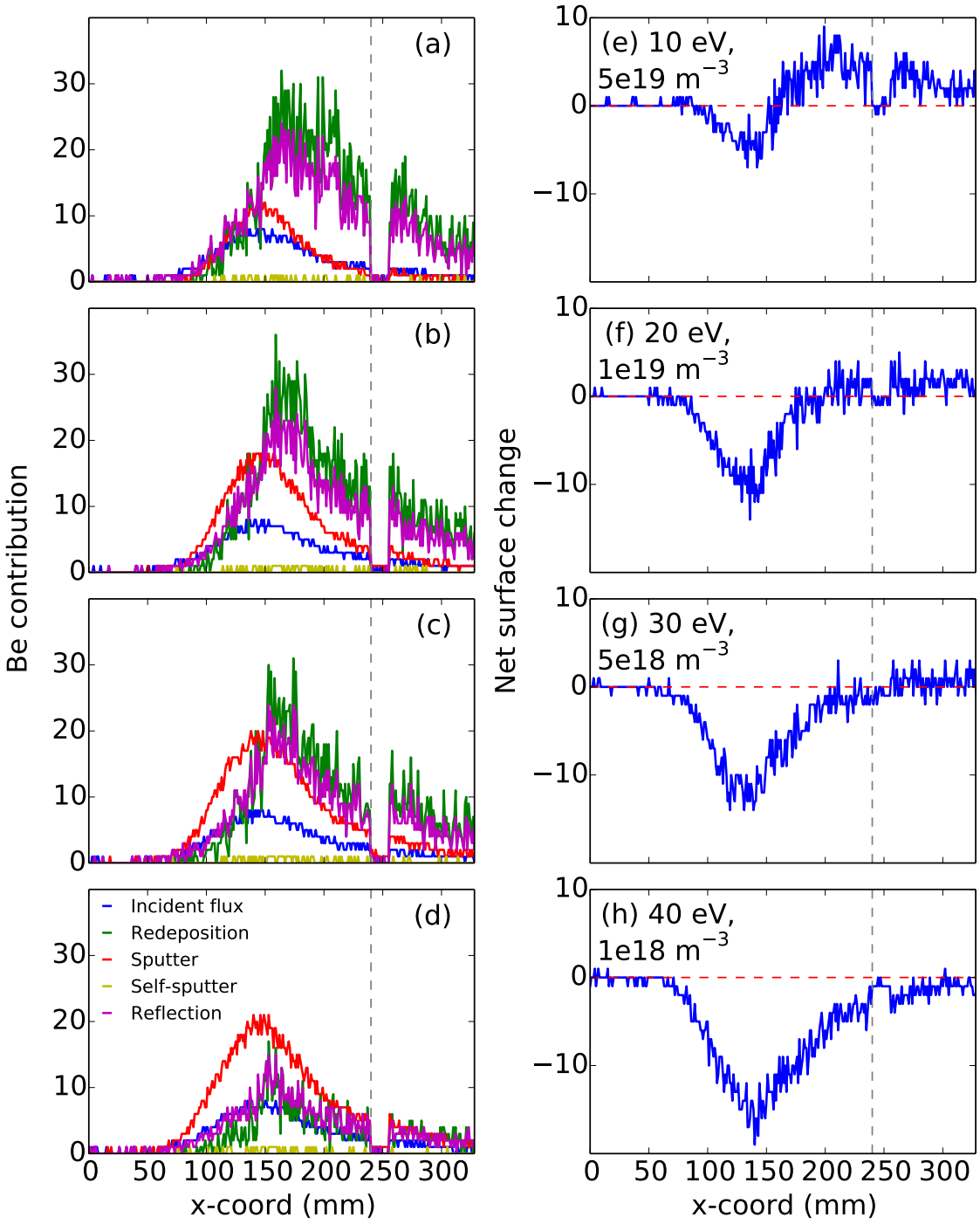

Figure 7.11: Plots showing the beryllium surface coverage changes over a single time step for different plasma **temperatures and densities** (the peak values of these parameters in each case are labelled on the plots). Plots a)-d) show the contributions of different processes to the surface changes and plots e)-h) show the corresponding net surface changes. Adjacent plots show the same temperature and density case.

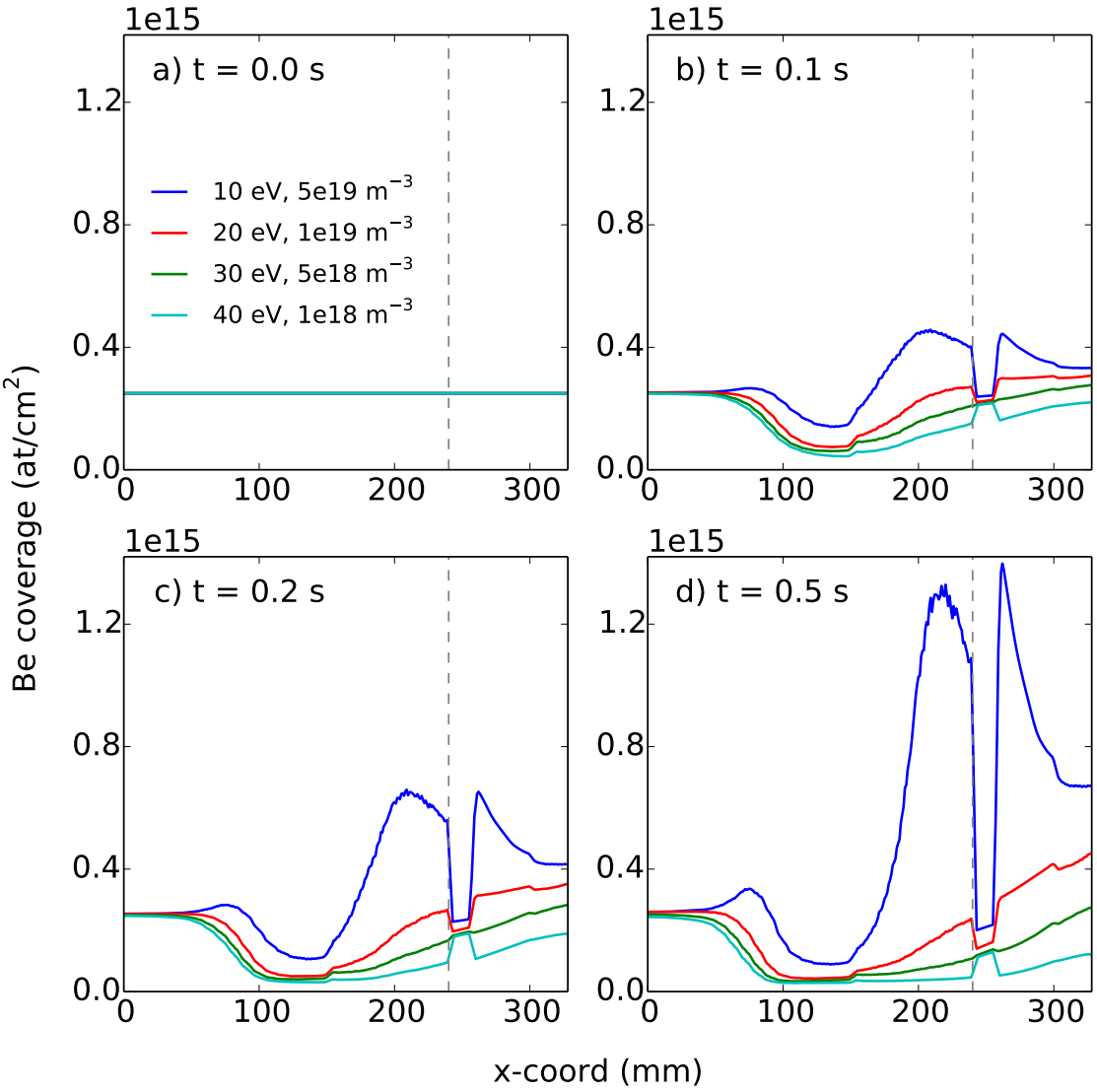

Figure 7.12: Plots showing the time-evolution of surface coverage for different plasma **temperatures and densities** (peak values are labelled on the plots). Different lines within each plot indicate different temperatures and densities; different plots a)-d) show snapshots of the coverages at different times during runs. (Due to the strong growth in coverage for the 10 eV case, the time-range has here been curtailed to 0 - 0.5 s in order to aid plotting; the growth of the 10 eV case continues, at a slowing rate, beyond this time.)

Figure 7.12 shows the time-evolution of the surface coverage for these different temperature and density cases. As expected from the considerations of a single time step, the low temperature and high density cases exhibit a slower rate of erosion from the strike point region and a greater propensity for redeposition of eroded beryllium. As well as this occurring at larger x-values than the strike point, for the highest density case this is also evident to some extent high up tile 5. The directions of the eroded beryllium neutrals are randomly selected over an offset cosine distribution, which allows some to travel inboard of the strike point (i.e. to lower x-values) and redeposit. For these conditions, this contribution overcomes the low sputtering yields high up

tile 5 (caused by the low plasma temperatures in this region). For the higher temperature and lower density cases, erosion from the surface dominates over ionisation and redeposition. This results in rapid depletion of the beryllium surface coverage on the tiles.

In general, the results of this section have shown low temperature and high density plasma to suppress sputtering of beryllium from tiles and promote redeposition. Conversely, high temperatures and low densities cause rapid beryllium erosion and limit ionisation of neutrals and subsequent redeposition on the tiles, depleting surface coverage.

7.6 Conclusions

This chapter has presented results from Monte Carlo modelling of erosion, deposition and material transport in the JET-ILW outer divertor. This incorporates processes such as sputtering, self-sputtering, reflection, ionisation and redeposition. The aim of this work is to investigate the beryllium erosion/deposition that occurs with a range of different experimental conditions. This dynamic distribution and redistribution of beryllium impurities on divertor tiles is difficult to study by other means and is important for the amount of deposition and retention in remote regions.

The modelling was motivated by consideration of calculated and spectroscopic beryllium sputtering yields from divertor surfaces. The limited availbility of beryllium impurities in JET-ILW means that the local beryllium surface coverage has a significant impact on the amounts of erosion, deposition and reflection seen. The effects of a range of parameters on the time-varying beryllium distribution have been analysed in order to gain an understanding of the dependencies on strike point locations, beryllium flux fractions, initial beryllium coverages and plasma temperatures and densities. Results from these parameter scans have been presented and justified in terms of the physical mechanisms involved. The following chapter will focus on applying the model to more specific plasma and surface conditions in order to enable relation to and investigation of experimental results.

Chapter 8

Applications of Monte Carlo modelling to experimental erosion and deposition results

8.1 Introduction

In this chapter, results from the Monte Carlo model described in Section 4.2 are compared to and used to interpret experimental erosion and deposition results. This work builds on that presented in the preceding chapter, in which the variation of modelling results with different input conditions was explored.

In Section 8.2, modelled results will be compared to experimental results from rotating collectors, QMBs and spectroscopy. Section 8.3 will focus on the peaks in beryllium brightness that are often observed when the plasma first moves into the divertor phase. Observations of these in the modelling and experimental results are compared and their causes and significance are discussed. A summary of the conclusions from this chapter will be provided in Section 8.4.

8.2 Comparisons to experiment

The previous chapter explored how the spatially and temporally resolved erosion and deposition at the divertor tiles vary with different input parameters. It is also instructive to compare deposition results seen experimentally to those found using the Monte Carlo model. This enables an improved understanding of the physical processes and dominant dependencies involved.

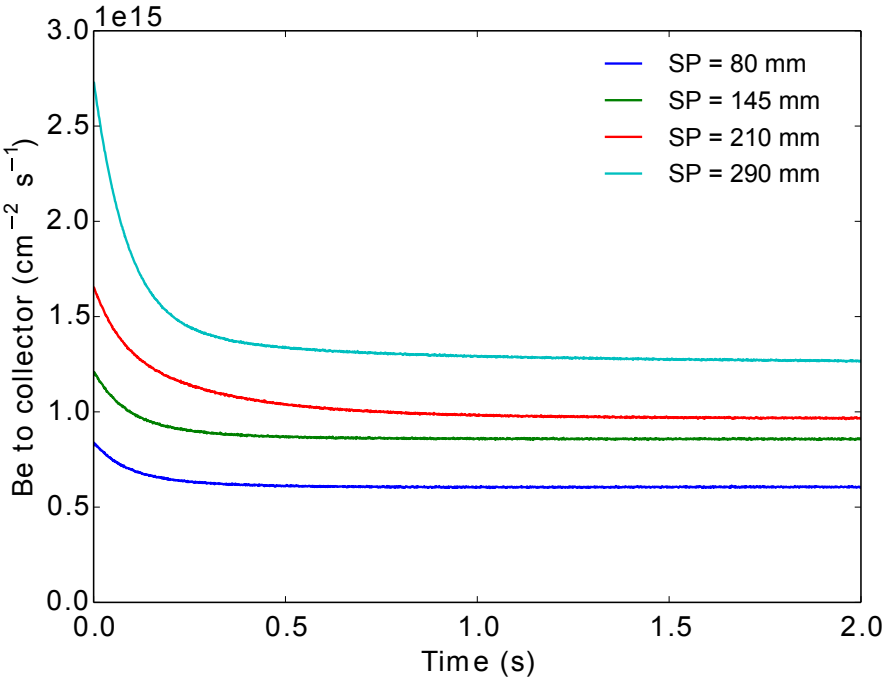

Figure 8.1: Plot showing the time-dependent modelled deposition rate on the outer corner rotating collector for different strike point locations.

8.2.1 Rotating collectors

The rotating collector located in the outer divertor corner of JET-ILW provides quantitative deposition results with a finite time dependence. In this section, the deposition magnitude, variation with changing plasma parameters and previous modelling efforts are discussed in light of modelling results from the Monte Carlo code.

8.2.1.1 Deposition rates

The campaign-averaged deposition rate on the rotating collector was 2.36 $\times$ 10^{14} $cm^{-2}s^{-1}$, with an error of as much as 20% mostly due to uncertainty in measurement cross-sections. In the Monte Carlo modelling, transport of beryllium to the outer divertor corner, and to the rotating collector located in this region, occurs after sputtering or reflection of beryllium neutrals from the divertor tiles. Based on the reference case (see Table 7.1), the average modelled deposition rate on the collector was 8.59 $\times$ 10^{14} $cm^{-2}s^{-1}$, a factor of $\sim$3 greater than that seen experimentally. Potentially, this overestimate of deposition could be due to some reflection or re-erosion of beryllium from the collector surface. However, the experimental conditions also vary considerably and these may be such as to on average reduce transport to the collector relative to the reference case.

When performing the parameter scans described in Section 7.5, the beryllium deposition at the rotating collector location was also calculated for the different conditions. Generally, an initial peak in modelled collector deposition is seen at the start of runs (examined in detail in Section 8.3). After this initial peak, in most cases the beryllium deposition decreases and settles at an equilibrium level as the beryllium

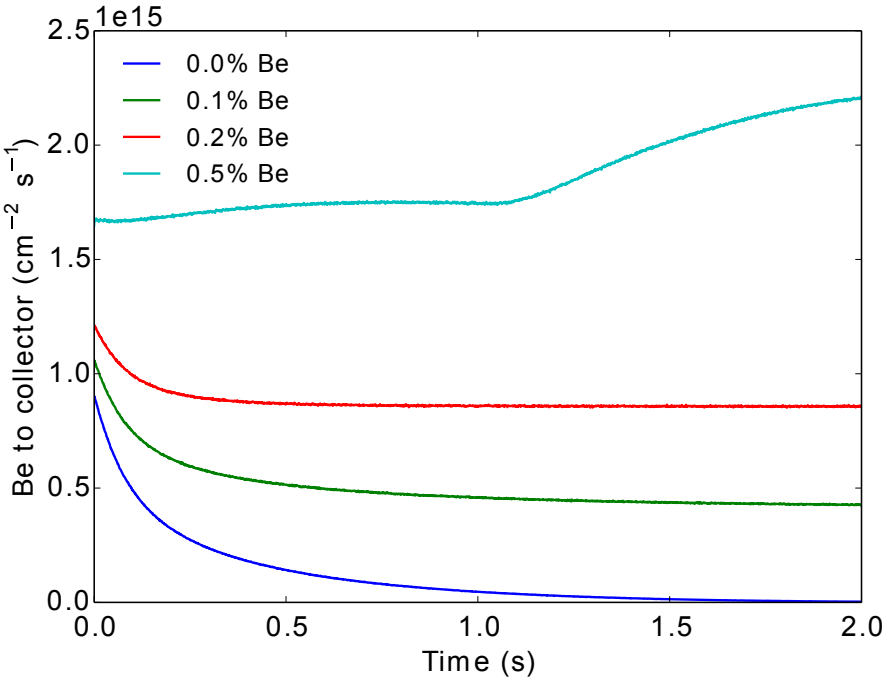

Figure 8.2: Plot showing the time-dependent modelled deposition rate on the outer corner rotating collector for different beryllium flux fractions.

coverage of the tiles equilibrates. Some results for the parameter-dependencies of the modelled collector deposition are shown here in order to aid understanding of the dependencies of the experimental deposition.

Figure 8.1 shows the modelled deposition on the outer corner collector for different outer strike point locations (these cases match those considered in Section 7.5.1). It is observed that strike points closer to the outer corner result in a larger deposition rate on the rotating collector. This is because these strike points have a larger range of acceptance angles that allow deposition on the collector relative to the strike points at lower x-values. More distant strike points at lower x-values may also sputter beryllium which is either redeposited and re-eroded or reflected from the tiles over multiple steps. However, if more of these steps are required to reach the outer corner, the probability of losses to other regions is higher and the deposition on the collector is reduced.

Figure 8.2 shows the modelled deposition on the collector for varying beryllium flux fractions (matching the cases shown in Section 7.5.2). For the 0.0 - 0.2% cases, the deposition rate decreases after an initial peak. For the 0.5% flux fraction case, the flux fraction is sufficient to support slight growth of beryllium coverage on tiles, resulting in increasing deposition on the collector. The change in gradient at ∼1.1 s corresponds to the time after which burn-off from tile 5 has stabilised. Over this timescale, the beryllium source from tile 5 is redistributed to tile 6. From ∼1.1 s onwards, the dominant process is then the re-erosion of tile 6 deposits with a high sputtering yield, resulting in a high beryllium source for deposition on the outer corner rotating collector.

In all cases, the total modelled collector deposition is found to be strongly affected by the flux fraction, showing an almost linear dependence. This is because, for 'large' time values, the beryllium source for sputtering/reflection is dominated by the

constant incoming source from the incident flux. This implies that further limitation of the impurity transport to remote regions may be achieved in JET, and in ITER, by further limiting the degree of erosion in the main chamber and hence the impurity influx to the divertor.

The modelled collector deposition is also found to increase with increasing initial coverage due to the higher beryllium source this provides. However, since this initial coverage is transient, the deposition rates fall to similar levels after ∼1-2 s. Thus, over whole discharges, the average deposition rate is not strongly affected. Low plasma temperatures and high plasma densities resulted in decreased modelled deposition on the rotating collector. This is due to the low temperatures causing low sputtering yields and the high densities encouraging redeposition of beryllium on tiles rather than transport to the corner region. At moderate temperatures and densities, higher deposition on the collector was found. However, decreasing the density (and increasing the temperature) further caused the modelled collector deposition to decrease again. This was due to a greater proportion of the eroded beryllium remaining unionised and leaving the modelled region rather than being redeposited or reflected and progressing towards the outer corner.

These parameter dependencies may be used to infer reasons for the overestimate of the experimental collector deposition by the Monte Carlo model. The comparison of magnitudes was done using the reference modelling case. Thus, on average experimental conditions may have had more distant strike points from the corner, lower flux fractions, lower initial coverages or differences in the temperatures and densities relative to this reference case. Of these parameters, the beryllium flux fraction appears to affect the modelled collector deposition particularly strongly. The 0.2% reference case flux fraction is at the upper range of the 0.1-0.2% suggested in [127] (and references therein). Thus, a lower beryllium concentration in the incident flux would make a significant contribution to bringing the modelled and experimental collector deposition rates to a similar magnitude. Addionally, detachment in the outer divertor causes lower temperatures and higher densities, which would also reduce the modelled collector deposition.

8.2.1.2 Relation to geometrical model

In Chapter 5 and Chapter 6, time-dependent collector deposition results were compared to results from a simple geometrical model, showing good qualitative agreement. Much of this agreement was attributed to the inclusion of experimental data in the modelling, which helped to link the modelled description to the operational conditions. In particular, the strike point location was found to be very important for the deposition on the collectors. The dependence of the modelled collector deposition on the strike point location seen with the Monte Carlo model supports this dependence. Similarly, by scaling the sputtering source by the beryllium spectroscopy brightness around the strike point, a measure of the availibility of beryllium on the tile surface and in the incident flux was incorporated. Again, the Monte Carlo modelling results here show a corresponding dependence on these input conditions. The similar parameter dependencies for collector deposition in the geometrical and Monte Carlo models adds confidence that the simplifications made in the geometrical case were appropriate.

Despite the qualitative agreement of the geometrical modelling and the experimental collector deposition, the long timescales involved did impose significant limitations on the modelling. Discrepancies between the geometrically modelled and experimental collector depositions remain and are most likely due to variations in plasma conditions for particular discharges causing different erosion/deposition behaviour. These are not taken into account in the geometrical model, resulting in inaccuracies (the exposure to which is limited by the poor time resolution of the collectors and the smoothing that this imposes). This demonstrates the different focuses and purposes of the models. While the geometrical model focuses on qualitative, long-term variations in erosion and deposition, the Monte Carlo model examines the migration of beryllium in more detail, over shorter timescales, and for a greater range of input conditions.

Since the geometrical model only aimed at qualitative comparison of time-dependent deposition profiles, the modelled deposition was scaled by constant attenuation factors to fit to experimental deposition magnitudes. For this ITER-like wall outer divertor case, the attenuation factor was found to be 0.17. This attenuation factor describes the fraction of beryllium neutrals eroded from the strike point travelling in the direction of the collector that deposit on the collector. In the Monte Carlo model, no attenuation factors are applied since the ionisations of individual neutrals are treated directly. However, since the Monte Carlo model records the propensity of these ionisations, a corresponding factor may be calculated. The attenuation factor for the reference case is 0.45.

However, the use of an attenuation factor is of limited value in the Monte Carlo case, since it is defined using only erosion from the strike point. The geometrical model used the simplification that all erosion occurred from the strike point in order to efficiently describe the long timescales that the collectors operate for. However, in the Monte Carlo model, even when the strike point is on tile 5, a significant fraction of the collector deposition comes from the tail of the strike point on tile 6 (though some of this is likely to originally be from tile 5 via a multistep process). In both geometrical and Monte Carlo models, the collector deposition increases when the strike point moves closer to the outer corner due to the larger acceptance angles. Hence, although the trend of deposition with strike point location was preserved in the geometrical model, the source of the sputtered beryllium was only partially correct. The Monte Carlo model, which includes a spatial distribution of erosion/deposition and allows multiple sputtering/reflection steps, provides a more physical description of the relevant processes.

The collector deposition rate predicted by the Monte Carlo model overestimates the experimental rate by a factor of $\sim$3. Analysis of the parameter dependencies of the modelled collector deposition provide possibilities for resolving this difference, in particular through a lower beryllium flux fraction. The inclusion of experimental data in the geometrical modelling allowed good qualitative accuracy over the long timescales involved, but the simplifications resulted in discrepancies relative to the experimental results, e.g. when plasma temperatures or densities varied. The spatially-resolved erosion and deposition, and the treatment of ionisation and redeposition/reflection, in the Monte Carlo model enable a more physical description of the relevant experimental processes.

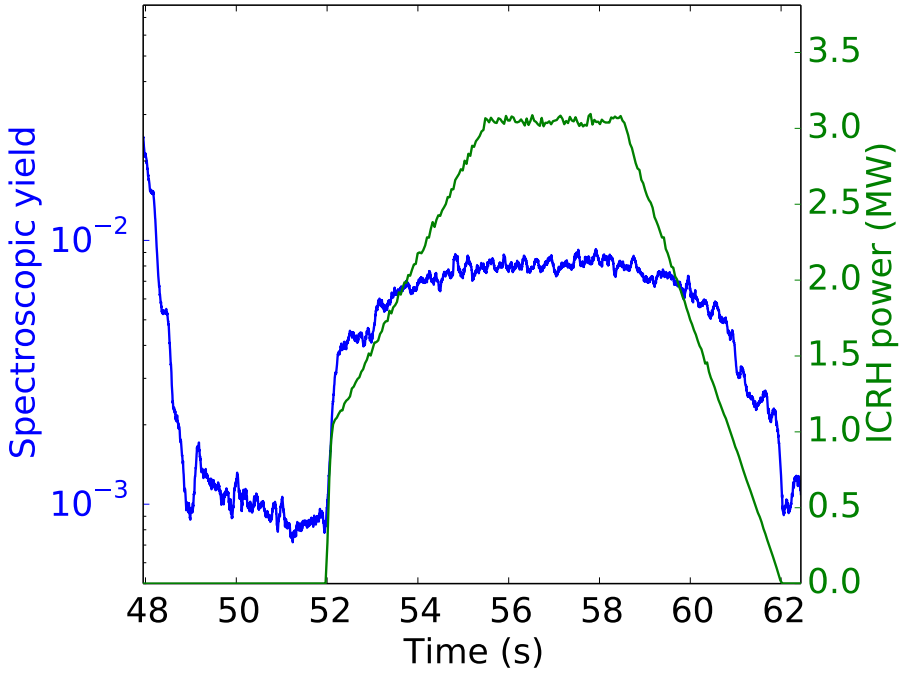

Figure 8.3: Plot showing the spectroscopic sputtering yield from the strike point and the input ICRH power during discharge 85894. The sputtering yield falls off after the initial period of the divertor phase, before increasing again when ICRH is begun.

8.2.2 ICRH

ICRH (Ion Cycloctron Resonance Heating) uses electromagnetic waves to impart energy to plasma ions and hence heat the plasma. In this section, the effect of this heating method on the erosion and deposition in the JET divertor will be considered with the use of spectroscopy data and the Monte Carlo code.

Figure 8.3 shows the spectroscopic sputtering yield in the outer divertor, as calculated using the procedure described in Figure 7.1, as well as the input ICRH power. This discharge featured a divertor phase initially using only Ohmic heating, a ramp up of ICRH heating to 3 MW, a flat top phase, and a ramp down of ICRH to zero. The spectroscopic sputtering yield is seen to start relatively high and thereafter decrease in magnitude (see Section 8.3 for a detailed examination of initial peaks). However, when ICRH is begun, the sputtering yield increases by a factor of 8-10, before returning to low levels after the ICRH is ramped down. This increase of the spectroscopic sputtering yield during periods when ICRH is used has also been observed for a large number of other discharges.

The use of ICRH has been shown to increase the sputtering of impurities from the main chamber walls in the region of the ICRH antennae in both ASDEX Upgrade [145] and JET [146]. The application of ICRH was deduced to lead to the creation of radio frequency electric fields parallel to the magnetic field lines, which rapidly accelerate the more mobile electrons into the main chamber wall. The resulting increase in the plasma potential accelerates the positively charged ions towards the wall in the sheaths close to the plasma-facing surfaces. This was found to increase the influx of tungsten and beryllium impurities in the ASDEX Upgrade and JET-ILW cases respectively [145], [146].

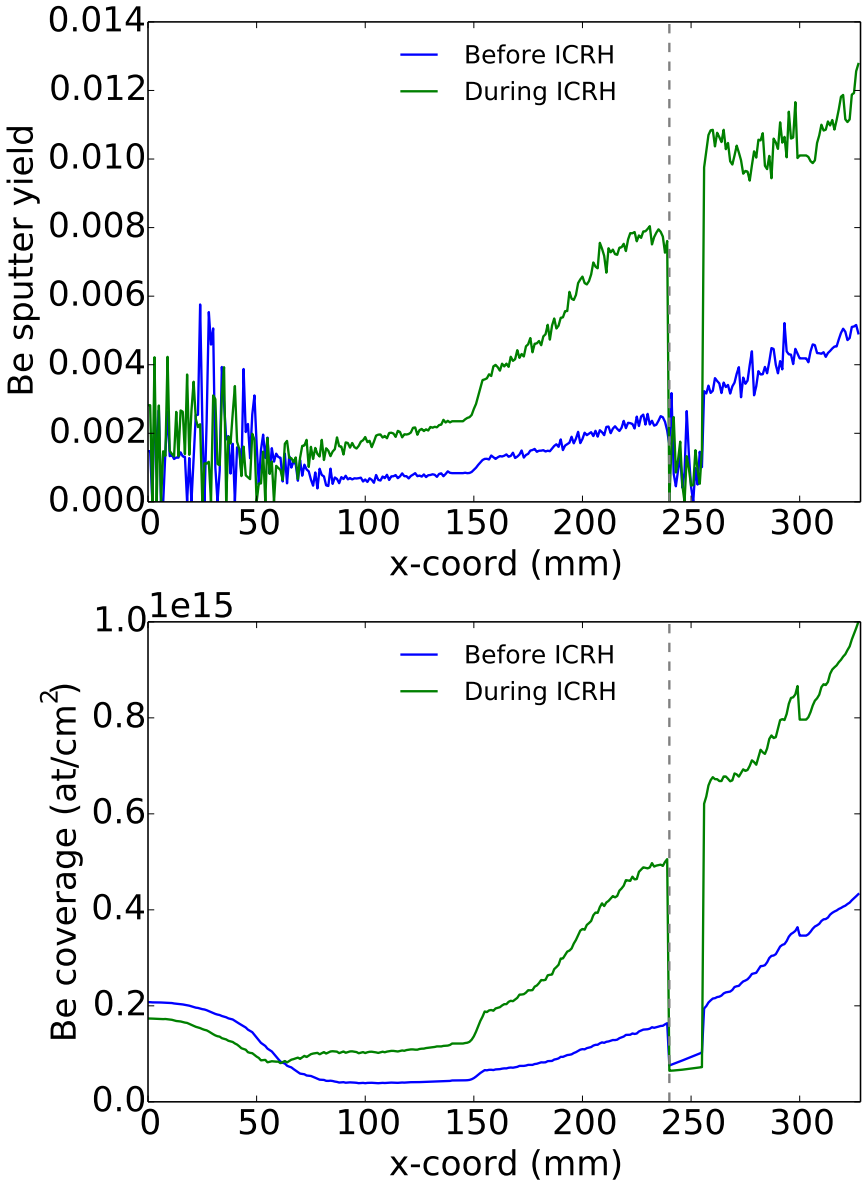

Figure 8.4: Plots showing modelled sputtering yields (upper) and tile surface coverages (lower). These profiles are shown at two different times before and after ICRH heating is represented by increasing the incident flux fraction.

Increased main chamber and divertor beryllium brightnesses during periods when ICRH was used have also been observed as part of the current study. The higher influx of beryllium into the SOL in general will lead to a higher beryllium fraction in the ion flux incident on the divertor. Thus, an approximate replication of the effects of ICRH was applied in the modelling by varying the beryllium flux fraction. The code was run with 2 seconds of the reference conditions (with 0.2% beryllium flux fraction), followed by 2 seconds with 0.5% beryllium flux fraction.

The results of this modelling are shown in Figure 8.4, with the two periods identified as 'Before ICRH' and 'During ICRH' respectively. The latter period with the increased flux fraction shows increased beryllium surface coverage and sputtering

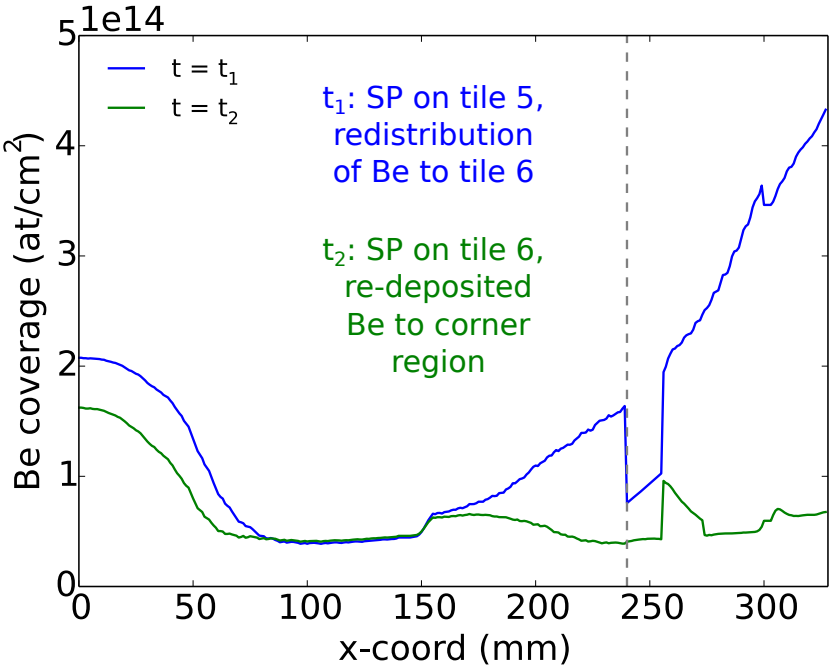

Figure 8.5: Plot showing modelled beryllium surface coverage at two different times during a run in which the strike point was moved from tile 5 to tile 6. Beryllium redistributes from tile 5 to tile 6, before being re-eroded from tile 6 when the strike point moves there and migrating to the corner region.

yields, to first order replicating the effects seen experimentally. It is further noted that this in turn leads to increased deposition in the outer divertor corner. This underlines the importance of the control of impurities in JET-ILW and ITER and suggests that particular attention must be paid to this when ICRH is used. Possible mitigation methods, such as operating with configurations that maximize the distance between the plasma and the ICRH antennae, have been suggested for limitation of the ICRH-induced impurity influx in the main chamber [145].

8.2.3 QMBs

The QMB in the outer corner of JET-ILW provides experimental data for comparison to the modelled deposition results. Absolute comparisons of deposition rate magnitudes to those found from the rotating collectors and modelling are problematic due to the differing acceptance angles and limited shutter opening times of the QMB. However, the average deposition rate on the QMB, while the shutter was opened, of approximately 1.2×10^{15} cm^{-2}s^{-1} is at least of the same order of magnitude as that found from the corresponding collector and the modelling. More usefully, the improved time resolution of the QMBs relative to the collectors allows the effects of different plasma conditions on deposition in the outer corner to be examined in more detail.

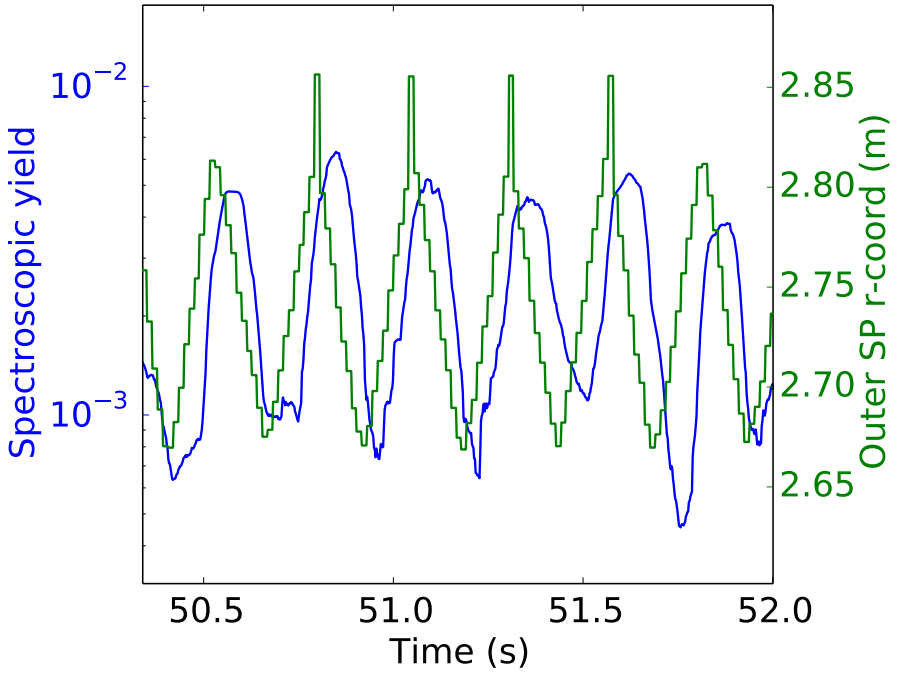

Figure 8.6: Plot showing the refreshing of the spectroscopic beryllium sputtering yield (blue) during sweeping of the strike point (green). The yield increases when the strike point moves closer to the corner during each sweep.

8.2.3.1 Shot history

The average depositions on the QMB and their associated errors may be calculated for different categories of discharges. Insight can be gained by looking specifically at discharges for which the strike point varies with time. While some of the discharges for which the QMB shutter was opened had strike points on tile 6 from the start of the divertor phase, others had strike points that moved from tile 5 to tile 6. Although the QMBs only provide one data point for each discharge in which they are used, comparing these two subsets of discharges provides a method for analysing the influence of shot history on erosion and deposition. Those strike points that moved from tile 5 to tile 6 before the shutter was opened resulted in average deposition of $(3.4 \pm 0.9) \times 10^{15}$ cm^{-2}s^{-1}, whereas those that stayed on tile 6 for the whole divertor phase resulted in deposition of $(1.1 \pm 0.3) \times 10^{15}$ cm^{-2}s^{-1}. This represents a factor of ∼3 higher deposition rate for discharges with outer strike points that moved from tile 5 to 6.

The agreement of the modelling results with this varied depending on the amount of time the strike point was on tile 5 for prior to moving to tile 6 and on the plasma density. Increases in both of these parameters led to higher redeposition on tile 6, giving a greater source of beryllium when the strike point subsequently moved to tile 6. This process is demonstrated in Figure 8.5. The factor of 3 increase in deposition was able to be replicated with long periods of strike point time on tile 5 and high densities, but factors of ∼1.5 - 2 were found to be more usual. This is lower than the difference found experimentally, though the figures do approximately agree within the experimental errors. The shot history effect seen from the QMB data and the modelling reinforces the importance of the beryllium surface coverage on the divertor

tiles for the degree of erosion and deposition that occurs.

8.2.3.2 Sweeping strike points

The effects of moving strike points can be further investigated by considering those that sweep back and forth on tile 5. Figure 8.6 shows an example of this for discharge 87223. Each time the strike point moves further down tile 5, the spectroscopic beryllium yield increases. This may be due to refreshing of the beryllium deposits at large x-values when the strike point is located higher up tile 5, providing a larger reservoir of beryllium for re-erosion when the strike point subsequently moves outward.

Modelling of this strike point sweeping shows increases in the corner deposition rate by factors of 5 - 30%, depending on the plasma density. Higher plasma densities resulted in greater redeposition and therefore increased refreshing of deposits. This caused greater sputtering when the strike point moved back towards the outer corner and hence higher deposition at the QMB location. Sweeping of strike points offers one way of protecting plasma-facing materials in the divertors of future high-power tokamaks through limiting the time for which different surfaces are exposed to the peak power fluxes. However, refreshing of beryllium deposits and the associated periodic recovery of beryllium sputtering yields suggests that this can lead to increased remote deposition of impurities.

The measurements taken during sweeping strike points resulted in an average QMB deposition of $(1.6 \pm 0.2) \times 10^{15}$ cm^{-2}s^{-1}, while those that were approximately stationary yielded $(1.1 \pm 0.2) \times 10^{15}$ cm^{-2}s^{-1}. The 5 - 30% increase in corner deposition rate for sweeping strike points is lower than this ∼50% increase seen experimentally (though the relative size of the uncertainties here are large). This mismatch may be due to the fact that some of the measured discharges with sweeping strike points also had ELMs, possibly increasing the corner deposition further.

8.2.3.3 ELMs

First attempts have been made at representing ELMs within the Monte Carlo model. The approach used follows that implemented in [127], with the reference plasma conditions interspersed with 50 Hz, 500 μs periods with ELM-like conditions. The divertor conditions during ELMs are a matter of ongoing scientific enquiry. Theoretical treatments [147] and recent measurements [148] have indicated that the electron temperatures are surprisingly low. The 'free-streaming' model suggests that the electrons are forced to transfer most of their energy to ions in order to preserve quasineutrality of ELM filament parallel transport. Hence, while the modelled electron temperature T_e is kept at 25 eV, the assumption of $T_i = T_e$ is clearly not valid here. Following the analysis in [148], electron densities n_e of 10^{20} m^{-3}, ion impact energies E_i of ∼3 keV and a tripling of the ion flux with regard to the reference conditions are applied for the ELMy periods in the Monte Carlo model. In addition, a doubling of the beryllium fraction in the incident flux is also applied, originating from increased plasma-wall interaction in the main chamber [149].

Figure 8.7 shows the modelled beryllium brightness due to these ELMy conditions. The higher influxes of beryllium during the ELMs cause periodic recoveries of the

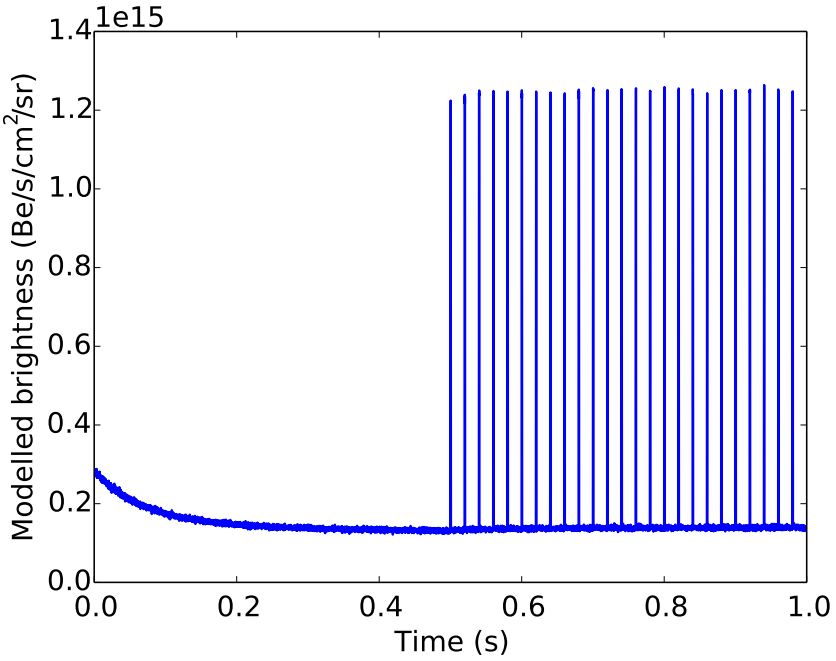

Figure 8.7: Plot showing the spatially-averaged modelled beryllium brightness including ELMy conditions. The first 0.5 s show the reference conditions at the start of the divertor phase; the following 0.5s include 50 Hz, 500 μs ELMs. The brightness periodically recovers during and immediately after these ELMs.

beryllium brightness after the initial fall-off at the start of the divertor phase. The recoveries also resulted in increased beryllium migration to the outer corner; the corner deposition rate during the whole ELMy period was increased by ∼15% relative to the reference conditions. This initial study suggests that the ELMs contributed to the increase in the experimental deposition on the QMB and reinforces their importance as a driver of first wall erosion and thereby remote deposition.

This section has used the Monte Carlo modelling of erosion and deposition to compare to and investigate experimental results. The deposition on the outer corner rotating collector has been modelled for different plasma conditions. Using this work, the experimental depositions and the results of the long-term, geometrical modelling of collector deposition have been analysed. The importance of ICRH has been considered in terms of its effects on the divertor erosion/deposition. Investigation using spectroscopy and modelling has shown an increase in beryllium coverage and sputtering yields due to the increased beryllium source from the main chamber. The deposition rate on the outer corner QMB has been considered for different plasma conditions, with modelling of these conditions indicating similar dependencies. In particular, movement of the strike point has been seen to increase the deposition rate in the outer corner due to the strike point falling on surfaces where significant redeposition had previously occurred. First attempts at describing ELMs within the Monte Carlo code have also resulted in increased modelled deposition in the outer corner. The following section will further investigate experimental results through modelling of the initial peaks seen in beryllium spectroscopy signals at the start of the divertor phase.

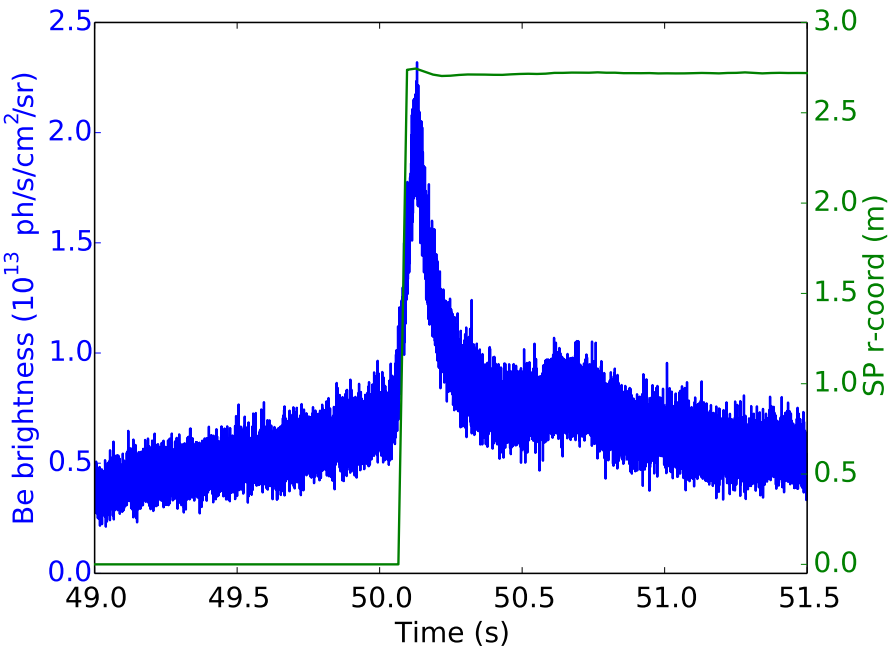

Figure 8.8: Plot demonstrating the initial peak seen in the outer divertor beryllium brightness signal when the strike point first forms (discharge 82,200).

8.3 Peaking of the beryllium brightness during the initial divertor phase

In Section 7.3 it was observed that when the strike point first forms, the spectroscopic beryllium yield is often of a similar magnitude to that calculated using analytical yield equations. However, the spectroscopic yield quickly falls below the calculated yield, suggesting that beryllium may be removed from tile surfaces during this initial period. The start of the divertor phase can thus contribute a disproportionately high fraction of the total divertor beryllium erosion. These initial beryllium peaks have been investigated using a combination of the Monte Carlo model and divertor spectroscopy.

8.3.1 Observation of initial peaks

The JET divertor surfaces are viewed by a series of spectroscopic chords, which provide the beryllium brightness signals as a function of time. When the plasma moves from limiter phase to divertor phase, peaks in the beryllium brightness signals are observed for large numbers of discharges. An example of these experimental observations is shown in Figure 8.8. Before the strike point forms at ~50.1 s, the beryllium brightness is low and in any case is likely to contain a significant contribution originating from light reflected from the main chamber. After formation of the strike point, the beryllium brightness decays from its peak value to an approximate equilibrium level in a few tenths of a second.

Given these experimental observations, it is worth considering whether similar be-

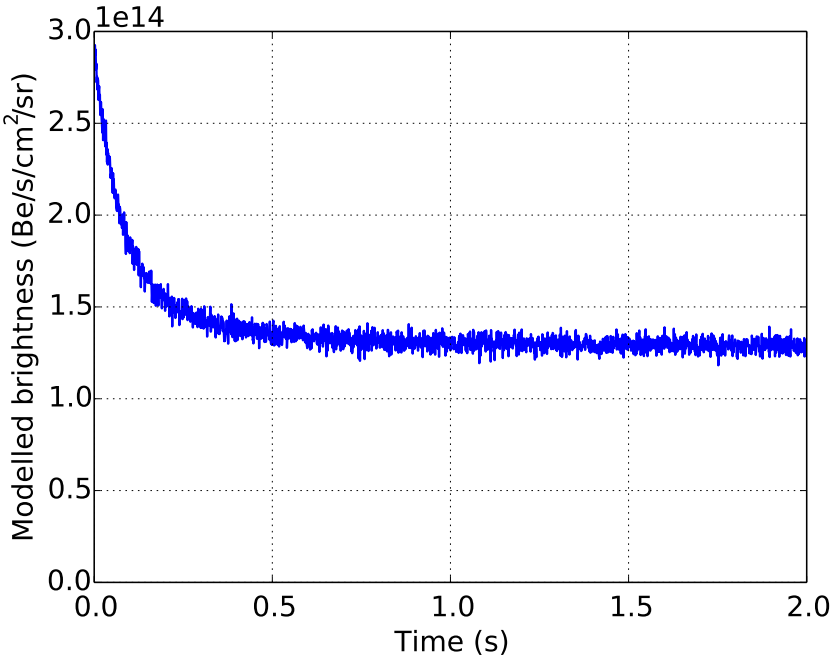

Figure 8.9: Total modelled beryllium brightness as a function of time for the reference case. Direct comparison of the magntidude of Figure 8.8 with this signal would require multiplication of the former by the SXB value. The difference in magnitude by a factor of ∼10-15 is in approximate agreement with SXB values corresponding to the relevant conditions.

haviour is evident in the Monte Carlo modelling results. Since the model records temporally and spatially resolved ionisation of beryllium neutrals, a synthetic diagnostic giving modelled beryllium brightnesses may be constructed. Figure 8.9 shows the total modelled outer divertor beryllium brightness for the reference case described in Section 7.4. The fall-off of the brightness from the initial peak level shows good qualitative agreement with the experimental results (i.e. in timescale and reduction in magnitude). In the modelling, this initial peak is seen to be associated with the initial burn-off of beryllium from the tile surfaces. The similarity of the experimental and modelled profiles thus may suggest that a similar effect contributes to the experimental initial peaks. However, it is noted that if this is the case, the burn-off of beryllium from the tiles and the evolution of the brightness profile will vary depending on the surface and plasma conditions. Such variations are therefore investigated in the following section.

8.3.2 Modelling

The modelling indicates that the burn-off of initial beryllium coverage on the tiles is important for the formation of the observed initial peaks. Indeed, it is reasonable to expect that the relative height and/or width of the peaks will depend on this initial coverage. However, the amount of beryllium on the tiles is also affected by the incoming beryllium fraction in the incident flux. A 2-dimensional parameter scan over varying initial coverages and flux fractions has been performed in order to investigate their effects on the initial peaks. By characterising these initial peaks for

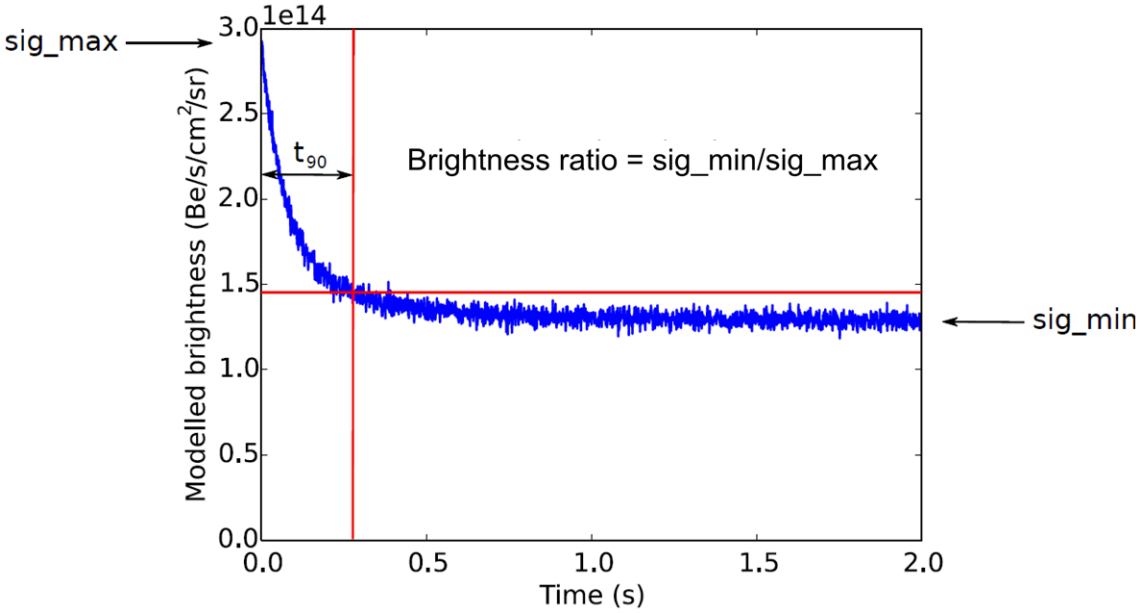

Figure 8.10: Total modelled beryllium brightness for the reference case, used to define the brightness ratio and t_{90} parameters. These describe the inverse size of the peak and the temporal width of the peak respectively.

different conditions, it is hoped that it will become possible to further analyse their experimental causes and significance.

In order to perform the analysis in a systematic way, it is necessary to make some definitions in order to quantify the characteristics of the peaks. Figure 8.10 again shows the modelled brightness profile from the reference case, with these definitions super-imposed over the plot. The brightness ratio is defined as the minimum, equilibrium brightness signal level divided by the peak signal level. It therefore describes the inverse of the relative magnitude of the peak. High brightness ratio values indicate a peak that is small in height relative to the equilibrium signal magnitude; low brightness ratio values indicate that the brightness drops significantly from the peak to the equilibrium level. On a practical level, this inverse definition has the advantage that for large reductions in brightness, the ratio tends towards zero rather than infinity. The second defined parameter is the time taken for the brightness to fall 90% of the way from the peak level to the equilibrium level. Thus, this t_{90} value describes the time taken for the peak to dissipate.

Figure 8.11 shows the variation of the brightness ratio parameter with the initial coverage and beryllium flux fraction applied in different modelling runs. For the runs represented in the bottom right corner of the plot, the initial coverage was high, but there was little or no beryllium in the incident flux. Equivalently, there was a large initial source of beryllium, but little replenishment of this source. This results in a large initial peak and subsequent strong decay of this peak as the beryllium coverage depletes. Thus, the ratios of final to initial brightnesses are very low for these conditions.

The upper left of the parameter space described by the plot corresponds to lower initial beryllium coverage and increased beryllium fractions in the incident flux.

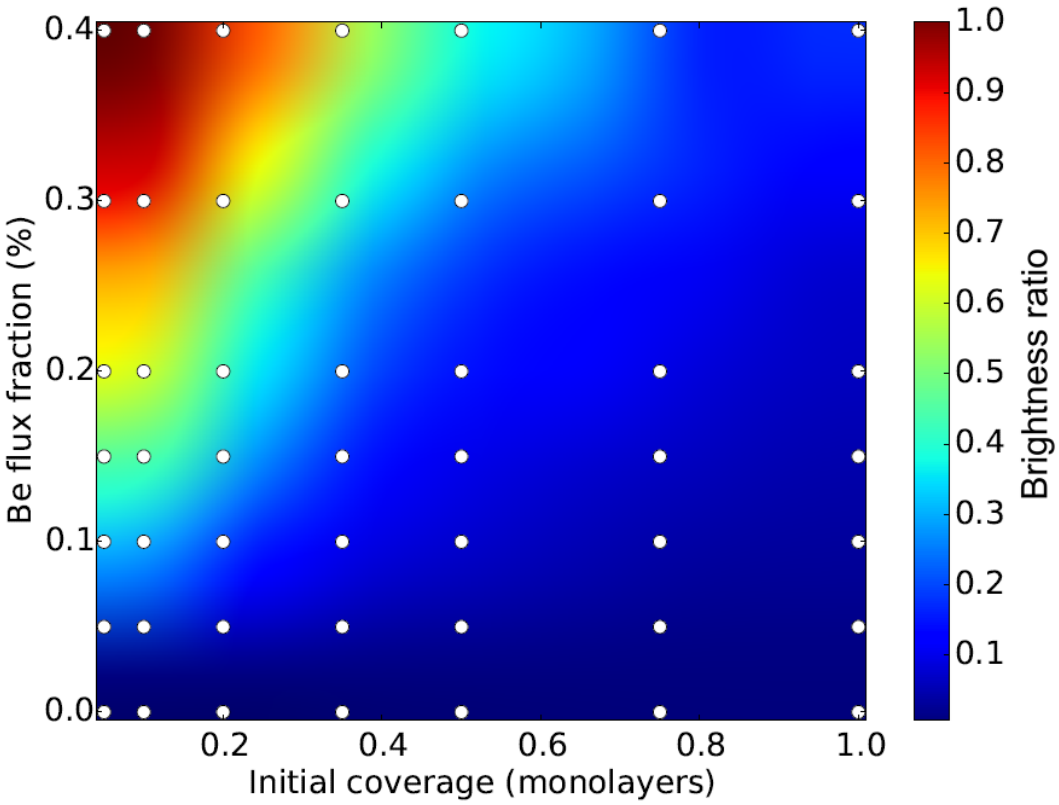

Figure 8.11: Plot showing the brightness ratio for different input conditions of initial coverage and beryllium flux fraction. The white circles indicate the parameters for which individual runs were performed. A 2-D interpolation has been performed over these data points.

These runs had a lower initial beryllium source, but an increased constant, incoming source that replenished the beryllium. Decreasing the initial beryllium level and increasing the equilibrium level results in relatively small initial peaks. Thus, lower initial coverages and higher flux fractions are seen to increase the brightness ratio parameter.

Figure 8.12 shows the effects that variations in initial coverage and flux fraction have on the timescale of the peaks, described using the t_{90} parameter. The brightness ratio parameter describing the peak magnitude showed a strong dependence on both the initial coverage and the flux fraction. Figure 8.12 indicates that t_{90} has a more pronounced dependence on the initial beryllium coverage. Higher initial coverages provide larger initial beryllium sources, which take longer to burn-off from the tiles. However, it is noted that the higher spatial coverages also cause higher initial erosion yields, which weakens the dependence of the peak timescales on coverage. Thus, for relatively low flux fractions, there is only a factor of two or less increase in t_{90} for 1 monolayer initial coverage relative to 0.05 monolayer initial coverage. The colour bar demonstrates the relative narrowness of the range of timescales observed from the modelling.

Though the initial coverage appears to be the most important parameter for the peak timescales, there is also a dependence on the flux fraction. For high initial coverage cases, a higher flux fraction in general causes a larger t_{90} value. Physically this is explained by the higher incoming source from the incident flux partially offsetting the burn-off of the initial source, spreading its depletion over longer timescales. However,

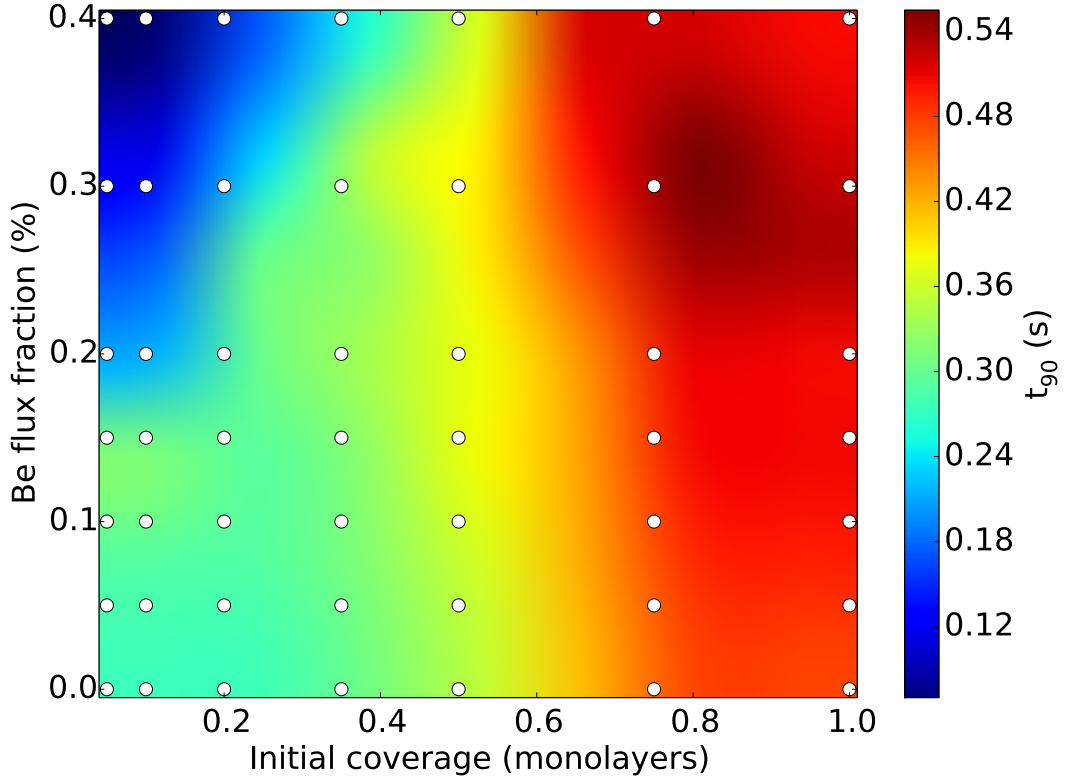

Figure 8.12: Plot showing the t_{90} parameter for different initial coverages and beryllium flux fractions. The white circles indicate the parameters for which individual runs were performed. A 2-D interpolation has been performed over these data points.

for low initial coverages, an explanation of the decrease of t_{90} with increasing flux fraction is less obvious. Figure 8.11 shows that these conditions result in small initial peaks, i.e. small reductions in brightness magnitudes. Because the brightness magnitudes fall by so little for these cases, the times taken for these decreases to occur are also themselves low.

A systematic study of the modelled dependence of the initial peaks on initial coverage and flux fraction has been performed. This has demonstrated larger relative magnitudes of initial peaks for high initial coverages and low flux fractions. It has also shown that the peaks take longer to dissipate for higher initial coverage and that the timescales additionally depend on the flux fractions. In Section 8.3.4, these modelled dependencies will be used to help interpret initial peaks seen from experimental spectroscopy. Before this is considered, the following section will provide a brief analysis of the spatial profile of the sputtering yield and how it evolves during and after the initial peak period.

8.3.3 Yield profile

Figure 8.13 shows spatial yield profiles and surface coverages at different times during a run using the reference conditions. At the start of the run, when the strike point

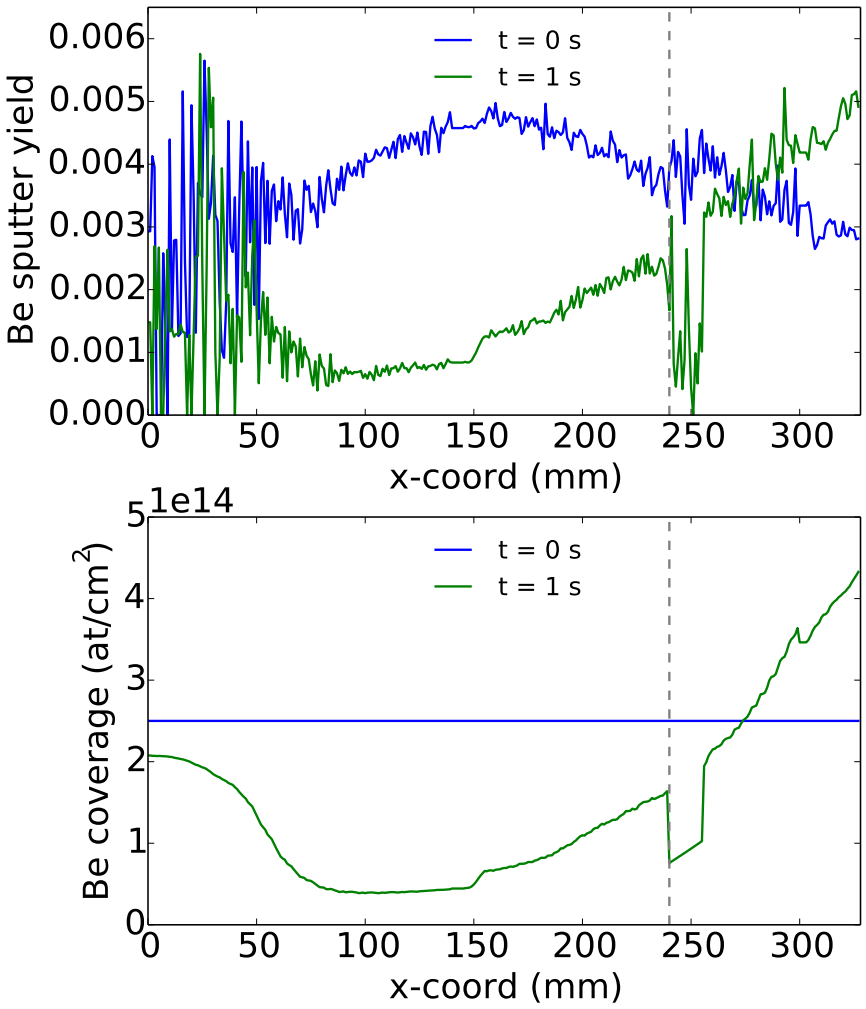

Figure 8.13: Plot to show modelled spatial profiles of the beryllium sputtering yield (upper) and beryllium surface coverage (lower) after 0 and 1 s of the reference case. Depletion of beryllium coverage around the strike point leads to a reduction in the yield and a movement of the location of the peak yield to tile 6.

first forms, the yield peaks around the strike point on tile 5. However, at later times, the beryllium yield peaks closer to the corner on tile 6. Some of the beryllium neutrals sputtered from the strike point region escape from the vicinity and only get ionised at larger x-coordinates. This broadens the beryllium peak and shifts it to larger x-values, an effect that is present throughout the modelling runs.

However, the outward movement of the location of the peak spectroscopic yield is mostly caused by the changes in the beryllium surface coverage. As the beryllium coverage close to the strike point is depleted, the yield from this region also decreases. The spatial coverage on tile 6 is greater (for tile 5 strike points) due to lower erosion from here previously and redeposition of beryllium previously eroded from tile 5. This higher spatial coverage allows significant sputtering yields to be maintained for longer on tile 6 relative to tile 5. Thus, after the initial period, the peak of the spectroscopic yield profile is seen to shift from tile 5 to tile 6.

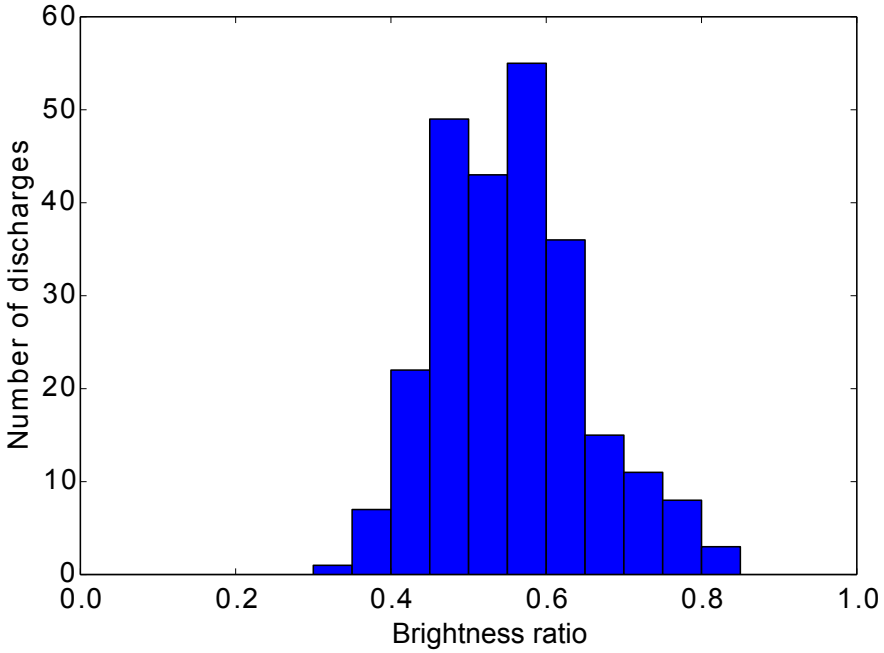

Figure 8.14: Distribution of the brightness ratio parameter for experimental intial peaks.

8.3.4 Experimental initial peaks

It is hoped that comparison of experimental and modelled initial peaks will enable a greater physical understanding of the dominant processes involved. A database of discharges with suitable properties for experimental investigation of the initial peaks was created. The discharges were selected to have strike points on tile 5, to not have strike point movement of more than 2 cm in the first second of divertor time, and to have no significant variations in plasma current or heating over this first second. This filtering allowed closer comparison with the modelling results and reduced the parameter space. Some discharges did not display a recognisable peak in the beryllium brightness and these cases were neglected. However, even with the filtering, a large number of discharges with intial peaks were observed. The brightness ratio and t_{90} parameters, as defined in Figure 8.10, were calculated for each of these discharges.

Figure 8.14 shows binned data for the numbers of discharges with brightness ratio parameters in different ranges. The ratios range from ∼0.4-0.8 and peak between 0.5 and 0.6 (i.e. a fall in signal magnitude by a factor of ∼2). Similarly, Figure 8.15 shows the numbers of discharges with t_{90} parameters in different ranges. The initial peaks are seen to last for between 0.1 and 0.5 s, peaking at 0.25 - 0.3 s. These values may be compared with the modelled parameter ranges in Figure 8.11 and Figure 8.12. In general, the ranges of values seen experimentally agree well with the ranges found from the modelling. Though a point is not uniquely defined by them, the peak experimental values suggest a location in the 2-D parameter space close to but not at the top left corners of Figure 8.11 and Figure 8.12. In the ranges described by the plots, this corresponds to low to medium initial coverages of ∼0.1 - 0.4 monolayers and medium to high flux fractions of ∼0.1 - 0.4% (with the possible range of each of these parameters dependent on the value of the other).

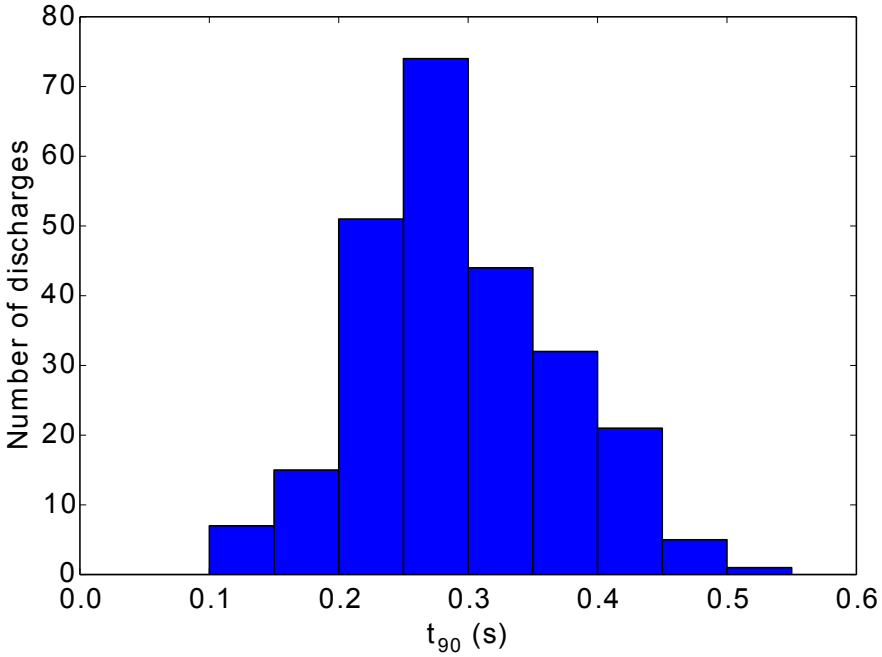

Figure 8.15: Distribution of the t_{90} parameter for experimental initial peaks.

It is also worth considering whether similar initial peak results are seen with other modelling efforts. WallDyn modelling has indeed been used to demonstrate higher beryllium brightnesses at the start of the divertor phase relative to later during the discharge [118]. The 40% drop in brightness for the outer divertor case corresponds to a brightness ratio of 0.6, which agrees well with the experimental and modelled brightness ratios identified above.

While it is useful to consider the overall experimental ranges of the brightness ratio and t_{90} parameters, it is desirable to be able to identify dependencies within the data in order to further understanding of the physical processes involved. To this end, various correlations of the brightness ratio and t_{90} parameters with experimental data from the relevant discharges were attempted. However, in general these yielded only poor correlations, which prompted a closer study of the transition from the limiter to the divertor phase.

The inner wall gap is the horizontal distance between the inner wall and the plasma at the midplane. When the plasma transitions from limiter to divertor phase, this wall gap gradually opens up. The rate at which this occurs was found to have a strong effect on the timescale of the initial peak (Figure 8.16). Taking 2.5 cm as a characteristic gap size, larger times taken for the plasma to reach this gap size are found to correspond to longer peak timescales.

When there is a smaller gap between the plasma and the wall, more sputtering of the beryllium tiles can occur. Since the magnetic flux lines lead from the region near the wall to the divertor, it is reasonable to assume that the discharges with plasma that stays closer to the wall for longer have larger initial beryllium fractions in the flux to the divertor. The convective transport along field lines is orders of magnitude faster than the diffusive transport across field lines, resulting in migration of beryllium to the divertor from the main chamber. As the plasma moves away from the wall, the beryllium fraction should decrease, leading to a decrease in the beryllium brightness

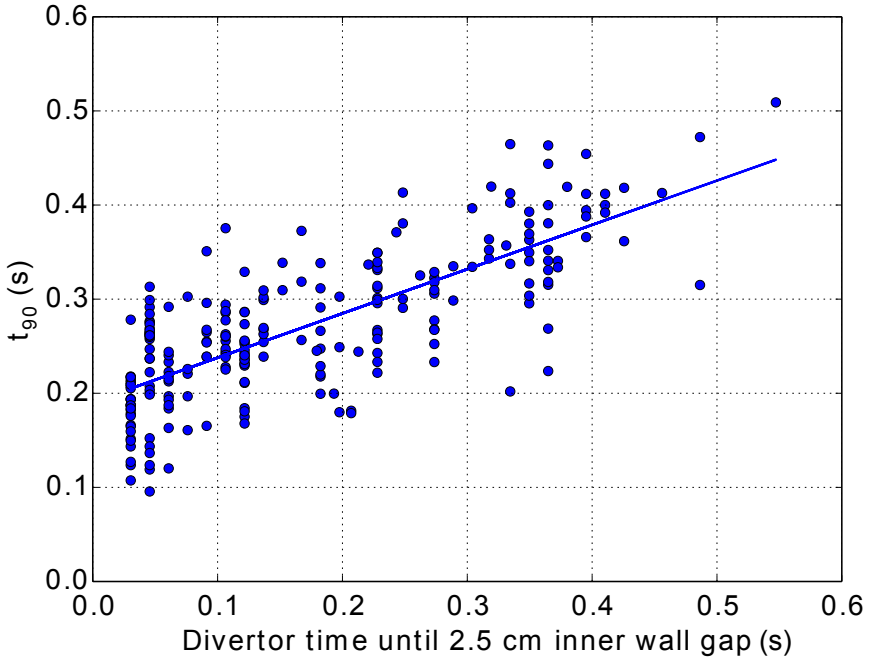

Figure 8.16: Correlation of t_{90} with the time between the start of the divertor phase and the time when a 2.5 cm gap has opened between the inner wall and the plasma. The trend line has a r^2 value of 0.58.

observed in the divertor. These results imply that such time-varying beryllium flux fractions are a key cause of the initial peaks that are observed experimentally.

This analysis offers an alternative reason for the initial peaks to the previous modelling work, which assumed a constant flux fraction and had a greater focus on the initial beryllium coverage on the divertor tiles (though this is adressed in Section 8.3.5). However, the non-zero y-intercept of the trend line in Figure 8.16 suggests that there may be a residual dependence on initial coverage. Even for wall gaps that become large almost immediately, an initial peak remains. This non-zero offset remains in place even if 5 cm rather than 2.5 cm is chosen as the limiting gap distance.

It is further noted that the plot still shows considerable variation in t_{90} even along constant values of the 'gap time' (i.e. in the y-direction). The spacing of the points along the x-axis reflects the finite time resolution of the EFIT data that gives the wall gap information. The first two 'columns' of points, for which the time taken to reach the gap was less than 50 ms, were selected from the plot. These points should correspond to discharges for which the inner wall gap had the least effect on the divertor erosion/deposition behaviour through time-varying beryllium flux fractions. Therefore, the discharges corresponding to these points were analysed in more detail as they offer the best opportunity to identify dependencies on conditions other than the plasma-wall gap.

Within this data, dependencies of the brightness ratio and t_{90} parameters on the limiter operations preceding the divertor phases were identified (Figure 8.17). The data selected represented a relatively small range of discharges, which were found to broadly separate into two groups of short and long limiter phases. Averages have been taken over each group, with error bars representing the standard deviations.

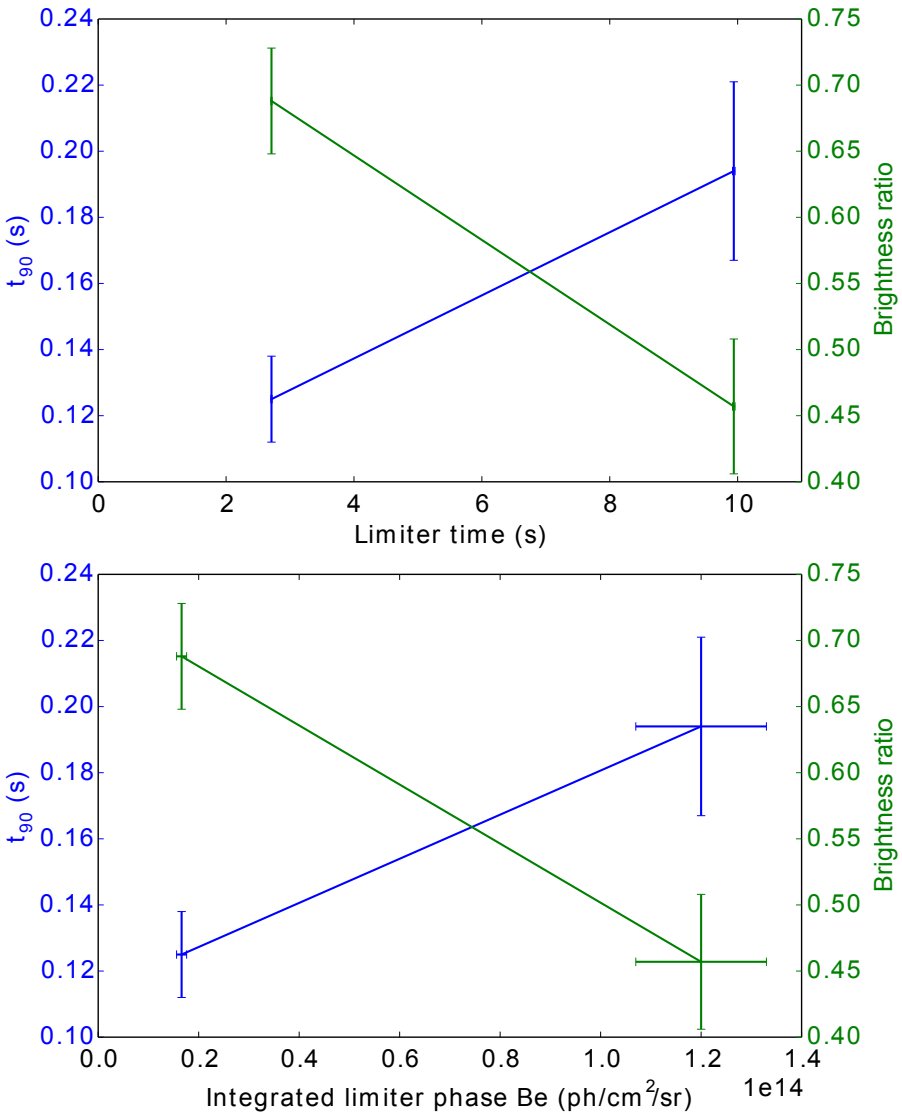

Figure 8.17: Plots showing the residual dependence of the brightness ratio and t_{90} parameters on limiter time (upper) and integrated main chamber beryllium brightness during the limiter phase (lower) for discharges in which the wall gap became large immediately after the start of the divertor phase. The relatively small range of selected discharges approximately separated into two groups of short and long limiter times. These groups have been averaged over, with the standard deviations represented by error bars. The lines between points are intended to guide the eye only.

The upper plot shows that for longer limiter phases, the initial peak lasts longer and the brightness ratio parameter is smaller (i.e. the relative magnitude of the peak is greater). The same dependencies of peak timescales and relative magnitudes on the integrated main chamber beryllium observed by spectroscopy during the limiter phase are shown in the lower plot.

In [119] and [118], transport of beryllium from the main chamber to the divertor during the limiter phase is inferred. Increases in this transport to the divertor for increasing limiter time and main chamber beryllium source are expected. The dependencies of the initial peak parameters shown in Figure 8.17 similarly indicate that

initial coverage of beryllium on the divertor tiles increases with the limiter time and the integrated limiter beryllium source. As has been previously shown (see Figure 8.16), the details of the transition from limiter to divertor phase strongly affects the initial peaks through the influence of initially high beryllium flux fractions. However, Figure 8.17 also indicates that an initial coverage formed during the limiter phase and burnt off at the start of the divertor phase contributes to the formation of these initial peaks.

The initial peaks have implications for the amount of deposition that occurs in remote areas. From the modelling, this peaks in the outer corner during the initial period when the beryllium source is greatest, before gradually reaching an equilibrium level in most cases. This suggests that the total deposition in the remote areas has a dependence on the total length of each discharge. In ITER, discharges are planned to last 400-500 s. The initial peak period contributes the highest deposition rate and constitutes only a small fraction of the total discharge time. In other words, were the Monte Carlo model to be run for a repeated series of identical 2 s runs, the average remote deposition rate would be higher than that for a single 400 s run. This is related to the effect of the initial peaks and the refreshing of divertor deposits. If similar behaviour occurs in ITER to that observed in JET, which the matching plasma-facing materials and similar geometries provide confidence of, the implication is that the remote beryllium deposition rate may be suppressed.

For minimisation of remote divertor deposition, the duration of the limiter phase, and the duration of the transition from the limiter to divertor phase, should be minimised. There exist 'large bore' ITER scenarios that start up with relatively large plasma volumes, allowing divertor phases after only ∼13 s [150]. This represents ∼3% of the total discharge time in ITER, relative to limiter phases in JET that often comprise in the region of ∼30% of the discharge time. Such early transitions to the divertor phase should limit beryllium transport to the divertor and deposition in remote divertor locations (though it is noted that the absolute magnitude of deposition is likely to be higher than in JET due to the larger surfaces involved). It is sensible to focus the majority of strong plasma-material interaction on the thermally and physically robust tungsten tiles in the divertor rather than on the beryllium tiles in the main chamber, which are relatively susceptible to damage by comparison.

8.3.5 Time-varying flux fractions

The previous section demonstrated the importance of an initially high, decreasing beryllium flux fraction for the experimental initial peaks. However, in the modelling, the flux fraction has been kept constant during each run. Here, a varying flux fraction is implemented in the model in order to check whether it can contribute to the modelled initial peaks as it is seen to do experimentally.

Figure 8.18 shows results from modelling runs incorporating time-varying beryllium flux fractions. The flux fraction is decreased from 1% or 0.5% to 0.2% in the first 0.2 s of each run. This is performed for zero initial coverage and 0.1 monolayer initial coverage. In the zero initial coverage case, no initial peak is observed for a constant 0.2% flux fraction. However, when an initially high flux fraction is applied, peaks are evident and increase in magnitude for larger initial flux fractions. For the 0.1 monolayer initial coverage case, the higher initial flux fractions increase the

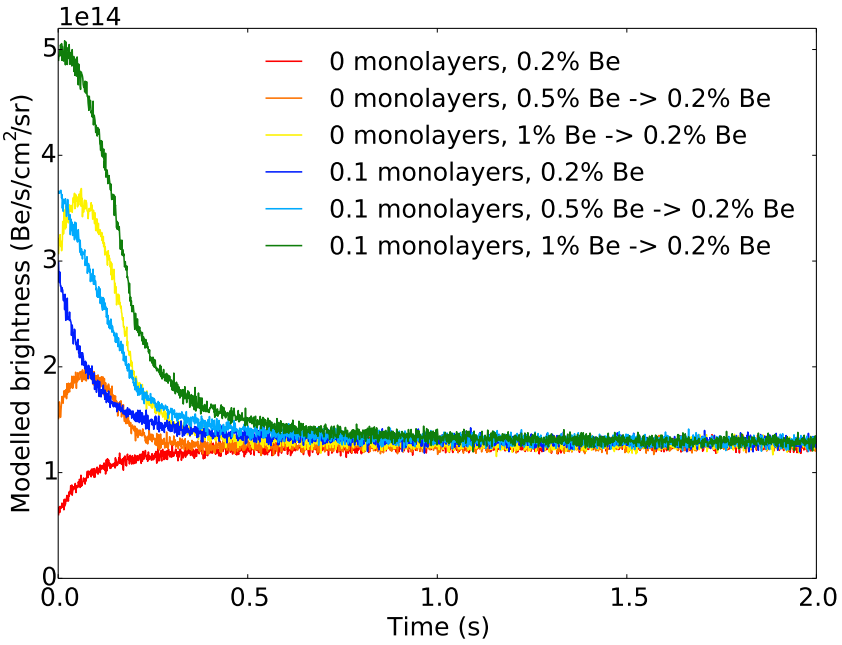

Figure 8.18: Plot showing the modelled beryllium brightnesses for runs with initially large beryllium flux fractions, which reduce to constant levels after 0.2 s. Also shown for reference are the relevant constant flux fraction cases.

magnitude of the initial peak that was already present. Thus, the model reproduces the contribution of an initially high beryllium flux to the initial peaks as inferred from the experimental data analysis.

This section has investigated the initial beryllium brightness peaks seen from experiments and modelling when the strike point first forms. In the modelling, the initial beryllium surface coverage and flux fraction were identified as important for the magnitude and timescale of the peaks and parameter scans were performed over these quantities. Analysis of the initial peaks seen experimentally indicated that an initially high flux fraction, due to the proximity of the plasma to the main chamber inner wall, constituted a major contribution to the intial peaks. Further analysis revealed an additional dependence on the limiter phases preceding the transitions to divertor phases, from which transport of beryllium to the divertor and a dependence of the initial peaks on surface coverage were inferred. The application of time-varying flux-fractions in the model were found to reproduce the behaviour seen experimentally.

8.4 Conclusions

This chapter has compared and contrasted results gained from Monte Carlo modelling of erosion, deposition and migration of beryllium in the JET-ILW outer divertor with corresponding experimental results. This enables the physicality of the description provided by the model to be analysed and the significant mechanisms driving experimental results to be elucidated.

Experimental results from rotating collectors, QMBs and spectroscopy have been analysed, showing reasonable agreement with results from corresponding modelling efforts. The modelled deposition rate on the outer corner rotating collector (for the reference case) is approximately a factor of three greater than the average deposition rate seen experimentally. This may be due to an overestimate of the characteristic beryllium flux fraction. A combination of Monte Carlo modelling and spectroscopy has been used to investigate an increase in divertor beryllium erosion and deposition when ICRH is applied, which is attributed to a greater main chamber beryllium source. QMBs and the Monte Carlo model have been used to demonstrate the importance of strike point locations/movements and ELMs for increasing erosion and deposition at the tiles and in remote regions.

Initial peaks in beryllium brightness seen at the start of the divertor phase from both spectroscopy signals and modelling have been investigated. The modelling revealed the dependencies of these peaks on the input initial coverages and beryllium flux fractions. Analysis of experimental data demonstrated the importance of the transition from the limiter to the divertor phase as well as the effects of impurity transport to the divertor during the limiter phase.

The Monte Carlo model has proved flexible and useful in the investigation of erosion, deposition and material migration in the JET-ILW divertor. It both incorporates, and enables investigations of, experimental results. The simplicity of use, efficiency and versatility of the model facilitates its application to a wide range of different plasma and surface conditions.

Chapter 9

Conclusions

This chapter will draw together the material presented in the preceding chapters to give a comprehensive understanding of the scope and key features of this study. Section 9.1 provides a summary of each previous chapter and serves as a reminder of the work presented. In section 9.2, a non-exhaustive selection of the most important points of this study are highlighted. Their significance and relation to current scientific knowledge are outlined in general terms. Finally, section 9.3 looks ahead to work that is either forthcoming or that would be advantageous in furthering understanding of erosion and deposition in tokamaks.

9.1 Summary

The aim of the presented study is to investigate erosion, deposition and material migration in the JET divertor and to compare between the behaviour observed under JET-C and JET-ILW operation. Determination and analysis of the different characteristics exhibited by the different plasma-facing materials provides vital information for the efficient, economic and safe operation of ITER. A combination of different diagnostics and modelling techniques have been applied in different areas in order to produce a detailed study of the relevant processes and results.

Chapter 1 introduced the importance of the diversification of energy supply in the context of rising populations, increasing energy demand, depletion of fossil fuels and environmental considerations. The mechanisms underpinning nuclear fusion were described and its potential as a future method for energy production was stressed. Currently, the most promising device for achieving industrial nuclear fusion is a magnetic confinement vessel known as a tokamak. The workings of these devices were described and JET, the tokamak on which the current study is based, was introduced. The mechanisms causing erosion and deposition of plasma-facing materials in tokamaks, and their deleterious consequences, were outlined in anticipation of the work detailed in the following chapters.

Chapter 2 described and critiqued previous studies of erosion, deposition and material migration, providing context and motivation for the current study. Sputtering yields were introduced, providing a metric for the quantification of the lifetimes and

expected influxes to the plasma for different plasma-facing materials. Post-mortem tile analysis techniques provide the most fundamental measure of surface change, but suffer from a lack of temporal resolution. This is addressed through the use of time-resolved diagnostics such as rotating collectors and quartz microbalances, which allow erosion and deposition to be related to the corresponding plasma conditions. Techniques such as spectroscopy further provide access to sub-millisecond time resolutions. Modelling supplements these techniques by enabling investigation of mechanisms that are spatially or temporally inaccessible to experimental analysis.

Though erosion and deposition studies implicitly concern long-term changes to material surfaces, the relevant mechanisms driving these surface changes can vary by orders of magnitude over small length and time scales. From the review of the current literature, the role of the current study was identified. The approach outlined was to focus on diagnostics that provide medium time resolution data, namely the rotating collectors and QMBs, while comparing to and taking inputs from both ends of the time resolution spectrum.

Chapter 3 introduced the experimental tools and techniques used in the current study. The main diagnostics used are rotating collectors, which vary the surfaces deposited on and thus provide a time history of deposition, and QMBs, which exploit the dependence of the vibrational frequency of a quartz crystal on mass to measure erosion/deposition rates. Ion beam analysis provides a means of identifying and quantifying the deposits on different surfaces through the interaction of high energy ions with target nuclei.

Chapter 4 described the modelling techniques used to investigate erosion and deposition. Since the collectors provide data over long timescales, a simplified, geometrical model incorporating a range of experimental data was used to describe the time-varying deposition on them. In contrast to this, an alternative modelling approach was used to investigate the erosion, deposition and transport in the JET-ILW divertor in more detail and at higher time resolutions. This Monte Carlo code involves more explicit analysis of the ionisation, redeposition and reflection of eroded beryllium. It was written to be flexible so as to enable application to a wide range of different experimental conditions.

In Chapter 5, time-dependent, species-specific deposition results from rotating collectors located in the central JET-C and JET-ILW divertors were presented. Time-dependent deposition profiles from the geometrical modelling showed good qualitative agreement with those found experimentally. The JET-ILW collector demonstrated a replacement of carbon by beryllium as the dominant deposit and additionally showed a reduction in the retained deuterium. The deposition on the JET-ILW collector was reduced by an order of magnitude relative to that on the JET-C collector, demonstrating the success of the ITER-like wall in the context of erosion and deposition.

Chapter 6 extended the analysis of Chapter 5 to rotating collectors located in the inner and outer divertor corners. In general, modelled and experimental deposition profiles showed good qualitative agreement, but this was only achieved in the JET-C outer divertor by neglecting deposition due to tile 6 strike points. Analysis of outer divertor quartz microbalances further indicated net deposition for tile 5 strike points, but net erosion for tile 6 strike points in JET-C.

The lack of deposition for tile 6 strike points in JET-C was explained via the high surface temperatures limiting carbon deposition and promoting thermally-driven chemical re-erosion. The different chemical properties of beryllium mean that it is not chemically eroded, resulting in net deposition occurring in the outer JET-ILW divertor for both tile 5 and tile 6 strike points (as observed from QMB results and inferred from the collector modelling). This resulted in a higher deposition rate in the JET-ILW outer divertor corner than in the inner divertor corner, contrasting with the higher JET-C inner corner depositions seen from both the rotating collectors and a multitude of previous studies. Thus, the reversal of deposition asymmetry was attributed to the different chemical properties of carbon and beryllium and the associated responses to elevated temperatures.

Chapter 7 presented results from Monte Carlo modelling of erosion, deposition and material transport in the JET-ILW outer divertor, incorporating processes such as sputtering, self-sputtering, reflection, ionisation and redeposition. The limited availability of beryllium impurities in JET-ILW and analysis of spectroscopy data suggested that the local beryllium surface coverages have a considerable impact on the erosion and deposition behaviour. The effects of modelling input parameters such as strike points, beryllium flux fractions, initial beryllium coverages and plasma temperatures/densities on the time-varying beryllium distributions and redistributions were presented and discussed. This modelling provides a way of analysing the distribution and redistribution of deposits due to various experimental conditions, which are otherwise difficult to diagnose.

In Chapter 8, Monte Carlo modelling was used to investigate results from rotating collectors, quartz microbalances and spectroscopy. The importance of different plasma parameters, surface conditions and strike point movements for outer corner beryllium deposition was discussed. Spectroscopy and modelling both demostrated the presence of initial peaks in the beryllium brightness at the start of the divertor phase. The effects of the modelled initial coverage and beryllium flux fraction on the peak magnitudes and timescales were investigated through a parameter scan. Experimental data analysis demonstrated the importance of the transition from the limiter to the divertor phase transiently increasing the impurity transport to the divertor. It additionally suggested that beryllium transport from the main chamber to the divertor during the limiter phase contributed to these initial peaks.

While this section has provided a summary of the material presented in previous chapters, the following section will identify and describe some of the most important features of this research in order to highlight their significance.

9.2 Key points

A selection of the most important results and methods of the current study is presented here for reference. Their relation to the current state of scientific knowledge and their significance in the context of furthering fusion research are also described.

Reduction in the deposition on rotating collectors by an order of magitude in JET-ILW relative to JET-C.

One of the key motivations for replacing the carbon plasma-facing materials of JET with beryllium and tungsten was the expectation of reductions in chemical erosion/sputtering, hopefully resulting in reduced inpurity deposition and fuel retention. The rotating collectors have shown a replacement of carbon by beryllium as the dominant deposit, as well as large reductions in impurity deposition and deuterium retention in these remote areas. This demonstrates the success of the ITER-like wall in terms of erosion, deposition and material migration and provides confidence of similar behaviour in ITER. Since JET-ILW is on the critical path for the success of ITER, several other studies have investigated remote deposition since the installation of the ITER-like wall and shown complementary results. These high-level ion beam analysis results from the collectors thus represent a confirmation of the results of other studies, but they are results that are crucial to be certain of for efficient and safe operation of ITER.

Exploitation of the rotating collector diagnostic and the data it provides.

The rotating collectors are a novel diagnostic developed, and solely used, at JET. They retain the benefits of surface science by enabling quantitative, species-specific measurements from different vessel locations, while adding a time-dependence that allows relation of changes in deposition to changing plasma conditions. An explanation of the working mechanism of the collectors and limited comparisons of results from two collectors to experimental conditions have previously been presented. However, prior to the current study, a detailed exploration and exploitation of the data generated from this diagnostic was lacking. The current study has made extensive use of the rotating collectors, allowing the understanding of erosion/deposition to be furthered. It has also demonstrated the considerable uses of the data from this diagnostic, enabling improved exploitation of the rotating collectors in continuing fusion research.

Reversal in deposition asymmetry between the inner and outer divertor corners.

Under ITER-like wall operation, the deposition in the outer divertor corner was determined to be greater than that in the inner divertor corner. This represents a departure from decades of carbon wall experience, during which inner divertor deposits dominated. It is important to gain an understanding of where deposits are likely to accumulate in ITER, not least because these impurity deposits generally have high levels of retained fuel. Other studies reported higher deposits in the outer divertor than in the inner divertor at similar times to the rotating collector results, but the significance of the results does not appear to have been stressed. As part of the current study, this reversal of deposition asymmetry was independently diagnosed and its importance as a result in itself was highlighted and discussed.

Explanation of differing distributions of deposits under ITER-like wall operation based on chemical and thermal effects.

The rotating collector results/modelling and QMB results suggested: i) a reversal in deposition asymmetry in the JET-ILW divertor and ii) a lack of outer divertor deposition in JET-C when the strike point was close to the outer corner. The greater susceptibility of carbon to chemical sputtering/erosion relative to beryllium, and the

temperature dependence of these chemical effects, are well known. However, the self-consistent explanation of the above results based on these chemical/thermal effects and strike point locations is a new contribution. The proposed explanantion represents one possible interpretation of the results, to which there may be other contributing factors that need further elucidation. Such other effects may be studied with the help of the experimental erosion/deposition results presented herein. The nature and degree of plasma-material interactions in tokamaks are strong functions of the compositions of the material surfaces. The understanding of the processes underpinning the differences in erosion/deposition between JET-C and JET-ILW, contributed to by these invesitigations, is vital for predicting the behaviour in further experiments and future tokamaks.

Use of empirical modelling techniques to describe erosion and deposition.

Incorporating experimental data into modelling efforts is a well-known technique, both within fusion research and in other fields. This has been exploited and extended in the current study through the new approach of incorporating data over whole campaigns to supplement the geometrical modelling of collector deposition. While Monte Carlo modelling is a popular approach for describing plasma-material interaction, this study had a greater focus than most on incorporating and comparing to experimental results. Additionally, there was a strong focus on the flexibility and efficiency of the model, especially as regards user modification. 'Empirical' modelling techniques similar to those applied here may be of considerable importance in studying erosion/deposition in tokamaks moving forwards. In particular, they provide a means of bridging the gap between the very small length and timescales relevant for atomistic erosion/deposition processes and the macroscopic erosion/deposition effects that manifest on the timescale of whole campaigns and are relevant for vessel longevity. The potential uses, and limitations, of such empirical modelling techniques have been explored and demonstrated in this study.

Importance of evolving surface composition for erosion and deposition processes.

It is well-known that the the nature and degree of plasma-material interaction processes is contingent on the composition of the relevant surfaces. Indeed, this was a key motivator for the transition from carbon to metal plasma-facing materials in JET. This study has furthered understanding of this area through investigations of the importance of beryllium coverage on divertor tile surfaces. Analysis of divertor spectroscopy, in combination with analytical calculations, enabled the importance of this coverage to be identified. It is clear that tungsten tiles with large beryllium coverages maximise sputtering of beryllium, but minimise beryllium reflection due to efficient Be-on-Be sticking. Conversely, low beryllium coverages minimise sputtering (since there is little beryllium to be sputtered), but maximise reflection from the bare tungsten tiles. These opposite dependencies weaken the overall dependence of beryllium ejection on surface coverage, but there remains an increasing beryllium reservoir on the tiles with increasing coverage that results in larger Be sources. Monte Carlo modelling has been used to demonstrate how different plasma conditions affect this distribution and redistribution of beryllium on surfaces and the importance of this for remote deposition. This modelling provides a flexible tool for analysing the evol-

ution of beryllium surface coverages. It has been used to investigate time-dependent effects such as how movements of the strike point can lead to increases in beryllium erosion due to the formation of beryllium reservoirs on surfaces.

Significance of limiter phase and initial divertor phase for impurity transport to remote areas.

The transport of beryllium from the main chamber to the divertor during the limiter phase has previously been inferred from spectroscopy and modelling using WallDyn. This knowledge was built on in the current study through investigation of the initial peaks in beryllium spectroscopy signals observed at the start of the divertor phase. Divertor spectroscopy and Monte Carlo modelling were used to develop understanding of the role of the initial beryllium coverage on tiles, the beryllium fraction in the incident deuterium flux and the transition from the limiter to the divertor phase. These analyses showed the significance of these features for contributing to deposition in remote areas. The investigation of the initial peaks is important in furthering understanding of what may be done to limit remote impurity deposition and fuel retention in ITER, which is crucial for safety and fuel efficiency.

This section has highlighted a subset of the most important results and methods presented in the current study. This research has furthered understanding of the different erosion/deposition behaviour in JET-C and JET-ILW, which is crucial for successful ITER operations and for progressing towards the goal of achieving net fusion energy. The following section will describe outstanding research that is imminent and/or desirable for improving the understanding of erosion, deposition and material migration further.

9.3 Outlook

The diagnostic that has been used most extensively in the current study is the rotating collector. These provide reliable, time-resolved deposition data in remote areas. However, the finite size of the collector discs and of the ion beam used to quantify deposits limits the pulse ranges that can be studied to ∼3,000 discharges. In the past, this has generally resulted in the deposition corresponding to discharges late in a campaign aggregating into a single large deposition peak, removing the time resolution over this period. It is desirable to be able to additionally measure the time-dependent deposition over these later discharges, especially since they often involve relatively high input powers or more advanced physics studies.

Recently, the rotating collectors have been redeveloped at JET in order to increase their operational lifetime. The previous iteration of the collector discs rotated only once about their axes, resulting in single bands of deposition around the discs. The new collectors rotate twice, producing two distinct bands of deposition on the discs and therefore greatly increasing the number of discharges that can be studied. After one full rotation, a mechanism shifts the position of a hole in the collector cover, preventing overlap of the two deposition bands. These new rotating collectors have been used in the most recent campaign; the increase in measurement capacity will

enable the relation of a greater range of discharges, and hence a greater range of plasma conditions, to their resultant depositions.

This increase in the number of discharges does not however affect the relatively poor time resolution of the rotating collectors. Resolution on the order of seconds is provided by the QMBs, but these have only been available for a limited number of discharges in recent campaigns. The vulnerability of electronics in the tokamak environment has led to a propensity for malfunction, which can only be addressed between campaigns. Successive efforts involving shielding and grounding of the relevant electronic components have aimed at improving the reliability of the QMBs.

It is hoped that it may become possible to operate the QMBs for a large fraction of the discharges of a campaign. This would offer benefits for relation to the rotating collector depositions and improve the statistics associated with relating deposition to different discharge types. The availibility of deposition data on the timescale of seconds for a large range of plasma conditions would be of great benefit for comparison to and benchmarking of modelling results. Through the application of plasma-material interaction codes such as ERO, this would enable improved predictive capabilities for erosion and deposition in future devices such as ITER.

In order to efficiently describe the long timescales relevant in erosion and deposition studies, there may also be a need to apply more empirical modelling approaches that can be flexible in accommodating different input plasma conditions and experimental data. This empirical modelling approach has been pursued in the current study and would benefit from further use and development in the future. It is planned that the geometrical modelling approach will be applied to the rotating collectors from the most recent campaign, the data for which was not yet available for the current study. The Monte Carlo model would benefit from relation to a greater range of experimental conditions and other modelling results. It has potential to be used as a scenario tool to aid planning and analysis of different experiments. Through parameterization of different reference discharge types it may be possible to describe beryllium migration over campaign-relevant timescales and to perform predictive studies.

An experiment of great significance to be performed at JET in the coming years is the deuterium-tritium (D-T) experiment. Current tokamaks generally use only deuterium fuel since it is cheaper and easier to work with radiologically. However, the D-T fuel mix replicates what will be used in future attempts at energy production. One of the major purposes of studying erosion and deposition in tokamaks is to understand and thereby restrict fuel retention. Tritium retention in remote areas must be strictly limited for reasons of fuel economy and radiological safety. Thus, the ability to study this with tritium, rather than the deuterium proxy, represents an opportunity of great significance and should reveal the impacts of any isotopic effects.

The previous D-T experiment in JET in 1997 resulted in large tritium deposits in remote areas of the JET-C divertor. Analysis of the corresponding retention with the all-metal wall of JET-ILW will provide a major feasibility study for future tokamak operations in ITER and beyond. The tritium retention is expected to be significantly reduced in this JET-ILW experiment relative to JET-C, as has been seen for the case of deuterium. Experimental verification of this is crucial given the potential implications of high fuel retention and the large investments involved.

JET will continue to act as an arena for the study of plasma physics, fusion technology and erosion/deposition in anticipation of ITER's completion. The similar geometries and identical plasma-facing materials make it ideal for this work and enable it to contribute to the efficient exploitation of ITER. ITER will provide an opportunity to study plasma-material interaction at higher powers, on a greater spatial scale and over longer timescales. Its ability to produce a significant net energy gain and to manage the erosion and deposition issues is critical for the realisation of power-to-grid fusion tokamaks of the future.

Appendices

Appendix A

Physical and chemical sputtering yields

A.1 Physical sputtering

The physical sputtering yields for target surfaces impacted by incident ions have been found to be well described by the empirical formulae proposed by Eckstein in [28], which were based on the earlier work of Bohdansky [29]. These formulae describe the yield as functions of ion species, target species, incident energy, incident angle and a series of physical quantities and material-dependent fitting parameters. They produce particularly close matches to modelling and experimental results at the relatively low incident energies that are most relevant for fusion devices. A summary and explanation of the calculations is provided here (for a full description see [28] and references therein). The physical sputtering yield $Y(E_0)$ for an incident ion with energy E_0 at normal incidence to a surface is given by

$$Y(E_0) = qS_n^{KrC}(\epsilon)\frac{\left(\frac{E_0}{E_{th}} - 1\right)^{\mu}}{\lambda + \left(\frac{E_0}{E_{th}} - 1\right)^{\mu}}. \tag{A.1}$$

The S_n^{KrC} parameter within this equation is the nuclear stopping power, given by

$$S_n^{KrC} = \frac{0.5ln(1 + 1.2288\epsilon)}{\epsilon + 0.1728\sqrt{\epsilon} + 0.008\epsilon^{0.1504}}, \tag{A.2}$$

With the reduced energy

$$\epsilon = E_0\frac{M_2}{M_1 + M_2}\frac{a_L}{Z_1 Z_2 e^2} \tag{A.3}$$

And the Lindhard screening length

$$a_L = \left(\frac{9\pi^2}{128}\right)^{1/3} a_B (Z_1^{2/3} + Z_2^{2/3})^{-1/2}, \tag{A.4}$$

which relates to the interatomic potential felt by the incident ion. In these equations, a_B is the Bohr radius, M_1 and M_2 are the atomic masses of the incident ions and target atoms and Z_1 and Z_2 are the atomic numbers of the incident ions and target atoms. The threshold energy above which physical sputtering occurs E_{th} and q, λ and μ are fitting parameters, which vary with the incident and target species and are obtained through a Bayesian statistical analysis. The sputtering yield also varies with the incident angle of the ion relative to the surface normal α. This generalised sputtering yield is given by

$$Y(E_0, \alpha) = Y(E_0, 0) \left\{ \cos\left[\left(\frac{\alpha}{\alpha_0} \frac{\pi}{2} \right)^c \right] \right\}^{-f} \exp\left(b \left\{ 1 - 1/\cos\left[\left(\frac{\alpha}{\alpha_0} \frac{\pi}{2} \right)^c \right] \right\} \right), \tag{A.5}$$

Where c, f and b are fitting parameters. The α_0 parameter describes the refraction towards the surface normal due to the ion experiencing a binding energy E_{sp} and is given by

$$\alpha_0 = \pi - \arccos\left(\sqrt{\frac{1}{1 + E_0/E_{sp}}} \right). \tag{A.6}$$

Listings of the fitting parameters and comparisons to experimental/modelling results are available in [30]. In the current study, these equations are used to describe the physical sputtering yields of beryllium target surfaces due to impact by deuterium or beryllium ions.

A.2 Chemical sputtering and erosion

For carbon PFCs, chemical erosion and sputtering processes are also significant, introducing additional dependences on substrate temperature and incident ion flux. This section provides a summary of the calculations performed for carbon erosion, which follows the analysis in [32] (and references therein). This description includes a treatment of the erosion of weakly bound surface hydrocarbons from hydrogenated amorphous carbon films. The total sputtering yield Y_{tot} is given by the sum of the separate contributions:

$$Y_{tot} = Y_{phys} + Y_{therm}(1 + DY_{dam}) + Y_{surf}. \tag{A.7}$$

The physical sputtering yield Y_{phys} is similar to that described in the previous section. Y_{therm} is the thermally-activated chemical erosion process that occurs due to the reaction of thermal hydrogen isotopes with carbon surface atoms. This is enhanced by radiation damage since this breaks carbon-carbon bonds and thus provides additional reaction sites for hydrogen isotopes. D is a constant that depends on the

particular hydrogen isotope being considered and Y_{dam} is the radiation damage yield (i.e. the damage production rate). Y_{surf} is the yield associated with the low-energy sputtering of weakly bound surface hydrocarbons.

For an incident ion flux Φ, the thermal chemical erosion yield is given by

$$Y_{therm} = c^{sp^3} \frac{0.033 \exp\left(-E_{therm}/kT\right)}{2 \times 10^{-32}\Phi + \exp\left(-E_{therm}/kT\right)}, \tag{A.8}$$

Where c^{sp^3} describes the concentration of weakly bound sp^3 hydrocarbons and is given by

$$c^{sp^3} = C \frac{2 \times 10^{-32}\Phi + \exp\left(-E_{therm}/kT\right)}{2 \times 10^{-32}\Phi + \left[1 + \frac{2\times10^{29}}{\Phi} \exp\left(-E_{rel}/kT\right)\right] exp\left(-E_{therm}/kT\right)}. \tag{A.9}$$

The factor C reduces the chemical erosion yield at high ion fluxes:

$$C = \frac{1}{1 + (\Phi/6 \times 10^{21})^{0.54}} \tag{A.10}$$

And E_{therm} and E_{rel} are activation energies for chemical erosion and thermal hydrogen release. The Boltzmann constant is represented as k and T is the substrate temperature. The radiation damage yield Y_{dam} takes a similar form to the physical sputtering yield described in the previous section. The chemical sputtering yield Y_{surf} is given by

$$Y_{surf}(E_0, T) = c^{sp^3} Q S_n(E_0) \frac{\left[1 - \left(\frac{E_{des}}{E_0}\right)^{2/3}\right]\left(1 - \frac{E_{des}}{E_0}\right)^2}{1 + \exp\left(\frac{E_0 - 65eV}{40eV}\right)}, \tag{A.11}$$

Where Q depends on the hydrogen isotope, $S_n(E_0)$ is a nuclear stopping power similar to that used in the previous section and E_{des} is the activation energy for near-surface desorption. The denominator restricts the chemical sputtering to near-surface, low-energy processes. Further discussion of these formulae and listings of fitting parameters are provided in [30]. In the current study, these equations are used to calculate the total sputtering yield for carbon erosion from PFCs.

Glossary

A non-exhaustive definitions list covering some of the most important terms and acronyms as they are used in this report is provided here for reference. Further information is available in the relevant sections of the main text.

Campaign A period of operations on a tokamak during which a series of experiments are conducted. Campaigns typically last from several months to a year and comprise thousands of discharges. Between campaigns, there are shutdown or intervention periods when there are no experiments conducted and in-vessel components may be accessed and replaced.

Discharge A single period of approximately 20 - 30 s (for JET) during which plasma is generated and studied inside the tokamak. Thousands of discrete discharges make up a campaign. A discharge often comprises a limiter phase and a divertor phase, when the dominant areas of plasma-wall interaction are at the limiters and the divertor respectively.

Divertor A region of a tokamak located at the bottom (and/or top) of the vessel. In the divertor phase, the magnetic topology is be altered to induce the majority of the plasma-material interaction to occur in this region. Its distant location from the main chamber reduces the chances of sputtered impurities reaching the core plasma. The inner divertor is the side closest to the centre of the tokamak; the outer divertor is the side located closer to the extreme edge of the tokamak.

ELMs Edge-Localised Modes are quasi-periodic instabilities that occur in the edge region of tokamak plasmas. They result in large fluxes of heat and particles being incident on the vessel walls over short timescales.

Fusion The combination of light atomic nuclei to form a heavier nucleus and a net release of energy. Most terrestrial attempts at achieving fusion for energy generation use deuterium and tritium reactants, which fuse to make helium and a neutron.

IBA Ion Beam Analysis comprises a range of diagnostic techniques that probe the constituents or structures of material surfaces using high-energy ion beams. Such techniques offer highly sensitive, species-specific measurements through the interaction of the ions with constituents of the surfaces on the atomic scale.

ITER The International Thermonuclear Experimental Reactor is a fusion tokamak currently under construction in Cadarache, France. It has dimensions approximately double that of JET in every dimension and is expected to produce net energy from fusion for the first time.

ICRH Ion Cyclotron Resonance Heating launches electromagnetic waves into the plasma. These electromagnetic waves have frequencies comparable to the frequencies of ion orbits around magnetic field lines, resulting in energy transfer to the plasma.

JET The Joint European Torus is currently the world's largest and most powerful fusion tokamak. It is located at Culham Centre for Fusion Energy and used collectively by European fusion laboratories to further fusion research.

JET-C The JET tokamak as it was until 2010, with carbon fibre composite plasma-facing materials. It has become clear that the retention of fuel these carbon vessel walls allow would be unacceptably high in power plant scale fusion reactors.

JET-ILW The JET tokamak as it has been since 2010, with beryllium plasma-facing materials in the main chamber and tungsten plasma-facing materials in the divertor. This vessel wall is known as the ITER-like wall, since it mimics the materials to be used in ITER (though on a smaller scale).

Limiter A solid material projection of the main chamber vessel wall into the tokamak plasma. In the limiter phase, the majority of the plasma-material interaction occurs at the limiters, which can cause impurity contamination of the core plasma.

Main chamber A region comprising the majority of the volume of a tokamak, where the core plasma and the majority of the fusion reactions are located. The quasi-elliptical poloidal cross-section of JET consists of the main chamber region located above the divertor region.

NRA Nuclear Reaction Analysis is a particular technique within the field of ion beam analysis. It relies on incident ions undergoing nuclear reactions with nuclei in the surface regions of materials, which results in the ejection of reaction products with energies characteristic of the constituents of these material surfaces.

PFCs Plasma-Facing Components are material surfaces that are subject to plasma-material interaction due to their location in the vessel walls of tokamaks. They thus provide the basis for the study of erosion, deposition and material migration in tokamaks.

Plasma A plasma is an ionised gas comprising a quasineutral ensemble of ions and electrons that exhibit collective effects. Significant fusion cross-sections are only achieved by heating the reactants to very high temperatures, whereby they exist in the plasma state.

Poloidal In a tokamak, the poloidal plane is identified by taking a cross-section of the torus at a location around its toroidal extent. The approximate toroidal symmetry of tokamaks means that many phenomena can be considered largely by looking at a single poloidal plane. The polodail cross-section of a tokamak is quasi-elliptical in shape.

QMBs Quartz Microbalances are used to measure small-scale erosion and deposition on surfaces. A vibrating quartz crystal has a resonant frequency that changes when material is added or removed from its surface. By monitoring

the frequency, and subtracting the effects of changing temperatures, the erosion or deposition may be determined.

RBS Rutherford Backscattering Spectrometry is a form of ion beam analysis. Ions undergo Coulombic collisions with the nuclei of material surfaces and their reflected energies are measured. These energies depend on the masses of the surface nuclei, allowing their species to be determined.

SOL The Scrape Off Layer is a region of a tokamak plasma exterior to the core plasma. It has open field lines and represents the source of much of the heat and particle flux to plasma-facing components. Transport within the SOL is predominantly convective along field lines, in contrast to the diffusive transport across field lines that is prevalent in most of the plasma.

Sputtering yield The ratio of the average number of ejected atoms from a material surface to the number of ions incident on that surface. This can depend on the incident ion species, angle and flux, the atom species and the surface temperature. Physical, chemical and thermal effects can contribute to the sputtering yield.

Strike point The strike points are the locations in the inner and outer divertor where large heat and particle fluxes from the SOL are incident on the divertor surfaces. The locations of these strike points for different plasma conditions can strongly affect the erosion, deposition and material migration characteristics.

SXB SXBs give the number of ionisations per photon for impurity influxes from surfaces. They are used to relate spectroscopic measurements to the real number of ions of a particular species ejected from a surface. They are calculated through atomic physics modelling and depend on the plasma temperature and density.

Toroidal In a tokamak, the toroidal direction is pointed 'the long way' around the torus, passing through poloidal cross-sections of the tokamak.

Tokamak A tokamak is a toroidal chamber with magnetic coils. The plasma is magnetically confined around field lines that pass around the tokamak with helical orientations. Tokamaks represents the most industrially developed configuration for generating fusion energy.

X-point The X-point is a region of zero poloidal magnetic field in the divertor configuration of a tokamak plasma. In the poloidal plane, this represents the location where the inner and outer SOL intersect close to the strike points in the divertor.

Bibliography

[1] United Nations Department of Economic and Social Affairs: Population Division, "World population prospects: The 2015 revision - key findings and advance tables," tech. rep., 2015.

[2] International Energy Agency, "World energy outlook 2014: Executive summary," tech. rep., 2014.

[3] United Nations Development Programme, "Human development report 2015," tech. rep., 2015.

[4] B. Dale, "Growing poor slowly: why we must have renewable energy," 2014. Available from: http://www.ourenergypolicy.org/growing-poor-slowly-why-we-must-have-renewable-energy/, accessed September 2015.

[5] S. Shafiee and E. Topal, "When will fossil fuel reserves be diminished?," *Energy Policy*, vol. 37, no. 1, pp. 181 – 189, 2009.

[6] Intergovernmental Panel on Climate Change, "Climate change 2013: The physical science basis," tech. rep., 2013.

[7] Eurofusion, "JET technology: Magnets," 2014. Accessed September 2015.

[8] J. Wesson, *Tokamaks*, vol. 149. Oxford University Press, 2011.

[9] EFDA: European Fusion Development Agreement, "Limiters and divertors," 2011. Accessed August 2013.

[10] Lorne Horton, "JET forward programme and opportunities for collaboration." Presentation, FESAC strategic planning panel, Maryland, US, July 2014. Accessed September 2015.

[11] J. Coad, J. Likonen, M. Rubel, E. Vainonen-Ahlgren, D. Hole, T. Sajavaara, T. Renvall, G. Matthews, and JET EFDA Contributors, "Overview of material re-deposition and fuel retention studies at JET with the Gas Box divertor," *Nuclear Fusion*, vol. 46, no. 2, p. 350, 2006.

[12] G. F. Matthews, M. Beurskens, S. Brezinsek, M. Groth, E. Joffrin, A. Loving, M. Kear, M. L. Mayoral, R. Neu, P. Prior, *et al.*, "JET ITER-like wall - overview and experimental programme," *Physica Scripta*, vol. 2011, no. T145, p. 014001, 2011.

[13] V. Philipps, R. Neu, J. Rapp, U. Samm, M. Tokar, T. Tanabe, and M. Rubel, "Comparison of tokamak behaviour with tungsten and low-Z plasma facing materials," *Plasma Physics and Controlled Fusion*, vol. 42, no. 12B, p. B293, 2000.

[14] R. V. Jensen, D. Post, W. Grasberger, C. Tarter, and W. Lokke, "Calculations of impurity radiation and its effects on tokamak experiments," *Nuclear Fusion*, vol. 17, no. 6, p. 1187, 1977.

[15] M. Greenwald, J. L. Terry, S. M. Wolfe, S. Ejima, M. G. Bell, S. M. Kaye, and G. H. Neilson, "A new look at density limits in tokamaks," *Nuclear Fusion*, vol. 28, no. 12, p. 2199, 1988.

[16] M. Rubel, T. Tanabe, V. Philipps, B. Emmoth, A. Kirschner, J. Von Seggern, and P. Wienhold, "Graphite–tungsten twin limiters in studies of material mixing processes on high heat flux components," *Journal of nuclear materials*, vol. 283, pp. 1089–1093, 2000.

[17] R. Doerner, M. Baldwin, and R. Causey, "Beryllium–tungsten mixed-material interactions," *Journal of nuclear materials*, vol. 342, no. 1, pp. 63–67, 2005.

[18] J. P. Coad, P. L. Andrew, and A. T. Peacock, "Carbon deposition and hydrogen isotope retention in JET," *Physica Scripta*, vol. 1999, no. T81, p. 7, 1999.

[19] R. D. Monk, C. H. Amiss, H. Y. Guo, G. F. Matthews, G. M. McCracken, and M. F. Stamp, "The behaviour of the apparent chemical sputtering yield in the JET tokamak," *Physica Scripta*, vol. 1999, no. T81, p. 54, 1999.

[20] S. Brezinsek, M. F. Stamp, D. Nishijima, D. Borodin, S. Devaux, K. Krieger, S. Marsen, M. O'Mullane, C. Bjoerkas, A. Kirschner, *et al.*, "Study of physical and chemical assisted physical sputtering of beryllium in the JET ITER-like wall," *Nuclear Fusion*, vol. 54, no. 10, p. 103001, 2014.

[21] G. J. Van Rooij, J. W. Coenen, L. Aho-Mantila, S. Brezinsek, M. Clever, R. Dux, M. Groth, K. Krieger, S. Marsen, G. F. Matthews, *et al.*, "Tungsten divertor erosion in all metal devices: Lessons from the ITER like wall of JET," *Journal of Nuclear Materials*, vol. 438, pp. S42–S47, 2013.

[22] Y. Hirooka, R. W. Conn, T. Sketchley, W. K. Leung, G. Chevalier, R. Doerner, J. Elverum, D. M. Goebel, G. Gunner, M. Khandagle, *et al.*, "A new plasma-surface interactions research facility: PISCES-B and first materials erosion experiments on bulk-boronized graphite," *Journal of Vacuum Science & Technology A*, vol. 8, no. 3, pp. 1790–1797, 1990.

[23] B. de Groot, Z. Ahmad, R. P. Dahiya, R. Engeln, W. J. Goedheer, N. J. Lopes Cardozo, and V. Veremiyenko, "Magnum-psi, a new linear plasma generator for plasma-surface interaction studies in ITER relevant conditions," *Fusion engineering and design*, vol. 66, pp. 413–417, 2003.

[24] R. Doerner, A. Grossman, S. Luckhardt, R. Seraydarian, F. Sze, D. Whyte, and R. Conn, "Response of beryllium to deuterium plasma bombardment," *Journal of nuclear materials*, vol. 257, no. 1, pp. 51–58, 1998.

[25] J. P. Biersack and W. Eckstein, "Sputtering studies with the Monte Carlo program TRIM. SP," *Applied Physics A*, vol. 34, no. 2, pp. 73–94, 1984.

[26] W. Takeuchi and Y. Yamamura, "Computer studies of the energy spectra and reflection coefficients of light ions," *Radiation Effects*, vol. 71, no. 1-2, pp. 53–64, 1983.

[27] M. T. Robinson and I. M. Torrens, "Computer simulation of atomic-displacement cascades in solids in the binary-collision approximation," *Physical Review B*, vol. 9, no. 12, p. 5008, 1974.

[28] W. Eckstein and R. Preuss, "New fit formulae for the sputtering yield," *Journal of nuclear materials*, vol. 320, no. 3, pp. 209–213, 2003.

[29] J. Bohdansky, "A universal relation for the sputtering yield of monatomic solids at normal ion incidence," *Nuclear Instruments and Methods in Physics Research Section B: Beam Interactions with Materials and Atoms*, vol. 2, no. 1, pp. 587–591, 1984.

[30] R. Behrisch and W. Eckstein, *Sputtering by particle bombardment: experiments and computer calculations from threshold to MeV energies*, vol. 110. Springer, 2007.

[31] J. Roth, J. Bohdansky, W. Poschenrieder, and M. K. Sinha, "Physical and chemical sputtering of graphite and SiC by hydrogen and helium in the energy range of 600 to 7500 ev," *Journal of Nuclear Materials*, vol. 63, pp. 222–229, 1976.

[32] J. Roth and C. Garcia-Rosales, "Analytic description of the chemical erosion of graphite by hydrogen ions," *Nuclear Fusion*, vol. 36, no. 12, p. 1647, 1996.

[33] J. Roth, "Chemical erosion of carbon based materials in fusion devices," *Journal of nuclear materials*, vol. 266, pp. 51–57, 1999.

[34] J. Roth, R. Preuss, W. Bohmeyer, S. Brezinsek, A. Cambe, E. Casarotto, R. Doerner, E. Gauthier, G. Federici, S. Higashijima, *et al.*, "Flux dependence of carbon chemical erosion by deuterium ions," *Nuclear fusion*, vol. 44, no. 11, p. L21, 2004.

[35] A. Widdowson, C. Ayres, S. Booth, J. Coad, A. Hakola, K. Heinola, D. Ivanova, S. Koivuranta, J. Likonen, M. Mayer, and M. Stamp, "Comparison of JET main chamber erosion with dust collected in the divertor," *Journal of Nuclear Materials*, vol. 438, Supplement, no. 0, pp. S827 – S832, 2013. Proceedings of the 20th International Conference on Plasma-Surface Interactions in Controlled Fusion Devices.

[36] K. Heinola, C. F. Ayres, A. Baron-Wiechec, J. P. Coad, J. Likonen, G. F. Matthews, A. Widdowson, and JET-EFDA contributors, "Tile profiling analysis of samples from the JET ITER-like wall and carbon wall," *Physica Scripta*, vol. 2014, no. T159, p. 014013, 2014.

[37] A. Widdowson, E. Alves, C. F. Ayres, A. Baron-Wiechec, S. Brezinsek, N. Catarino, J. P. Coad, K. Heinola, J. Likonen, G. F. Matthews, *et al.*, "Material migration patterns and overview of first surface analysis of the JET ITER-like wall," *Physica Scripta*, vol. 2014, no. T159, p. 014010, 2014.

[38] D. G. Whyte, J. P. Coad, P. Franzen, and H. Maier, "Similarities in divertor erosion/redeposition and deuterium retention patterns between the tokamaks ASDEX Upgrade, DIII-D and JET," *Nuclear Fusion*, vol. 39, no. 8, p. 1025, 1999.

[39] J. P. Coad, S. Gruenhagen, D. E. Hole, A. Hakola, S. Koivuranta, J. Likonen, M. Rubel, A. Widdowson, *et al.*, "Overview of JET post-mortem results follow-

ing the 2007–9 operational period, and comparisons with previous campaigns," *Physica Scripta*, vol. 2011, no. T145, p. 014003, 2011.

[40] A. Widdowson, S. Brezinsek, J. P. Coad, D. E. Hole, J. Likonen, V. Philipps, M. Rubel, M. F. Stamp, *et al.*, "An overview of erosion–deposition studies for the JET Mk II high delta divertor," *Physica Scripta*, vol. 2009, no. T138, p. 014005, 2009.

[41] J. P. Coad, N. Bekris, J. D. Elder, S. K. Erents, D. E. Hole, K. D. Lawson, G. F. Matthews, R.-D. Penzhorn, and P. C. Stangeby, "Erosion/deposition issues at JET," *Journal of nuclear materials*, vol. 290, pp. 224–230, 2001.

[42] J. P. Coad, E. Alves, N. P. Barradas, A. Baron-Wiechec, N. Catarino, K. Heinola, J. Likonen, M. Mayer, G. F. Matthews, P. Petersson, *et al.*, "Surface analysis of tiles and samples exposed to the first JET campaigns with the ITER-like wall," *Physica Scripta*, vol. 2014, no. T159, p. 014012, 2014.

[43] M. Rubel, J. P. Coad, A. Widdowson, G. F. Matthews, H. G. Esser, T. Hirai, J. Likonen, J. Linke, C. P. Lungu, M. Mayer, *et al.*, "Overview of erosion–deposition diagnostic tools for the ITER-like wall in the JET tokamak," *Journal of Nuclear Materials*, vol. 438, pp. S1204–S1207, 2013.

[44] J. P. Coad, D. E. Hole, E. Kolodinska, J. Likonen, S. Lindig, G. F. Matthews, M. Mayer, V. Philipps, V. Riccardo, and A. Widdowson, "Testing of tungsten coatings in JET for the ITER-like wall," *Journal of Nuclear Materials*, vol. 390, pp. 992–995, 2009.

[45] H. Bergsåker, B. Emmoth, P. Petersson, G. Possnert, J. Coad, J. Likonen, and T. Renvall, "Nuclear reaction analysis with ion microbeam of cross sections of surface layers deposited in a tokamak divertor," *Journal of nuclear materials*, vol. 362, no. 2, pp. 215–221, 2007.

[46] P. Petersson, G. Possnert, M. Rubel, T. Dittmar, B. Pégourié, E. Tsitrone, and E. Wessel, "An overview of nuclear micro-beam analysis of surface and bulk fuel retention in carbon-fibre composites from Tore Supra," *Journal of Nuclear Materials*, vol. 415, no. 1, pp. S761–S764, 2011.

[47] H. Bergsåker, I. Bykov, P. Petersson, G. Possnert, J. Likonen, S. Koivuranta, J. Coad, and A. Widdowson, "Microstructure and inhomogeneous fuel trapping at divertor surfaces in the JET tokamak," *Nuclear Instruments and Methods in Physics Research Section B: Beam Interactions with Materials and Atoms*, vol. 332, pp. 266 – 270, 2014. 21st International Conference on Ion Beam Analysis.

[48] H. Bergsåker, I. Bykov, P. Petersson, G. Possnert, J. Likonen, S. Koivuranta, J. Coad, W. V. Renterghem, I. Uytdenhouwen, and A. Widdowson, "Microscopically nonuniform deposition and deuterium retention in the divertor in JET with ITER-like wall," *Journal of Nuclear Materials*, vol. 463, pp. 956 – 960, 2015. Proceedings of the 21st International Conference on Plasma-Surface Interactions in Controlled Fusion Devices Kanazawa, Japan May 26-30, 2014.

[49] G. Giruzzi, R. Abgrall, L. Allegretti, J. Ané, P. Angelino, T. Aniel, A. Argouarch, J. Artaud, S. Balme, V. Basiuk, P. Bayetti, A. Bécoulet, M. Bécoulet, L. Begrambekov, M. Benkadda, F. Benoit, G. Berger-by, B. Bertrand, P. Beyer,

J. Blum, D. Boilson, H. Bottollier-Curtet, C. Bouchand, F. Bouquey, C. Bourdelle, F. Brémond, S. Brémond, C. Brosset, J. Bucalossi, Y. Buravand, P. Cara, S. Carpentier, A. Casati, O. Chaibi, M. Chantant, P. Chappuis, M. Chatelier, G. Chevet, D. Ciazynski, G. Ciraolo, F. Clairet, J. Clary, L. Colas, Y. Corre, X. Courtois, N. Crouseilles, G. Darmet, M. Davi, R. Daviot, H. D. Esch, J. Decker, P. Decool, E. Delchambre, E. Delmas, L. Delpech, C. Desgranges, P. Devynck, L. Doceul, N. Dolgetta, D. Douai, H. Dougnac, J. Duchateau, R. Dumont, G. Dunand, A. Durocher, A. Ekedahl, D. Elbeze, L. Eriksson, A. Escarguel, F. Escourbiac, F. Faisse, G. Falchetto, M. Farge, J. Farjon, N. Fedorczak, C. Fenzi-Bonizec, X. Garbet, J. Garcia, J. Gardarein, L. Gargiulo, P. Garibaldi, E. Gauthier, A. Géraud, T. Gerbaud, M. Geynet, P. Ghendrih, C. Gil, M. Goniche, V. Grandgirard, C. Grisolia, G. Gros, A. Grosman, R. Guigon, D. Guilhem, B. Guillerminet, R. Guirlet, J. Gunn, S. Hacquin, J. Hatchressian, P. Hennequin, D. Henry, C. Hernandez, P. Hertout, S. Heuraux, J. Hillairet, G. Hoang, S. Hong, C. Honore, J. Hourtoule, M. Houry, T. Hutter, P. Huynh, G. Huysmans, F. Imbeaux, E. Joffrin, J. Johner, J. Journeaux, F. Jullien, F. Kazarian, M. Kočan, B. Lacroix, V. Lamaison, J. Lasalle, G. Latu, Y. Lausenaz, C. Laviron, C. L. Niliot, M. Lennholm, F. Leroux, F. Linez, M. Lipa, X. Litaudon, T. Loarer, F. Lott, P. Lotte, J. Luciani, H. Lütjens, A. Macor, S. Madeleine, P. Magaud, P. Maget, R. Magne, L. Manenc, Y. Marandet, G. Marbach, J. Maréchal, C. Martin, V. Martin, A. Martinez, J. Martins, R. Masset, D. Mazon, L. Meunier, O. Meyer, L. Million, M. Missirlian, R. Mitteau, P. Mollard, V. Moncada, P. Monier-Garbet, D. Moreau, P. Moreau, M. Nannini, E. Nardon, H. Nehme, C. Nguyen, S. Nicollet, M. Ottaviani, D. Pacella, S. Pamela, T. Parisot, H. Parrat, P. Pastor, A. Pecquet, B. Pégourié, V. Petrzilka, Y. Peysson, C. Portafaix, M. Prou, N. Ravenel, R. Reichle, C. Reux, P. Reynaud, M. Richou, F. Rigollet, F. Rimini, H. Roche, S. Rosanvallon, J. Roth, P. Roubin, R. Sabot, F. Saint-Laurent, S. Salasca, T. Salmon, F. Samaille, A. Santagiustina, B. Saoutic, Y. Sarazin, J. Schlosser, K. Schneider, M. Schneider, F. Schwander, J. Ségui, J. Signoret, A. Simonin, S. Song, E. Sonnendruker, P. Spuig, L. Svensson, P. Tamain, M. Tena, J. Theis, M. Thonnat, A. Torre, J. Travére, E. Trier, E. Tsitrone, F. Turco, J. Vallet, A. Vatry, L. Vermare, F. Villecroze, D. Villegas, D. Voyer, K. Vulliez, W. Xiao, D. Yu, L. Zani, X. Zou, and W. Zwingmann, "Investigation of steady-state tokamak issues by long pulse experiments on Tore Supra," *Nuclear Fusion*, vol. 49, no. 10, p. 104010, 2009.

[50] B. Pégourié, C. Brosset, E. Tsitrone, A. Beauté, S. Brémond, J. Bucalossi, S. Carpentier, Y. Corre, E. Delchambre, C. Desgranges, *et al.*, "Overview of the deuterium inventory campaign in Tore Supra: Operational conditions and particle balance," *Journal of Nuclear Materials*, vol. 390, pp. 550–555, 2009.

[51] J. Roth, E. Tsitrone, T. Loarer, V. Philipps, S. Brezinsek, A. Loarte, G. F. Counsell, R. P. Doerner, K. Schmid, O. V. Ogorodnikova, and R. A. Causey, "Tritium inventory in ITER plasma-facing materials and tritium removal procedures," *Plasma Physics and Controlled Fusion*, vol. 50, no. 10, p. 103001, 2008.

[52] M. Shimada, R. Pitts, S. Ciattaglia, S. Carpentier, C. Choi, G. D. Orco, T. Hirai, A. Kukushkin, S. Lisgo, J. Palmer, *et al.*, "In-vessel dust and tritium control strategy in ITER," *Journal of Nuclear Materials*, vol. 438, pp. S996–

S1000, 2013.

[53] T. Loarer, C. Brosset, J. Bucalossi, P. Coad, H. G. Esser, J. Hogan, J. Likonen, M. Mayer, P. Morgan, V. Philipps, V. Rohde, J. Roth, M. Rubel, E. Tsitrone, A. Widdowson, and JET EFDA contributors, "Gas balance and fuel retention in fusion devices," *Nuclear Fusion*, vol. 47, no. 9, p. 1112, 2007.

[54] E. Tsitrone, C. Brosset, B. Pégourié, E. Gauthier, J. Bouvet, J. Bucalossi, S. Carpentier, Y. Corre, E. Delchambre, L. Desgranges, T. Dittmar, D. Douai, A. Ekedahl, A. Escarguel, P. Ghendrih, C. Grisolia, A. Grosman, J. Gunn, S. Hong, W. Jacob, F. Kazarian, M. Kocan, H. Khodja, F. Linez, T. Loarer, Y. Marandet, A. Martinez, M. Mayer, O. Meyer, P. M. Garbet, P. Moreau, J. Pascal, B. Pasquet, F. Rimini, H. Roche, I. Roure, S. Rosanvallon, P. Roubin, J. Roth, F. Saint-Laurent, F. Samaille, and S. Vartanian, "Deuterium inventory in Tore Supra: reconciling particle balance and post-mortem analysis," *Nuclear Fusion*, vol. 49, no. 7, p. 075011, 2009.

[55] T. Dittmar, E. Tsitrone, B. Pégourié, I. Čadež, P. Pelicon, E. Gauthier, P. Languille, J. Likonen, A. Litnovsky, S. Markelj, C. Martin, M. Mayer, J.-Y. Pascal, C. Pardanaud, V. Philipps, J. Roth, P. Roubin, and P. Vavpetič, "Deuterium Inventory in Tore Supra (DITS): 2nd post-mortem analysis campaign and fuel retention in the gaps," *Journal of Nuclear Materials*, vol. 415, no. 1, Supplement, pp. S757 – S760, 2011. Proceedings of the 19th International Conference on Plasma-Surface Interactions in Controlled Fusion.

[56] T. Dittmar, P. Roubin, E. Tsitrone, E. Gauthier, A. Hakola, J. Likonen, F. Linez, C. Martin, M. Mayer, C. Pardanaud, J. Y. Pascal, B. Pasquet, B. Pégourié, J. Roth, I. Roure, and R. Ruffe, "Deuterium Inventory in Tore Supra: status of post-mortem analyses," *Physica Scripta*, vol. 2009, no. T138, p. 014027, 2009.

[57] Y. Gotoh, J. Yagyu, K. Masaki, K. Kizu, A. Kaminaga, K. Kodama, T. Arai, T. Tanabe, and N. Miya, "Analyses of erosion and re-deposition layers on graphite tiles used in the W-shaped divertor region of JT-60U," *Journal of Nuclear Materials*, vol. 313-316, pp. 370 – 376, 2003. Plasma-Surface Interactions in Controlled Fusion Devices 15.

[58] Y. Oya, Y. Hirohata, T. Tanabe, T. Shibahara, H. Kimura, M. Oyaidzu, T. Arai, K. Masaki, Y. Gotoh, K. Okuno, N. Miya, T. Hino, and S. Tanaka, "Hydrogen isotope distributions and retentions in the inner divertor tile of JT-60U," *Fusion Engineering and Design*, vol. 75-79, pp. 945 – 949, 2005. Proceedings of the 23rd Symposium of Fusion Technology - SOFT 23.

[59] Y. Gotoh, T. Tanabe, Y. Ishimoto, K. Masaki, T. Arai, H. Kubo, K. Tsuzuki, and N. Miya, "Long-term erosion and re-deposition of carbon in the divertor region of JT-60U," *Journal of Nuclear Materials*, vol. 357, no. 1-3, pp. 138 – 146, 2006.

[60] T. Tanabe, K. Masaki, K. Sugiyama, and M. Yoshida, "An overview of recent erosion/deposition and hydrogen retention studies in JT-60U," *Physica Scripta*, vol. 2009, no. T138, p. 014006, 2009.

[61] K. Heinola, A. Widdowson, J. Likonen, E. Alves, A. Baron-Wiechec, N. Barradas, S. Brezinsek, N. Catarino, P. Coad, S. Koivuranta, *et al.*, "Fuel retention

in JET ITER-like wall from post-mortem analysis," *Journal of Nuclear Materials*, 2014.

[62] J. Linke, R. Duwe, A. Gervash, R. Qian, M. Rödig, and A. Schuster, "Material damage to beryllium, carbon, and tungsten under severe thermal shocks," *Journal of nuclear materials*, vol. 258, pp. 634–639, 1998.

[63] C. H. Skinner and G. Federici, "Is carbon a realistic choice for ITER's divertor?," *Physica Scripta*, vol. 2006, no. T124, p. 18, 2006.

[64] J. Winter, "A comparison of tokamak operation with metallic getters (Ti, Cr, Be) and boronization," *Journal of Nuclear Materials*, vol. 176, pp. 14–31, 1990.

[65] D. Naujoks, K. Asmussen, M. Bessenrodt-Weberpals, S. Deschka, R. Dux, W. Engelhardt, A. Field, G. Fussmann, J. Fuchs, C. Garcia-Rosales, *et al.*, "Tungsten as target material in fusion devices," *Nuclear fusion*, vol. 36, no. 6, p. 671, 1996.

[66] J. Coenen, V. Philipps, S. Brezinsek, B. Bazylev, A. Kreter, T. Hirai, M. Laengner, T. Tanabe, Y. Ueda, U. Samm, *et al.*, "Analysis of tungsten melt-layer motion and splashing under tokamak conditions at TEXTOR," *Nuclear fusion*, vol. 51, no. 8, p. 083008, 2011.

[67] S. Takamura, N. Ohno, D. Nishijima, and S. Kajita, "Formation of nanostructured tungsten with arborescent shape due to helium plasma irradiation," *Plasma and fusion research*, vol. 1, pp. 051–051, 2006.

[68] V. Philipps, "Tungsten as material for plasma-facing components in fusion devices," *Journal of nuclear materials*, vol. 415, no. 1, pp. S2–S9, 2011.

[69] A. Von Keudell, C. Hopf, T. Schwarz-Selinger, and W. Jacob, "Surface loss probabilities of hydrocarbon radicals on amorphous hydrogenated carbon film surfaces: Consequences for the formation of re-deposited layers in fusion experiments," *Nuclear Fusion*, vol. 39, no. 10, p. 1451, 1999.

[70] M. Mayer, V. Rohde, *et al.*, "Further insight into the mechanism of hydrocarbon layer formation below the divertor of ASDEX Upgrade," *Nuclear fusion*, vol. 46, no. 11, p. 914, 2006.

[71] M. Mayer, A. von Keudell, V. Rohde, P. Coad, and JET-EFDA contributors, "Mechanism of hydrocarbon layer formation in remote areas of fusion devices," in *30th EPS Conference on Controlled Fusion and Plasma Physics*, vol. 27, 2003.

[72] S. Krat, Y. Gasparyan, A. Pisarev, M. Mayer, U. von Toussaint, P. Coad, A. Widdowson, *et al.*, "Hydrocarbon film deposition inside cavity samples in remote areas of the JET divertor during the 1999-2001 and 2005-2009 campaigns," *Journal of Nuclear Materials*, 2014.

[73] M. J. Rubel, G. De Temmerman, J. Coad, J. Vince, J. R. Drake, F. Le Guern, A. Murari, R. A. Pitts, C. Walker, and JET-EFDA contributors, "Mirror test for International Thermonuclear Experimental Reactor at the JET tokamak: An overview of the program," *Review of scientific instruments*, vol. 77, no. 6, p. 063501, 2006.

[74] M. Rubel, J. P. Coad, G. De Temmerman, D. Hole, D. Ivanova, J. Likonen, M. Rödig, A. Schmidt, I. Uytdenhouwen, A. Widdowson, *et al.*, "Comprehensive First Mirror Test for ITER at JET with carbon walls," in *Proceedings of the 23rd IAEA Fusion Energy Conference*, 2010.

[75] D. Ivanova, M. Rubel, A. Widdowson, P. Petersson, J. Likonen, L. Marot, E. Alves, A. Garcia-Carrasco, G. Pintsuk, and JET-EFDA contributors, "An overview of the comprehensive First Mirror Test in JET with ITER-like wall," *Physica Scripta*, vol. 2014, no. T159, p. 014011, 2014.

[76] J. P. Coad, H. G. Esser, J. Likonen, M. Mayer, G. Neill, V. Philipps, M. Rubel, and J. Vince, "Diagnostics for studying deposition and erosion processes in JET," *Fusion engineering and design*, vol. 74, no. 1, pp. 745–749, 2005.

[77] J. P. Coad, D. E. Hole, M. Rubel, A. Widdowson, and J. Vince, "Deposition results from rotating collector diagnostics in JET," *Physica Scripta*, vol. 2009, no. T138, p. 014023, 2009.

[78] H. G. Esser, V. Philipps, P. Wienhold, K. Sugiyama, A. Kreter, J. P. Coad, T. Tanabe, JET-EFDA contributors, *et al.*, "Post mortem analysis of a JET quartz microbalance system," *Journal of nuclear materials*, vol. 363, pp. 146–151, 2007.

[79] D. Bourgoin, G. G. Ross, S. Savoie, Y. Drolet, and E. Haddad, "Use of a quartz microbalance for plasma-wall interaction studies," *Journal of nuclear materials*, vol. 241, pp. 765–770, 1997.

[80] O. Vermesan, T. Rispal, and L. Soulier, "Low power ASIC for high temperature applications," in *High-Temperature Electronic Materials, Devices and Sensors Conference, 1998*, pp. 81–85, IEEE, 1998.

[81] G. F. Neill, J. P. Coad, H. G. Esser, and D. J. Wilson, "High temperature quartz microbalance for the measurement of deposition inside an experimental fusion device," in *HITEN Conference, Oslo, 5–8 June*, 2001.

[82] V. Rohde and M. Mayer, "On the formation of aC:D layers and parasitic plasmas underneath the roof baffle of the ASDEX upgrade divertor," *Journal of nuclear materials*, vol. 313, pp. 337–341, 2003.

[83] H. G. Esser, V. Philipps, M. Freisinger, P. Coad, G. F. Matthews, G. Neill, and JET-EFDA contributors, "Carbon deposition in the inner JET divertor measured by means of Quartz Microbalance," *Physica Scripta*, vol. 2004, no. T111, p. 129, 2004.

[84] A. Kreter, S. Brezinsek, J. P. Coad, H. G. Esser, W. Fundamenski, V. Philipps, R. A. Pitts, V. Rohde, T. Tanabe, and A. Widdowson, "Dynamics of erosion and deposition in tokamaks," *Journal of Nuclear Materials*, vol. 390, pp. 38–43, 2009.

[85] A. Kreter, H. G. Esser, S. Brezinsek, J. P. Coad, A. Kirschner, W. Fundamenski, V. Philipps, R. A. Pitts, and A. Widdowson, "Nonlinear impact of edge localized modes on carbon erosion in the divertor of the JET tokamak," *Physical review letters*, vol. 102, no. 4, p. 045007, 2009.

[86] K. Behringer, B. Denne, M. Forrest, M. Stamp, H. P. Summers, and Commission of the European Communities (CEC), Abingdon, United Kingdom, JET

Joint Undertaking, *Spectroscopic determination of impurity influx from localised surfaces*. Commission of the European Communities (CEC) JET Joint Undertaking, 1989.

[87] S. Brezinsek, A. Pospieszczyk, M. F. Stamp, A. Meigs, A. Kirschner, A. Huber, and P. H. Mertens, "Identification of molecular carbon sources in the JET divertor by means of emission spectroscopy," *Journal of nuclear materials*, vol. 337, pp. 1058–1063, 2005.

[88] S. Brezinsek, A. G. Meigs, S. Jachmich, M. F. Stamp, J. Rapp, R. Felton, R. A. Pitts, V. Philipps, A. Huber, R. Pugno, *et al.*, "The impact of divertor detachment on carbon sources in JET L-mode discharges," *Journal of Nuclear Materials*, vol. 390, pp. 267–273, 2009.

[89] G. F. Matthews, M. Stamp, P. Coad, J. Likonen, V. Philipps, M. Rubel, J. D. Strachan, and JET-EFDA contributors, "Material migration in JET," in *30th EPS Conference on Controlled Fusion and Plasma Physics*, vol. 27, 2003.

[90] S. Brezinsek, S. Jachmich, M. F. Stamp, A. G. Meigs, J. W. Coenen, K. Krieger, C. Giroud, M. Groth, V. Philipps, S. Grünhagen, *et al.*, "Residual carbon content in the initial ITER-like wall experiments at JET," *Journal of Nuclear Materials*, vol. 438, pp. S303–S308, 2013.

[91] J. W. Coenen, M. Sertoli, S. Brezinsek, I. Coffey, R. Dux, C. Giroud, M. Groth, A. Huber, D. Ivanova, K. Krieger, *et al.*, "Long-term evolution of the impurity composition and impurity events with the ITER-like wall at JET," *Nuclear Fusion*, vol. 53, no. 7, p. 073043, 2013.

[92] H. P. Summers, "The ADAS User Manual version 2.6," 2004. Available from: http://adas.phys.strath.ac.uk, accessed September 2015.

[93] A. Kallenbach, G. Fussmann, H.-M. Mayer, S. Pitcher, *et al.*, "The influence of spatially and temporally varying edge conditions on the interpretation of spectroscopic flux measurements," *Plasma physics and controlled fusion*, vol. 36, no. 8, p. 1299, 1994.

[94] N. H. Cho, D. K. Veirs, J. W. Ager Iii, M. D. Rubin, C. B. Hopper, and D. B. Bogy, "Effects of substrate temperature on chemical structure of amorphous carbon films," *Journal of applied physics*, vol. 71, no. 5, pp. 2243–2248, 1992.

[95] D. N. Hill, R. Ellis, W. Ferguson, D. E. Perkins, T. Petrie, and C. Baxi, "Infrared thermography of the DIII-D divertor targets," *Review of Scientific Instruments*, vol. 59, no. 8, pp. 1878–1880, 1988.

[96] E. Gauthier, H. Roche, E. Thomas, S. Droineau, B. Bertrand, J. B. Migozzi, W. Vliegenthart, L. Dague, P. Andrew, T. Tiscornia, *et al.*, "ITER-like wide-angle infrared thermography and visible observation diagnostic using reflective optics," *Fusion Engineering and Design*, vol. 82, no. 5, pp. 1335–1340, 2007.

[97] E. Gauthier, P. Andrew, G. Arnoux, Y. Corre, and H. Roche, "Plasma wall interaction during ELMs in JET," *Journal of nuclear materials*, vol. 363, pp. 1026–1031, 2007.

[98] G. Arnoux, I. Balboa, M. Clever, S. Devaux, P. De Vries, T. Eich, M. Firdaouss, S. Jachmich, M. Lehnen, P. Lomas, *et al.*, "Power handling of the JET ITER-like wall," *Physica Scripta*, vol. 2014, no. T159, p. 014009, 2014.

[99] P. Andrew, J. P. Coad, Y. Corre, T. Eich, A. Herrmann, G. F. Matthews, J. I. Paley, L. Pickworth, R. A. Pitts, and M. F. Stamp, "Outer divertor target deposited layers during reversed magnetic field operation in JET," *Journal of nuclear materials*, vol. 337, pp. 99–103, 2005.

[100] R. P. Doerner, M. J. Baldwin, G. De Temmerman, J. Hanna, D. Nishijima, J. Roth, K. Schmid, G. R. Tynan, and K. Umstadter, "Codeposition of deuterium with ITER materials," *Nuclear Fusion*, vol. 49, no. 3, p. 035002, 2009.

[101] R. A. Pitts, J. P. Coad, D. P. Coster, G. Federici, W. Fundamenski, J. Horacek, K. Krieger, A. Kukushkin, J. Likonen, G. F. Matthews, *et al.*, "Material erosion and migration in tokamaks," *Plasma physics and controlled fusion*, vol. 47, no. 12B, p. B303, 2005.

[102] A. Loarte, R. D. Monk, J. R. Martin-Solis, D. J. Campbell, A. V. Chankin, S. Clement, S. J. Davies, J. Ehrenberg, S. K. Erents, H. Y. Guo, *et al.*, "Plasma detachment in JET Mark I divertor experiments," *Nuclear Fusion*, vol. 38, no. 3, p. 331, 1998.

[103] G. Federici, C. H. Skinner, J. N. Brooks, J. P. Coad, C. Grisolia, A. A. Haasz, A. Hassanein, V. Philipps, C. S. Pitcher, J. Roth, *et al.*, "Plasma-material interactions in current tokamaks and their implications for next step fusion reactors," *Nuclear Fusion*, vol. 41, no. 12, p. 1967, 2001.

[104] R. Simonini, A. Taroni, M. Keilhacker, G. Radford, J. Spence, G. Vlases, M. L. Watkins, and S. Weber, "Modelling impurity control at JET," *Journal of nuclear materials*, vol. 196, pp. 369–373, 1992.

[105] D. Reiter, C. May, D. Coster, and R. Schneider, "Time dependent neutral gas transport in tokamak edge plasmas," *Journal of nuclear materials*, vol. 220, pp. 987–992, 1995.

[106] E. Cupini, A. De Matteis, and R. Simonini, "NIMBUS-Monte Carlo Simulation of Neutral Particle Transport in Fusion Devices, NET Rep," tech. rep., EUR XII-324/9, 1984.

[107] A. Kallenbach, Y. Andrew, M. Beurskens, G. Corrigan, T. Eich, S. Jachmich, M. Kempenaars, A. Korotkov, A. Loarte, G. Matthews, *et al.*, "EDGE2D modelling of edge profiles obtained in JET diagnostic optimized configuration," *Plasma physics and controlled fusion*, vol. 46, no. 3, p. 431, 2004.

[108] J. P. Coad, P. Andrew, S. K. Erents, D. E. Hole, J. Likonen, M. Mayer, R. Pitts, M. Rubel, J. D. Strachan, E. Vainonen-Ahlgren, *et al.*, "Erosion and deposition in the JET MkII-SRP divertor," *Journal of nuclear materials*, vol. 363, pp. 287–293, 2007.

[109] J. F. Ziegler, J. P. Biersack, and M. D. Ziegler, *SRIM, the stopping and range of ions in matter*. Lulu, 2008.

[110] J. N. Brooks, "Modeling and analysis of erosion and redeposition for limiter and divertor impurity control systems," 1983.

[111] J. N. Brooks and D. G. Whyte, "Modelling and analysis of DIII-D/DiMES sputtered impurity transport experiments," *Nuclear Fusion*, vol. 39, no. 4, p. 525, 1999.

[112] A. Kirschner, V. Philipps, J. Winter, and U. Kögler, "Simulation of the plasma-wall interaction in a tokamak with the Monte Carlo code ERO-TEXTOR," *Nuclear Fusion*, vol. 40, no. 5, p. 989, 2000.

[113] D. Naujoks, R. Behrisch, J. P. Coad, and L. C. J. M. De Kock, "Material transport by erosion and redeposition on surface probes in the scrape-off layer of JET," *Nuclear fusion*, vol. 33, no. 4, p. 581, 1993.

[114] A. Kirschner, P. Wienhold, V. Philipps, J. P. Coad, A. Huber, and U. Samm, "Modelling of carbon transport in fusion devices: evidence of enhanced re-erosion of in-situ re-deposited carbon," *Journal of nuclear materials*, vol. 328, no. 1, pp. 62–66, 2004.

[115] D. Borodin, M. F. Stamp, A. Kirschner, C. Björkas, S. Brezinsek, J. Miettunen, D. Matveev, C. Silva, O. Van Hoey, M. Groth, *et al.*, "Spectroscopic measurements of Be erosion at JET ILW and interpretation with ERO modelling," *Journal of Nuclear Materials*, vol. 438, pp. S267–S271, 2013.

[116] K. Schmid, M. Reinelt, and K. Krieger, "An integrated model of impurity migration and wall composition dynamics for tokamaks," *Journal of Nuclear Materials*, vol. 415, no. 1, pp. S284–S288, 2011.

[117] P. C. Stangeby and J. D. Elder, "Calculation of observable quantities using a divertor impurity interpretive code, DIVIMP," *Journal of nuclear materials*, vol. 196, pp. 258–263, 1992.

[118] K. Schmid, K. Krieger, S. W. Lisgo, G. Meisl, S. Brezinsek, and JET EFDA Contributors, "Quantitative modeling of fuel retention in the JET-C and JET-ILW wall configurations by WallDYN and predictions for ITER," *Journal of Nuclear Materials*, 2014.

[119] K. Krieger, S. Brezinsek, M. Reinelt, S. W. Lisgo, J. W. Coenen, S. Jachmich, S. Marsen, A. Meigs, G. Van Rooij, M. Stamp, *et al.*, "Beryllium migration and evolution of first wall surface composition in the JET ILW configuration," *Journal of Nuclear Materials*, vol. 438, pp. S262–S266, 2013.

[120] H. Esser, V. Philipps, M. Freisinger, A. Widdowson, K. Heinola, A. Kirschner, S. Möller, P. Petersson, S. Brezinsek, A. Huber, *et al.*, "Material deposition on inner divertor quartz-micro balances during ITER-like wall operation in JET," *Journal of Nuclear Materials*, vol. 463, pp. 796–799, 2015.

[121] H. G. Esser, G. Neill, P. Coad, G. F. Matthews, D. Jolovic, D. Wilson, M. Freisinger, V. Philipps, *et al.*, "Quartz microbalance: a time resolved diagnostic to measure material deposition in JET," *Fusion engineering and design*, vol. 66, pp. 855–860, 2003.

[122] Insituto Superior Técnico, "Laboratory of accelerators and X-rays diffraction," January 2015. Available from http://www.fermentas.com/techinfo/nucleicacids/maplambda.htm, accessed September 2015.

[123] D. Schmaus and I. Vickridge, "MeV ion beam analytical methods," in *Analytical methods for corrosion science and engineering*, CRC Press, 2005.

[124] M. Mayer, "Nuclear reaction analysis (NRA)," 2003. Workshop on nuclear data for science and technogy: materials analysis, Trieste, Italy.

[125] W.-K. Chu, J. W. Mayer, and M.-A. Nicolet, "Backscattering spectroscopy," 1978.

[126] E. C. A. W. S. Bundle, C R, "Ion scattering techniques," in *Encyclopedia of Materials Characterization*, Butterworth-Heinemann, 1992.

[127] A. Kirschner, D. Matveev, D. Borodin, M. Airila, S. Brezinsek, M. Groth, S. Wiesen, A. Widdowson, J. Beal, H. G. Esser, *et al.*, "Modelling of the material transport and layer formation in the divertor of JET: Comparison of ITER-like wall with full carbon wall conditions," *Journal of Nuclear Materials*, 2014.

[128] J. Beal, A. Widdowson, K. Heinola, A. Baron-Wiechec, K. Gibson, J. Coad, E. Alves, B. Lipschultz, A. Kirschner, G. Matthews, *et al.*, "Analysis of rotating collectors from the private region of JET with carbon wall and metallic ITER-like wall," *Journal of nuclear materials*, vol. 463, pp. 818–821, 2015.

[129] L. L. Lao, H. S. John, R. D. Stambaugh, A. G. Kellman, and W. Pfeiffer, "Reconstruction of current profile parameters and plasma shapes in tokamaks," *Nuclear fusion*, vol. 25, no. 11, p. 1611, 1985.

[130] M. Mayer, V. Rohde, T. Pütterich, P. Coad, P. Wienhold, ASDEX Upgrade Team, JET-EFDA Contributors, *et al.*, "Carbon erosion and migration in fusion devices," *Physica Scripta*, vol. 2004, no. T111, p. 55, 2004.

[131] K. Schmid, M. Mayer, C. Adelhelm, M. Balden, S. Lindig, *et al.*, "Impact of gyro-motion and sheath acceleration on the flux distribution on rough surfaces," *Nuclear Fusion*, vol. 50, no. 10, p. 105004, 2010.

[132] J. Beal, A. Widdowson, K. Heinola, A. Baron-Wiechec, K. J. Gibson, J. P. Coad, E. Alves, B. Lipschultz, A. Kirschner, H. G. Esser, G. F. Matthews, S. Brezinsek, and JET Contributors, "Deposition in the inner and outer corners of the JET divertor with carbon wall and metallic ITER-like wall," *Physica Scripta*, vol. 2016, no. T167, p. 014052, 2016.

[133] G. De Temmerman and R. Doerner, "Revised scaling equation for the prediction of tritium retention in beryllium co-deposited layers," *Nuclear Fusion*, vol. 49, no. 4, p. 042002, 2009.

[134] S. Brezinsek, A. Widdowson, M. Mayer, V. Philipps, P. Baron-Wiechec, J. Coenen, K. Heinola, A. Huber, J. Likonen, P. Petersson, *et al.*, "Beryllium migration in JET ITER-like wall plasmas," *Nuclear fusion*, vol. 55, no. 6, p. 063021, 2015.

[135] H. G. Esser, A. Kreter, V. Philipps, A. Widdowson, J. P. Coad, and M. Stamp, "Erosion and deposition behaviour of a-C:H layers in the private flux region of the JET MKII-HD divertor," *Journal of Nuclear Materials*, vol. 390-391, pp. 148 – 151, 2009. Proceedings of the 18th International Conference on Plasma-Surface Interactions in Controlled Fusion Devices.

[136] M. Rubel, D. Ivanova, J. P. Coad, G. D. Temmerman, J. Likonen, L. Marot, A. Schmidt, A. Widdowson, and JET-EFDA contributors, "Overview of the second stage in the comprehensive mirrors test in JET," *Physica Scripta*, vol. 2011, no. T145, p. 014070, 2011.

[137] A. Baron-Wiechec, A. Widdowson, E. Alves, C. Ayres, N. Barradas, S. Brezinsek, J. Coad, N. Catarino, K. Heinola, J. Likonen, G. Matthews, M. Mayer, P. Petersson, M. Rubel, W. van Renterghem, and I. Uytdenhouwen, "Global erosion and deposition patterns in JET with the ITER-like wall," *Journal of Nuclear Materials*, vol. 463, pp. 157 – 161, 2015. Proceedings of the 21st International Conference on Plasma-Surface Interactions in Controlled Fusion Devices, Kanazawa, Japan, May 26-30, 2014.

[138] A. Kirschner, V. Philipps, D. P. Coster, S. K. Erents, H. G. Esser, G. Federici, A. S. Kukushkin, A. Loarte, G. F. Matthews, J. Roth, *et al.*, "Experimental observations and modelling of carbon transport in the inner divertor of JET," *Journal of nuclear materials*, vol. 337, pp. 17–24, 2005.

[139] A. Von Keudell, W. Möller, and R. Hytry, "Deposition of dense hydrocarbon films from a nonbiased microwave plasma," *Applied physics letters*, vol. 62, no. 9, pp. 937–939, 1993.

[140] G. Duxbury, M. Stamp, and H. Summers, "Observations and modelling of diatomic molecular spectra from JET," *Plasma physics and controlled fusion*, vol. 40, no. 3, p. 361, 1998.

[141] M. Mayer, R. Behrisch, H. Plank, J. Roth, G. Dollinger, and C. Frey, "Codeposition of hydrogen with beryllium, carbon and tungsten," *Journal of nuclear materials*, vol. 230, no. 1, pp. 67–73, 1996.

[142] G. De Temmerman, M. Baldwin, R. Doerner, D. Nishijima, R. Seraydarian, and K. Schmid, "Insight into the co-deposition of deuterium with beryllium: Influence of the deposition conditions on the deuterium retention and release," *Journal of Nuclear Materials*, vol. 390, pp. 564–567, 2009.

[143] M. Mayer, S. Krat, W. Van Renterghem, A. Baron-Wiechec, S. Brezinsek, I. Bykov, P. Coad, Yu. Gasparyan, K. Heinola, J. Likonen, A. Pisarev, C. Ruset, G. de Saint-Aubin, A. Widdowson, and JET Contributors, "Erosion and deposition in the JET divertor during the first ILW campaign." Presented at 15th International Conference on Plasma-Facing Materials and Components for Fusion Applications (PFMC-15), Aix-en-Provence, May 2015.

[144] K. Schmid, K. Krieger, S. Lisgo, G. Meisl, S. Brezinsek, and JET Contributors, "WALLDYN simulations of global impurity migration in JET and extrapolations to ITER," *Nuclear Fusion*, vol. 55, no. 5, p. 053015, 2015.

[145] V. V. Bobkov, F. Braun, R. Dux, A. Herrmann, L. Giannone, A. Kallenbach, A. Krivska, H. Müller, R. Neu, J.-M. Noterdaeme, *et al.*, "Assessment of compatibility of ICRF antenna operation with full W wall in ASDEX Upgrade," *Nuclear Fusion*, vol. 50, no. 3, p. 035004, 2010.

[146] C. Klepper, P. Jacquet, V. Bobkov, L. Colas, T. Biewer, D. Borodin, A. Czarnecka, C. Giroud, E. Lerche, V. Martin, *et al.*, "RF sheath-enhanced beryllium sources at JET's ICRH antennas," *Journal of Nuclear Materials*, vol. 438, pp. S594–S598, 2013.

[147] W. Fundamenski, R. A. Pitts, and JET EFDA contributors, "A model of ELM filament energy evolution due to parallel losses," *Plasma Physics and Controlled Fusion*, vol. 48, no. 1, p. 109, 2006.

[148] C. Guillemaut, A. Jardin, J. Horacek, A. Autricque, G. Arnoux, J. Boom, S. Brezinsek, J. W. Coenen, E. D. L. Luna, S. Devaux, T. Eich, C. Giroud, D. Harting, A. Kirschner, B. Lipschultz, G. F. Matthews, D. Moulton, M. O'Mullane, and M. Stamp, "Ion target impact energy during type I edge localized modes in JET ITER-like wall," *Plasma Physics and Controlled Fusion*, vol. 57, no. 8, p. 085006, 2015.

[149] N. D. Harder, S. Brezinsek, T. Pütterich, N. Fedorczak, G. Matthews, A. Meigs, M. Stamp, M. van de Sanden, G. V. Rooij, and JET Contributors, "ELM-resolved divertor erosion in the JET ITER-like wall," *Nuclear Fusion*, vol. 56, no. 2, p. 026014, 2016.

[150] R. Pitts, S. Carpentier, F. Escourbiac, T. Hirai, V. Komarov, A. Kukushkin, S. Lisgo, A. Loarte, M. Merola, R. Mitteau, A. Raffray, M. Shimada, and P. Stangeby, "Physics basis and design of the ITER plasma-facing components," *Journal of Nuclear Materials*, vol. 415, no. 1, Supplement, pp. S957 – S964, 2011. Proceedings of the 19th International Conference on Plasma-Surface Interactions in Controlled Fusion.